

AD-A165 864

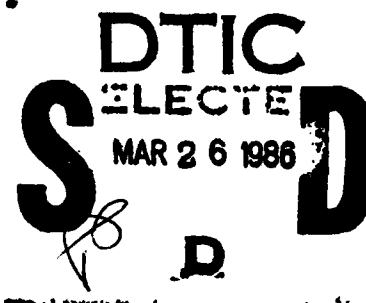
RADC-TR-85-165
Final Technical Report
September 1985



12

ACROSS ELEVEN (ACTIVE CONTROL OF SPACE STRUCTURES)

The Charles Stark Draper Laboratory, Inc.



Sponsored by
Defense Advanced Research Projects Agency (DOD)
ARPA Order No. 3655

APPROVED FOR PUBLIC RELEASE; DISTRIBUTION UNLIMITED

The views and conclusions contained in this document are those of the authors and should not be interpreted as necessarily representing the official policies, either expressed or implied, of the Defense Advanced Research Projects Agency or the U.S. Government.

DTIC FILE COPY

ROME AIR DEVELOPMENT CENTER
Air Force Systems Command
Griffiss Air Force Base, NY 13441-5700

86 3 26 001

This report has been reviewed by the RADC Public Affairs Office (PA) and is releasable to the National Technical Information Service (NTIS). At NTIS it will be releasable to the general public, including foreign nations.

RADC-TR-85-165 has been reviewed and is approved for publication.

APPROVED: *Richard W. Carman*

RICHARD W. CARMAN
Project Engineer

APPROVED: *Frank J. Rehm*

FRANK J. REHM
Technical Director
Surveillance Division

FOR THE COMMANDER: *John A. Ritz*

JOHN A. RITZ
Acting Chief, Plans Office

If your address has changed or if you wish to be removed from the RADC mailing list, or if the addressee is no longer employed by your organization, please notify RADC (OCSP) Griffiss AFB NY 13441-5700. This will assist us in maintaining a current mailing list.

Do not return copies of this report unless contractual obligations or notices on a specific document requires that it be returned.

ACOSS ELEVEN (ACTIVE CONTROL OF SPACE STRUCTURES)

D. R. Hegg
G. J. Kissel
N. H. McClamroch
M. J. Villalba
I. G. Rosen
J. D. Turner

H. M. Chun
F. N. R. Ayer
T. H. Brooks
T. C. Henderson
D. B. Kasle
J. P. Govignon

Contractor: The Charles Stark Draper Laboratory, Inc.
Contract Number: F30602-81-C-0180
Effective Date of Contract: 27 April 1981
Contract Expiration Date: 27 April 1984
Short Title of Work: ACOSS ELEVEN (Active Control of
Space Structures)
Program Code Number: 1E20
Period of Work Covered: Oct 83 - Jul 84

Principal Investigator: Dr. Keto Soosaar
Phone: (617) 484-3125

Project Engineer: Richard Carman
Phone: (315) 330-4481

Approved for public release; distribution unlimited.

This research was supported by the Defense Advanced Research Projects Agency of the Department of Defense and was monitored by Richard Carman (OCSP), Griffiss AFB NY 13441-5700 under Contract F30602-81-C-0180.

UNCLASSIFIED
SECURITY CLASSIFICATION OF THIS PAGE

REPORT DOCUMENTATION PAGE

1a. REPORT SECURITY CLASSIFICATION UNCLASSIFIED			1b. RESTRICTIVE MARKINGS N/A		
2a. SECURITY CLASSIFICATION AUTHORITY N/A			3. DISTRIBUTION/AVAILABILITY OF REPORT Approved for public release; distribution unlimited.		
2b. DECLASSIFICATION/DOWNGRADING SCHEDULE N/A					
4. PERFORMING ORGANIZATION REPORT NUMBER(S) CSDL-R-1721			5. MONITORING ORGANIZATION REPORT NUMBER(S) RADC-TR-85-165		
6a. NAME OF PERFORMING ORGANIZATION The Charles Stark Draper Laboratory, Inc.		6b. OFFICE SYMBOL (if applicable)	7a. NAME OF MONITORING ORGANIZATION Rome Air Development Center (OCSP)		
6c. ADDRESS (City, State, and ZIP Code) 555 Technology Square Cambridge MA 02139			7b. ADDRESS (City, State, and ZIP Code) Griffiss AFB NY 13441-5700		
8a. NAME OF FUNDING/SPONSORING ORGANIZATION Defense Advanced Research Projects Agency		8b. OFFICE SYMBOL (if applicable) STO	9. PROCUREMENT INSTRUMENT IDENTIFICATION NUMBER F30602-81-C-0180		
8c. ADDRESS (City, State, and ZIP Code) 1400 Wilson Blvd Arlington VA 22209			10. SOURCE OF FUNDING NUMBERS		
			PROGRAM ELEMENT NO. 62301E	PROJECT NO. C655	TASK NO. 01
			WORK UNIT ACCESSION NO. 04		
11. TITLE (Include Security Classification) ACOSS ELEVEN (ACTIVE CONTROL OF SPACE STRUCTURES)					
12. PERSONAL AUTHOR(S) D.R. Hegg, G.J. Kissel, N.H. McClamroch, M.J. Villalba, I.G. Rosen, J.D. Turner, (Cont'd)					
13a. TYPE OF REPORT Final		13b. TIME COVERED FROM Oct 83 TO Jul 84		14. DATE OF REPORT (Year, Month, Day) September 1985	
				15. PAGE COUNT 276	
16. SUPPLEMENTARY NOTATION N/A					
17. COSATI CODES			18. SUBJECT TERMS (Continue on reverse if necessary and identify by block number)		
FIELD	GROUP	SUB-GROUP			
17	08		Space-based IR Surveillance Systems		
22	02		Infrared Terrestrial Scene Simulation, (Cont'd)		
			Signal Processors		
19. ABSTRACT (Continue on reverse if necessary and identify by block number) <u>Simulation Extensions:</u> The overall objective of the Simulation Extensions project is to identify and quantify those generic mission, scenario and sensor parameters (as well as their interactions) which drive the performance of space-based staring IR surveillance systems. The approach taken to achieve this overall objective has proceeded along two main avenues: Simulation Enhancements and Simulation Applications. During the current reporting period the Simulation Enhancements effort has concentrated in three areas: continuation of the Generic Scene Simulation development: enhancements to the Signal Processor Simulation; and expansion of the capabilities of the Integrated Large Space Structures Simulation. The Simulation Applications effort has been focused most recently on simulation and evaluation of algorithms for line-of-sight jitter reduction. <u>HALO Optics/ROFT:</u> Within the framework of the ROFT program, the characterization of materials for large space mirrors is obtained by examining the impact of material properties on the performance of mirrors. The study recognizes major differences for					
20. DISTRIBUTION/AVAILABILITY OF ABSTRACT <input checked="" type="checkbox"/> UNCLASSIFIED/UNLIMITED <input type="checkbox"/> SAME AS RPT. <input type="checkbox"/> DTIC USERS			21. ABSTRACT SECURITY CLASSIFICATION UNCLASSIFIED		
22a. NAME OF RESPONSIBLE INDIVIDUAL RICHARD W. CARMAN			22b. TELEPHONE (Include Area Code) (315) 330-4481		22c. OFFICE SYMBOL RADC (OCSP)

DD FORM 1473, 84 MAR

83 APR edition may be used until exhausted.
All other editions are obsolete.

SECURITY CLASSIFICATION OF THIS PAGE

UNCLASSIFIED

UNCLASSIFIED

Block 18 (Cont'd)

Draper Integrated Simulations
Materials Characterization for Space Optics
Large Flexible Space Structures,
Line-of-Sight Stabilization,
Precision Pointing,
Vibration Control,
Wideband Disturbance Accommodation,
Reduced-Order Modeling,
Actuator/Sensor Selection,
Disturbance-Rejection Control,
Linear-Quadratic-Gaussian Control,
Loop Transfer Recovery,
Stability Robustness

→ stability and
Performance Robustness,
ACOSS Model No. 2,
Electromechanical Actuator Dynamics,
Transmission-type Actuator *→ a vcl*
Reaction-type Actuators,
High Resolution Spectrum Identification,
Autocorrelation Desampling,
Distributed Parameter System Identification,
Cubic Spline Approximation,
Large Angle Slew Control
Linear Tracking/Disturbance Accommodation
Control,
Analytic Fourier Transform.

Block 12 (Cont'd)

H.M. Chun, F.N.R. Ayer, T.H. Brooks, T.C. Henderson, D.B. Kasle, J.P. Govignon

Block 19 (Cont'd)

material requirements between IR systems and laser applications.

Active Control of Space Structures: The main lines of effort in flexible structure control have been: (a) Synthesis of reduced-order control for vibration suppression; (b) System identification, with special attention to the resolution of closely-spaced modes; and (c) Generation of smooth large-angle slew control. In this report, major accomplishments during the course of the contract are summarized, and current results are presented in detail. Highlights of current results are as follows. A final account is given of insights obtained during a systematic investigation of mutual interactions within the overall active control synthesis process between reduced-order modeling, actuator and sensor selection (not necessarily colocated), and controller feedback strategy determination. Using linear multivariable loop transfer recovery, full-order stability robustness to unmodeled high-frequency dynamics in the presence of wideband disturbances is demonstrated on ACOSS Model No. 2. A perspective on electromechanical actuator dynamics modeling is presented. Interface constraints with the controller synthesis process associated with the use of high-resolution spectrum estimation for reduced-order modeling are analyzed. Parametric use of the data sampling period to assist in the resolution of closely-spaced modes is discussed/demonstrated. An improved technique for parameter estimation in distributed-parameter systems is generated. The technique is applied to several hybrid systems (i.e., systems modeled with both lumped and distributed elements). Linear tracking solutions for large angle slew control incorporating discrete-frequency disturbance accommodation are presented. A strong emphasis is placed upon developing closed-form solutions to Riccati-like matrix equations to improve computational efficiency.

UNCLASSIFIED

ACKNOWLEDGEMENT

This report was prepared by The Charles Stark Draper Laboratory, Inc. (CSDL), under Contract F30602-81-C-0180. The research summarized herein was supported by the Advanced Research Projects Agency of the Department of Defense (STO/Lt. Col. Allen F. Herzberg) and monitored by the Rome Air Development Center (OCSP/Mr. Richard W. Carman).

The program manager for ACOSS-ELEVEN at CSDL was Dr. Keto Soosaar. The individual Project Leaders were: SIMULATION EXTENSIONS--Mr. Thomas H. Brooks; HALO OPTICS/ROFT--Dr. Virendra N. Mahajan (through August 1983) and Mr. Francois N. R. Ayer (thereafter); ACTIVE CONTROL OF SPACE STRUCTURES--Mr. Robert R. Strunce (through December 1983) and Dr. Daniel R. Hegg (thereafter). The authors of this report are: Mr. Thomas H. Brooks (Sections 1.1, 2.1), Photon Research Associates--Mr. David Anding, GENESSIS Program Manager (Section 2.2.1), Mr. Timothy Henderson (Section 2.2.2), Mr. David B. Kasle (Section 2.2.3), Mr. Jacques P. Govignon (Section 2.3), Mr. Francois N. R. Ayer (Sections 1.2, 3), Dr. Daniel R. Hegg (Sections 1.3, 4, 5), Mr. Glen J. Kissel (Section 6), Dr. N. Harris McClamroch of the University of Michigan (Section 7), Mr. Michael J. Villalba (Section 8), Dr. I. Gary Rosen (Section 9), and Dr. James D. Turner and Mr. Hon M. Chun (Section 10). Assistance from Mr. Saul Serben (Software support - Sections 2.2.1, 2.2.3, 2.3); Dr. Eliezer Fogel (Sections 5, 8); Mr. Glen J. Kissel (Section 5); Mr. David P. Latimer and Mr. Patrick B. Battstone (Software support - Sections 5, 6); Dr. N. Harris McClamroch (Section 5); Mr. Joel A. Storch, Mr. Stephen S. Gates, and Major James M. Crowley of the United States Air Force Academy (Section 9); and Dr. Jer-Nan Juang of the National Aeronautics and Space Administration Langley Research Center (Section 10) is gratefully acknowledged. Ms. Mary M. Markley and Ms. Janice M. McCarthy (Sections 1-4) and Ms. Lisa E. Kern (Sections 5-10) did the typing.



i/ii

Accession For	
NTIS CRA&I	<input checked="" type="checkbox"/>
DTIC TAB	<input type="checkbox"/>
Unannounced	<input type="checkbox"/>
Justification	
By	
Distribution/	
Availability Codes	
Dist	Avail and/or Special
A-1	

TABLE OF CONTENTS

<u>Section</u>	<u>Page</u>
1 INTRODUCTION	1
1.1 Simulation Extensions	1
1.2 Generic Requirements for the ROFT Program	1
1.3 Active Control of Space Structures	3
2 SIMULATION EXTENSIONS	7
2.1 Introduction	7
2.1.1 Simulation Enhancements	7
2.1.2 Simulation Applications	9
2.2 Simulation Enhancements	9
2.2.1 Generic Scene Simulation (GENESSIS)	9
2.2.2 Enhancements of the Integrated Large Space Structures Simulation (ILS ³)	13
2.2.3 Enhancements to the Signal Processor Simulation ..	16
2.3 Simulation Applications	23
2.3.1 Clutter Leakage Study	23
2.3.2 Evaluation of Algorithms for the Post-Detection Compensation of Line-of-sight (LOS) Jitter Effects	27
References	31
3 GENERIC MATERIAL REQUIREMENTS FOR THE ROFT PROGRAM	33
3.1 Introduction	33
3.2 Materials Characterization: Approach and Results Summary	35
3.3 Conclusions and Recommendations	37

TABLE OF CONTENTS (CONT.)

<u>Section</u>	<u>Page</u>
4 ACTIVE CONTROL OF SPACE STRUCTURES: OVERVIEW	43
4.1 Scope	43
4.2 Major Accomplishments	44
4.2.1 Vibration Control	44
4.2.2 System Identification	45
4.2.3 Large Angle Slew Control	46
4.3 Summary of Current Results	46
4.4 Applications	49
References	49
5 ACTIVE CONTROL SYNTHESIS FOR WIDEBAND DISTURBANCE ACCOMMODATION IN PRECISION FLEXIBLE SPACE STRUCTURES	53
5.1 Motivation	53
5.1.1 The Synthesis Problem	53
5.1.2 Initial Approaches to the Synthesis Problem	54
5.2 Current Results in Active Control Synthesis	58
5.2.1 Stability Robustness to Unmodeled High-Frequency Dynamics	58
5.2.2 Independent (Noncolocated) Sensor Selection	59
5.2.3 Incorporation of System Identification into the Synthesis Process	83
5.3 Principal Contributions	96
5.4 Open Questions	98
References	99
6 STABILITY ENHANCEMENT IN STRUCTURAL CONTROL	103
6.1 Introduction	103
6.2 Present Controller Results	104
6.3 Frequency Domain Conditions for Stability Robustness ...	105
6.4 Design Procedure to Enhance Stability Robustness	113

TABLE OF CONTENTS (CONT.)

<u>Section</u>	<u>Page</u>
6.5 Demonstration of Stability Enhancement	123
6.6 Discussion, Conclusions, and Recommendations	137
References	138
 7 MODELING FOR FLEXIBLE STRUCTURE CONTROL WITH ELECTROMECHANICAL ACTUATOR DYNAMICS	 141
7.1 Introduction	141
7.2 A Generic Case: Models for Possible Actuator Configurations	 142
7.2.1 Structure and Inertial-Based Actuator	142
7.2.2 Structure and Structure-based Transmission-type Actuator	 144
7.2.3 Structure and Structure-based Reaction-type Actuator	 146
7.3 Feedback Control Issues	149
7.4 Summary	150
References	150
 8 POLE LOCATION MANIPULATION FOR IMPROVED SPECTRAL RESOLUTION .	153
8.1 Introduction	153
8.2 Sampling Considerations for Continuous-Time Spectrum Estimation	 154
8.3 The Use of Desampling to Improve Spectral Resolution ...	166
8.4 Conclusion	169
References	176
 9 APPROXIMATION TECHNIQUES FOR PARAMETER ESTIMATION AND FEEDBACK CONTROL WITH DISTRIBUTED MODELS OF LARGE FLEXIBLE STRUCTURES	 177
9.1 Introduction	177

TABLE OF CONTENTS (CONT.)

<u>Section</u>	<u>Page</u>
9.2 The Identification Problem	181
9.2.1 A Distributed Parameter Model	181
9.2.2 Weak Solutions	184
9.2.3 Strong Solutions	185
9.2.4 Formulation of the Identification Problem	191
9.3 An Approximation Scheme	192
9.3.1 Approximating Identification Problems	192
9.3.2 Convergence Results	195
9.4 Numerical Results	205
References	215
10 LARGE ANGLE SPACECRAFT MANEUVERS USING AN ANALYTIC SOLUTION FOR TRACKING AND DISTURBANCE ACCOMMODATION	219
10.1 Overview	219
10.2 Introduction	220
10.3 The Optimal Tracking and Disturbance-Accommodation Control Problem	221
10.4 Necessary Conditions and Solutions for the Optimal Control	223
10.4.1 Closed Form Solution for the Riccati Equation ...	223
10.4.2 Closed Form Solution for the Prefilter Equation .	224
10.5 Closed Form Solution for the State Trajectory Equation .	226
10.6 Closed Form Solution for the Residual State Trajectory Equation	229
10.7 Illustration Examples	230
10.8 Analytic Fourier Transform for the Control	242
10.8.1 Reducing Subspace Coordinate Transformation	244
10.8.2 Solution for the Uncoupling Transformation Vector	245

TABLE OF CONTENTS (CONT.)

<u>Section</u>	<u>Page</u>
10.8.3 Example Application	246
10.9 Appendix	250
10.9.1 Closed Form Solution for the Prefilter Equation Matrix Integrals	250
10.9.2 Closed Form Solutions for the Residual State Trajectory Matrix Integrals	252
10.10 Conclusions	254
References	255

SECTION 1

INTRODUCTION

1.1 Simulation Extensions

Within the context of the overall ACOSS Eleven Program, the objective of the Simulation Extensions Project has been to identify and quantify those generic mission, scenario and sensor parameters (as well as their interactions) which drive the performance of staring infrared (IR) space-based surveillance systems. This project has been divided into two broad tasks: Simulation Enhancements, and Simulation Applications.

Work in the Simulation Enhancement Task has been directed toward generalizing those models in the Draper Integrated Simulations (DIS) which are too limited in scope or perhaps restricted to one particular system. This task has been the primary focus of the Simulation Extensions Project, and, accordingly, has received the bulk of the available support. The Simulation Applications Task has studied issues related to generic surveillance system performance drivers using tools developed under the Simulation Enhancements Task.

Section 2 summarizes the technical accomplishments of the Simulation Extensions Project and provides a guide to detailed technical documentation generated during the course of the project.

1.2 Generic Requirements for the ROFT Program

The development of space-based infrared surveillance systems and space-based lasers is subordinated primarily to the availability of very large, high precision optics. Current technology and existing facilities cannot produce in a timely fashion, high performance mirrors, both in quality and quantity, to respond to the needs of the systems envisioned. The Rapid Optics Fabrication Technology (ROFT) Program will attempt to discover and develop technologies which will significantly decrease the time it takes to produce optics.

The objective of this study reported in Section 3, is to provide broad requirements and constraints for the mechanical and thermal properties of materials envisioned for the design and rapid fabrication of large space mirrors. By inspecting the constitutive equations relating mirror deformations to input disturbances, the relative importance of material parameters is identified. It is also recognized that the requirements on mirror material properties can vary widely depending on the space applications. Surveillance systems, operating at cryogenic temperatures impose different demands on materials than do the laser systems for which the operational temperature is expected to vary between 300° K and 400° K. Dynamic environments exhibit significant differences as well, and this difference may impact the choice of other properties required of the mirror materials.

It must be emphasized that this study does not presuppose a specific mirror concept with defined structural and configurational characteristics. While this approach is intentional for the findings to remain general, it limits our ability to obtain specific requirements for the contemplated mirror materials. Furthermore the effectiveness of possible controls (whether thermal or mechanical), in terms of relieving demands on material properties can only be evaluated in the context of a defined mirror concept. As a result only estimates on mirror material requirements can be provided and they have been derived from simplified analytical expressions and engineering experience in the design, modelling and analyses of space mirrors.

For a large number of existing and potential materials, that include metals, composites and ceramics, all relevant properties have been tabulated for two extreme operational temperatures (150° K and 350° K). The plots relating important material parameters can be useful in delineating domains of acceptability for a potential new material. The proposed material requirements can be viewed as somewhat flexible so as to permit trade-offs between properties for a particular design concept. Past experience has shown that the most likely candidate for such a mirror will probably be a thin face-sheet on actuators supported by a thermally stable substrate.

However, it is hoped that dramatic changes and/or improvements in some thermal properties, especially, might lead to completely novel concepts that ultimately could be produced at the desired rapid rate.

It should be remembered that the objective of the ROFT program is the rapid fabrication of high precision large space optics. The results of this study can only support this attempt by providing guidelines to the designer and fabrication engineer who selects possible materials. The generic specifications of mirror materials, therefore, can be viewed as constraints to the selection of a material amenable to rapid fabrication processes. Many other issues related to optical and perhaps electrical material properties need to be considered. Finally the fabrication process could be adversely affected by some mechanical and thermal properties of a material that is otherwise acceptable in the final product.

1.3 Active Control of Space Structures

Surveillance missions envisioned for future spaceborne optical systems strongly suggest the need for active control and embody several factors which--taken together--pose a formidable challenge from the perspective of control science and technology. First, the supporting structures for the optical system can be expected to be substantially non-rigid, exhibiting low and clustered characteristic frequencies of vibration and very small inherent damping. Moreover because of their anticipated geometric complexity, substantial deterministic uncertainty in available finite-element structural models will persist. Second, the disturbance environment may be severe, involving disturbances with nonnegligible power spectral density over a wide frequency range. Finally, high precision performance specification in regard to rapid reorientation and attitude regulation of the optical axis are certain. Such requirements imply the capacity for effective suppression of structural vibrations.

The factors cited motivate the three main lines of effort in active control technology development that have been pursued under the present contract: (1) Synthesis of reduced-order control for vibration

suppression; (2) System identification, with special attention to the problem of resolving closely-spaced modes; and (3) Generation of smooth large-angle-slew control.

An overview of the work accomplished and principal contributions made in these three areas over the span of the contract is given in Section 4. The remaining sections detail the accomplishments of investigations carried out during the final semiannual reporting period. One of the principal efforts in reduced-order vibration control has been an experimental (not in hardware) approach to the study of mutual interactions between reduced-order modeling, active transducer (actuator and sensor) selection, and controller feedback strategy determination in the context of wideband disturbance accommodation for representative precision flexible structures. The specific insights obtained from this approach are discussed in Section 5; current results relate to suggested approaches for independent sensor selection, and to constraints imposed upon the synthesis process by the use of certain system identification techniques for reduced-order modeling. The enhancement of stability robustness to unmodeled high-frequency dynamics has been a major objective of the experimental synthesis study. Through the use of linear-quadratic-Gaussian (LQG) control employing loop transfer recovery (LTR), reduced order controllers have been obtained which stabilize the full 150-mode model of ACOSS Model No. 2. This successful application, and the limitations of the LQG/LTR approach in the present context, are presented in Section 6. An overview of our approach to the modeling of actuator dynamics, together with its connection to other relevant work, is given in Section 7. A principal focus of work in system identification has been the development of techniques for estimating the spectral characteristics of lumped-parameter systems with closely-spaced modes of vibration. Advances in this development are detailed in Section 8; special emphasis is given to the role of the sampling period used in obtaining input data for the identification process. Interest in identification processes for systems described by distributed-parameter models is rising because of current hardware developments with distributed actuation and sensing devices for flexible structure

vibration control. Theoretical development of an efficient computational algorithm based upon cubic splines for parameter estimation in distributed systems is given in Section 9. Finally, some current advances in large angle slew control are discussed in Section 10. The particular topic emphasized is linear tracking controllers incorporating the capacity for accommodating discrete disturbances. An underlying thrust in this and prior work in large angle slew control has been to develop closed-form analytic solutions to the Riccati-like matrix equations arising in the mathematical development. This leads to considerable increases in the computational efficiency of related algorithms for computing the control.

SECTION 2

SIMULATION EXTENSIONS

2.1 Introduction

2.1.1 Simulation Enhancements

Over the period of performance of the ACOSS Eleven Program, the Simulation Extensions Project has been focussed principally in one task, the Simulation Enhancements Task. The broad objective of this task has been to generalize those portions of the Draper Integrated Simulations (DIS) which initially were too limited in scope or flexibility. Figure 2-1 presents a simplified block diagram of the DIS. Within this category, the major effort has been directed toward freeing the DIS user from complete dependence on outside vendors for obtaining infrared (IR) background radiance maps (i.e., "scenes") required for use in simulation studies. This effort, the Generic Scene Simulation (GENESSIS) subtask, has resulted in the augmentation of the DIS with an additional set of software modules and data bases which give the DIS user a limited but powerful capability for the generation and manipulation of synthetic terrestrial scenes. The GENESSIS models and software were developed by Photon Research Associates (PRA) under subcontract to CSDL.

In addition to the GENESSIS work, the Simulation Enhancements Task has supported enhancements to the Integrated Large Space Structures Simulation (ILS³) as well as enhancements to the Signal Processor Simulation. As initially developed, the ILS³ was mainly geared to address platform and structural issues arising in the context of a HALO-like system. The goal of the ILS³ enhancements subtask was to develop a package of algorithms and software to enable the ILS³ to analyze both multi-mirror ray-traced sensor systems as well as single-surface, paraboloidal or spherical reflector systems.

The Signal Processor Simulation was developed originally as part of the DARPA-sponsored program at CSDL for end-to-end performance analysis and simulation of the Mini-HALO system. During the course of this work a

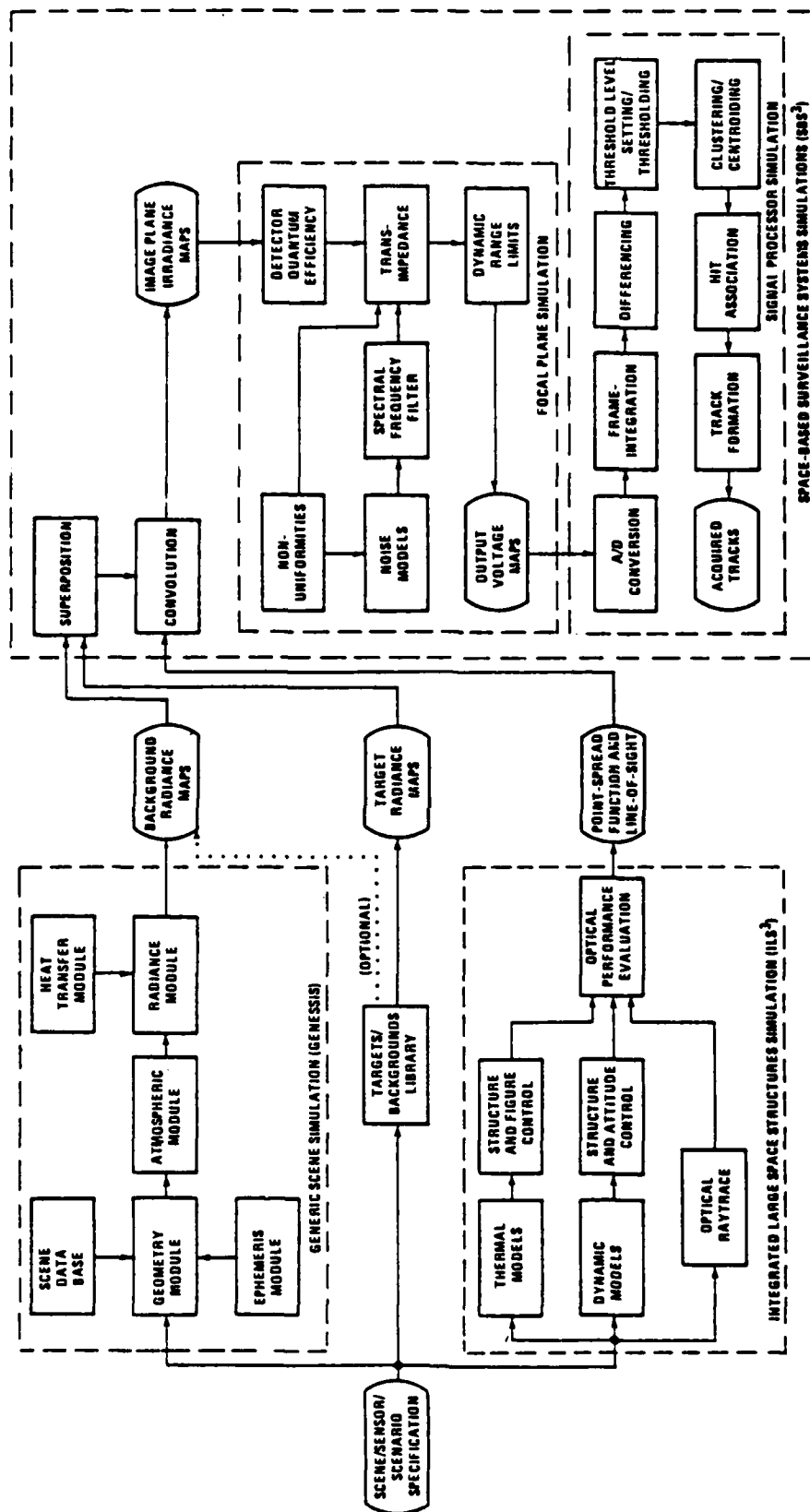


Figure 2-1. DIS Block diagram.

number of natural as well as potentially powerful generalizations of key algorithms suggested themselves. Some of these generalized algorithms have been implemented and studied as part of the Signal Processor Simulation Enhancements subtask.

2.1.2 Simulation Applications

Above and beyond the cases that have been examined as part of specifying, implementing and evaluating the enhancements to the simulation discussed above, the simulation has been used to study several areas of generic concern to space-based IR staring mosaic sensor systems. The most significant of these were the following: clutter leakage as a function of spectral interval and scene local time-of-day through the signal processor of a generic space-based IR staring mosaic sensor; and effectiveness as well as limitations of a class of algorithms proposed by D. Fried for the post-detection reduction of line-of-sight (LOS) jitter effects.

2.2 Simulation Enhancements

2.2.1 Generic Scene Simulation (GENESSIS)

In support of the Draper Integrated Simulations Extensions effort, Photon Research Associates (PRA) has developed (under subcontract to CSDL) a computer code capable of generating and manipulating terrestrial scenes as a function of major surveillance system and mission parameters. This code (called GENESSIS) has the capability to interface with the Defense Mapping Agency (DMA) data base of terrestrial scenes as the source of scene input data. Consequently, the code is able to simulate any scene for which DMA data exists.

The GENESSIS scene simulation is based upon a point-by-point algorithm, a single cycle of which consists of collecting (and in some instances, computing) inputs specific to a single point on the scene, calculating the apparent radiance of that point from the collected inputs, and finally weighting and assigning the calculated radiance to the appropriate pixel in the observer's field-of-view. If the density of points is large enough, the scene will be properly sampled and the radiances computed by

repeated point calculations can be combined to produce an accurate pixel radiance map of the scene. The parameters of these radiance grid points are computed from the three-dimensional scene itself.

Scene data consists of discrete altitude, material type pairs specified at regular intervals on a planar rectangular grid. Continuous surfaces are produced from the discrete scene data using a bi-cubic spline fitting technique. Point data can be computed from these surfaces at any desired spatial resolution.

The computed apparent radiances consist of four terms combined additively. These are reflected solar, thermal emission, reflected skyshine and path radiance. Each major calculational operation is performed with a separate software module. The atmospheric, geometric and radiance modules have stand-alone capabilities, but are normally executed in sequence to produce a final result.

The simulations' primary output is an $N \times M$ viewer-perspective pixel apparent radiance map. Diagnostic output is also available to check proper code execution. Figure 2-2 presents a block diagram of the GENESSIS software architecture.

The GENESSIS code is comprised of six (6) modules (subroutine packages) each with a single specific task. These are geometric, atmospheric, heat transfer, radiance, image and ephemeris. These are combined into three major modules, each with stand-alone capabilities. Modular stand-alone capabilities allow flexibility of operation while maintaining a simplicity of structure, user interaction and memory requirements.

The geometric module performs shadowing and the viewer perspective projection of the scene. Its output is required by the radiance module.

The atmospheric module supplies atmospheric parameters required by the radiance module. It is run least often since its output covers a wide range of solar and observer geometries.

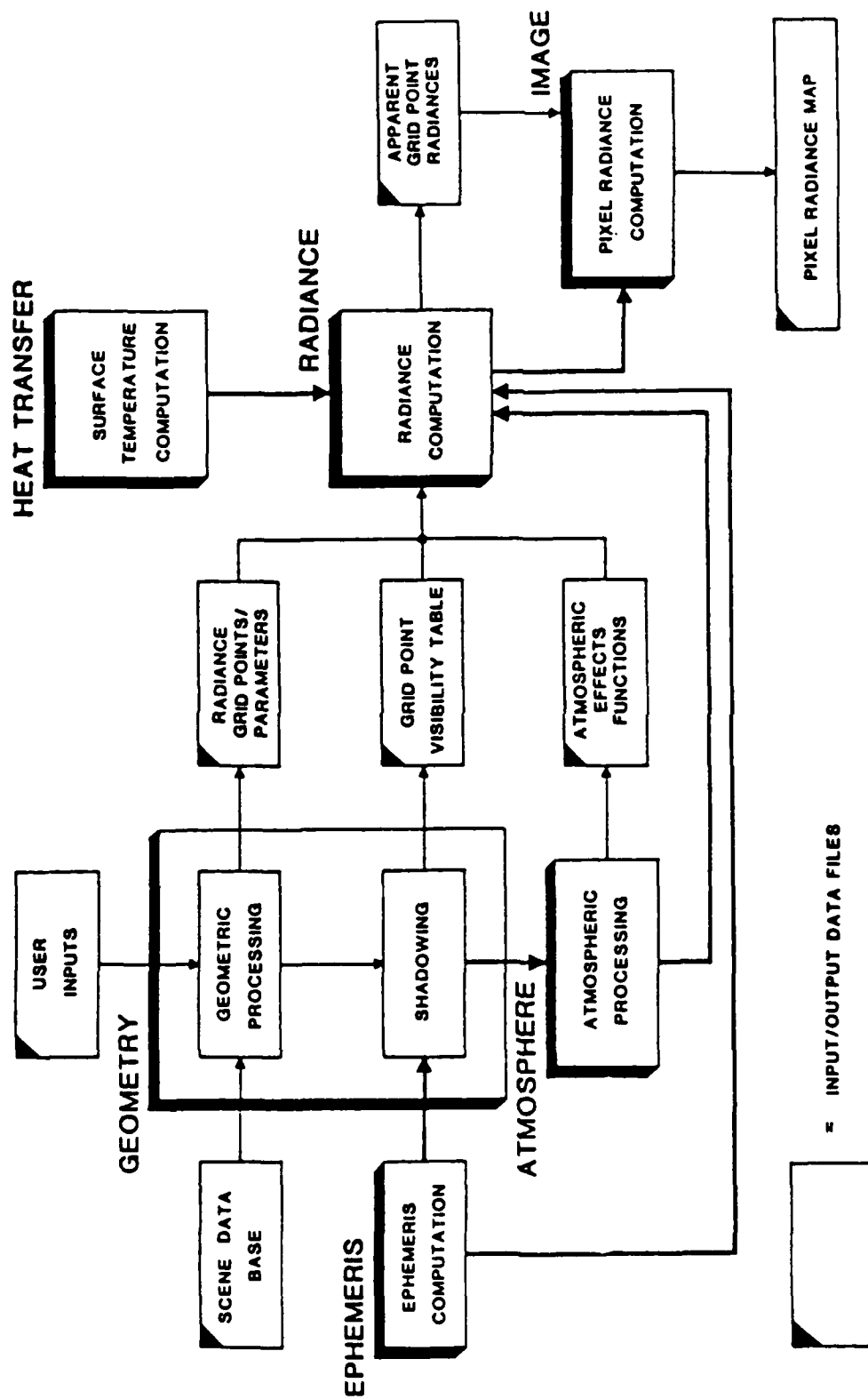


Figure 2-2. GENESIS software architecture.

The radiance module produces a viewer perspective, pixel apparent scene radiance map from information supplied by the atmospheric and geometric modules. It calls upon the heat transfer and image modules to produce, respectively, surface temperatures and viewer image. The heat transfer module currently does not have a stand-alone capability. Both the geometric and radiance modules utilize the ephemeris module.

User inputs are categorized according to purpose. These are geometric, sensor and atmospheric. The elements of these are:

A. Geometric Inputs

1. The date and time of the simulation, used to compute the position of the sun,
2. The latitude and longitude of the viewer subsatellite point,
3. The observer altitude in kilometers.

B. Sensor Inputs

1. The vertical and horizontal angular field-of-view,
2. Focal plane rotation in degrees,
3. The vertical and horizontal spatial resolution in meters.

C. Atmospheric Inputs

1. Atmospheric model (six LOWTRAN standard atmospheres),
2. Aerosol model,
3. Haze model,
4. Visibility in kilometers.

Scene data inputs consist of the altitude, material type pairs plus thermal, atmospheric and reflectance data. The elements of these inputs are:

1. Material thermal properties (solar absorptance, thermal emittance, thermal conductance and thermal mass) required by the heat transfer module,

2. Material in-band diffuse reflectance,
3. Cloud in-band bi-directional reflectance,
4. Surface level atmospheric properties (temperature, wind speed and humidity).

Table 2-1 presents a summary of GENESSIS features. More detailed information on GENESSIS may be found elsewhere.[3,5]

2.2.2 Enhancements to the Integrated Large Space Structures Simulation (ILS³)

The ILS³ structures/optics simulation is a tool for use in simulating the performance and response of a flexible optical system subject to onboard and environmental disturbances and control system forces. The principal output of this program is a time-history of the system optical point-spread function (PSF) which can then be used as an input to the SBS³ sensor simulation. The efforts summarized here represent the first in a series of enhancements whose objectives were to broaden the types of systems which could be simulated by removing the modelling restrictions that were part of the original program. The overall structure of ILS³ is shown in Figure 2-3. It consists of three groups of basic functional modules. In the first group, the node-point displacements of a finite-element model subjected to static or dynamic loads are computed. In the second group, these node-point displacements are transformed into optical wavefront errors. Finally, in the third group the wavefront errors are processed to compute LOS errors, PSF, etc.

The focus of this effort has been the enhancement of the second group of modules, known as the interface programs. In these programs the previously computed displacements at the node-points of the finite-element model of the surface are transformed into optical wavefront errors at a rectangular grid of points. This is accomplished by interpolating the known node-point displacements to find the displacements at the points in the output grid for each reflective surface in the system. These displacements can then be combined using the information obtained from a raytrace of the system to determine the wavefront error at each point in the grid.

Table 2-1. Generic scene simulation (GENESSIS) features.

MAJOR USER-SPECIFIED VARIABLES

- Observer altitude, zenith angle
- Spectral interval (2.5-13.0 μm)
- Atmospheric model (LOWTRAN family)
- Field-of-view location (within overall scene)
- Scene angular resolution
- Continuously variable surface level wind speeds and temperatures

FIVE REPRESENTATIVE TERRAIN DATA BASES

- California Coast (north of Santa Cruz)
- Brooks Range Mountains of Alaska
- Arctic Tundra
- Middle East
- Central Europe

FOUR CLOUD SCENES

- Stratus
- Altocumulus
- Cirrus
- Cumulus

EACH DATA BASE TOPOLOGY EXTRACTED FROM DEFENSE MAPPING AGENCY
(DMA) DATA BASE

EACH DATA BASE REGISTERED WITH LANDSAT DATA TO OBTAIN MATERIALS
MATERIALS ASSIGNMENTS

- Limited to 14 material types

TERRAIN SCENE SIZE: APPROXIMATELY 40 km \times 40 km

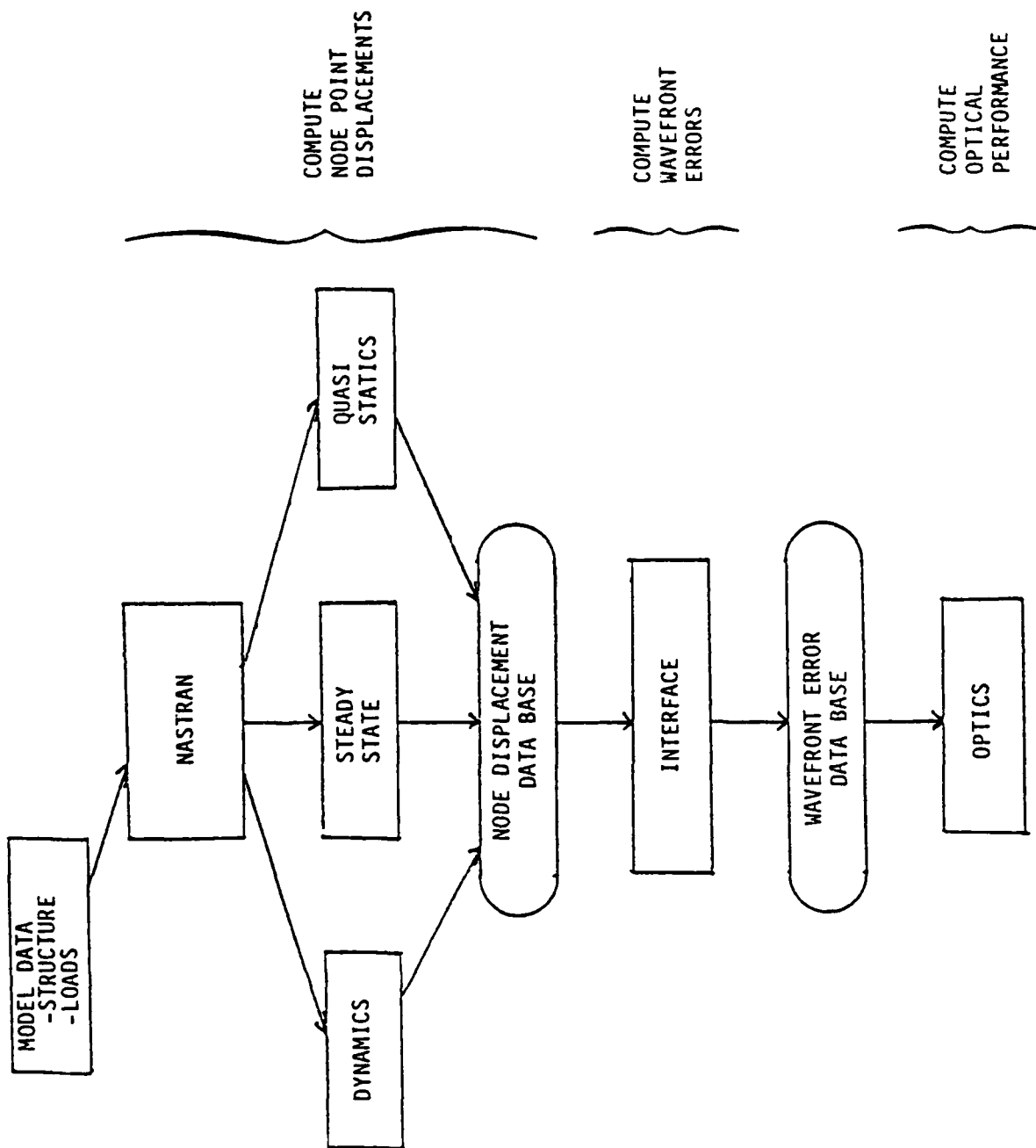


Figure 2-3. ILS³ structure.

The principal result of this effort has been to generalize the ILS³ so that if the system contains only one mirror (which is spherical or paraboloidal) and a point feed, the wavefront errors for on-axis operation can be computed directly from the geometry of the system without the need for a ray-trace.

The methods used to perform the interpolation of the node-point displacements used to find the displacements on the optical grid are described in detail elsewhere.^[5] The interpolation actually involves two steps: 1) a search to determine where on the finite-element model each optical grid point lies; and 2) the computation of the interpolation coefficients for each point. The algorithms used in both steps have been designed to allow any type of finite-element model for the mirror surface.

2.2.3 Enhancements to the Signal Processor Simulation

The signal processor simulation is a key part of the Draper Integrated Simulations (DIS). The DIS is a sophisticated analysis tool developed under DARPA support for overall evaluation and performance assessment of space-based surveillance systems. The DIS models in detail the mechanical, optical, control, signal collection and signal processing subsystems in a highly interactive fashion. It is composed of a number of large data bases (including a library of simulated earth scenes) and two principal simulation packages: the Integrated Large Space Structures Simulation (ILS³); and the Space-Based Surveillance Systems Simulation (SBS³). ILS³ simulate the space platform; it assesses the geometrical and pointing performance of satellites and their sensors as influenced by thermal, structural, dynamic, and control forces. SBS³ uses the ILS³ outputs and models the performance of space-based surveillance systems with respect to their intended missions using nominal and perturbed values for the target, background, optics, LOS, optical filters, focal plane, and signal processor. Figure 2-4 presents a simplified block diagram of the DIS.

Initial development of the Signal Processor Simulation was driven by a requirement from an earlier DARPA-sponsored program at CSDL to model the HALO Signal Processor (HSP). As indicated in Figure 2-5, the HSP was com-

ILS³

SBS³

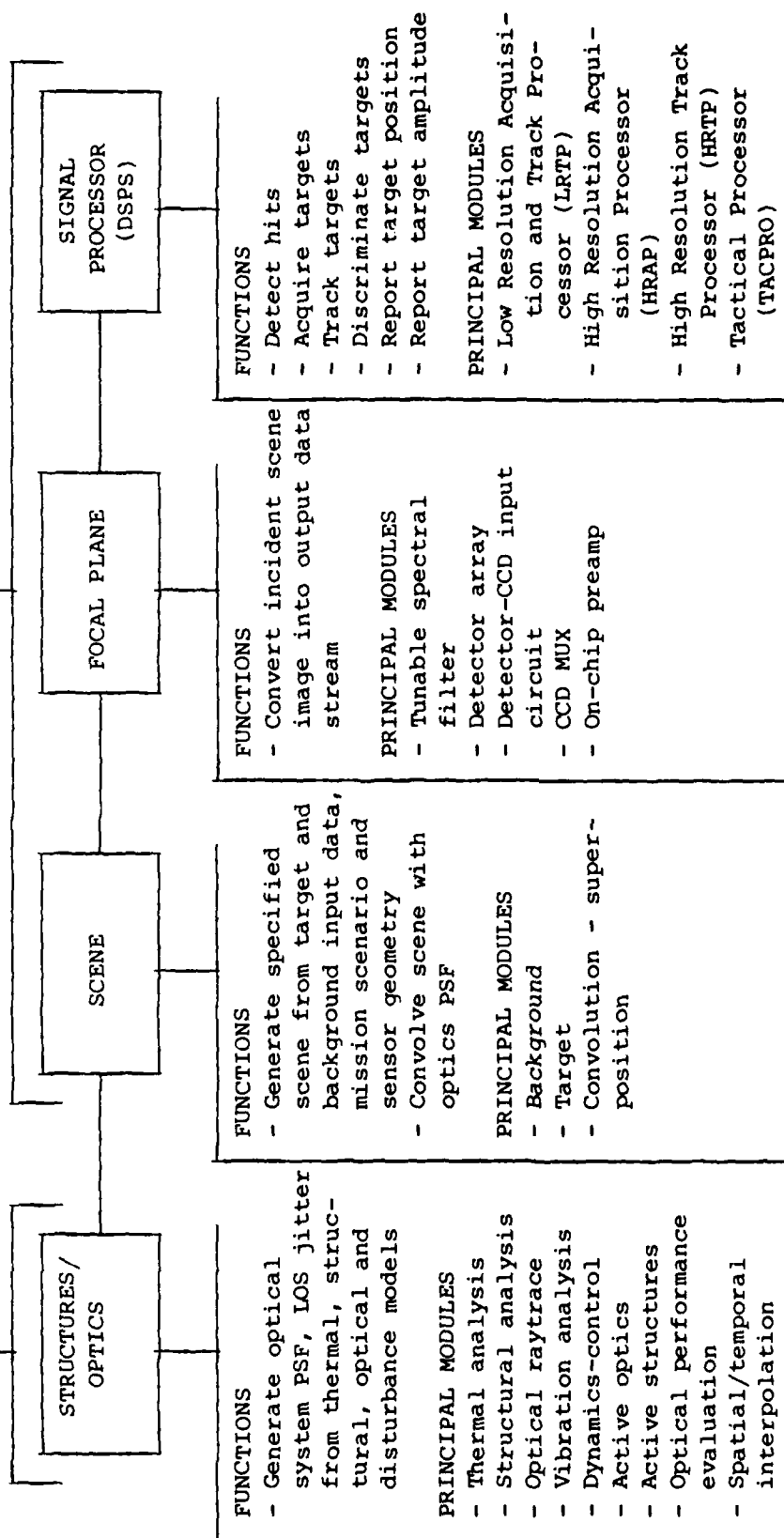


Figure 2-4. Draper integrated simulations simplified block diagram.

SIGNAL PROCESSOR	FUNCTION
High Resolution Acquisition Processor (HRAP)	Acquire Point-Source Targets
High Resolution Track Processor (HRTTP)	Track Point-Source Targets Acquired by HRAP
Low Resolution Acquisition and Track Processor (LRTP)	Acquire and Track Resolved Targets (e.g. Plumes)
Tactical Processor (TACPRO)	Detect Explosions and Other Tactical Events

Figure 2-5. Components of Draper Signal Processor Simulation (DSPS).

prised of four separate processor modules. Subsequent work under the Simulation Extensions Project has focussed on the High Resolution Acquisition Processor (HRAP) and the Low Resolution Acquisition and Track Processor (LRTP), and for efficiency, these two simulations have been combined into one software package. The simulation user has the option of selecting the HRAP or the LRTP for processing a given set of input data frames (the HRAP and LRTP run independently, not interactively). In addition, there are numerous other options available to the user, comprising a menu which specifies the signal processor configuration for a given run. In fact, by tailoring the input parameters, the user can implement a number of different signal processor configurations which go far beyond either the HRAP or the LRTP. The CSDL HRAP/LRTP simulation is divided into a number of modules, which generally perform operations on the input data in a sequential fashion, frame by frame. Depending upon the processing sequence specified by the user, some of the modules may or may not be used.

The first of the modules performs either temporal integration of successive frames or spatial integration within each frame (or both).

The next module is the differencing module, which computes the zeroth-, first-, second-, or third-order differences (as specified by the simulation user) for a set of input data frames. A difference is essentially a derivative of the signal amplitude with time; zeroth order corresponds to raw data, first-order differencing corresponds to a first derivative, and so on.

Next is the thresholding module, which detects potential targets by comparing one or more difference frames with templates (normalized to a predetermined threshold level) that correspond to the minimum expected pattern in the differencing that a moving target would generate. Variations on this technique include simple thresholding (which employs only one frame at a time), Multi-Threshold Detection (or MTD, which employs a multi-frame template), and Rationalized Exceedance Thresholding (RET, which is similar to MTD but has more rigorous requirements). A variety of thresholding templates can be used, depending on the difference order employed.

The threshold level setting module is called by the thresholding module in order to determine the signal level to which the thresholding templates will be normalized. The threshold level can be read in, computed on the basis of a noise estimate, or set to be proportional to the standard deviation of the current frame of data or differencing. The threshold level can be periodically reset by a Constant False Alarm Rate (CFAR) loop.

Clustering and centroiding follow threshold level setting and thresholding. The clustering module selects groups of thresholded hits for centroiding. The centroiding module either computes the moment of each group of hits or will select just the peak value. There are several options for the amplitude basis for clustering and centroiding, or, if the user chooses, these modules can be bypassed altogether.

The output of the centroiding module is fed to the acquisition module. The acquisition module can employ the two tier algorithm or the one tier algorithm for high resolution or low resolution targets, respectively. The acquisition algorithms form tracks by associating any set of sequential and contiguous hits subject to certain rules. There are flexible criteria for determining when a track has a sufficient number of data points to be considered acquired.

Tracks which are generated by the acquisition module are handed over to the least-squares line fitting module or the correlation coefficient module. These modules eliminate false tracks by rejecting any tracks which have, 1) points at a greater than acceptable distance from the track's least-squares generated line, or 2) a correlation coefficient less than some minimum allowable limit.

Table 2-2 summarizes the major user variables for the enhanced signal processor simulation. Figure 2-6 illustrates the collection of modules which comprise the CSDL HRAP/LRTP simulation. Further information can be found elsewhere.[5]

Table 2-2. Major user variables for the enhanced signal processor simulation

VARIABLE	RANGE
Difference Order	<ul style="list-style-type: none"> • Zeroth (i.e., no frame differencing) • First order • Second order • Third order
Threshold Level Selection	<ul style="list-style-type: none"> • User specified • (Noise estimate) \times (Threshold-to-noise Ratio)
Track Acquisition Algorithm	<ul style="list-style-type: none"> • Low resolution type • High resolution type
Difference order for use in low resolution noise estimate	<ul style="list-style-type: none"> • First order • Second order • Third order
Thresholding Polarity	<ul style="list-style-type: none"> • Negative contrast only • Positive contrast only • Arbitrary contrast
Thresholding Algorithm	<ul style="list-style-type: none"> • Simple • HSP Multi-Threshold Detection (MTD) • CSDL MTD • Idealized MTD • Rationalized exceedance thresholding
Constant False Alarm Rate (CFAR) Option	<ul style="list-style-type: none"> • Number of allowed false alarms and maximum number of iterations
Centroid Algorithm	<ul style="list-style-type: none"> • Conventional • Peak value
Cluster/Centroid Basis	<ul style="list-style-type: none"> • Raw data • Difference data • Threshold exceedance
System Track Criterion	<ul style="list-style-type: none"> • M1 hits out of N1 frames ($M1 \leq N1$)
Acquired Track Criterion	<ul style="list-style-type: none"> • M2 hits out of N2 frames ($M2 \leq N2$)
Frame Temporal Integration	<ul style="list-style-type: none"> • Number of frames to be integrated
Frame Spatial Integration	<ul style="list-style-type: none"> • Number of pixels to be integrated
Noise Estimation	<ul style="list-style-type: none"> • Number of frames to be used
False Track Rejection Algorithm	<ul style="list-style-type: none"> • Least-Squares • Correlation coefficient
Acquired Track Linearity	<ul style="list-style-type: none"> • Maximum allowed deviation from best-fit straight line

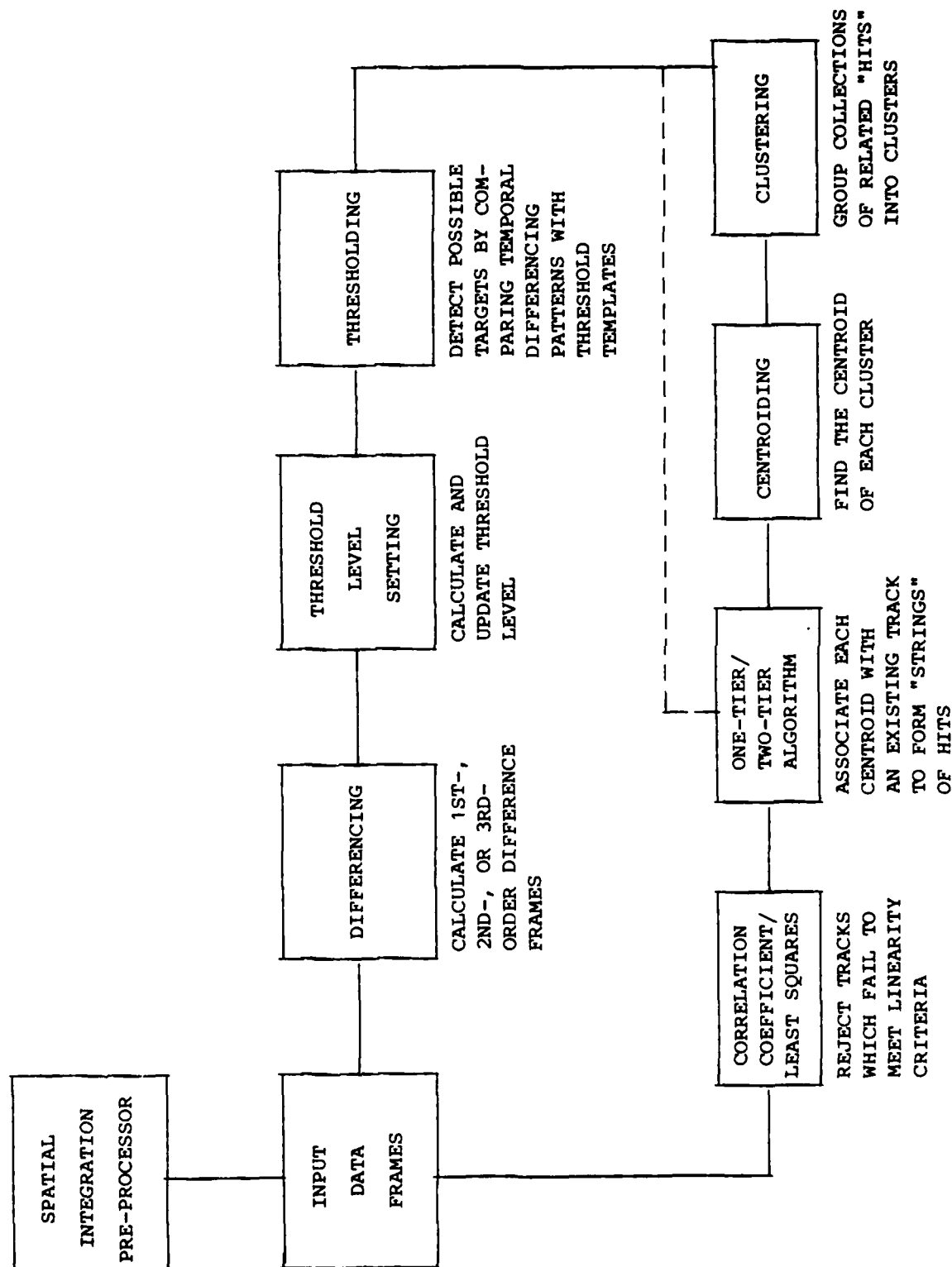


Figure 2-6. HRAP/LRTP Modules and data flow.

2.3 Simulation Applications

2.3.1 Clutter Leakage Study

The Simulation Enhancements described above have considerably expanded the scope and capability of the DIS to conduct end-to-end performance assessments of space-based staring infrared surveillance systems. As an illustration of this new capability, the DIS has been used to study the effect of choice of spectral interval and selection of scene local time of day on clutter leakage through a generic signal processor.[4] The basic approach was to begin with the California coast (Santa Cruz) data base and to use GENESIS to produce two scenes in the 3.6-4.0 μm band and two scenes in the 8.0-9.0 μm band, each pair of scenes corresponding to 8 AM and to noon local time, respectively. A nominal surveillance system mission and configuration were assumed, and the above scenes were processed through the DIS under varying levels of (LOS) jitter. Tables 2-3 and 2-4 summarize the scenario, sensor and signal processor configurations for this investigation. These parameter values reflect the basic configuration for a system whose principal objective is the detection of strategic aircraft against a terrestrial background. The figure of merit used to measure clutter leakage in the signal processor was average number of threshold exceedances per frame.

Since the average number of threshold exceedances per frame is a function of threshold level in the signal processor as well as the level of LOS jitter, the results of this study may be presented from those two points of view. Figure 2-7 illustrates the dependence on LOS jitter level of the average number of threshold exceedances per frame. The particular threshold level selected is representative of what would be used to acquire a target with a relatively high signal-to-noise ratio. The general trend of the data is such that, for a given level of LOS jitter, higher numbers of exceedances are found in the LWIR band (i.e., 8.0-9.0 μm) than in the SWIR band (i.e., 3.6-4.0 μm). In either band, the higher numbers of exceedances always occur at noon local time as opposed to 8 AM.

Table 2-3. Scenario and sensor specification for GENESSIS Santa Cruz investigation.

PARAMETER	VALUE
<u>Target</u>	None
<u>Backgrounds</u>	
-Location	Santa Cruz (GENESSIS)
-Spectral Bands	3.6-4.0 μm 8.0-9.0 μm
-Times of Day (Local)	8 AM NOON
<u>Spacecraft</u>	
-Drift	None
-Jitter	0.1 $\mu\text{rad rms}$ 0.5 $\mu\text{rad rms}$ 1.0 $\mu\text{rad rms}$
-Altitude	35,700 km
-Boresight	NADIR
<u>Optics</u>	
-Aperture Diameter	1.4 m
-Obscuration Ratio	0.35
-Thruput	0.135
-Point-spread Function	Gaussian ($\sigma = 5.01 \mu\text{rad}$)
<u>Focal Plane</u>	
-Detector Geometry	25 \times 25 Array of 100 μm (20 μrad) Square Pixels
-Frame Duration	3.4 sec
-D*	$2.8 (10)^{12} \text{ cm } \sqrt{\text{Hz}}/\text{W}$
-Responsivity non-uniformity	
.Fixed Pattern	0%
.Random	15%

Table 2-4. Signal processor configuration for GENESSIS Santa Cruz investigation.

PARAMETER	VALUE
Difference Filter	3rd Order
Threshold Level	User Input
Assumed Target Contrast	Negative
Threshold Templates	CSDL MTD
Threshold Algorithm	CSDL Rationalized Exceedance Thres- holding (Version 1)
Cluster Basis	Threshold Exceedances
Centroid Basis	Threshold Exceedances
System Track Criterion	3 out of 3
Acquired Track Criterion	10 out of 12
System Track Threshold Scaling	0.5
Least Squares Track Linearity Criterion	± 1.8 Pixels

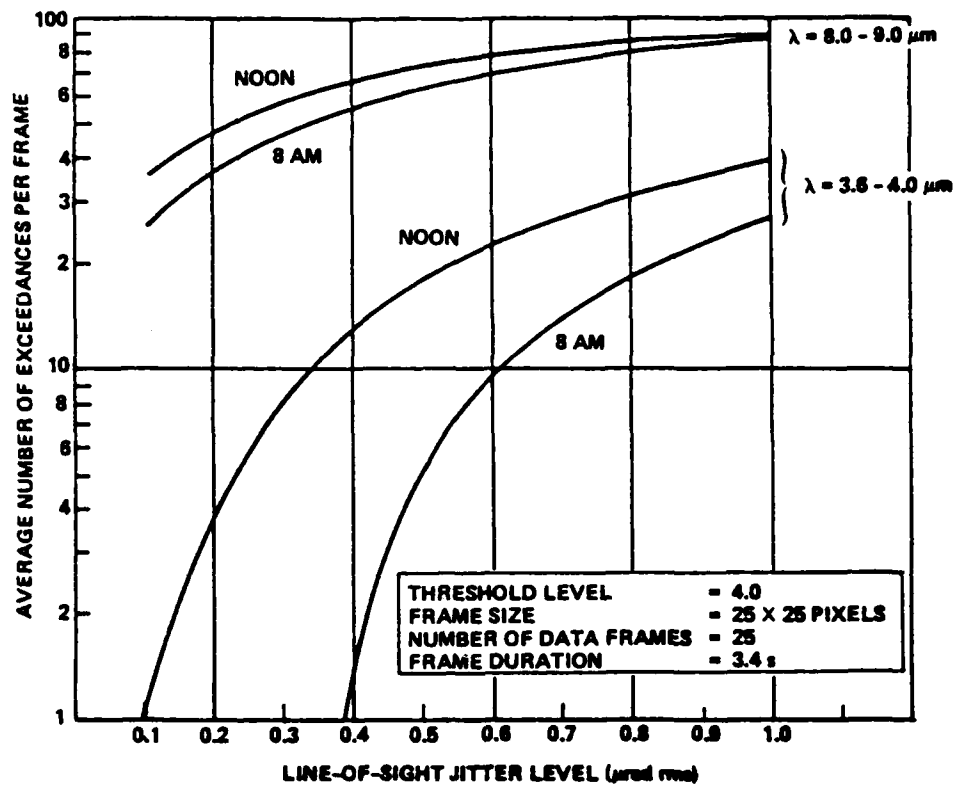


Figure 2-7. Average clutter leakage as a function of line-of-sight jitter level for the GENESIS Santa Cruz scene, with local time-of-day and spectral band as parameters.

Figure 2-8 shows the typical dependence of average number of threshold exceedances per frame on threshold level for a given value of LOS jitter. Many of the same trends discussed above are also evident in this data. Decreasing the threshold results in a rapid increase in threshold exceedances. At a given threshold value, higher numbers of threshold exceedances always occur in the LWIR band as opposed to the SWIR, and, within each band, higher numbers of exceedances occur at noon in comparison with 8 AM. Increasing the LOS jitter level results in a translation upward of the curves at higher threshold values. In addition, there is a compression within each spectral band of the exceedance curves corresponding to noon and to 8 AM.

2.3.2 Evaluation of Algorithms for the Post-Detection Compensation Of Line-of-sight (LOS) Jitter Effects

The Draper Integrated Simulations (DIS) in general provides a natural test bed for examining the behavior of current and proposed space-based surveillance systems. In particular, since LOS stability has been found to be a major performance-limiting factor for a broad class of downward-staring surveillance systems, the DIS has been used to evaluate a technique proposed by D. Fried^[5] for reduction of the LOS jitter effects.

Moving targets are most commonly detected by mosaic sensors through differencing of successive frames. Unfortunately, the changes in the detectors' output are not only due to moving or changing targets, but also to jitter and drift of the sensor LOS as well as to detector noise. Under certain assumptions, there is some retrievable information about the jitter contained in the sequence of frame outputs from the detector array. Thus, assume that the focal plane data rate is higher than the cut-off frequency of the jitter and that the jitter amplitude is much smaller than the spatial resolution of the sensor optics/detector. Then, in the absence of detector noise, the movement of the sensor between two arbitrary frames can be estimated and this estimate used to correct the output before further processing to extract the target.

The estimation method used is essentially that proposed by D. Fried, et. al. Figure 2-9 is a schematic of a portion of the mosaic array which has moved by δx and δy between two frames at times t and t' respectively. If $S_{A,t}$ (respectively, $S_{A,t'}$) and $S_{B,t}$ (respectively, $S_{B,t'}$) are the voltage outputs of adjacent detectors A and B at time t (respectively, t'), and Δ is the center-to-center detector spacing, then, with the restrictions mentioned previously,

$$S_{A,t'} \approx S_{A,t} + \alpha_A \delta x + \beta_A \delta y$$

$$S_{B,t'} \approx S_{A,t} + \alpha_A \Delta$$

$$S_{B,t'} \approx S_{A,t} + \alpha_A (\Delta + \delta x) + \beta_A \delta y$$

Using these approximations, it can be shown that

$$\hat{\delta x} = \frac{\Delta}{4} \left\langle \frac{(S_{A,t} - S_{B,t'})^2 - (S_{A,t'} - S_{B,t})^2}{(S_{A,t} - S_{B,t})^2} \right\rangle$$

is a good estimate of the displacements δx . The symbols $\langle \rangle$ represent the averaging operator over a portion of, or perhaps the entire, focal plane. A similar expression can be obtained for δy by using pairs of detectors A and C. With the same restrictions as before, it follows that

$$S_{C,t'} \approx S_{A,t} + \beta_A \Delta$$

$$S_{C,t'} \approx S_{A,t} + \alpha_A \delta x + \beta_A (\Delta + \delta y)$$

and thus

$$\hat{\delta y} = \frac{\Delta}{4} \left\langle \frac{(S_{A,t} - S_{C,t'})^2 - (S_{A,t'} - S_{C,t})^2}{(S_{A,t} - S_{C,t})^2} \right\rangle$$

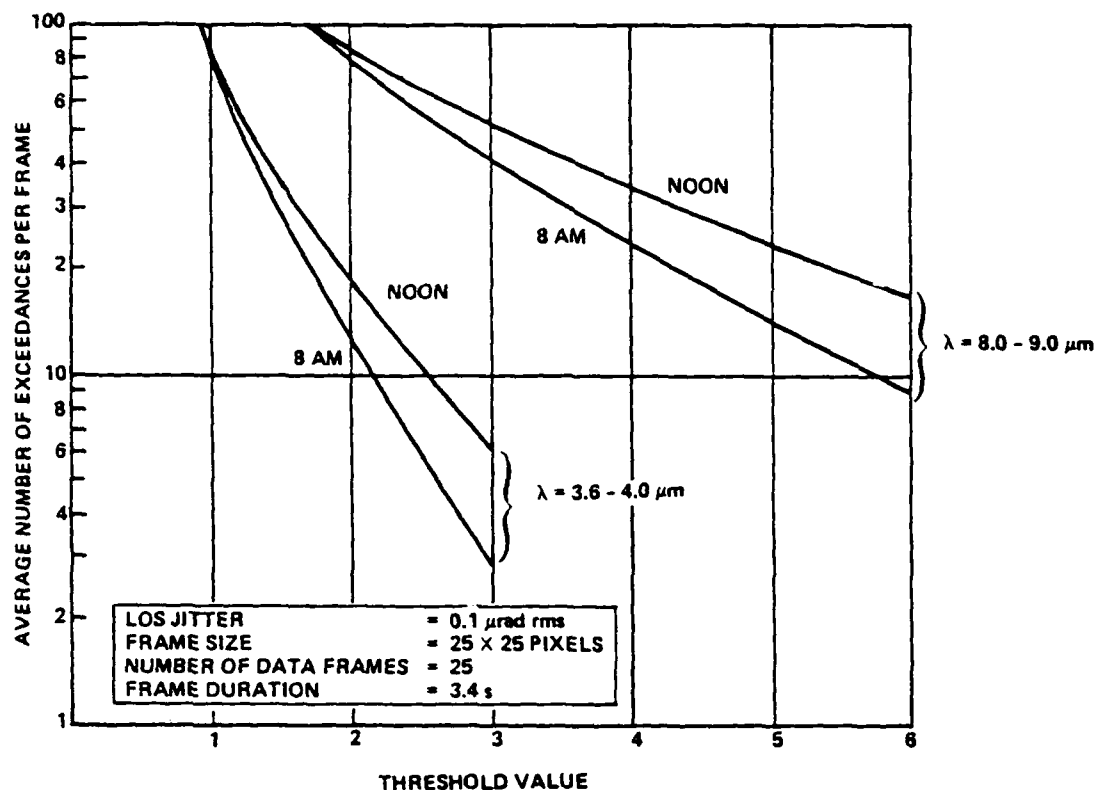


Figure 2-8. Average clutter leakage as a function of threshold level for the GENESIS Santa Cruz scene, with local time of day and spectral band as parameters. (LOS Jitter = $0.1 \mu\text{rad RMS}$)

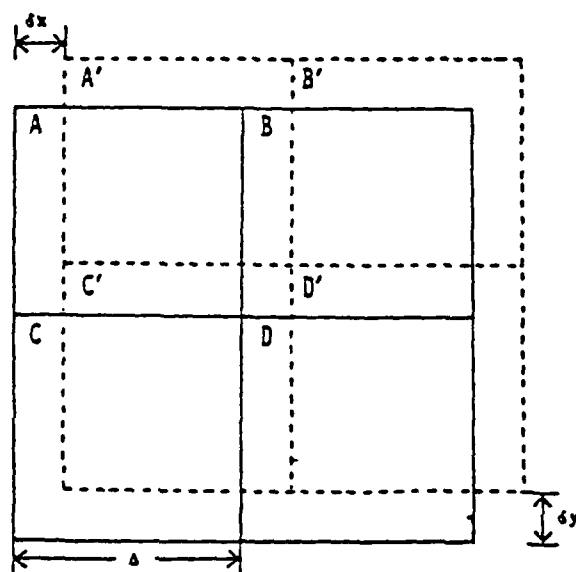


Figure 2-9. Two arbitrary frames displaced by δx and δy .

Depending on the scenario selected, there are several ways of implementing the correction of the jitter effects. One method is to employ a stabilization mirror with a feedback using the estimated values of the jitter, but this approach may be difficult to implement in the case of sensors with a wide field-of-view. The method selected here accomplishes the correction through data processing. It has the advantage of allowing for localized correction of the jitter effects when the field-of-view is large and/or the aperture is large and requires segmentation of the optical elements.

In order to make the correction scheme possible, some of the hardware parameters of the focal plane must be appropriately selected. For the estimation of the jitter, the information regarding the spatial slope of the pixel output as a function of position must be preserved. Therefore, if the focal plane has a reset function, it must be suppressed. This could be achieved by selecting an initial reference voltage approximately equal to the mid-value over the array of the voltage outputs of the multiplexer for the scene considered and by selecting an off-chip amplifier gain small enough so that no detectors reach saturation. Note that this second point creates the need for a finer discretization level in the A/D conversion process.

A study of the influence of the PSF size has shown that a larger PSF allows for better improvement in clutter reduction compared to a small PSF. Also, for highly structured backgrounds it was found that the fixed pattern noise induces a reduction of the estimated value of the jitter, and therefore, a poorer correction when compared to a homogeneous background. For the cases considered, the jitter correction scheme was used over a range of rms jitter values from 0.1 to 1 microradians. In this range it was found that, for highly structured backgrounds and an optimized PSF size, the effect of the correction scheme was equivalent to a reduction of the LOS jitter by approximately a factor of five.

REFERENCES

1. ACOSS Eleven Semi-Annual Technical Report, Vol. 1, CSDL Report CSDL-R-1536, February 1982.
2. ACOSS Eleven Second Semi-Annual Technical Report, Vol. 1, CSDL Report CSDL-R-1583, August 1982.
3. ACOSS Eleven Third Interim Technical Report, Vol. 1, CSDL Report CSDL-R-1598, December 1982.
4. ACOSS Eleven Fourth Semi-Annual Technical Report, Vol. 1, CSDL Report CSDL-R-1648, June 1983.
5. ACOSS Eleven Fifth Semi-Annual Technical Report, CSDL Report CSDL-R-1687, November 1983.

SECTION 3
GENERIC MATERIAL REQUIREMENTS FOR THE ROFT PROGRAM

3.1 Introduction

The development of space-based infrared surveillance systems and space-based lasers is subordinated primarily to the availability of very large, high precision optics. Current technology and existing facilities cannot produce in a timely fashion high performance mirrors, both in quality and quantity, to respond to the needs of the systems envisioned. The Rapid Optics Fabrication Technology (ROFT) Program will attempt to discover and develop technologies which will significantly decrease the time it takes to make such optics. The goal of the ROFT program is to make possible a significant increase in mirror production rate, from the traditional one square meter per year to about 100 M² per year. Such an increase represents a giant step forward and it will be necessary to exhaust all possible avenues capable of enhancing rapid fabrication procedures of high quality optics.

The technology has been developed to make single mirrors having acceptable weight and appropriate performance characteristics for laser and multi-mission surveillance systems. Programs like HALO and LAMP recently have demonstrated the ability to make mirrors capable of controlling their figure to the required surface accuracy under the disturbances of both orbital and control environments. The design of these mirrors was pre-occupied mainly with adequate performance in orbit, but did not address the question of making these high quality optics in large quantities. Significant departure in the design approach and in the fabrication procedures of these mirrors must be incorporated. In attempting to achieve the desired high rate of production, new technology must be concerned with each step of the mirror fabrication process: material production, blank fabrication, mirror generation, grinding, polishing, metrology and assembly. In order to remain completely general in its approach, the ROFT program will also address unconventional system concepts which could have the potential to circumvent the need for large high quality traditional mirrors. Addition-

ally, some effort will be channeled towards the rapid development of optical metering trusses since the fabrication here is also crucial, but not nearly as much as for the mirrors.

The overall objective of this CSDL effort is to provide broad requirements and constraints for the mechanical, thermal and optical properties of materials envisioned for the design and fabrication of new optics concepts. This study, which is a subset of the ROFT program plan, provides only generic specifications so as not to restrict the freedom of the designer in his attempt to develop a new technology and thus enhance the chances for the successful development of a rapid fabrication process.

In addressing the design of the space mirrors, two distinct applications have been considered: (a) optics appropriate for use as the main optics in an infrared (IR) surveillance systems; (b) optics appropriate for use as the primary mirror of a beam expander for a space-based laser system. The incident flux in the aperture plane of the IR system differs greatly from that of a laser and the respective operating temperatures (150° K for IR and 300° to 400° for lasers) pose different problems for each system.

The general requirements for mirror materials for both applications are that the mirror surface be of good optical properties. These materials should have a very low coefficient of thermal expansion and a very small variation of this coefficient. They should exhibit a low density combined with a high modulus of elasticity and micro-yield strength. A very important requirement for the ROFT program is that a proposed mirror material must be amenable to rapid fabrication or replication at low cost and remain within reasonable weight constraints. Finally the mirror concepts must be deployable in space and exhibit very little outgassing.

This section summarizes the approach used in this study to define the mirror material requirements and presents some of the important results. Most of the technical derivations have been presented in some detail earlier and the interested reader should refer to Section 3 of the

ACOSS Eleven Fifth Semiannual Technical Report.* The conclusions and recommendations presented here include additional design suggestions that could be explored with the promise of significant pay-offs.

3.2 Materials Characterization: Approach and Results Summary

The performance of a large high precision space mirror is subordinated to a number of variables that are, in some cases, closely interrelated. Starting with the definition of a structural concept, fabrication and assembly procedures must be devised so as to permit the rapid production of the mirror. In addition the material selected must exhibit optical, elastic and thermal properties that will insure an acceptable performance for the mirror exposed to the rigors of environmental and control disturbances.

The performance of a mirror structure, regardless of its structural concept, can be estimated from the equations expressing the distortions as a function of the structural characteristics and the expected loadings. The mirror deformation δ is affected by the three following contributions:

- (1) geometry and boundary conditions of the structure (F_G),
- (2) the material mechanical and thermal properties (F_M), and
- (3) the loading conditions (F_L) in an expression of the form

$$\delta = F_G \cdot F_M \cdot F_L$$

The approach suggested here attempts to uncover those materials properties (entering the equation through F_M) that affect most adversely a mirror exposed to the various loading conditions expected in space applications.

The behavior of a mirror was, for simplicity, associated with the central deflection or sag δ of a thin circular plate with an initial curva-

* ACOSS Eleven Fifth Semiannual Technical Report, CSDL-R-1687, March 1984.

ture of radius R . The plate is assumed simply supported along its periphery. (See Figure 3-1) The equations can be expressed either in terms of constant mass per unit area (m) or constant mirror thickness (h).

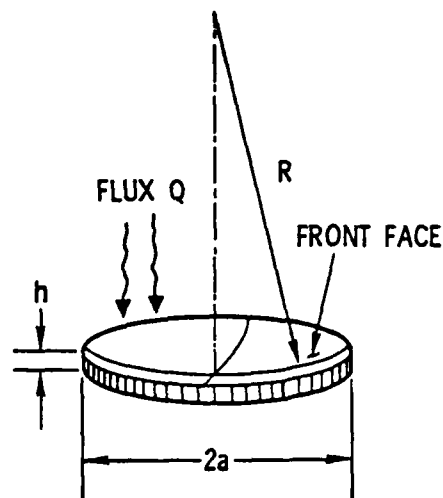


Figure 3-1. Mirror description.

The equations expressing the sag of a typical mirror plate have been derived for the following loading conditions:

- uniform pressure (examples are gravity and polishing loads)
- harmonic forcing function (dynamic responses)
- thermal steady state and transient responses
- thermal conditions with α inhomogeneities and laser beam spikes
- bulk temperature changes due to orbit insertion.

The derived equations furnish the engineer with a useful tool to assess the respective merits of various mirror materials. It is apparent that materials properties such as α , $\Delta\alpha$, k , C , E and ρ determine to a great extent the mirror distortions likely to be encountered in space applications. A large number of candidate materials were examined that include: (a) metals, (b) composites, and (c) glassy materials. Some of

these materials are well known while others are still developmental. Table 3-1 presents the list of 34 materials with their elastic and thermal properties at the 150° K expected in IR applications.

Table 3-2 was prepared as an attempt to place some desirable bounds on the most important material properties and critical parameters involving several constants. They are best estimates based on both analytical derivations and engineering experience with space mirror designs and analyses. It is understood that these constraints are not mandatory but can serve as reasonable guidelines to initiate trade-offs between them. The table also identifies the existing materials that exhibit the best properties in each category

In order to appreciate where the existing material properties fall with respect to desired values, several plots relating critical parameters have been generated. It is possible to see more directly which materials proposed for mirror applications fall within a region of acceptability. For example, Figure 3-2 identifies the materials on the left of the $\frac{\rho(1-\nu^2)}{E} \cdot \frac{\alpha}{K} = 10^{-15}$ line as the most promising for a IR surveillance system. Other similar plots presented earlier for other important parameters provide a more direct insight into the merits of candidate mirror materials and identify interesting and promising groups.

3.3 Conclusions and Recommendations

The objective of this study was to provide broad requirements and constraints for the mechanical and thermal properties of materials envisioned for the design and rapid fabrication of large space mirrors. By inspecting the constitutive equations relating mirror deformations to input disturbances, the relative importance of material parameters was identified. It was also recognized that the requirements on mirror material properties can vary widely depending on the space applications. Surveillance systems, operating at cryogenic temperatures impose different demands on materials than do the laser systems for which the operational temperature is expected to vary from 300° K to 400° K. Dynamic environments ex-

Table 3-1. Materials properties for IR applications (150° K).

Material	Temp. (°K)	Rho (kg/m ³) (N/m ²)	E (N/m ²)	ν _m	α _p (1/°K)	d-α _p (1/°K)	α ₁ (1/°K)	α ₂ (1/°K)	k (W/m-°K)	C (J/kg-°K) (N/m ²)	γ (N/m ²)
		10E3	10E10		10E-6	10E-6	10E-6	10E-6			10E6
Aluminum	150	2.70	7.50	0.33	17.00	12.00	20.00	20.0	248.0	640.0	150.0
BeCu	150	8.20	12.70	0.21	16.70	1.70	16.70	16.7	173.0	420.0	100.0
Beryllium	150	1.83	29.30	0.05	3.70	6.00	0.00	0.0	451.0	627.0	30.0
Copper	150	8.90	11.00	0.36	16.50	1.70	16.50	16.5	393.0	380.0	NA
Invar	150	8.10	15.50	0.29	1.40	0.60	1.00	1.0	12.0	400.0	NA
LA-685	150	8.13	13.80	0.29	0.10	0.01	0.10	0.1	12.0	400.0	NA
Molybdenum	150	10.20	31.40	0.32	5.40	0.50	5.40	5.4	134.0	250.0	200.0
Nickel	150	8.90	19.30	0.36	13.30	0.07	13.30	13.3	83.0	460.0	55.2
OFHC Copper	150	8.90	11.70	0.35	17.60	0.09	17.60	17.6	390.0	305.0	10.0
StSt (410)	150	7.90	20.00	0.31	10.20	0.51	10.20	10.2	25.0	460.0	241.0
Titanium	150	4.50	11.00	0.30	18.00	0.90	18.00	18.0	17.0	540.0	NA
Carbon/Carbon	150	2.00	4.00	0.30	-0.54	0.03	-0.54	-0.5	130.0	837.0	15.2
Carbon/Graphite	150	1.85	10.00	0.04	0.30	3.00	0.30	0.3	120.0	690.0	70.0
Graphite/Aluminum	150	2.39	16.00	0.25	5.00	5.00	5.00	16.0	125.0	620.0	NA
Graphite/Epoxy	150	1.85	10.30	0.30	0.07	0.70	0.07	40.0	0.7	800.0	70.0
Graphite/Mg14Li	150	1.65	32.00	0.30	1.34	5.00	1.10	19.0	60.0	810.0	NA
Beryllium oxide	150	3.00	36.50	0.26	5.60	0.20	5.60	5.6	210.0	1045.0	172.0
Boron carbide	150	2.50	48.00	0.20	3.10	0.16	3.10	3.1	30.0	960.0	NA
CERVIT	150	2.50	10.30	0.20	0.15	0.01	0.15	0.2	1.5	920.0	NA
Diamond	150	3.51	95.00	0.20	0.95	0.05	0.95	1.0	900.0	520.0	400.0
Fused Quartz	150	2.20	7.00	0.20	0.55	0.03	0.55	0.6	NA	NA	NA
Ge-Cordierite	150	2.70	5.52	0.02	-0.07	.00	-0.07	-0.1	2.9	350.0	NA
Glassy Carbon	150	1.50	3.50	0.20	2.20	0.11	3.00	3.0	7.0	700.0	NA
Graphite (para.)	150	2.30	24.10	0.20	0.12	0.01	0.12	0.1	400.0	794.0	NA
Graphite (perp.)	150	2.30	0.69	0.20	5.00	0.29	5.00	5.0	3.0	711.0	NA
Pyrex-7740	150	2.35	6.00	0.20	3.20	0.16	3.20	3.2	NA	NA	NA
Pyroceram-9608	150	2.50	8.70	0.20	0.40	0.02	0.40	0.4	NA	NA	NA
SiC	150	3.20	45.00	0.20	3.00	4.00	3.30	3.3	140.0	255.0	NA
SiO2 (7940)	150	2.20	6.60	0.14	0.07	0.20	0.21	0.2	1.0	410.0	NA
Silicon	150	2.40	14.00	0.10	3.00	0.15	3.00	3.0	110.0	700.0	140.0
Slip-Cast Silica	150	1.90	7.00	0.20	0.54	0.03	0.54	0.5	1.0	420.0	NA
ULE Silica (7971)	150	2.20	6.60	0.17	-0.50	0.40	-0.26	-0.3	1.0	420.0	NA
Vycor-7900	150	2.10	6.70	0.20	0.00	0.04	0.00	0.0	NA	NA	NA
Zerodur	150	2.55	9.03	0.20	0.15	0.01	0.15	0.2	6.0	821.0	NA

Table 3-2. Desirable elastic and thermal properties for potential mirror materials.

• THESE VALUES ARE BEST ESTIMATES BASED ON BOTH ANALYTICAL DERIVATIONS AND ENGINEERING EXPERIENCE WITH MIRROR DESIGN AND ANALYSES

	E	ρ	α	$\Delta\alpha$	ρ/E	α/k	$\alpha/\rho c$
	N/m^2	kg/m^3	$1^\circ K$	$1^\circ K$	$kg/N \cdot m$	m/W	m^3/J
IR	$\geq 10 \times 10^{10}$	$\leq 2 \times 10^3$	$\leq 5 \times 10^{-6}$	$\leq 1 \times 10^{-6}$	$\leq 2 \times 10^{-8}$	$\leq 10^{-7}$	$\leq 2 \times 10^{-12}$
LASER	$\geq 10 \times 10^{10}$	$\leq 2 \times 10^3$	$\leq 0.1 \times 10^{-6}$	$\leq 0.02 \times 10^{-6}$	$\leq 2 \times 10^{-8}$	$\leq 10^{-8}$	$\leq 0.5 \times 10^{-12}$
BEST VALUE (350° K) MATERIAL	48×10^{10} •BoC	1.50×10^3 •Glassy-C	$< 0.1 \times 10^{-6}$ •Gr/Ep*	0.01×10^{-6} •CERVIT	0.5×10^{-8} •Gr/MgLi •BoC	1.7×10^{-9} •C/Gr	0.02×10^{-12} •LA-685 •Ge-Cord. •ULE

* α can vary widely with different ply orientation.
 α varies with T, can even be negative.

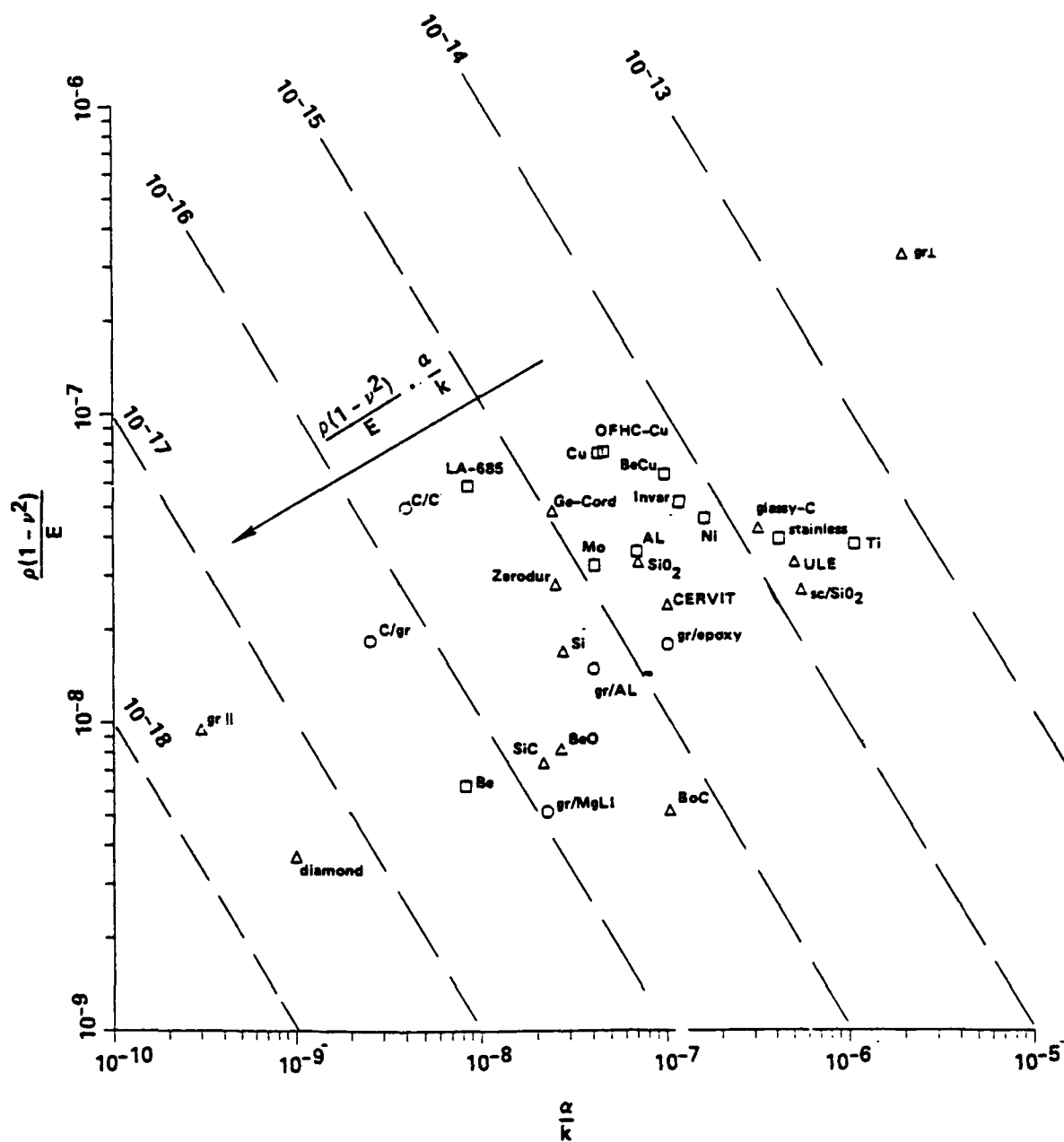


Figure 3-2. Plot of $\frac{\rho(1 - \nu^2)}{E}$ versus $\frac{\alpha}{k}$ for mirror materials.
(IR applications at 150° K)

hibit significant differences as well, and this difference may impact the choice of other properties on the mirror materials.

It must be emphasized that this study did not presuppose a specific mirror concept with defined structural and configurational characteristics. While this approach was intentional for the findings to remain general, it limits our ability to obtain specific requirements for the contemplated mirror materials. Furthermore the effectiveness of possible controls (whether thermal or mechanical), in terms of relieving or modifying demands on material properties can only be evaluated in the context of a defined mirror concept. As a result only estimates on mirror material requirements could be provided and they have been derived from simplified analytical expressions and engineering experience in the design, modelling and analyses of space mirrors.

For a large number of existing and potential materials, that include metals, composites, glass and ceramics, all relevant properties have been tabulated for two extreme operational temperatures (150°K and 350°K). The plots relating important material parameters can be useful in delineating domains of acceptability for a potential new material. One should emphasize that the proposed material requirements should be viewed as somewhat flexible so as to permit tradeoffs between properties for a particular design concept. Past experience has shown that the most likely candidate for such a mirror will probably be a thin face-sheet on actuators supported by a thermally stable substrate. However, it is hoped that dramatic changes and/or improvements in some thermal properties, especially, might lead to completely novel concepts that ultimately could be produced at the desired rapid rate.

A promising approach would be one that recognizes in the mirror design and its responses the intricate relationships between the elastic and thermal characteristics of the structural materials. The structural concept and configuration acquires importance as well since they could be manipulated in such a way as to optimize the thermo-elastic responses of

the mirror. Some ideas, as the ones described below, could be explored to assess their potential payoffs.

- (1) Take advantage of the use of different materials where dissimilar thermal and elastic properties combine to enhance structural behavior and optical performance.
- (2) Based on an optimal range for material properties (for a specific mirror concept) modify properties of constitutive materials of a nominal design to match desired ideal mix of parameters. (Today's materials technology shows promise in tempering with "nominal" material characteristics.)
- (3) Investigate the many possible thermal control capabilities that would advantageously modify mirror temperature distributions and ultimately enhance optical performance.

It should be remembered that the objective of the ROFT program is the rapid fabrication of high precision large space optics. The results of this study can only support this attempt by providing guidelines to the designer and fabrication engineer who selects possible materials. The generic specifications on mirror materials, therefore, can be viewed as constraints to the selection of a material amenable to rapid fabrication processes. Many other issues related to optical and perhaps electrical material properties need to be considered. Finally the fabrication process could be adversely affected by some mechanical and thermal properties of a material that is otherwise acceptable in the final product.

SECTION 4

ACTIVE CONTROL OF FLEXIBLE SPACE STRUCTURES: OVERVIEW

4.1 Scope

Surveillance missions envisioned for future spaceborne optical systems strongly suggest that active control will be needed to ensure that the mission objectives are achieved. Moreover, such missions embody several factors which--taken together--pose a formidable challenge from the perspective of control science and technology. First, the supporting structures for the optical system can be expected to be substantially nonrigid, exhibiting low and clustered characteristic frequencies of vibration and very small inherent damping. Moreover because of the anticipated geometric complexity of such structures, substantial deterministic uncertainty in finite-element models of the structures will persist. Second, the disturbance environment may be severe, involving disturbances with nonnegligible power spectral density over a wide frequency range. For example, the dynamics of fluid flow associated with the cooling of optical surfaces may produce such disturbances. Finally, performance specifications requiring high precision in regard to rapid reorientation of and attitude regulation of the optical axis are certain. The ability to satisfy these performance specifications requires an (implied) capacity for effective suppression of structural vibrations.

The factors cited above motivate the three main lines of effort in active control technology development that have been pursued under the present contract: (1) Synthesis of reduced-order control for vibration

suppression; (2) System identification, with special attention to the problem of resolving closely-spaced modes; and (3) Generation of smooth large-angle-slew control.

4.2 Major Accomplishments

Significant results have been obtained in the course of pursuing each of the main lines of effort. They are summarized in turn.

4.2.1 Vibration Control

The principal objective in this effort has been to synthesize active controllers that maintain specified optical performance (including full-order stability) in the presence of wideband disturbances. Initial experience indicated the need for a systematic examination of the mutual interactions between three principal elements of the overall synthesis process: reduced-order modeling; active transducer (actuator and sensor) selection; and controller feedback strategy determination [Ref. 4-3 (Sec. 5)]. A new analytical approach to the selection of active transducers from among a large class of candidates was conceived [Ref. 4-2 (Sec. 3)]. The approach was then developed into an efficient tool for examining the influence of active transducer placement (including non-colocated configurations) upon closed-loop stability and performance [Refs. 4-4 (Secs. 2, 3), 4-5 (Sec. 5)]. An encouraging degree of stability robustness to unmodeled high-frequency dynamics, attributable to active transducer placement alone, was demonstrated. Finally, by applying recent insights [Ref. 4-6] to modifying the controller feedback strategy, closed-loop stability of the full-order (150-mode) model of a spaceborne optical system [Refs. 4-7, 4-8] with a reduced-order (18-mode) controller was demonstrated (Section 6 herein). During the latter demonstration, the inadequacy of current technology for maintaining performance robustness was clarified.

Several notable theoretical contributions relevant to vibration control have been made independent of the synthesis demonstration

studies. New insights into the modeling of actuator dynamic processes [Ref. 4-3 (Sec. 3), and Section 7 herein] and sampled-data processes [Refs. 4-4 (Sec. 4), 4-5 (Sec. 6)] have been generated. The key to these insights is the use of natural second-order dynamic models--which retain physical insight--rather than first-order state-space models--which obscure such insight.

Although most of the theoretical and applied investigations under the contract employed lumped-parameter (finite-element) structural models, some significant theoretical results for systems retaining a distributed-parameter representation were obtained. Such investigations appear timely in view of the increasing level of interest in developing distributed hardware devices for the control and estimation of vibrating systems [e.g., Ref. 4-9]. Convergence of an algorithm employing a sequence of (finite-dimensional) stochastic optimal output feedback compensators for the control of a distributed system was established [Refs. 4-1 (Sec. 7), 4-10].

4.2.2 System Identification

Motivation for this effort lies in the unavoidable (deterministic) uncertainty in the available models for complex structures, which leads to the potential for instability under feedback control. The principal objective of efforts in this direction has been to develop estimation processes appropriate for generating reduced-order models of flexible space structures for the purpose of controller synthesis. A new approach to spectrum estimation for lumped-parameter systems based on discrete-time signal processing ideas was conceived [Ref. 4-3 (Sec. 2)]. The approach is specifically designed to accommodate the special characteristics exhibited by flexible space structures (e.g., closely-spaced vibration modes). It is particularly distinguished by the use of the sampling period (for input data to the identification process) as a parameter to aid in high resolution. The approach has been developed into a systematic and effective tool for high resolution spectrum estimation [Ref. 4-5 (Sec. 7) and Sec. 8 herein; cf. also Sec. 5.2.3 herein].

Several approaches to parameter estimation in distributed-parameter systems have also been developed [Ref. 4-5 (Sec. 8), and Sec. 9 herein)]. Convergence of solutions to finite-dimensional identification problems formulated with cubic-spline approximations has been proved, and numerical results have been generated to demonstrate a variety of applications.

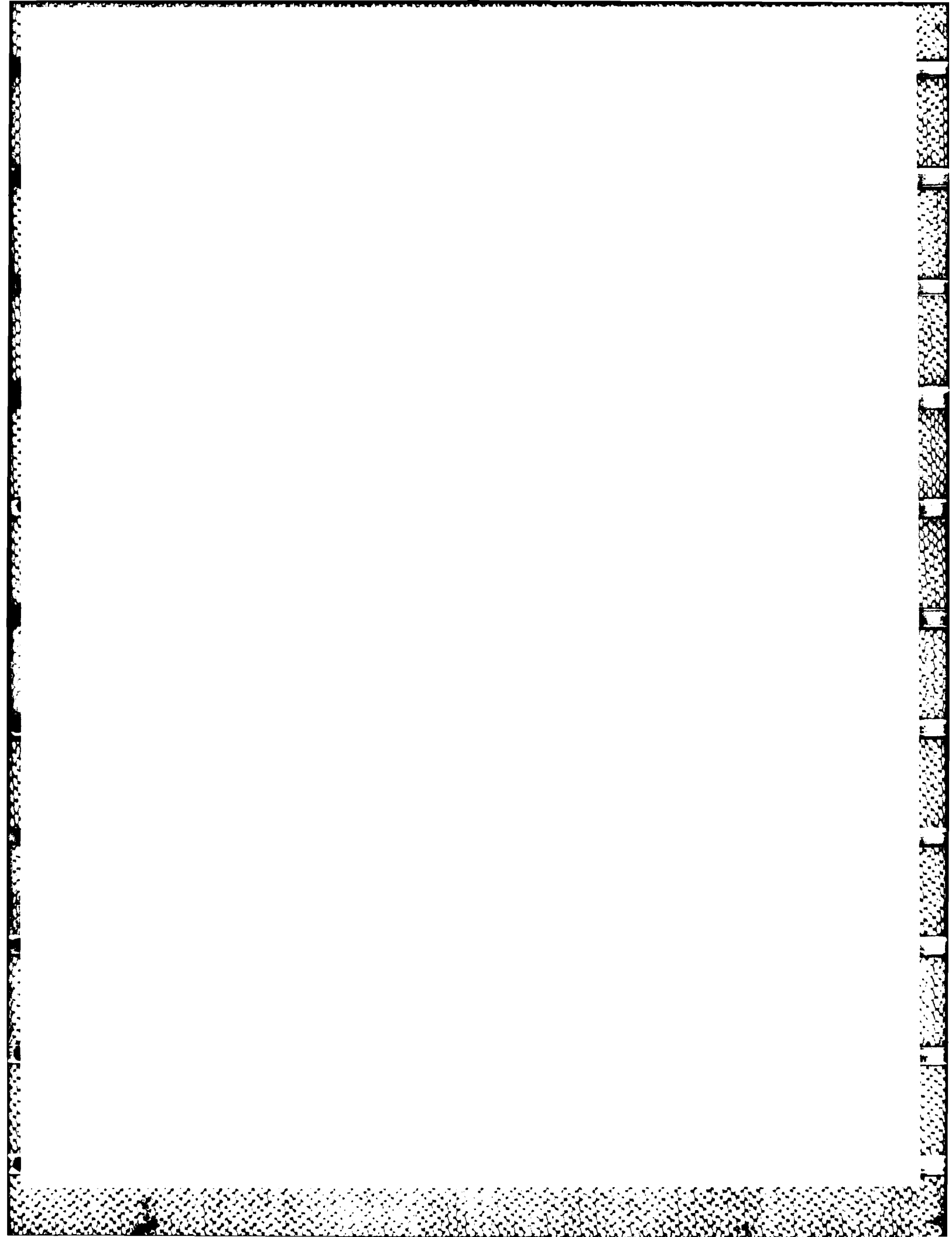
4.2.3 Large Angle Slew Control

The principal objective of this effort has been to synthesize active control strategies that enable large-angle spacecraft reorientation between specifically constrained end conditions with a minimal excitation of structural vibrations. Although the general approach being developed is applicable to nonlinear problems [Ref. 4-11], the emphasis of work in this direction has been placed upon problems with linear dynamics (e.g., tracking) so as to obtain sharper results. In particular, this allows the use of techniques in (closed-loop) linear multivariable control [e.g., Ref. 4-12] to be employed, in addition to techniques in (open-loop) optimal control [e.g., Ref. 4-13] applicable to nonlinear problems. Simulation results representing motion of a rotating rigid hub with four flexible appendages and demonstrating both open-loop and closed-loop control have been given [Refs. 4-1 (Sec. 8), 4-2 (Sec. 7), 4-4 (Sec. 5)]. A significant aspect of the results relating to linear closed-loop slew control is the obtaining of closed-form solutions for various matrix Riccati-like equations arising in the mathematical development. Such representations enable considerable improvement in the efficiency of related algorithms used for computing the control.

4.3 Summary of Current Results

The remaining sections of the present report detail the accomplishments of investigations carried out during the final semiannual reporting period. One of the principal efforts in reduced-order vibration control has been an experimental (not in hardware) approach to the study of mutual interactions between reduced-order modeling, active

transducer (actuator and sensor) selection, and controller feedback strategy determination in the context of wideband disturbance accommodation for representative precision flexible structures. The specific insights obtained from this approach are discussed in Section 5; current results relate to suggested approaches for independent sensor selection, and to constraints imposed upon the synthesis process by the use of high-resolution spectrum estimation techniques for reduced-order modeling. The enhancement of stability robustness to unmodeled high-frequency dynamics has been a major objective of the experimental synthesis study. Through the use of linear-quadratic-Gaussian (LQG) control employing loop transfer recovery (LTR) [Ref. 4-6], reduced-order controllers have been obtained which stabilize the full 150-mode model of ACOSS Model No. 2. This successful application, and the limitations of the LQG/LTR approach in the flexible structure control context, especially in regard to performance robustness, are presented in Section 6. A mature perspective on our approach to the modeling of actuator dynamics, together with its connection to other relevant work, is given in Section 7. As indicated in the preceding subsection, a principal focus of work in system identification has been the development of techniques for estimating the spectral characteristics of lumped-parameter systems with closely-spaced modes of vibration. Advances in this development are detailed in Section 8; a thorough account of the parametric use of the data sampling period to improve spectral resolution is given. Theoretical development of a more efficient computational algorithm based upon cubic splines for parameter estimation in distributed systems is given in Section 9. Finally, some current advances in large angle slew control are discussed in Section 10. The particular topic emphasized is linear tracking controllers incorporating the capacity for accommodating discrete disturbances. Analytic representations of closed-loop solutions for matrix Riccati-like equations are discussed in detail.



4.4 Applications

The emphasis in the work reported here has been upon independent development--in some-depth--of the three main lines of effort identified in Section 4.1. Results obtained reflect substantial maturity in each of the developments. However, for system-level applications of the technology represented, an integrated approach embracing each of three lines of effort is required. Except for the analytical results of Sec. 5.2.3 of the present report, no such interdisciplinary work has been undertaken.

References

- 4-1. Lin, J. G., et. al., ACOSS-Eleven Semiannual Technical Report, Vol. 2, Report CSDL-R-1536, Charles Stark Draper Laboratory, Cambridge, MA, February 1982.
- 4-2. Strunce, R. R., et. al., ACOSS-Eleven Second Semiannual Technical Report, Vol. 2: Active Controller Designs, Report CSDL-R-1583, Charles Stark Draper Laboratory, Cambridge, MA, August 1982.
- 4-3. Fogel, E., et. al., ACOSS-Eleven Third Interim Technical Report, Vol. 2, Report CSDL-R-1598, Charles Stark Draper Laboratory, Cambridge, MA, December 1982.
- 4-4. Hegg, D. R., et. al., ACOSS-Eleven Fourth Semiannual Technical Report, Vol. 2, Report CSDL-R-1648, Charles Stark Draper Laboratory, Cambridge, MA, August 1983.
- 4-5. Brooks, T. H., et. al., ACOSS-Eleven Fifth Semiannual Technical Report, Report CSDL-R-1687, Charles Stark Draper Laboratory, Cambridge, MA, March 1984.
- 4-6. Doyle, J. C., and Stein, G., "Multivariable Feedback Design: Concepts for a Classical/Modern Synthesis," IEEE Trans. Automatic Control, Vol. AC-26, No. 1, Feb. 1981, pp. 4-16.

- 4-7. Henderson, T., "Active Control of Space Structures (ACOSS) Model 2," Report C-5437, Charles Stark Draper Laboratory, Cambridge, MA, September 1981.
- 4-8. Henderson, T., "Modification to ACOSS Model No. 2 Design; Technical Report, Data Base (Final)," Report CSDL-R-1585, Charles Stark Draper Laboratory, Cambridge, MA, October 1982.
- 4-9. Bailey, T. and Hubbard, J. E., Jr., "Distributed Control of a Cantilever Beam Using PVF2," USAF/AFWAL/FDL Vibration Damping Workshop, Long Beach, CA, February 1984.
- 4-10. Pearson, R. K., "Optimal Velocity Feedback Control of Flexible Structures," Ph.D Dissertation, Department of Electrical Engineering and Computer Science, Massachusetts Institute of Technology, Cambridge, MA, January 1982.
- 4-11. Turner, J. D. and Chun, H. M., "Optimal Distributed Control of a Flexible Spacecraft During a Large-Angle Maneuver," J. Guidance, Control, and Dynamics, Vol. 7, No. 3, May-June 1984, pp. 257-264.
- 4-12. Kwakernaak, H. and Sivan, R., Linear Optimal Control Systems, Wiley, New York, NY 1972.
- 4-13. Pontryagin, L. S., Boltyanskii, V. G., Gamkrelidze, R. V., and Mishchenko, E. F., The Mathematical Theory of Optimal Processes (English translation), Wiley, New York, NY, 1962.

SECTION 5

ACTIVE CONTROL SYNTHESIS FOR WIDEBAND DISTURBANCE ACCOMMODATION IN PRECISION FLEXIBLE SPACE STRUCTURES

5.1 Motivation

5.1.1 The Synthesis Problem

Surveillance missions envisioned for future spaceborne optical systems lead quite directly to some challenging problems in structural control. Because of size, material properties, and certain structural symmetries, the support structure housing the optical train can be expected to exhibit low and clustered characteristic frequencies--low enough to be excited by any attitude controller--and very small inherent damping. To satisfy mission requirements, the spacecraft must have the capacity for rapid reorientation, timely suppression of structural vibrations, and regulation of the optical axis along a specified direction to high precision. Finally, this performance is to be maintained in the presence of disturbances having nonnegligible power spectral density over a wide band of frequencies--for example, disturbances generated by fluid flow for mirror thermal regulation. Achieving the specified level of performance under the constraints imposed pushes the frontier of current knowledge in control science and technology. In this section, we summarize our present understanding of--and contributions toward--a solution to the problems of active structural vibration suppression and precision optical axis regulation while accommodating wideband disturbances. The problem of flexible spacecraft reorientation is considered separately in Section 10.

Because of the geometric complexity of the optical support structures being considered, a distributed-parameter model of the structural dynamics is generally not feasible. Although lumped-parameter models are readily obtainable via the finite-element method, quite high orders for such models (in terms of the number of vibrational modes retained) are needed to give an adequate representation of the structural dynamics. For the process of synthesizing an active controller, however, a reduction in model order is virtually unavoidable. Although the computational burden connected with carrying out the mathematical operations involved in a design is a consideration in this, the more fundamental reason is the unresolvable (deterministic) uncertainty in the computation of the higher characteristic structural frequencies. This exposes two matters with serious implications for control:

(1) Parameters characterizing the full-order structural model are not known precisely; and (2) The reduced-order model used to represent the structure in the controller synthesis process ignores potentially important dynamics, mostly at high frequencies.

5.1.2 Initial Approaches to the Synthesis Problem

For relatively small amplitude motions, the problems of structural vibration suppression and optical axis regulation are legitimately treated using linear dynamic models. Because of the geometric complexity of the structures, however, nonnegligible coupling of the structural modes through the actuators (and the disturbances) is to be expected. A multi-input multi-output context for the controller synthesis is therefore essential. Fortunately, the science of control for linear multi-variable systems--although still a fruitful research field--is quite mature [e.g., Refs. 5-1, 5-2, 5-3]. Many systematic design approaches are known.

Our initial approach to the synthesis problem consisted of applying several variants of the linear-quadratic-Gaussian (LQG) method for the determination of controller feedback strategy, each one assuming different degrees of availability of information about the disturbance. The object of control for the design exercises was (and remains) the generic ACOSS Model No. 2 (shown in Fig. 5-1) representing an optical support structure [cf. Refs. 5-4, 5-5]. Initial results, together with a description of the specific wideband disturbance affecting the structure, were given in Reference 5-6. With the feedback loop closed around a reduced-order (10 mode) model, each of the three initial designs exhibited stability; in addition, substantial reduction of the optical axis pointing error was affected (in fact, the performance specifications were satisfied when full knowledge of the disturbance statistics was assumed). These designs proved unstable, however, when the feedback loop was closed around an enlargement of the reduced-order design model incorporating 10 additional structural modes (mostly at higher frequencies). Without making unreasonable assumptions in regard to inherent structural damping, attempts to modify the basic LQG design so as to obtain closed-loop stability relative to the enlarged structural model (e.g., by incorporating an inner loop for velocity output feedback [Ref. 5-7], and/or by incorporating actuator and sensor synthesizers [Ref. 5-8]) proved fruitless. We note that this sort of impasse is not an isolated occurrence [Ref. 5-9]; often, such impasses are not highly publicized, however--perhaps unfortunately so.

One of the principal conclusions we drew from this impasse was that not enough serious attention had been given to the questions of selecting reduced-order models or of selecting active transducers (actuators and sensors). In fact, these two processes are strongly

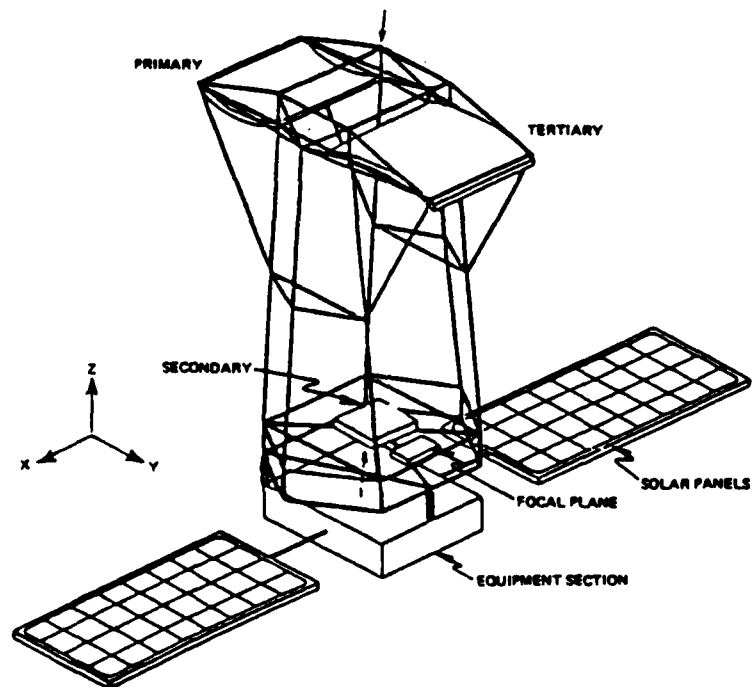


Figure 5-1. Generic space optical system: ACOSS Model No. 2.

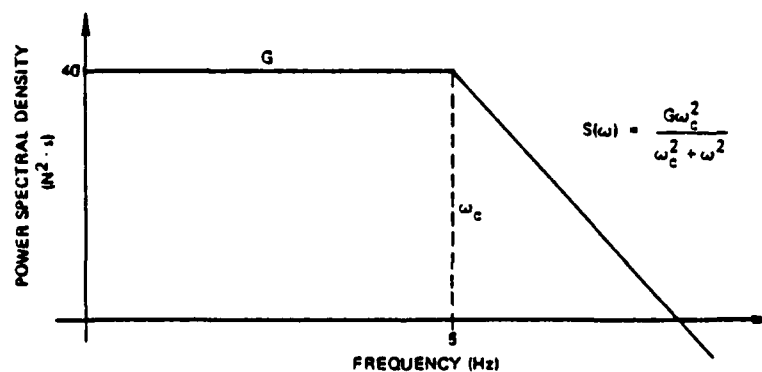


Figure 5-2. Power spectral density of wideband disturbance.

interdependent. Together, they have a decisive influence upon the effectiveness of any controller feedback strategy. We also observed that whereas model selection, transducer selection, and (especially) feedback strategy determination have each received detailed study--in isolation from one another--very little is understood about the details of their interaction. Among the reasons for this is that such interaction studies with models of significant complexity do not lend themselves well to theoretical inquiry. We therefore resolved to undertake an experimental approach (not in hardware) in the spirit of Reference 5-10 to increase our understanding of these crucial interactions. This approach was presented in detail in Reference 5-11. In brief, it consists of a sequence of end-to-end synthesis trials--from model selection, through transducer selection, to feedback control design and evaluation--with one or more aspects of one of these principal factors in the synthesis process being changed at each trial. Individual trials aim not so much at the best possible design as at exposing some important feature of the interactions within the synthesis process.

Progress with this experimental approach was reported in References 5-12 through 5-14. The emphasis there was placed primarily upon expanding our development of a particular approach to active transducer selection and upon exploring the influence of various transducer selections on the synthesis process--the controller feedback strategy being fixed (an LQG-strategy incorporating full knowledge of the disturbance statistics [Ref. 5-15]). Reduced-order controllers were obtained that exhibit stability in the presence of enlarged structural models containing modes well beyond the frequency extent of the reduced-order design model.

In the remainder of this section, a final account of progress with the active control synthesis experiment is given. A detailed description of results obtained during the current reporting period is provided in Section 5.2. The principal contributions throughout the course of this

contract toward the synthesis of vibration controllers for spaceborne optical systems are summarized and placed in perspective in Section 5.3. Finally, several research questions growing out of the work reported here that remain open and that have profound implications for future flexible space systems, including directed-energy systems, are discussed in Section 5.4.

5.2 Current Results in Active Control Synthesis

During the final reporting period under the contract, work toward active control synthesis for wideband disturbance accommodation focused on the following specific topics: (a) Modification of LQG compensation strategy to enhance stability robustness relative to unmodeled high-frequency dynamics; (b) Examination of the potential for independent (noncollocated) selection of sensors to improve sensing of disturbance effects; and (c) Incorporation of high-resolution spectrum estimation data-processing in the active control synthesis process to provide more accurate reduced-order modeling information. Primary emphasis was placed on the first of these three topics.

5.2.1 Stability Robustness to Unmodeled High-Frequency Dynamics

Initial study of interactions between principal elements of the synthesis process [Refs. 5-13 through 5-15] was done without changing the controller feedback strategy. In spite of this, a surprising degree of stability robustness to high-frequency modes excluded from the design model was observed, reflecting in part a compatibility between the selections of a reduced-order design model and of (collocated) active transducers. Stability in the presence of unmodeled modes up to a frequency of 14.8 Hz was demonstrated (compared to the design model bandwidth of 0.148 - 3.24 Hz). This fact generated optimism that a substantial improvement in stability robustness could be demonstrated by appropriate modification of the LQG disturbance-rejection strategy. A systematic approach to such modification (LQG/Loop Transfer Recovery) has

recently been developed [Refs. 5-16, 5-17] which provides substantial frequency-domain insight reflecting the spirit of classical servo-mechanism theory. A careful exposition of the LQG/LTR approach as employed in the context of the synthesis problem being considered here, together with the results obtained in applying the approach, is presented separately in Section 6. The results validate the use of this approach in the flexible space structure application: several designs were obtained exhibiting stability when connected across the full-order (150-mode) structural model. In addition, limitations of the approach reflecting the fundamental tradeoff between stability and performance that are observed in this type of application are discussed.

5.2.2 Independent (Noncollocated) Sensor Selection

The structural dynamic model--expressed in modal coordinates--of the system to be controlled is briefly recalled:

$$\ddot{\eta} + 2Z\Omega\dot{\eta} + \Omega^2\eta = (\phi^T B_A) u_A + (\phi^T B_D) u_D \quad (5-1)$$

$$y = (\phi^T C_P)^T \eta + (\phi^T C_V)^T \dot{\eta} \quad (5-2)$$

$$z = (\phi^T D^T)^T \eta \quad (5-3)$$

Here $\eta \equiv (\eta_1, \dots, \eta_n)^T$ is the vector of modal coordinates retained in the reduced-order structural model; $\Omega \equiv \text{diag}(\omega_1)$: $n \times n$ is the matrix of characteristic structural frequencies; ϕ : $v \times n$ (mode shapes of the reduced-order model) is the truncation of the principal-axis matrix of transformation defining the modal coordinates, v being the number of physical generalized coordinates; $Z \equiv \text{diag}(\zeta_1, \dots, \zeta_n)$: $n \times n$ is the matrix of assumed modal damping ratios representing inherent structural damping; $u_A \equiv (u_1, \dots, u_m)^T$ is the vector of inputs to the actuators;

$u_D \equiv (w_1, \dots, w_\gamma)^T$ is the vector of disturbance inputs; $y \equiv (y_1, \dots, y_\ell)^T$ is the vector of outputs from the sensors; $z \equiv (\epsilon_{\text{LOSX}}, \epsilon_{\text{LOSX}}, \epsilon_{\text{DEFOCUS}})^T$ is the vector of optical system line-of-sight (LOS) errors to be regulated; and $B_A: v \times m$, $B_D: v \times \gamma$, $C_p: \ell \times v$, $C_v: \ell \times v$, $D: 3 \times v$ are the geometric influence matrices associated with the actuators, disturbances, displacement sensors, rate sensors, and regulated variables, respectively. The superscript "T" denotes matrix transpose.

The approach to actuator selection we have proposed [Refs. 5-18, 5-12 (Part 1)] seeks to extract from a (relatively large) class of actuator candidates a (relatively small) subclass which retains sufficient control authority over the variables to be regulated to achieve the specified performance (with an appropriate feedback strategy). A sequence of least-squares approximations associated with equations having the form

$$Ax = b^{\text{LOSX}} \quad (5-4)$$

$$Ay = b^{\text{LOSX}} \quad (5-5)$$

is computed, where the columns of A consist of actuator modal influence vectors $\phi^T b_A^j: n \times 1$ from Eq. (5-1) representing candidate actuator locations, and the objective vectors are the (transposed) modal coefficients $b^{\text{LOSX}} \triangleq \phi^T d_{\text{LOSX}}$, $b^{\text{LOSX}} \triangleq \phi^T d_{\text{LOSX}}: n \times 1$ of the line-of-sight error vector from Eq. (5-3). Successive iterations exhibit a monotonic decrease in the column dimension of A in Eqs. (5-4), (5-5) corresponding to a deletion of actuator candidates. (Criteria for decisions on the deletion of actuators is discussed in detail in Reference 5-12.) The iteration is terminated when an appropriate measure of either one of the least-squares residual vectors $b^{\text{LOSX}} - Ax$, $b^{\text{LOSX}} - Ay$ exceeds a specified tolerance. One or more minimal selections (which do not exceed the tolerance parameter) are obtained.

5.2.2.1 Algorithm for Sensor Selection

In the light of this strategy for actuator selection, examination of Eqs. (5-1) through (5-3) suggests a completely analogous but complementary approach to the selection of sensors in which selections are keyed to a potential capacity for detecting disturbance effects. We seek to extract from a (relatively large) class of sensor candidates a (relatively small) subclass which retains sufficient information content about the effects of the disturbances upon the structure to provide for an appropriate level of disturbance rejection. To clarify this interpretation, we give a precise formulation of the sensor selection problem, referring to Reference 5-12 (Part 1) for details of its solution. The sensor selection may be defined using the following two sets of parameters:

- (1) A collection \mathcal{S} of sensor candidates, consisting of the modal coefficient vectors $\phi^T c^j: n \times 1$, where c^j is the j -th row of the geometric sensor coefficient matrix C_p (for a displacement sensor) or C_v (for a rate sensor) in Eq. (5-2); and
- (2) A collection \mathcal{J} of disturbance objective vectors, consisting of the modal influence vectors $\phi^T b_D^j: n \times 1$, where b_D^j is the j -th column of the geometric disturbance influence matrix B_D in Eq. (5-1).

To sharpen the succeeding discussion, the disturbance vector u_D is identified with the two-vector $u_D \equiv (u_{37}, u_{46})^T$ representing the two disturbance inputs denoted in Fig. 5-1, where the subscripts denote the specific nodes (nos. 37 and 46) of the finite-element structural model at which the disturbances are applied. The collection \mathcal{J} then consists of the two elements

$$t^{37} \triangleq \phi^T b_D^{37}, \quad t^{46} \triangleq \phi^T b_D^{46}$$

where b_D^{37} and b_D^{46} are the columns of the matrix B_D corresponding to the disturbance inputs u_{37} and u_{46} , respectively, in Eq. (5-1). The mathematical selection problem is a weighted-least-squares minimization corresponding to the algebraic equations

$$Sx = t^{37} \quad (5-6)$$

$$Sy = t^{46} \quad (5-7)$$

where the columns of S are elements from the collection \mathcal{P} of sensor candidates to be considered. Several notational conventions will facilitate a precise statement of the sensor selection problem. Let λ denote the number of candidates in a particular collection \mathcal{P} , and let \mathcal{P}' be a subcollection of \mathcal{P} . Denote by $I(\mathcal{P}')$ the subset of $\{1, \dots, \lambda\}$ that identifies which elements of \mathcal{P} are retained in \mathcal{P}' , and let S' be a matrix whose columns are the elements of \mathcal{P}' .

Sensor Selection Problem. Find a subcollection \mathcal{P}' of \mathcal{P} and corresponding coefficient vectors $x' \equiv (x_j)$, $y' \equiv (y_j)$, $j \in I(\mathcal{P}')$ such that

$$(1) \quad J_W(x'; S', t^{37}) \triangleq (t^{37} - S'x')^T W(t^{37} - S'x') \quad \text{and} \quad (5-8)$$

$$J_W(y'; S', t^{46}) \triangleq (t^{46} - S'y')^T W(t^{46} - S'y') \quad (5-9)$$

are minimized, where $S' \triangleq [\mathcal{P}']$; and

- (2) the subcollection \mathcal{P}' is minimal with respect to acceptable increases in the minimum values:

$$J_{\min}(S', t^{37}) \triangleq \min_{x'} J_W(x'; S', t^{37}) \quad (5-10)$$

$$J_{\min}(S', t^{46}) \triangleq \min_{y'} J_W(y'; S', t^{46}) \quad (5-11)$$

In the above, the weighting matrix, W : $n \times n$ is chosen to be real, symmetric, and positive definite. The problem statement is independent of the choice of column arrangement within S' [Ref. 5-12 (Part 1), Proposition 2-7].

Since the sensor selection problem has the same mathematical structure as the selection problem defined for actuators (cf. Eqs. (2-34) through (2-37) of Reference 5-12), the algorithm used to generate actuator selections may also be applied to sensor selection. Details of the algorithm have been given previously [Ref. 5-12, Sec. 2.2]. In brief, one begins by selecting an initial class of sensor candidates \mathcal{S} . A sequence of least-squares minimizations of functionals having the form of Eqs. (5-8), (5-9) is then performed. At each stage of the sequence, the least-squares residual vectors just computed suggest one or more deletions of sensor candidates from \mathcal{S} for the succeeding stage according to guidelines indicated in the algorithm description. A lattice of eliminations is thereby generated. Termination of the sequence occurs when the minimum value in Eq. (5-10) or (5-11) (equivalently, an appropriate norm of the residual vector associated with either Eq. (5-6) or (5-7)) exceeds a specified tolerance.

5.2.2.2 Applications with ACOSS Model No. 2

For a specified configuration of actuators, the length (however defined) of the least-squares residual vectors associated with Eqs. (5-4), (5-5) provides a measure of how well the actuators (as represented by the actuator modal influence vectors appearing as columns of the A matrix) can be combined linearly to approximate the optical line-of-sight (as represented by the modal coefficient vectors b_{LOS}).

and b_{LOS}). In results reported previously [Refs. 5-13, 5-14], all of the actuator selections were generated so that this approximation was quite good (residual vector tolerance parameter $\approx 10^{-6}$). It should be noted in passing that the quality of this sort of static criterion of approximation can only be judged in the light of dynamic performance of a closed-loop design employing such actuators.

However, in previously reported work, rate sensors were assumed to be colocated with the actuators selected without a corresponding (static) evaluation of the resulting sensor configuration. The sensor selection procedure presented in the preceding subsection provides a mechanism for making such evaluations. For any configuration of sensors, the length of the least-squares residual vectors associated with Eqs. (5-6), (5-7) and arising out of the minimization of the functionals in Eqs. (5-8), (5-9) provides a measure of how well the sensors (as represented by the sensor modal coefficient vectors appearing as columns of the S matrix) can be combined linearly to approximate the disturbances (as represented by the modal influence vectors t^{37} and t^{46}). One may now ask how well (in the above sense) the (colocated) sensor configurations assumed in previous work approximate the disturbances. The answer--in some cases--is: not so good. Correlation of this observation with the performance and stability robustness of controller designs reported previously is interesting, as is indicated shortly.

The specific assumptions under which design experiments have been conducted to date are briefly recalled. The structural model representing the object of control is Revision 1 of ACROSS Model No. 2 [Ref. 5-5]. A modal damping ratio of $\zeta_1 = 0.001$ is assumed for all modes (cf. Eq. (5-1)). The model is subject to (wide-sense stationary) wideband disturbance excitation with frequency content as shown (one-sided) in Fig. 5-2. The disturbance is applied at two (uncorrelated) locations (cf. Fig. 5-1): node 37 on the upper optical support truss, and node 46 on the equipment section (Figs. 5-3 ff. display the node points explicitly). To hold down computation costs, it

is further assumed that the points of application do not change with time, and that each disturbance is constant in direction (at an equal angle with each body axis). The specified optical performance is to regulate the optical axis (z-body-axis) rotation errors (LOSX, LOSY) about the two lateral axes (x and y body axes) so that

$$\text{LOSX} \leq 0.05 \mu \text{ rad} \quad (\text{rms}) \quad (5-12)$$

$$\text{LOSX} \leq 0.05 \mu \text{ rad} \quad (\text{rms}) \quad (5-13)$$

and to regulate the mirror relative positions so that a sharp image focus is maintained:

$$\text{DEFOCUS} \leq 10^{-3} \text{ m} \quad (\text{rms}) \quad (5-14)$$

where each inequality is in the root-mean-square (rms) sense. (Explicit expressions for the parameters LOSX, LOSY, and DEFOCUS as a linear function of nodal displacements are given in Reference 5-5.)

Choice of reduced-order models for design is based upon ranking the response of the (uncoupled) modes of vibration for the open-loop (i.e., $u_A = 0$ in Eq. (5-1)) structure to the total disturbance excitation. An abbreviated ranking is shown in Table 5-1. A corresponding interlaced reduced-order design model, together with a contiguous counterpart obtained by adding interleaved modes, is illustrated in Table 5-2. A family of variable-order contiguous models is used for evaluations of closed-loop stability and optical system performance with reduced-order controllers.

Table 5-1. Ranking of open-loop modal responses to wideband disturbance.

Rank	Mode	RMS LOS-Error (μ -rad)	Rank	Mode	RMS LOS-Error (μ -rad)
1	7 o	600.97	26	11	1.19
2	24 o	455.77	.	.	.
3	23 o	105.89	.	.	.
4	13 o	92.65	35	21	0.72
5	22 o	77.04	.	.	.
6	12 o	72.43	.	.	.
7	16 o	32.47	42	20	0.25
8	14 o	15.91	.	.	.
9	10 o	12.94	.	.	.
10	8 o	12.22	47	17	0.09
11	9 o	5.06	.	.	.
12	39	5.01	.	.	.
.	.	.	78	18	0.005
.
22	15	1.45	.	.	.
.	.	.	145	19	1E-22
.
.

Table 5-2. Characteristic frequencies for ACOSS Model No. 2 and reduced-order models;
o Design (interlaced)
• Design (contiguous) ■ Evaluation (contiguous).

Mode	Frequency (Hz)	Mode	Frequency (Hz)
7	o • ■ 0.148	25	■ 5.162
8	o • ■ 0.282	26	■ 5.170
9	o • ■ 0.319	27	■ 7.877
10	o • ■ 0.335	28	■ 7.918
11	• ■ 0.468	29	■ 8.772
12	o • ■ 0.583	30	■ 8.776
13	o • ■ 0.601	31	■ 8.838
14	o • ■ 0.673	32	■ 8.980
15	• ■ 0.960	33	■ 9.620
16	o • ■ 1.092	34	■ 10.40
17	• ■ 1.839	35	■ 11.67
18	• ■ 1.844	36	■ 12.27
19	• ■ 1.889	37	■ 13.39
20	• ■ 1.990	38	■ 13.62
21	• ■ 2.060	39	■ 14.77
22	o • ■ 2.452	40	■ 16.43
23	o • ■ 2.472	41	20.83
24	o • ■ 3.262	42	21.79
		43	21.84

5.2.2.2.1 Evaluation of Sensor Configurations Defined by Colocation

A summary of the minimal actuator selections generated in the context of the experimental approach to the synthesis process is presented in Table 5-3. The number of actuators p in a minimal selection is a function (among other things) of the number of modes n retained in the reduced-order design model, the functional type of the actuator candidates (\mathcal{A}) considered, and the tolerance parameter τ_0 for the least-squares computation used to terminate the selection algorithm. The tolerance parameter is applied (as a maximum permissible upper bound) to the maximum (in absolute value) component $\rho_i(\cdot)$ of the current residual vector. The value of the tolerance parameter was allowed to fluctuate slightly (between 10^{-6} and 5×10^{-5}) as an experimental variable. Note (Table 5-3) that for each selection:

$$\max_{i=1, \dots, n} \rho_i^{\text{LOSX}} \leq \tau_0 \quad (5-15)$$

$$\max_{i=1, \dots, n} \rho_i^{\text{LOS Y}} \leq \tau_0 \quad (5-16)$$

$$\max_{i=1, \dots, n} \rho_i^{\text{DEFOCUS}} \leq \tau_0 \quad (5-17)$$

although only Eqs. (5-15), (5-16) were enforced to terminate the selection algorithm. This is another reflection of the fact that Eq. (5-14) is the least stressful of the performance criteria Eqs. (5-12) through (5-14). The actuator locations for the minimal selections of examples A, B, C, E, and F of Table 5-3 are pictured in Figs. 5-3a, 5-4a, 5-5a & 5-5b, 5-6a, and 5-7a, respectively (there being two minimal selections for example C).

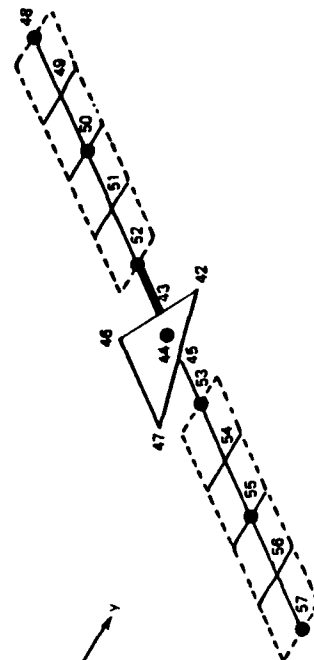
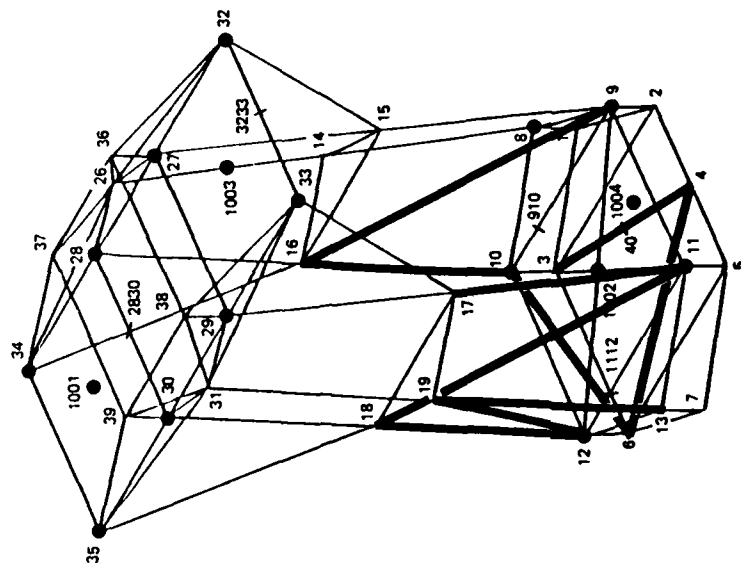
We now examine the sensor configurations that result from placing (rate) sensors of the corresponding type at the locations of the various actuator selections. Recall that each minimal actuator selection is

Table 5-3. Minimal selections for actuators; comparative quality of collocated sensor configurations.

Example	Design Model	Actuator Candidate Class (\mathcal{A})	Size of Minimal Actuator Selection(p)	Actuator Level of Reduction (Δ)	Tolerance Parameter (τ_0)	Maximum Residual Vector Component				
						Actuators Selected		Collocated Sensors		
						LOSX	LOSX	DEFOCUS	DS37	DS46
A	Rank 1-11 Interlaced (n = 11)	Axial only	10 (axial)	1	2×10^{-5}	1.87E-5	2.23E-6	7.55E-10	1.67E-4	2.98E-4
B		($\mu = 137$)	14 (axial)	4	3×10^{-6}	2.73E-6	1.07E-6	8.23E-11	8.79E-5	4.24E-5
C	Rank 1-11 Contiguous* (n = 18)	Axial and Nodal Translation ($\mu = 311$)	12 (translation)	6	5×10^{-5}	5.71E-7	3.37E-5	3.12E-7	5.37E-4	3.51E-4
		Axial and Nodal Transl. & Rotation ($\mu = 485$)				8.17E-8	1.99E-5	1.98E-7	6.19E-6	4.73E-5
D		Axial and Restricted Nodal Translation ($\mu = 289$)	9 (translation)	9	1×10^{-6}	5.70E-7	7.59E-7	6.20E-7	4.30E-7	1.98E-3
		Axial and Nodal Rotation ($\mu = 311$)	5 (rotation)	13	7×10^{-6}	3.31E-6	3.38E-6	1.58E-6	8.16E-3	1.02E-2
E		Axial and Restricted Nodal Rotation ($\mu = 299$)	10 (rotation)	8	7×10^{-6}	4.47E-6	2.11E-6	1.22E-6	2.71E-4	4.74E-3
F		Kinematic Mount Translation Dir. ($\mu = 23$)	7 (translation)	11	7×10^{-6}	3.34E-6	5.64E-6	1.26E-6	3.07E-4	2.31E-2
G		LOS-Error-Model Degrees of Freedom ($\mu = 21$)	8 (translation)	10	7×10^{-6}	4.75E-7	5.50E-6	6.21E-7	9.72E-6	2.31E-2

* Mode 19 excluded from design model

11 SENSORS



10 ACTUATORS

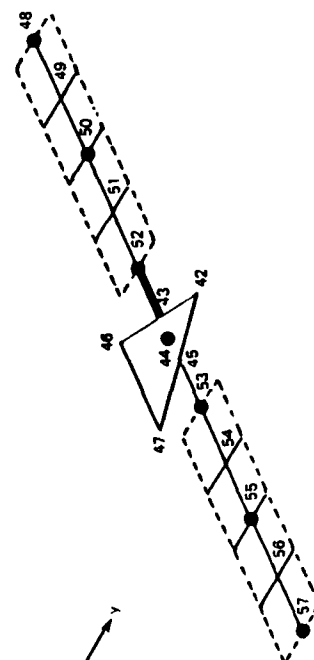
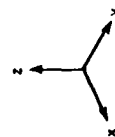
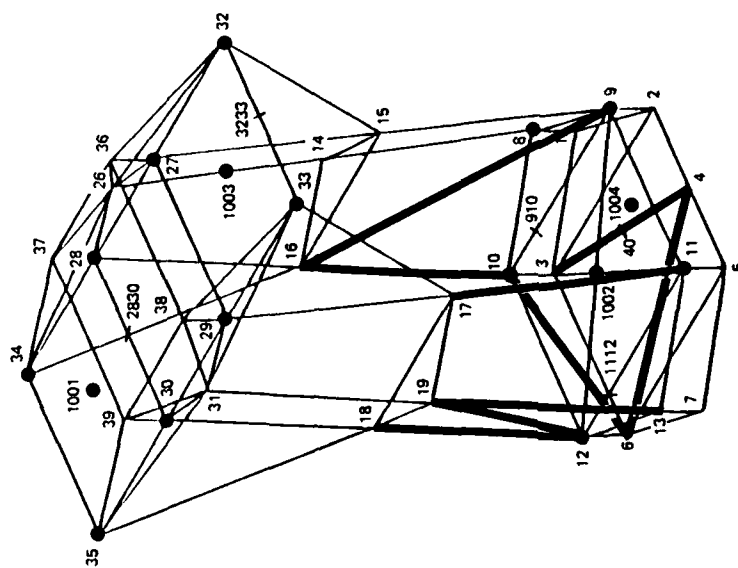
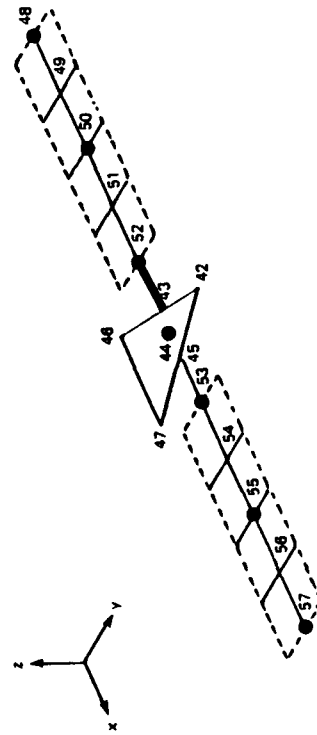
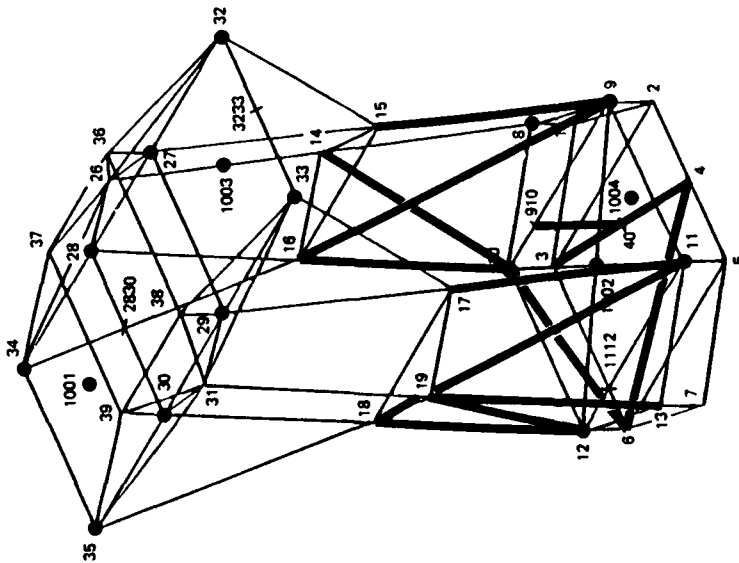


Figure 5-3b. Minimal sensor selection, example A.

Figure 5-3a. Minimal actuator selection, example A.

14 ACTUATORS



16 SENSORS

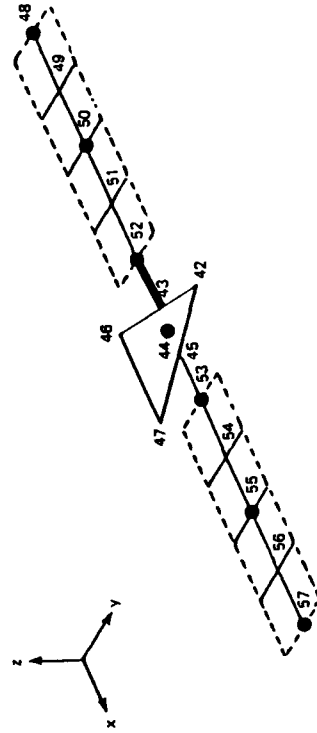
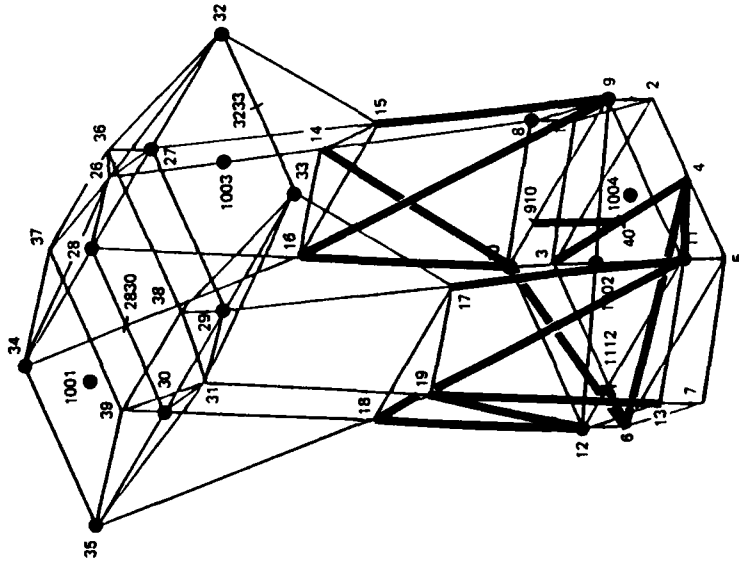
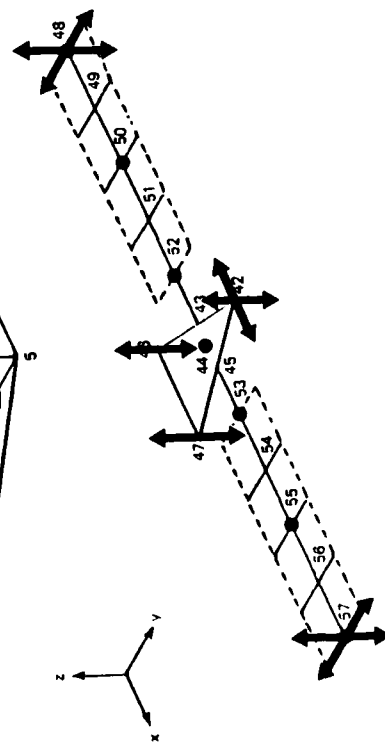
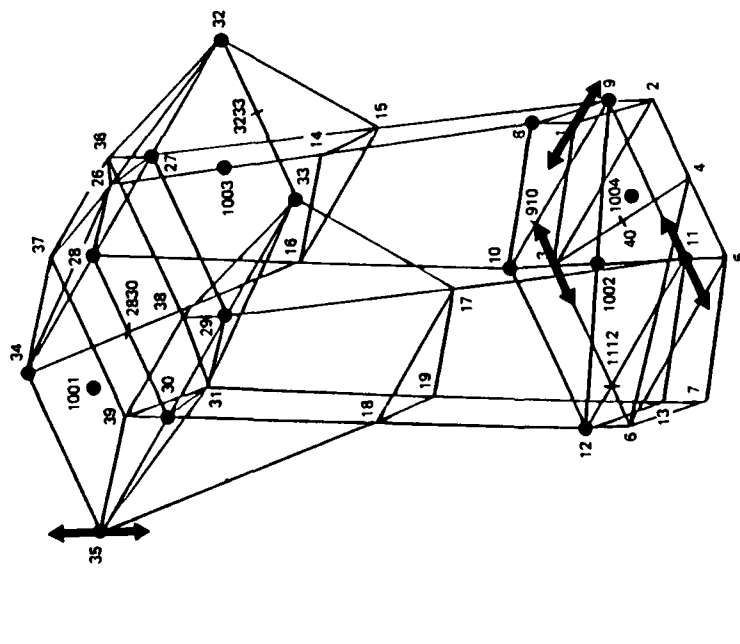


Figure 5-4a. Minimal actuator selection, example B. Figure 5-4b. Minimal sensor selection, example B.

12 ACTUATORS



12 ACTUATORS

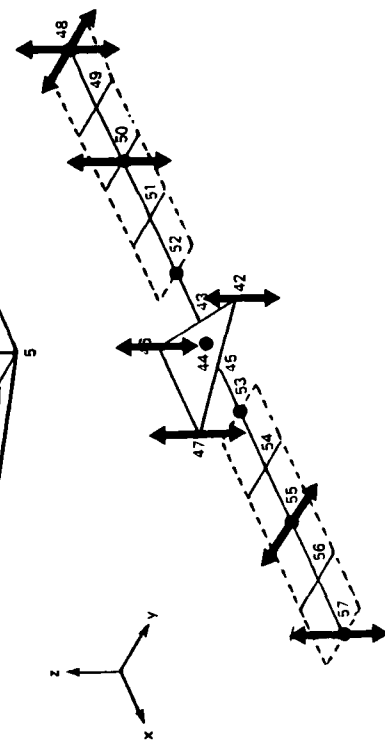
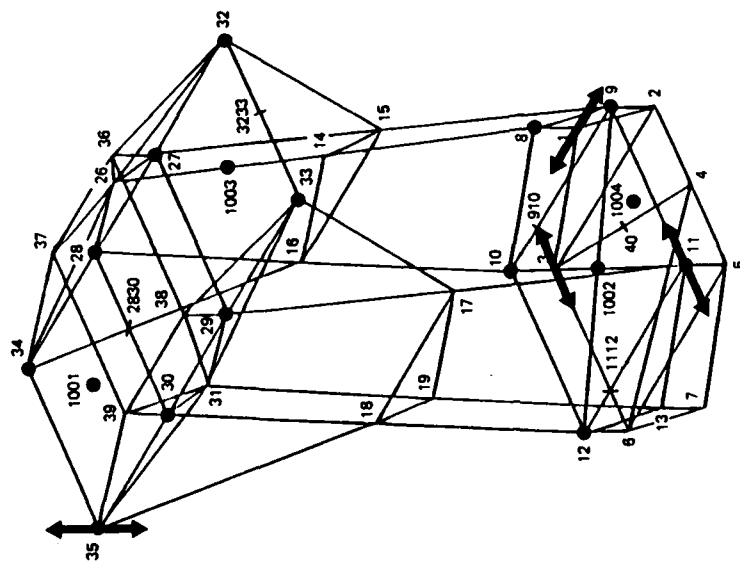
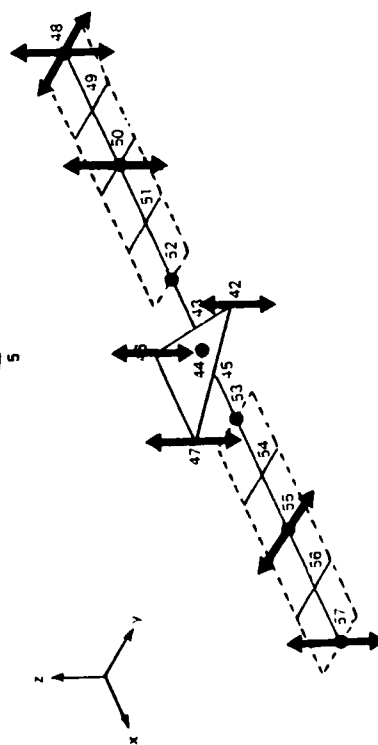
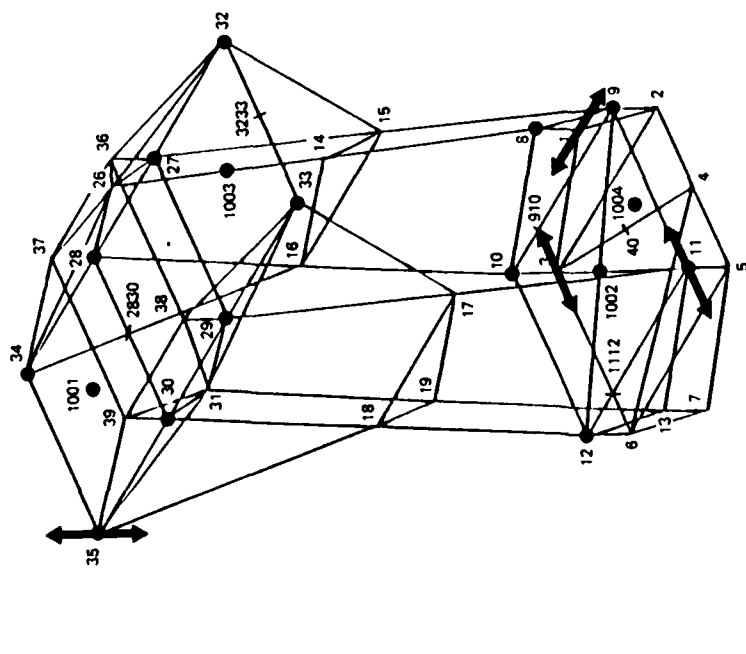


Figure 5-5a. Minimal actuator selection a, example C. Figure 5-5b. Minimal actuator selection b, example C.

12 SENSORS



12 SENSORS

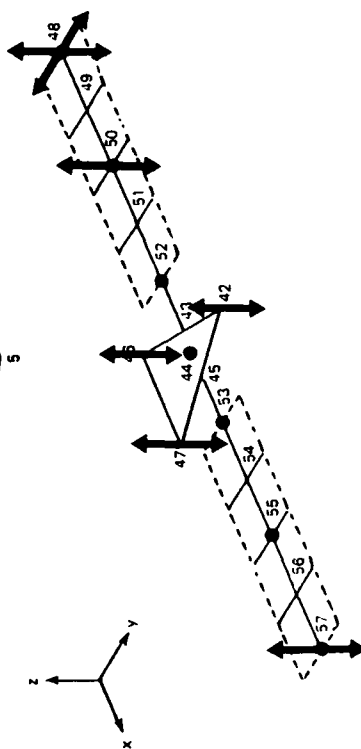
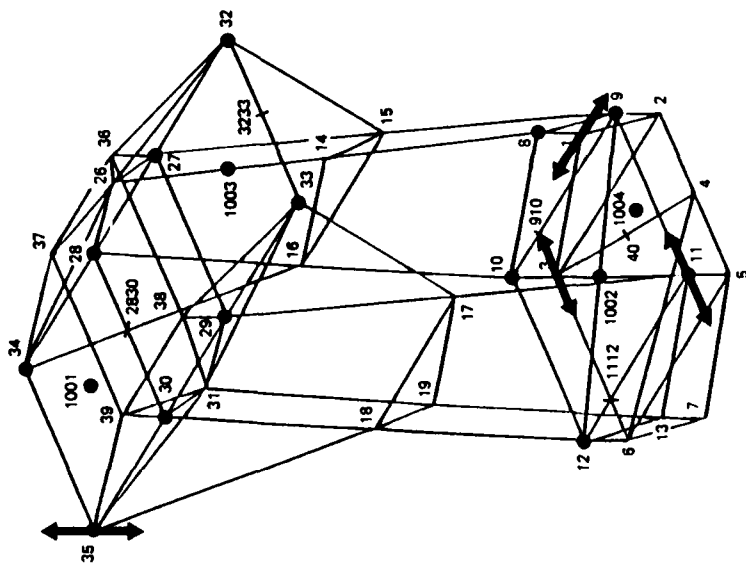
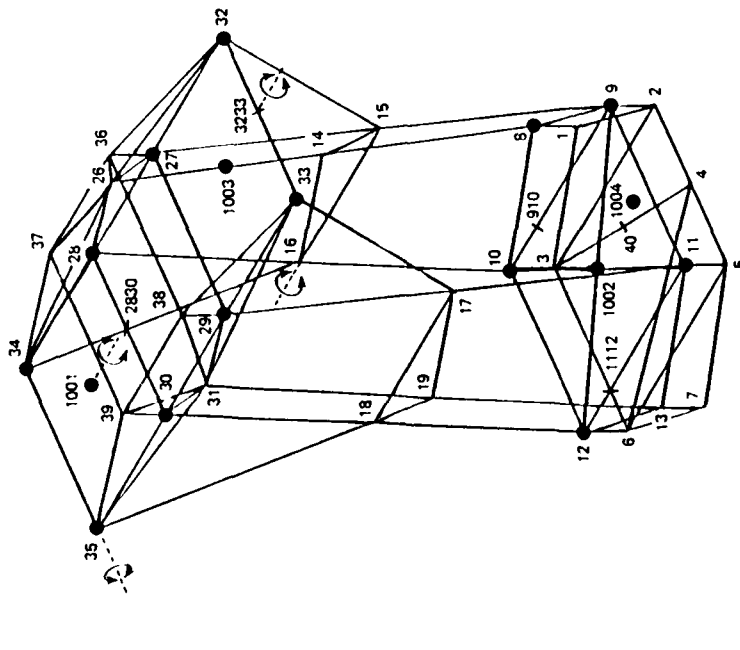


Figure 5-5c. Minimal sensor selection α , example C. Figure 5-5d. Minimal sensor selection β , example C.

5 ACTUATORS



15 SENSORS

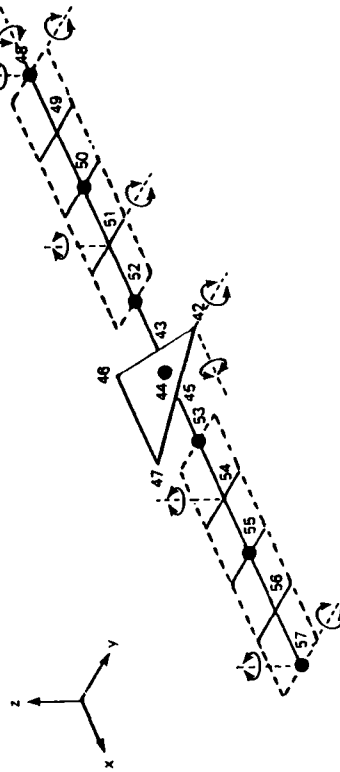
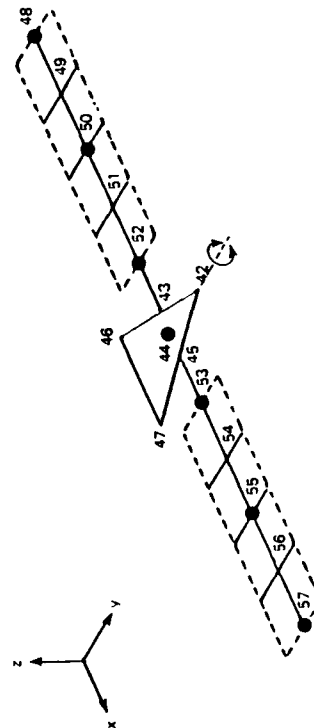
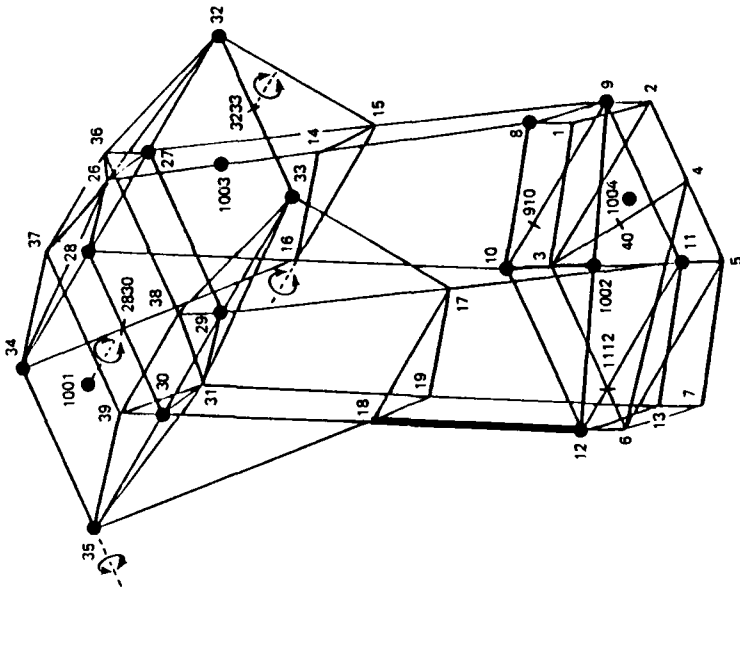
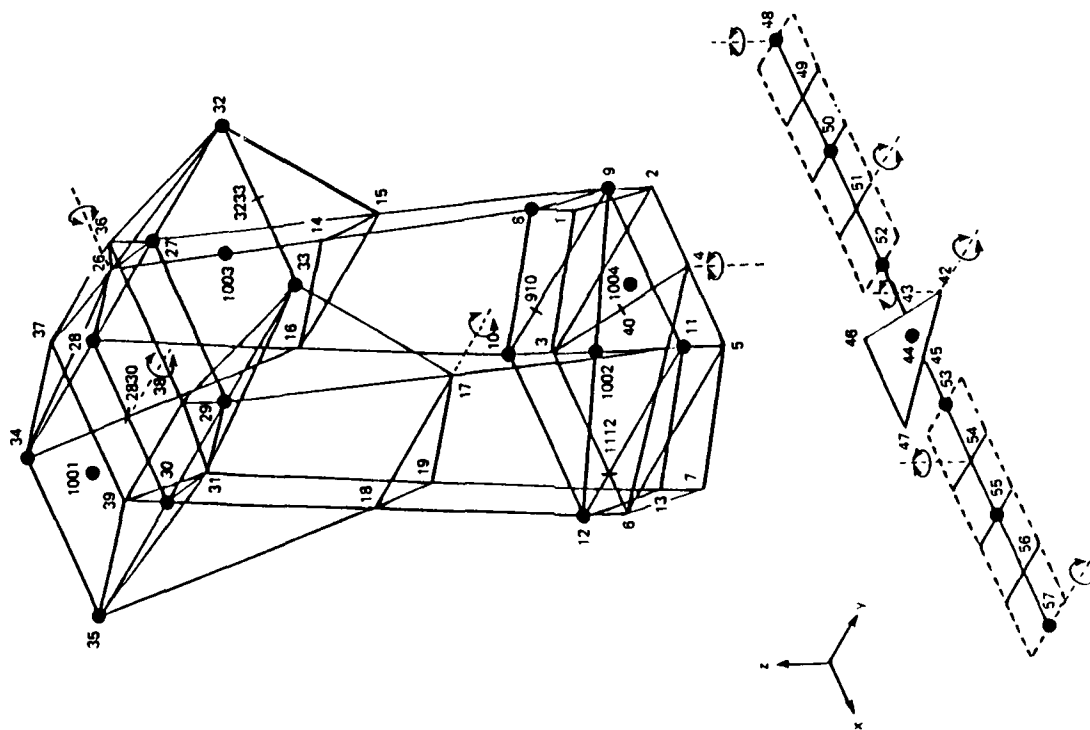


Figure 5-6b. Minimal sensor selection, example E.

Figure 5-6a. Minimal actuator selection, example E.

10 ACTUATORS



16 SENSORS

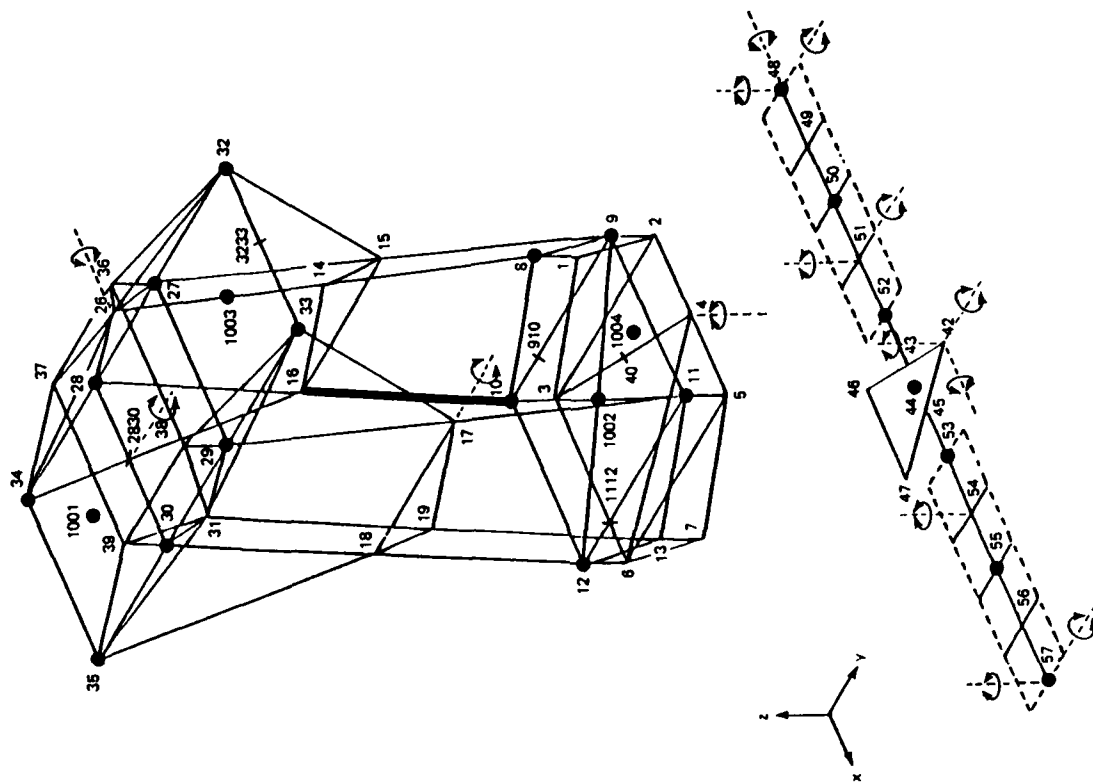


Figure 5-7b. Minimal sensor selection, example F.

Figure 5-7a. Minimal actuator selection, example F.

11 ACTUATORS

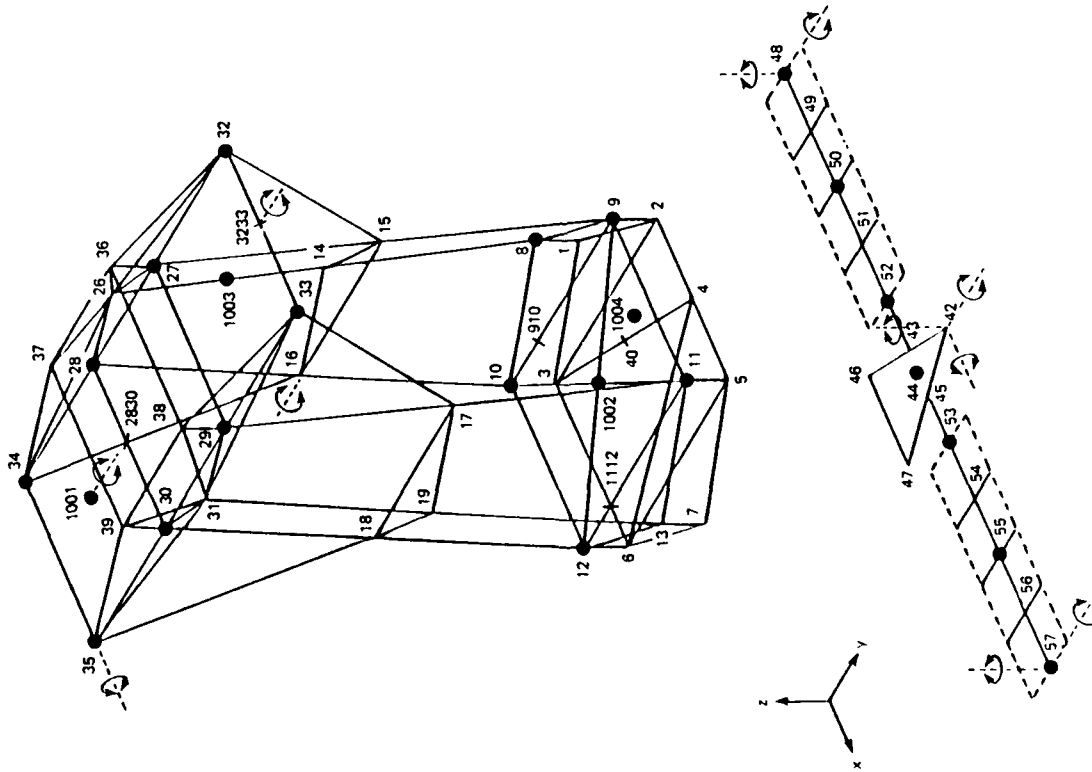


Figure 5-8a. Nonminimal actuator selection a (heuristic), example E.

11 ACTUATORS

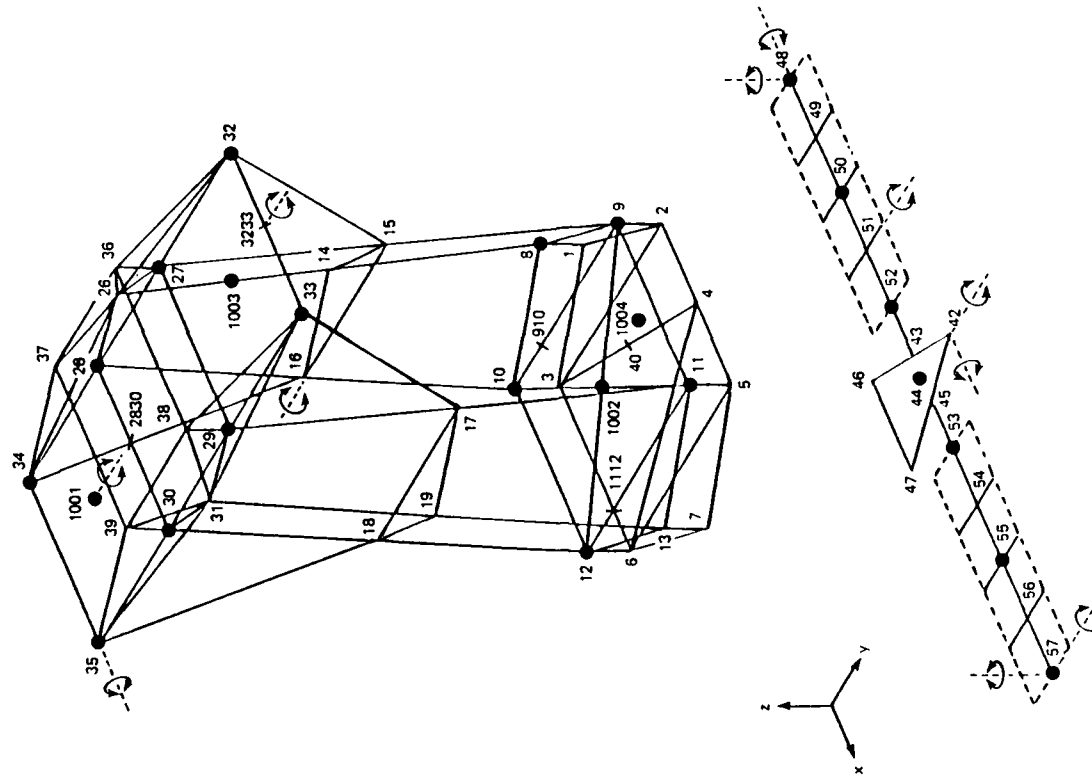


Figure 5-8b. Nonminimal actuator selection b (computed), example E.

identified with a matrix A' : $n \times p$ (where p is the number of actuators in the selection) and vectors x' , y' : $p \times 1$ corresponding to least-squares solutions of Eqs. (5-4) and (5-5), respectively. The functionals

$$J_W(\cdot; A', t^{37})$$

and

$$J_W(\cdot; A', t^{46})$$

defined by Eqs. (5-8) and (5-9), respectively, are then minimized, generating least-squares solutions x'' , y'' : $p \times 1$ of Eqs. (5-6), (5-7), respectively, with the actuator matrix A' playing the role of a sensor matrix S . Maximum components of the corresponding residual vectors ρ^{37} , ρ^{46} : $n \times 1$ are listed in the last two columns of Table 5-3. The results show that least-squares solutions of Eq. (5-7) that are possible using the various colocated sensor configurations is generally poor, and most notably so using the minimal selection of example E (in which case the least-squares solution corresponding to Eq. (5-6) also represents a poor approximation).

A correlation between these observations and dynamic performance under closed-loop control can be seen by examining Table 5-4. Data in this table summarizes design parameters for, and stability and performance obtained with, LQG/disturbance-rejection designs (not incorporating loop transfer recovery) that were done to examine the influence of reduced-order model selection and of active transducer selection upon the synthesis process. (Alphanumeric entries in the first column of Table 5-4 identify a specific actuator selection from among the selections described in Tables 5-3, 5-5, and 5-6. For example, C-12a refers to the colocated 12-actuator selection a of Example C described in Table 5-3.) Performance data in Table 5-4 for example E using the 5 colocated rotational actuators and (rate) sensors shows a marked degradation in the error parameter LOSY (and a lesser degradation in

Table 5-4. Controller design and evaluation; LOG/disturbance-rejection without loop transfer recovery.

Actuator Selection (collocated sensors)	Weights				L0 (modes 7-24)			LOG (modes 7-24)			LOG (modes 7-36)			Modes in Stable Evaluation
	q_1	q_2	q_3	ρ_R and ρ_0	LOSX (μ rad)	LOS (μ rad)	DEFOCUS (10^{-3} m)	LOSX (μ rad)	LOS (μ rad)	DEFOCUS (10^{-3} m)	LOSX (μ rad)	LOS (μ rad)	DEFOCUS (10^{-3} m)	
Design Objective	-	-	-	-	0.05	0.05	0.025	0.05	0.05	0.025	0.05	0.05	0.025	7-156
A (10 axial)	10^3	10^1	10^{-4}	10^{-17}	0.0364	0.02093	0.00180							Unstable
B (14 axial)	10^3	10^1	10^{-4}	10^{-17}	0.01958	0.01146	0.00408							7-29
C-12a (12 transl.)	10^0	10^{-1}	10^{-5}	10^{-17}	0.00532	0.00851	0.00136	0.00644	0.05073	0.00136	31.44	19.16	0.03848	7-39
D-14 (14 transl.)	10^{-1}	10^{-2}	10^{-6}	10^{-17}	0.02025	0.03204	0.00188	0.02124	0.06888	0.001883	15.84	9.2	0.01347	7-36
D-9a (9 transl.)	10^{-1}	10^{-2}	10^{-6}	10^{-17}	0.0257	0.03317	0.00345							7-29
E-5 (5 rot.)	10^1	10^{-1}	10^{-5}	10^{-17}	0.05587	0.04776	0.00496	0.06019	0.16216	0.00496				7-33
E-11a (11 rot.)	10^1	10^{-1}	10^{-5}	10^{-17}	0.01776	0.04917	0.00266							7-25
E-5/15* (5a/15s, rot.)	10^1	10^{-1}	10^{-5}	10^{-17}	0.05587	0.04776	0.00496	0.05689	0.09564	0.00496				7-32
G-23 (23 transl.)	10^0	10^{-1}	10^{-5}	10^{-15}	0.02868	0.08904	0.00360							7-61
G-17 (17 transl.)	10^0	10^0	10^{-5}	10^{-15}	0.03469	0.01381	0.00378							7-33

* Noncollocated selection

LOSX) when a Kalman filter is connected to the LQ regulator in the feedback compensator. Since sensor measurements are inputs to the Kalman filter, one would expect less degradation upon incorporation of the filter through the deployment of sensors which provide better information on disturbance effects. This expectation is confirmed, as we demonstrate shortly.

5.2.2.2.2 Independent Minimal Sensor Selections

Using the algorithm for sensor selection described in Section 5.2.2.1, several minimal selections for sensors have been generated. Data concerning them is summarized in Table 5-5, and they are illustrated in Figs. 5-3b, 5-4b, 5-5c & 5-5d, 5-6b, and 5-7b (there being two minimal selections for example C). In generating these selections, the same reduced-order design model, the same functional type of transducer candidates, and the same tolerance parameter were used as for the corresponding actuator selections (cp. Table 5-3). Note that in example A, the number of sensors cannot be reduced below the number of modes in the design model without one of the residual vector components exceeding the tolerance parameter. Sensor selections with example C are rather remarkable. Comparison of Figs. 5-5b and 5-5c reveals that the locations and functional type of sensors in sensor selection α are identical to that of the actuators in actuator selection b. Stated differently, the sensor configuration defined by colocating (rate) sensors of corresponding type with actuator selection b is a minimal selection in its own right with respect to the disturbance environment. This remarkable fact is reflected in closed-loop LQG design performance. (Designs have only been done employing actuator selection a, together with colocated sensors, but reference to Figs. 5-5a and 5-5b and the data in Table 5-3 indicate only slight differences relative to selection b.) Table 5-4 indicates that an LQG controller (without loop transfer recovery) employing colocated actuator/sensor selection C-12a exhibits completely acceptable performance degradation associated with

Table 5-5. Minimal Selections for sensors.

Example	Design Model	Sensor Candidate Class (\mathcal{S})	Size of Minimal Sensor Selection(p)	Sensor Level of Reduction (Δ)	Tolerance Parameter (τ_0)	Maximum Residual	
						Sensors Selected	
						DS37	DS46
A	Rank 1-11 Interlaced (n = 11)	Axial only	11 (axial)	0	2×10^{-5}	0	0
B	Rank 1-11 Contiguous*	($\lambda = 137$)	16 (axial)	2	3×10^{-6}	1.40E-6	2.07E-6
C		Axial and Nodal Translation ($\lambda = 311$)	12 (translation)	6	5×10^{-5}	6.19E-6	4.73E-5
						1.72E-5	2.18E-5
E	(n = 18)	Axial and Nodal Rotation ($\mu = 311$)	15 (14 rotation, 1 axial)	3	7×10^{-6}	6.27E-6	6.51E-6
F		Axial and Restricted Nodal Rotation ($\mu = 299$)	16 (15 rotation, 1 axial)	2	7×10^{-6}	5.05E-6	6.74E-6

* Mode 19 excluded from design model

incorporation of the Kalman filter into the feedback compensator, and displays the largest degree of robustness with respect to unmodeled high-frequency dynamics of any of the unrecovered designs for which $p \leq n$ is assumed.

Sensor selection with example E indicates a rapid deterioration in the least-squares approximations associated with Eqs. (5-6), (5-7) as sensors are reduced in number below n (the row rank of the sensor-candidate matrix S). In fact, the selection process terminates when p (the number of sensor candidates) is reduced to 15. This is consistent with the observations noted above regarding the poor least-squares approximation quality of the colocated sensors associated with example E (cf. Table 5-3). This suggests considering the (noncolocated) combination of the 5 actuators selected (Fig. 5-6a) with the 15 sensors selected (Fig. 5-6b). Note that this particular combination is noncolocated only in that the number of actuators and of sensors is not the same. As indicated in Table 5-4, the employment of this combination (designated E-5/15) in an LQG design leads to noticeable performance improvement relative to the colocated selection in example E. On the other hand, there is a slight degradation in robustness to unmodeled high-frequency dynamics associated with the additional sensors. The performance improvement (at the design model level) associated with the augmented transducer configuration is qualitatively predictable. The change in robustness to unmodeled dynamics is not.

5.2.2.2.3 Further Observations on Actuator Selection

The notation of a minimal selection (either of actuators or of sensors) is motivated in part by the potential for advantageous employment of nonminimal selections (to be obtained by the judicious enlargement of minimal selections). In particular, the process of convergence to a minimal selection gives sharp guidelines for such enlargement. Data for nonminimal selections referred to in Table 5-4 is given in Table 5-6. Design experience embodied in Table 5-4 indicates that the enlargement of minimal selections is not a predictable approach

Table 5-6. Nonminimal selections for actuators; comparative quality of collocated sensor configurations.

Example	Design Model	Actuator Candidate Class (\mathcal{A})	Number Selected	Number in Minimal Selection	Maximum Residual Vector Components				
					Actuators Selected			Collocated Sensors	
					LOSX	LOSZ	DEFOCUS	DS37	DS46
D	Rank 1-11	Axial and Restricted Nodal Translation ($\mu = 289$)	14 (translation)	9 (translation)	1.22E-10	4.63E-10	2.05E-10	2.26E-10	2.86E-7
					7.88E-8	8.88E-7	3.94E-7	2.04E-3	2.51E-3
E	Contiguous* ($n = 18$)	Axial and Nodal Rotation ($\mu = 311$)	11 (rotation)	5 (rotation)	8.73E-8	6.89E-8	1.61E-7	1.59E-4	1.82E-4
					0	0	0	0	0
G		Kinematic Mount Translation Dir. ($\mu = 23$)	23 (translation)	7 (translation)	0	0	0	0	0
			17 (translation)						

* Mode 19 excluded from design model

to enhancing robustness to unmodeled high-frequency dynamics. Whereas the enlargement in example D of minimal selection D-9a to nonminimal selection D-14 [cf. Ref. 5-12] results in enhanced robustness, just the opposite effect is observed in example E by enlarging minimal selection E-5 to nonminimal selection E-11a. (Selection E-11a, illustrated in Fig. 5-8a, is a heuristic augmentation of selection E-5 based on engineering intuition, and does not coincide with any of the several selections of 11 actuators--one of which is depicted in Fig. 5-8b--that occur during the convergence of the selection algorithm to configuration E-5 (Fig. 5-6a)). The role of enlargement to nonminimal selections remains to be given systematic attention.

The consequence of imposing appropriate constraints on the actuator (or sensor) candidate class needs to be understood at a deeper level for further exploitation of the selection process being applied here. It has been noted [Ref. 5-13] that selection E-5 (Fig. 5-6a) may not be feasible for an actual system since it implies an actuator at the center of mass of the primary mirror (node 1001). Example F (cf. Table 5-3) gives the selection that results if the actuator candidate class excludes actuation devices from any of the mirror mass-centers. The number of actuators in the minimal selection is doubled (cf. Fig. 5-7a).

A final remark is specific to ACOSS Model No. 2. The distinction between examples G and H (Table 5-3) reflects the subtle fact that the degrees of freedom in the LOS-error model are not identical to the degrees of freedom associated with the kinematic mounts [cf. Ref. 5-5]. Specifically, the degrees of freedom of the secondary mirror are defined in terms of z-translation at, and x-axis and y-axis rotation about, its mass center, rather than in terms of the kinematically equivalent kinematic mount displacements.

5.2.2.3 Remarks

Although the strategy for independent selection of sensors has sharpened insight regarding the effective deployment of active transducers, the full potential inherent in the selection process for selecting sensors to enhance information on disturbance effects has not been exploited. The initial step in the selection process executes a reduction in the number of candidates from λ (the size of the candidate class \mathcal{S}) to n (the number of modes retained in the reduced-order design model). The mechanism that realizes this reduction is the QR-factorization of the sensor candidate matrix S (cf. Eqs. (5-6), (5-7)), which generates a ranking among the sensor candidates based solely upon relative linear independence [cf. Ref. 5-12 (Part 1)]. Only in subsequent steps of the selection algorithm are eliminations of sensor candidates based upon least-squares approximation of disturbance influence vectors.

On the other hand, there is a serious question as to the advisability of tailoring a selection of sensors too tightly to parameters of the disturbance environment which are not precisely known. A more fundamental course would be to investigate robustness in both stability and performance with respect to uncertainty or change in parameters of the disturbance environment as it relates to sensor selection.

5.2.3 Incorporation of System Identification into the Synthesis Process

As discussed in Section 5.1.1, there are fundamental limitations on the accuracy with which complex flexible structures can be represented using finite-element techniques. Moreover, there are no feasible alternatives to such modeling approaches at present. These facts provide strong motivation for seeking to enhance modeling capability through the incorporation of system identification techniques, especially for the specific purpose of increasing the accuracy of reduced-order models to be used for the synthesis of active controllers. The use of appropriate

identification techniques has the potential to reduce uncertainty in the knowledge of basic structural parameters (e.g., mass or stiffness distribution), and to provide a quantitative assessment of the input-output effect produced by delays and small-amplitude nonlinearities associated with the dynamics of active transducers, the sampling and reconstruction of analog signals, and digital computation.

The high-resolution spectrum estimation procedure originally formulated by Fogel [Ref. 5-19] and extended by Villalba [Ref. 5-20 and Sec. 8 herein] is very attractive for application to reduced-order modeling of flexible spacecraft for several reasons. First, the mathematical formulation accommodates the essential constraints on data availability consistent with a flight environment. It assumes a capability for system excitation at the location of each actuator and at the location of each anticipated disturbance, and the availability of measurement data at each sensor location. Second, the procedure is aimed specifically at solving the problem of identifying modes that are closely-spaced in frequency--an inherent property of large flexible structures. In this subsection, we describe the data transformations required in order to incorporate this identification approach into the synthesis process, and point out a fundamental limitation which requires some adjustment of the synthesis process itself.

5.2.3.1 Data Transformation Required for Incorporation

The high-resolution spectrum estimation procedure is itself a dynamic process that observes the input-output behavior of the system to be identified, and generates the spectral characteristics (natural frequencies and damping ratios) of a linear time-invariant system which exhibits the same input-output behavior. It is assumed that actuator and sensors have been selected, both by functional type and by location, and that the locations of expected disturbance inputs to the system are known. Specific input data required by the identification process consists of discrete-time samples of all possible time histories of the form:

$$y_r(t; u_k) , \quad 0 \leq t \leq t_1 ; \quad k = 1, \dots, m , \quad r = 1, \dots, l \quad (5-18)$$

$$y_r(t; w_k) , \quad 0 \leq t \leq t_1 ; \quad k = 1, \dots, \gamma , \quad r = 1, \dots, l \quad (5-19)$$

where $y_r(\cdot; u_k)$ represents the response function at sensor location r to an impulsive excitation at actuator location k , and $y_r(\cdot; w_k)$ represents the response function at sensor location r to an impulsive excitation at disturbance location k (cf, Eqs. (5-1), (5-2)). Specific output data provided by the identification process are the numerical parameters in the modal representation for the estimate of the responses observed:

$$\hat{y}_r(t; u_k) = \sum_{i=1}^{\hat{n}} \operatorname{Re}[(a_{kr}^i + j b_{kr}^i) e^{p_i t}] \quad (5-20)$$

where

$$p_i \triangleq -\hat{\zeta}_i \hat{\omega}_i + j \hat{\omega}_i (1 - \hat{\zeta}_i^2)^{1/2} \quad (5-21)$$

\hat{n} is the estimate of the number of vibration modes, and $\hat{\omega}_i$ and $\hat{\zeta}_i$ are the estimates for the natural frequency and damping ratio of the i -th estimated mode. In what follows, the letter j represents the imaginary unit $\sqrt{-1}$.

In order to use the information contained in Eqs. (5-20), (5-21) for reduced-order modeling of the observed system, it is necessary to generate related estimates for the matrix products associated with the eigenvalues (i.e., Ω^2 and $2Z\Omega$) and eigenvectors (i.e., $\Phi^T B_A$, $\Phi^T B_D$, $C_P \Phi$, $C_Y \Phi$, and $D\Phi$) that appear in the dynamic equations Eqs. (5-1) through

(5-3). (Note that explicit generation of the eigenvalue matrix Ω and the eigenvector matrix Φ themselves is not needed.) It is immediately clear from elementary algebra that the entries of $\hat{\Omega}^2 \equiv \text{diag}(\hat{\omega}_i^2)$ and $2\hat{Z}\hat{\Omega} \equiv \text{diag}(2\hat{c}_i\hat{\omega}_i)$ are given, respectively, by

$$\hat{\omega}_i^2 = \text{Re}^2(p_i) + \text{Im}^2(p_i)$$

and

$$2\hat{c}_i\hat{\omega}_i = -2 \text{Re}(p_i)$$

where $\text{Re}(\cdot)$ and $\text{Im}(\cdot)$ represent the real and imaginary parts, respectively, of the indicated arguments. Generation of the eigenvector matrix products is somewhat more involved and leads to the need for imposing certain mild but subtle restrictions upon the synthesis process.

5.2.3.2 Deduced Estimates for Eigenvector Matrix Products

Estimates for the eigenvector matrix products are obtained by comparing the expressions Eqs. (5-20) to the analytic representations for the various impulse responses, which are easily written. First, it is quite helpful to develop a concise yet descriptive notation for representing the entries of the various matrix products. In the finite-element context, the matrix $\Phi: v \times n$ has the form

$$[\phi^1 : \dots : \phi^n] \quad (5-22)$$

where the i -th column vector ϕ^i consists of components $\phi_{(\sigma,\beta)}^i$ that represent the amplitude of the i -th mode shape at node σ of the finite element model and in the kinematic degree of freedom β (e.g., rotation about one of the body axes) at that node. The number of such distinct

pairs (σ, β) represented in the model is the total number v of generalized coordinates. The geometric actuator influence matrix $B_A: v \times m$ has the form

$$[b_A^1 : \dots : b_A^m]$$

where each column vector b_A^r represents a particular actuator, with a structure dependent upon the actuator type. For an actuator whose effect can be fully described at a single node (e.g., rotation about one of the body axes at that node), the corresponding vector b_A^r is a unit vector of the form

$$(0 \dots 0 \ 1 \ 0 \dots 0)^T$$

with the 1 at the index (σ, β) defining the relevant node and degree of freedom. For an actuator involving a connection between two nodes, the corresponding vector b_A^r is a unit direction-cosine vector with non-zero entries at the appropriate pairs (σ', β') , (σ'', β'') of indices.

Consequently, the modal actuator influence matrix $\phi^T B_A: n \times m$ can be represented in the form

$$\phi^T B_A = \begin{bmatrix} \phi_{(\text{act } 1)}^1 & \dots & \phi_{(\text{act } m)}^1 \\ \vdots & & \vdots \\ \phi_{(\text{act } 1)}^n & \dots & \phi_{(\text{act } m)}^n \end{bmatrix} \quad (5-23)$$

if each actuator represents nodal actuation or rotation. If one column (say the r -th) represents an axial node-connecting actuator, then the r -th column has the slightly different structure

$$(\psi_{(\text{act } r)}^1 \cdot \cdot \cdot \psi_{(\text{act } r)}^n)^T$$

where each entry is a sum

$$\psi_{(\text{act } r)}^i = \sum [\phi_{(\sigma', \beta')}^i - \phi_{(\sigma'', \beta'')}^i] \cos \theta(\sigma', \beta'; \sigma'', \beta'')$$

involving the direction cosines of the node-connector. The subscript "(act r)" denotes the index (σ_r, β_r) defining the node and degree of freedom corresponding to the r-th actuator. The notation of Eq. (5-23) is used repeatedly in what follows. A corresponding representation for the modal sensor influence matrices $C_{p\phi}$ and $C_{v\phi}$ may be given; e.g.,

$$C_{V\phi} = \begin{bmatrix} \phi_{(v\text{-sen } 1)}^1 & \cdot & \cdot & \cdot & \phi_{(v\text{-sen } 1)}^n \\ \vdots & & & & \vdots \\ \phi_{(v\text{-sen } \ell)}^1 & \cdot & \cdot & \cdot & \phi_{(v\text{-sen } \ell)}^n \end{bmatrix} \quad (5-24)$$

The modal disturbance influence matrix $\phi_{B_D}^T$ is represented similarly to Eq. (5-23) with the entries being denoted $\phi_{(\text{dist } k)}^i$ instead. The structure of the modal line-of-sight coefficient matrix $C_{LOS\phi} \triangleq D\phi: 3 \times n$ has no correspondingly simple representation. The entries are in general inner products of the form $\phi^i \cdot C^{LOSX}$, $\phi^i \cdot C^{LOSY}$, and $\phi^i \cdot C^{DEFOCUS}$, respectively, involving the full mode-shape vectors ϕ^i (cf. Eq. (5-22)) and the coefficient vectors in the LOS-error model [Ref. 5-5].

Analytic expressions for the various impulse responses with the system of Eqs. (5-1), (5-2) are presented next, employing the notation of Eqs. (5-23), (5-24). The details of the development are elementary and are therefore omitted. It is assumed that the zero-frequency modes are not represented (i.e., $\omega_1 \neq 0$) and that the system modal damping ratios ζ_1 satisfy

$$0 \leq \zeta_1 < 1 \quad (5-25)$$

To avoid obscuring the principal ideas, results are presented only for the employment of rate sensors (i.e., $C_p = 0$ in Eq. (5-2)) and for the employment of nodal actuators and sensors (i.e., Eqs. (5-23), (5-24) apply without change). The general case follows directly (though tediously). Under assumption Eq. (5-25), the r -th (rate) sensor response to a unit impulse at the k -th actuator is given by:

$$y_r(t; u_k) = \sum_{i=1}^n \phi_{(v-sen\ r)}^i \dot{\eta}_i(t; u_k) \quad (5-26)$$

where

$$\dot{\eta}_i(t; u_k) = \frac{\phi_{(act\ k)}^i}{\omega_{d_i}} e^{-\zeta_1 \omega_i t} [(-\zeta_1 \omega_i) \sin(\omega_{d_i} t) + \omega_{d_i} \cos(\omega_{d_i} t)] \quad (5-27)$$

and

$$\omega_{d_i} \triangleq \omega_i (1 - \zeta_1^2)^{1/2} \quad (5-28)$$

After some algebra, Eqs. (5-26) through (5-28) may be placed in the form of Eq. (5-20) (with the carets on ω_i , ζ_1 and n removed). The parameters a_{kr}^i , b_{kr}^i produced by the identification process are then seen to have the decomposition:

$$a_{kr}^i = \phi_{(v-sen\ r)}^i \phi_{(act\ k)}^i \quad (5-29)$$

$$b_{kr}^i = \phi_{(v-sen\ r)}^i \phi_{(act\ k)}^i \frac{\zeta_1}{(1 - \zeta_1^2)^{1/2}} \quad (5-30)$$

Noting that Eq. (5-30) is a scalar multiple of Eq. (5-29), the problem of constructing the desired matrix estimates reduces to solving Eq. (5-29) for the two (sets of) factors.

5.2.3.2.1 Estimates for the Actuator and Sensor Influence Matrices

We rewrite Eq. (5-29) emphasizing the associated array of indices:

$$a_{kr}^i = \phi_{(v-sen\ r)}^i \phi_{(act\ k)}^i, \quad k = 1, \dots, m, \quad r = 1, \dots, l; \quad i = 1, \dots, n \quad (5-29a)$$

corresponding to the totality of impulse responses. It appears that Eqs. (5-29a) do not point to a unique solution for the individual factors unless some restriction is imposed on the degree of noncolocation of the actuators and sensors. (For example, a single actuator and sensor--noncolocated--lead to a one-parameter family of solutions). Uniqueness of solutions can be demonstrated, however, under the following mild restrictions:

- (A1) The actuator and sensor configuration contains at least one colocated actuator/sensor pair (both by node and degree of freedom); and
- (A2) For each mode $i = 1, \dots, n$, there is a colocated actuator/sensor pair k_i for which the parameter $a_{k_i k_i}^i$ in Eq. (5-20) for the response estimate $\hat{y}_{k_i}(\cdot; u_{k_i})$ is nonzero.

Three cases are distinguished.

Case 1: Colocated actuator/sensor pairs. The appropriate subset of Eqs. (5-29a) corresponding to colocated actuator/sensor pairs is

$$a_{kr}^i = \phi_{(act\ r)}^i \phi_{(act\ k)}^i, \quad k = 1, \dots, M, \quad r = 1, \dots, M; \quad i = 1, \dots, n \quad (5-29b)$$

where $M \leq \min \{m, l\}$ is the number of colocated pairs. For each mode $i = 1, \dots, n$, solution for the factors may be obtained from the diagonal subsystem of Eqs. (5-29b):

$$a_{kk}^i = \phi_{(\text{act } k)}^i \phi_{(\text{act } k)}^i, \quad k = 1, \dots, M$$

and is easily seen to be

$$\hat{\phi}_{(\text{act } k)}^i \triangleq |a_{kk}^i|^{1/2} \text{sgn}(a_{kk}^i), \quad k = 1, \dots, M \quad (5-31)$$

where the caret " \wedge " denotes a (deduced) estimate of the indicated quantity.

Case 2: Noncolocated (rate) sensors. The appropriate subset of Eqs. (5-29a) corresponding to sensors which are not colocated with any actuator is:

$$a_{kr}^i = \phi_{(\text{v-sen } r)}^i \phi_{(\text{act } k)}^i, \quad k = 1, \dots, M, \quad r = M+1, \dots, l; \quad i = 1, \dots, n \quad (5-29c)$$

Fix a mode i in $\{1, \dots, n\}$. Estimates $\hat{\phi}_{(\text{act } k)}^i$, $k = 1, \dots, M$, have been determined in Case 1 by Eqs. (5-31). By assumption (A2), there is a number k_i in $\{1, \dots, M\}$ for which $a_{k_i k_i}^i \neq 0$. It follows from Eqs. (5-29c) that $\hat{\phi}_{(\text{act } k_i)}^i \neq 0$, and therefore that

$$\hat{\phi}_{(\text{v-sen } r)}^i = \frac{a_{k_i r}^i}{\hat{\phi}_{(\text{act } k_i)}^i} = \frac{a_{k_i r}^i}{|a_{k_i k_i}^i|^{1/2} \text{sgn}(a_{k_i k_i}^i)}, \quad r = M+1, \dots, l \quad (5-32)$$

Case 3: Noncollocated actuators. The appropriate subset of Eq. (5-29a) corresponding to actuators which are not colocated with any sensor is:

$$a_{kr}^1 = \phi_{(v-sen\ r)}^1 \phi_{(act\ k)}^1, \quad k = M+1, \dots, m, \quad r = 1, \dots, M; \quad i = 1, \dots, n \quad (5-29d)$$

Fix a mode i in $\{1, \dots, n\}$. The sensor factors $\phi_{(v-sen\ r)}^i$ appearing in Eqs. (5-29d) represent sensors colocated with actuators, for which estimates have been determined in Case 1 by the identification:

$$\hat{\phi}_{(v-sen\ r)}^i = \hat{\phi}_{(act\ r)}^i, \quad r = 1, \dots, M$$

together with Eqs. (5-31). By assumption (A2), there is a number r_i in $\{1, \dots, M\}$ for which $a_{r_i r_i}^i \neq 0$. It follows from Eqs. (5-29d) that

$\hat{\phi}_{(v-sen\ r_i)}^i \neq 0$, and therefore that

$$\hat{\phi}_{(act\ k)}^i = \frac{a_{kr_i}^i}{\hat{\phi}_{(v-sen\ r_i)}^i} = \frac{a_{kr_i}^i}{|a_{r_i r_i}^i|^{1/2} \text{sgn}(a_{r_i r_i}^i)}, \quad k = M+1, \dots, m \quad (5-33)$$

Taken together, Eqs. (5-30) through (5-32) constitute the desired estimates for the matrices ϕ_{BA}^T and $C_V \phi$ in Eqs. (5-23) and (5-24), respectively.

5.2.3.2.2 Estimates for the Disturbance and LOS-Error Influence Matrices

The analytic representation for the disturbance response is analogous to Eqs. (5-26) through (5-28). Under assumption Eq. (5-25), the r -th (rate) sensor response to a unit impulse at the k -th disturbance location is given by:

$$y_r(t; w_k) = \sum_{i=1}^n \phi_{(v-sen\ r)}^i \dot{\eta}_i(t; w_k) \quad (5-34)$$

where

$$\dot{\eta}_i(t; w_k) = \frac{\phi_{(dist\ k)}^i}{\omega_{d_i}} e^{-\zeta_i \omega_i t} [(-\zeta_i \omega_i) \sin(\omega_{d_i} t) + \omega_{d_i} \cos(\omega_{d_i} t)] \quad (5-35)$$

Upon placing Eqs. (5-34), (5-35) in the form of Eq. (5-20), the decompositions corresponding to Eqs. (5-29), (5-30) for the disturbance responses are:

$$a_{kr}^i = \phi_{(v-sen\ r)}^i \phi_{(dist\ k)}^i \quad (5-36)$$

$$b_{kr}^i = \phi_{(v-sen\ r)}^i \phi_{(dist\ k)}^i \frac{\zeta_i}{(1 - \zeta_i^2)^{1/2}} \quad (5-37)$$

Estimates $\hat{\phi}_{(v-sen\ r)}^i$, $r = 1, \dots, \ell$, $i = 1, \dots, n$ have been determined from the analysis of the preceding subsection. Fix a mode i in $\{1, \dots, n\}$. The corresponding vector

$$(\hat{\phi}_{(v-sen\ 1)}^i \ \dots \ \hat{\phi}_{(v-sen\ \ell)}^i)^T \quad (5-38)$$

is the i -th column vector of the estimate for the matrix $C_V \Phi$ (cf. Eq. (5-24)). It can be seen from Eq. (5-2) that if this vector were zero, then mode i would be unobservable with the current sensor configuration. Such an event is incompatible with the presence of mode i in the

reduced-order model. It can be assumed therefore that at least one component, say $\hat{\phi}_{(v\text{-sen } r_1)}^1$, of the vector in Eq. (5-38) is nonzero. Then from Eq. (5-36),

$$\hat{\phi}_{(\text{dist } k)}^1 = \frac{a_{kr_1}^1}{\hat{\phi}_{(v\text{-sen } r_1)}^1} \quad (5-39)$$

where the appropriate explicit expression (either Eq. (5-31) or (5-32) is to be used for $\hat{\phi}_{(v\text{-sen } r_1)}^1$ in Eq. (5-37). This establishes an estimate for the matrix $\phi^T B_D$.

An attempt to estimate the LOS-error influence matrix (cf. Eq. (5-3)) leads to a certain difficulty which directly affects the synthesis process. Recall that this matrix has the structure:

$$(C_{\text{LOS}}\phi)^T = \begin{bmatrix} (\phi^1.C^{\text{LOSX}}) & (\phi^1.C^{\text{LOS Y}}) & (\phi^1.C^{\text{DEFOCUS}}) \\ \vdots & \vdots & \vdots \\ (\phi^n.C^{\text{LOSX}}) & (\phi^n.C^{\text{LOS Y}}) & (\phi^n.C^{\text{DEFOCUS}}) \end{bmatrix} \quad (5-40)$$

In order to estimate the entries in $C_{\text{LOS}}\phi$, estimates of the modal vector components $\phi_{(\sigma,\beta)}^1$ at each index (σ,β) which is represented in the LOS-error model are required. However, estimates of such components are available only at indices (σ,β) corresponding to locations of actuators, sensors, or disturbance inputs (cf. Eqs. (5-31), (5-32), (5-33), (5-39)). In general, there is no guarantee that any of the required components $\phi_{(\sigma,\beta)}^1$ can be estimated based on the available data. A specific example helps to clarify this fundamental point. Consider the colocated actuator/sensor selection E-5 (cf. Tables 5-3, 5-4) consisting of 5 transducer pairs. The indices (σ,β) corresponding to actuator (and sensor) locations are (cf. Figs. 5-6a, 5-6b):

$$(\sigma, \delta) = (35, \theta_x), (16, \theta_y), (42, \theta_y), (1001, \theta_y), (3233, \theta_y)$$

where $\theta(\cdot)$ denotes the rotational degree of freedom about the indicated body axis. Indices corresponding to disturbance input locations are

$$(\sigma, \delta) = (37, x), (37, y), (37, z), (46, x), (46, y), (46, z)$$

where the second element in each pair represents the translational degree of freedom along the indicated body axis. It can be verified, however, [Ref. 5-5], that none of these index pairs appear in the LOS-error model. Therefore, for this example, the best estimate of the matrix $C_{LOS\phi}$ that can be computed (cf. Eq. (5-40)) with the available data is zero!

5.2.3.3 Implications for the Synthesis Process

The inability to generate feasible estimates for $C_{LOS\phi}$ bears upon the active controller synthesis process as follows. In the LOG/disturbance-rejection designs used to generate controller feedback strategy, the functional being minimized is [cf. Ref. 5-15]:

$$J \triangleq \int_0^{\infty} (z^T Q z + \rho_R u_A^T u_A) dt \quad (5-41)$$

where z : 3×1 is the variable to be regulated (LOS-error vector) appearing in Eq. (5-3). Therefore the matrix product $C_{LOS\phi}$ is a factor (twice) in the product $z^T Q z$. The use of poor (or zero!) estimates for $C_{LOS\phi}$ in Eq. (5-41) generally leads to poorly performing controllers, since no penalty for large LOS-errors is imposed in the design process.

There are several alternatives available to resolve the present impasse to the incorporation of the high resolution spectrum estimation technique into the synthesis process. The functional Eq. (5-41) may be

altered so as to weight only the sensor measurements of the system Eq. (5-1) (i.e., z is replaced by the sensor output y in Eq. (5-41)). More directly, the LOS-error vector could be treated as a sensor output itself, an apparently reasonable assumption for certain optical systems [Ref. 5-21]. Experience with LQ controller designs in which the LOS-error vector is not weighted in the cost functional Eq. (5-41) indicates difficulty in meeting the performance specifications [Ref. 5-6; Section 5]. Therefore, the latter alternative appears preferable.

Since neither of these alternatives has been implemented in the synthesis experiments performed to date, a database for evaluating the effect of incorporating the particular identification process under discussion into the synthesis process is not available. However, the process itself has been exercised on ACOSS Model No. 2 yielding excellent resolution.

5.3 Principal Contributions

The principal contributions toward an understanding of the active control synthesis process that are embodied in References 5-11 through 5-15 and 5-18, together with Sections 5 and 6 of the present report, are briefly summarized.

Several generally understood principles have been given a sharp focus in the specific context of wideband disturbance accommodation with precision flexible space structures. First, the inherent inseparability of reduced-order model selection, active transducer selection, and feedback strategy determination within the total synthesis process has been clearly demonstrated. In particular, the consequences of inadequate attention to the first two factors cannot be overcome by even the most sophisticated feedback strategy. Second, the value of an experimental approach to the study of the mutual interactions of these three factors has been established. In particular, a thorough understanding of the synthesis process is equally as important as (and the key to generation

of) a specific design product. Third, the fundamental compromise between stability and performance (more precisely, between stability robustness and performance robustness) with respect to unmodeled high-frequency dynamics has been clearly exhibited. In particular, the results obtained highlight the need for more systematic design tools to ensure performance robustness for high-precision flexible structures.

In addition, specific contributions have been made toward techniques of active transducer selection and controller feedback strategy determination.

Active Transducer Selection. First, a new and systematic approach to the selection of actuators and sensors has been developed. Selection of actuators is related directly to parameters of specified system performance, and a distinct selection of sensors may (if desired) be related directly to parameters of the anticipated disturbance environment. Selection algorithms are based on theoretically sound principles; reliable portable software for implementation is widely available. Second, the effectiveness of the selection strategy in the active control synthesis context has been demonstrated. In particular, the role of active transducer selection within the overall synthesis context has been clarified.

Controller Feedback Strategy Determination. First, the effectiveness of a systematic approach [Refs. 5-16, 5-17] for enhancing stability robustness to unmodeled high-frequency dynamics has been convincingly demonstrated in a stressful and realistic design context relevant to flexible structure control. Second, important limitations of this approach in obtaining performance robustness with high-precision flexible structures have been revealed.

5.4 Open Questions

Having given an account of the work accomplished, it is appropriate to discuss significant matters that remain unresolved. There are two categories: matters relating specifically to the work accomplished; and matters of general concern.

We begin with some specific matters. First, the strategy for active transducer selection that has been developed has been shown to work surprisingly well. However, a theoretical explanation for this success is lacking. Are the transducer selections optimal in some well-defined sense for the purposes of actuation or of measurement? How are the "static" criteria for selections linked with the closed-loop dynamic performance associated with the resultant selections? Answers to these and related questions would provide a key to much more efficient implementation of the selection strategy. For example, the strategy seems to be potentially valuable for predicting the consequences upon performance of prior constraints on transducer selection, or of transducer failures. Second, the emphasis to date in feedback strategy determination has been upon robustness to unmodeled high-frequency dynamics. Although we believe this to be a proper priority, robustness to model parameter variations is the logical--and no less important--next step. Third, the way has been cleared for the incorporation of high-resolution spectrum estimation into the reduced-order modeling process. Significant investigations should include the development of a data base of design experience to assess the observable effects upon stability and performance of such incorporation, and to assess the effect of accounting for additional delays in the signal path (e.g., due to actuator and sensor dynamics, or to data sampling, digital computation, and data reconstruction).

Finally, we touch upon several matters of overriding general concern. First is the matter of robustness in performance. Most systematic approaches to robustness enhancement for the feedback control

of systems with (deterministic) uncertainty focus principally upon robustness of stability. Guidelines for augmenting performance robustness typically amount to suggesting a tightening of the original performance specification. For very high precision systems such as the present application, such guidelines are not feasible. The need for effective guidelines to assist in augmenting performance robustness lies in the following fact: if a system exhibits (deterministic) uncertainty relative to its design model representation, performance is likely to deteriorate more sharply than stability. From an operational viewpoint, a stable system that is unable to accomplish the assigned mission is--at best--a waste of resources. The point is that fundamental research on this topic is needed. Second is the matter of robustness (in both stability and performance) with respect to disturbances. Disturbances that can be anticipated for real systems often defy precise characterization, both as to their analytic structure and parametric description, as well as to the location and direction of their influence upon the system. The consequences of inadequate characterization of disturbances, as well as techniques for enhancement of robustness with respect to disturbances are highly significant, and unresolved, questions.

References

- 5-1. Athans, M., ed., Special Issue on the Linear-Quadratic-Gaussian Estimation and Control Problem, IEEE Trans. Automatic Control, Vol. AC-16, No. 6, Dec. 1971, pp. 527-689.
- 5-2. Kwakernaak, H. and Sivan, R., Linear Optimal Control Systems, Wiley, New York, NY, 1972.
- 5-3. Sain, M. K., Special Issue on Linear Multivariable Control Systems, IEEE Trans. Automatic Control, Vol. AC-26, No. 1, Feb. 1981, pp. 1-295.

- 5-4. Henderson, T., "Active Control of Space Structures (ACOSS) Model 2," Report C-5437, Charles Stark Draper Laboratory, Cambridge, MA, September 1981.
- 5-5. Henderson, T., "Modifications to ACOSS Model No. 2 Design; Technical Report, Data Base (Final)", Report CSDL-R-1585, Charles Stark Draper Laboratory, Cambridge, MA, October 1982.
- 5-6. Strunce, R. R., et. al., ACOSS-Eleven Second Semiannual Technical Report, Volume 2: Active Controller Designs, Report CSDL-R-1583, Charles Stark Draper Laboratory, Cambridge, MA, August 1982.
- 5-7. Canavin, J. R., "The Control of Spacecraft Vibrations Using Multi-variable Output Feedback," Paper 78-1419, AIAA/AAS Astrodynamics Conference, Palo Alto, CA, August 1978.
- 5-8. Lin, J. G., "Three Steps to Alleviate Control and Observation Spillover Problems of Large Space Structures," Proc. 19th IEEE Conference on Decision and Control, Albuquerque, NM, December 1980, pp. 438-444.
- 5-9. Brennan, T. J., Compito, A. V., Doran, A. L., Gustafson, C. L. and Wong, C. L., "Matrix Transfer Function Control Design for Flexible Spacecraft: An Application," NASA/JPL Workshop on Identification and Control of Flexible Space Structures, San Diego, CA, June 1984.
- 5-10. Ho, Y.-C., "Is It Application or Is It Experimental Science?" (Editorial), IEEE Trans. Automatic Control, Vol. AC-27, No. 6, Dec. 1982, p. 1142.
- 5-11. Hegg, D. R., "A Controlled Experiment for ACOSS Design," ACOSS-Eleven Third Interim Technical Report, Vol. 2, Report CSDL-R-1598, Charles Stark Draper Laboratory, Cambridge, MA, December 1982; Section 5.

- 5-12. Hegg, D. R. and Kissel, G. J., "Progress on Synthesis of Active Control for Broadband Disturbance Accommodation--Part 1: Active Transducer Selection; Part 2: Control System Design and Evaluation," ACOSS-Eleven Fourth Interim Technical Report, Vol. 2, Report CSDL-R-1648, Charles Stark Draper Laboratory, Cambridge, MA, August 1983; Sections 2 and 3.
- 5-13. Hegg, D. R. and Kissel, G. J., "Progress on Synthesis of Active Control for Wideband Disturbance Accommodation with ACOSS Model No. 2," ACOSS-Eleven Fifth Interim Technical Report, Report CSDL-R-1687, Charles Stark Draper Laboratory, Cambridge, MA, March 1984; Section 5.
- 5-14. Hegg, D. R. and Kissel, G. J., "Wideband Disturbance Accommodation in Precision Flexible Space Structures," NASA/JPL Workshop on Identification and Control of Flexible Space Structures, San Diego, CA, June 1984.
- 5-15. Fogel, E., "Disturbance Rejection Control Design," in Reference 5-6; Section 4.
- 5-16. Doyle, J. C. and Stein, G., "Multivariable Feedback Design: Concepts for a Classical/Modern Synthesis," IEEE Trans. Automatic Control, Vol. AC-26, No. 1, Feb. 1981, pp. 4-16.
- 5-17. Stein, G. and Athans, M., "The LQG/LTR Procedure for Multivariable Feedback Control Design," American Control Conference, San Diego, CA, June 1984.
- 5-18. Fogel, E., "Sensor/Actuator Selection," in Reference 5-6; Section 3.
- 5-19. Fogel, E., "Structure Identification--the Resolution Problem and its Solutions," ACOSS-Eleven Third Semiannual Technical Report, Vol. 2, CSDL-R-1598, Charles Stark Draper Laboratory, Cambridge, MA, December 1982; Section 2.

- 5-20. Villalba, M., "On the Use of Autocorrelation Desampling in High Resolution Spectrum Estimation," ACOSS-Eleven Fifth Semiannual Technical Report, Report CSDL-R-1687, Charles Stark Draper Laboratory, Cambridge, MA, March 1984; Section 7.
- 5-21. Aubrun, J. N., et. al., "ACOSS Twelve (Active Control of Space Structures)," Rome Air Development Center Contractor Report RADC-TR-84-28, Lockheed Missiles and Space Company, Sunnyvale, CA, February 1984.

SECTION 6

STABILITY ENHANCEMENT IN STRUCTURAL CONTROL

6.1 Introduction

In our experimental approach to active control design for flexible space structures [Ref. 6-1], numerous actuator and sensor placements have been explored [Refs. 6-2, 6-3]. The main goal of the accompanying controller designs [Ref. 6-2] for these transducer selections has been to ensure that the state-feedback portion of each linear-quadratic-Gaussian (LQG) design met the line-of-sight (LOS) performance specifications as closely as possible. For each corresponding LQG design the largest set of modes, contiguous in frequency, that produced a stable evaluation was noted. In most instances to date closed-loop stability was maintained with modes well beyond the 18-mode design model, but stability with all 150 elastic modes of the structural model was not achieved.

This section presents sufficient conditions in the frequency domain for improved stability robustness to unmodelled high frequency dynamics and outlines a design procedure to enhance the robustness of our present LQG designs. We demonstrate these ideas on three of our previously reported controller designs, and indeed achieve closed-loop stability for two of them in the presence of all 150 elastic modes of the structural model. We conclude with observations on our controller results in the context of the experiment, and discuss some of the issues for flexible space structure control that have yet to be addressed.

6.2 Present Controller Results

The control design methodology used with the various actuator/sensor selections in connection with our experimental approach is detailed in Reference 6-2. In brief, the methodology involves the synthesis of an LQG controller for a design model consisting of the first 18 elastic modes (modes 7-24) of Revision 1 of ACOSS Model No. 2, augmented with a model of the two wideband disturbances which impact the structure at the points indicated in Fig. 5-1. A statistical description and state-space representation for the disturbances can be found in Reference 6-2. In the performance index for the linear-quadratic (LQ) regulator design the three LOS outputs, LOSX, LOSY (optical axis rotation errors) and defocus, are weighted with a diagonal matrix to ensure that the state feedback controller meets the LOS specifications [Ref. 6-2] as closely as possible. A Kalman filter is then used to estimate the states from the sensor outputs. Table 6-1 lists controller design results reported on thus far. Included in the table are LOS output weightings, q_1 , q_2 , q_3 , and the scalar control weighting, ρ_R , used in the LQ performance index. The scalar parameter, ρ_0 , which multiplies an identity matrix to represent the sensor noise covariance and ensure a nonsingular Kalman filter problem, is also listed. Relevant performance and stability results are noted in the table.

Up to this point in the experiment, the main focus has been the achievement of adequate LQ-regulator performance with different actuator/sensor selections, while the stability of the LQG controllers has been an observed variable. Even though no particular effort has been made to enhance whatever stability robustness properties our standard LQG designs [Ref. 6-2] may possess, the number of modes in the stable evaluations extends well beyond that of the 18-mode design model. However, closed-loop stability has not been achieved with all 150 elastic modes of the structural model, so the robustification of our designs must be of prime concern.

Fortunately, the lack of stability robustness has a clearly identifiable cause. Specifically, the only perturbation in our design model that we employ to test the robustness of our controllers is the addition of 132 modes, all of whose frequencies are above those of the 18 modes in the design model. Other perturbations, for example, variations in structural parameters which could change the frequencies and mode shapes of all 150 modes, have not yet been treated. Robustness to parameter variations is an important issue itself. The goal we pursue here is to modify the LQG controller design to enhance its robustness to high frequency modes not in the design model, preferably without using explicit knowledge of those modes.

6.3 Frequency Domain Conditions for Stability Robustness

In this subsection we present conditions which guarantee closed-loop stability of a control system when it is evaluated with high frequency dynamics excluded from a design model of the plant. We first discuss frequency domain descriptions of transfer matrices, and then describe appropriate matrix expressions for design model errors, as background to deriving the criteria for stability robustness. These frequency domain criteria motivate the design modification to our controller, presented in Section 6.4, intended to enhance stability robustness.

In our investigation of robustness to high frequency dynamics, we examine closely the frequency domain properties of the transfer matrix $H(s)P_d(s)$. Here $H(s)$ represents the transfer matrix for the compensator and $P_d(s)$ is the transfer matrix for the 18-mode design model of the plant (i.e., the structure to be controlled) without disturbance dynamics appended. The transfer matrices are shown in Fig. 6-1 as part of a closed-loop multi-input multi-output (MIMO) control system. The output y , the control u , and the reference variable r are also noted.

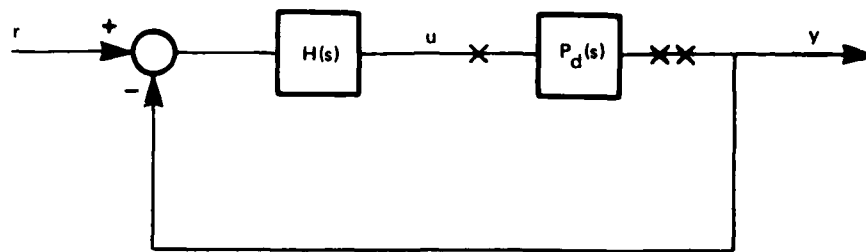


Figure 6-1. MIMO closed-loop system.

The product $H(s)P_d(s)$, which is sometimes referred to as a return ratio matrix, or a loop transfer matrix, is the matrix multiplying signals inserted in the control loop broken at the input to the plant, point x , to produce the signals at the output of the same breaking point. Similarly the loop can be broken at the output of the plant, point xx , to produce a corresponding loop transfer matrix $P_d(s)H(s)$. For single-input single-output (SISO) control systems, no difference exists between the transfer functions P_dH and HP_d (with the Laplace variable s suppressed in an obvious way) because they are both scalars. In general, for MIMO systems the products corresponding to different breaking points will be different because they are transfer matrices (matrix multiplication being generally noncommutative). Our reason for focusing on the loop transfer matrix HP_d corresponding to breaking the loop at the input to the plant will become apparent later.

The frequency response properties of a SISO system are determined from familiar gain and phase plots. For MIMO systems, analogous frequency domain information is available about the gain through the use of matrix norms. Here we make use of the matrix spectral norm. For any matrix A , the maximum singular value, $\bar{\sigma}(A)$, and the minimum singular value, $\underline{\sigma}(A)$, are defined as:

$$\bar{\sigma}(A) \triangleq (\lambda_{\max}[A^H A])^{1/2}$$

$$\underline{\sigma}(A) \triangleq (\lambda_{\min}[A^H A])^{1/2}$$

where $\lambda[\cdot]$ denotes an eigenvalue of the indicated matrix and the superscript H denotes complex conjugate transpose.

It is well known that these two singular values have the following important characterization:

$$\bar{\sigma}(A) = \max_{x \neq 0} \frac{\|Ax\|_2}{\|x\|_2} = \|A\|_2 \quad (6-1)$$

$$\underline{\sigma}(A) = \min_{x \neq 0} \frac{\|Ax\|_2}{\|x\|_2} \quad (6-2)$$

Equations (6-1) and (6-2) indicate that $\bar{\sigma}$ and $\underline{\sigma}$ represent, respectively, the maximum and minimum input-output gain ratio, viewing A as a transfer matrix [Ref. 6-4]. Therefore maximum and minimum singular values may be taken as appropriate measures of frequency response for a transfer matrix.

Before we develop our robustness criteria, we also need an appropriate matrix description of the error in the design model of the plant as compared to the evaluation model. As we have indicated, the error we are concerned about is the exclusion of high frequency modes from the design model. The most straightforward way of describing that error follows from partitioning the transfer matrix for the full order model (in our case the evaluation model):

$$\begin{aligned}
P_f(s) &= \begin{bmatrix} C_d & C_h \end{bmatrix} \begin{bmatrix} (sI - A_d)^{-1} & 0 \\ 0 & (sI - A_h)^{-1} \end{bmatrix} \begin{bmatrix} B_d \\ B_h \end{bmatrix} \\
&= C_d(sI - A_d)^{-1}B_d + C_h(sI - A_h)^{-1}B_h \\
&= P_d(s) + P_h(s)
\end{aligned} \tag{6-3}$$

where subscript "f" refers to the full order model, subscript "d" refers to the design model, and subscript "h" refers to the neglected high frequency modes.

Equation (6-3) is an additive description of the model error and is presented here to introduce the concept and notation associated with such error representations. An alternative manner of describing this same error yields the most useful information on how the loop shape HP_d should behave in the frequency domain for stability robustness. In particular, we use the so-called multiplicative form of the error, reflected at the input to the plant and written as:

$$P_f(s) = P_d(s)[I + L(s)] \tag{6-4}$$

where

$$L(s) \triangleq P_d^{-1}(s) [P_f(s) - P_d(s)] = P_d^{-1}(s) [P_h(s)]$$

As indicated in Reference 6-5, the frequency domain behavior of $L(s)$ as measured by the variation with frequency of its maximum singular value, $\bar{\sigma}(L)$, is smaller than unity in the low frequency region, but much larger than unity at high frequency where $P_h(s)$ has significant dynamics.

With this background material we can now proceed to determine sufficient conditions for closed-loop stability when evaluating our compensator on a full-order model.

Because the focus of our concern is the control loop broken at the input to the plant, we first examine the closed-loop transfer matrix between the reference variable r and the control variable u at the plant input of Fig. 6-1:

$$u(s) = [I + H(s)P_d(s)]^{-1}H(s) r(s)$$

The stability of the closed-loop system can be examined via the determinant $\det[I + HP_d]$. In particular, if $\phi_{OL}(s)$ represents the characteristic polynomial of the open-loop transfer matrix HP_d and $\phi_{CL}(s)$ represents the characteristic polynomial of the closed-loop system, then [Ref. 6-7]:

$$\phi_{CL}(s) = \phi_{OL}(s) \det[I + HP_d]$$

From this relationship the multivariable Nyquist criterion can be derived [Refs. 6-6, 6-7]. This criterion says that the closed-loop system of Fig. 6-1 is stable if and only if the number of clockwise encirclements of the origin, 0, by the image of the clockwise Nyquist contour, D_R , under the mapping $\det[I + HP_d]$ plus the number of unstable poles of the open loop transfer matrix, HP_d , is equal to zero. In symbols, this is sometimes written:

$$N(0, \det[I + HP_d], D_R) + P_{U,OL} = 0$$

By designing the compensator, $H(s)$, via the LOG methodology we are guaranteed that the closed-loop control system of Fig. 6-1, with 18 design modes of the plant, will be stable, which means of course that the multivariable Nyquist criterion is satisfied. The LQG methodology does not guarantee, however, that a closed-loop system in which the

compensator is connected with a plant other than the design model will be stable. Using the multivariable Nyquist criterion, we determine sufficient conditions which guarantee that closed-loop stability is maintained when the full-order plant, $P_f(s)$, is connected with the compensator; in symbols:

$$N(0, \det[I + HP_f], D_R) + P_{U,OL} = 0 \quad (6-5)$$

where here the open loop transfer matrix is HP_f .

Our discussion in part follows the presentations of References 6-8 and 6-6 and that of Reference 6-5. Consistent with Theorem 2.2 of Reference 6-6 and Theorem 2 of Reference 6-8 we assume that:

- (a) The number of unstable poles (including those on the $j\omega$ axis) of HP_f is the same as the number of unstable poles of HP_d ;
- (b) All poles of HP_f on the $j\omega$ axis are also poles of HP_d ;
- (c) The closed-loop system designed for P_d is stable.

By employing the LOG design methodology and by using design and evaluation models that include only elastic modes of the space structure, we are guaranteed that conditions (a) through (c) are satisfied.

With these assumptions we can focus on the conditions which guarantee that the encirclement count of the map of $\det[I + HP_d]$ does not change as the determinant is perturbed to $\det[I + HP_f]$. In fact, if the determinant is never zero as it goes from $\det[I + HP_d]$ to $\det[I + HP_f]$, then the encirclement count of the origin will not change, and Eq. (6-5) will hold.

Using our matrix error description of Eq. (6-4), we can parameterize the deformation of the resulting Nyquist diagram so that closed-loop stability is ensured. The condition is that

$$\det[I + HP_d(I + \epsilon L)] \neq 0 \quad (6-6)$$

for all ϵ in the interval $[0,1]$ and all s on the contour D_R .

Because both maximum singular values $\bar{\sigma}(P_d)$ and $\bar{\sigma}(P_f)$ approach zero as $|s| \rightarrow \infty$, we only need to verify Eq. (6-6) for values of s along the portion Ω_R of the contour D_R lying in the closed left-half plane, i.e.:

$$\Omega_R = \{s: s \in D_R \text{ and } \operatorname{Re}(s) \leq 0\}$$

Presuming that the inverse of HP_d exists, we can rewrite Eq. (6-6) as:

$$\det[(HP_d)(I + (HP_d)^{-1} + \epsilon L)] \neq 0$$

The condition to be satisfied then reduces to:

$$\det[I + (HP_d)^{-1} + \epsilon L] \neq 0 \quad (6-7)$$

for all ϵ on the interval $[0,1]$ and all s on the contour Ω_R .

Equation (6-7) is not considered a good measure of how close the perturbed system, with error represented by $L(s)$, is to being unstable, because the determinant of a matrix is a poor indicator of how close that matrix is to being singular. A more reliable measure of nearness to singularity is provided by matrix singular values. With this in mind we note that a general matrix sum $A + E$ is guaranteed to be nonsingular, or equivalently to have $\det[A + E] \neq 0$, if

$$\underline{\sigma}(A) > \bar{\sigma}(E)$$

so the condition of Eq. (6-7) will be true if

$$\underline{\sigma}[I + (HP_d)^{-1}] > \epsilon \bar{\sigma}(L)$$

for all ϵ on the interval $[0,1]$; and in particular if

$$\underline{\sigma}[I + (HP_d)^{-1}] > \bar{\sigma}(L) \quad (6-8)$$

Equation (6-8) is a well-known sufficient condition for stability derived from the multivariable Nyquist criterion which is valid if the design and evaluation models are related by Eq. (6-4).

Using the minimum singular value inequality:

$$\underline{\sigma}(I + A) \leq \underline{\sigma}(A) + 1$$

we have for Eq. (6-8):

$$1 + \underline{\sigma}[HP_d]^{-1} \geq \underline{\sigma}[I + (HP_d)^{-1}] > \bar{\sigma}(L) \quad (6-9)$$

for all $0 \leq \omega < \infty$.

In our earlier discussion of multiplicative model error we noted that

$$\bar{\sigma}(L) \gg 1$$

in the high frequency region of our unmodelled dynamics. So from Eq. (6-9) we have:

$$\underline{\sigma}[HP_d]^{-1} > \bar{\sigma}(L)$$

or, equivalently:

$$\frac{1}{\bar{\sigma}[\text{HP}_d]} > \bar{\sigma}(L)$$

i.e.,

$$\bar{\sigma}[\text{HP}_d] < \frac{1}{\bar{\sigma}(L)}$$

It follows that

$$\bar{\sigma}[\text{HP}_d](\omega) \ll 1 \quad (6-10)$$

for those frequencies such that $[\bar{\sigma}(L)](\omega) \gg 1$. Equation (6-10) establishes the design goal that is used to judge the robustness of our control system designs. It is the MIMO generalization of the SISO requirements of low loop gains in the frequency range of unmodelled dynamics.

6.5 Design Procedure to Enhance Stability Robustness

Now that we have identified the cause of instability in our LQG designs and have established a design goal to help alleviate that problem, we discuss in this subsection how our LQG controllers can be modified to more closely satisfy Eq. (6-10).

To illustrate the problem at hand explicitly, examine Fig. 6-3a which is a plot of the maximum and minimum singular values (σ -plot) of the loop transfer matrix HP_d for actuator/sensor selection E-5 of Table 6-1, consisting of five rotational actuators and sensors. At no frequency less than 100 Hz (mode 88 is at 99 Hz) does the maximum

Table 6-1. Controller design and evaluation.

Actuator/ Sensor Selection	Weights				LQ (modes 7-24)			LQG (modes 7-24)			LQG (modes 7-36)			Modes in Stable Eval- uation
	q_1	q_2	q_3	ρ_R and ρ_0	LOSX (μ rad)	LOSX (μ rad)	DEFOCUS (10^{-3} m)	LOSX (μ rad)	LOSX (μ rad)	DEFOCUS (10^{-3} m)	LOSX (μ rad)	LOSX (μ rad)	DEFOCUS (10^{-3} m)	
Design Objective	-	-	-	-	0.05	0.05	0.025	0.05	0.05	0.025	0.05	0.05	0.025	7-156
A (10 axial)	10^3	10^1	10^{-4}	10^{-17}	0.0364	0.02093	0.00180							Un- stable
B (14 axial)	10^3	10^1	10^{-4}	10^{-17}	0.01958	0.01146	0.00408							7-29
C-12a (12 transl.)	10^0	10^{-1}	10^{-5}	10^{-17}	0.00532	0.00851	0.00136	0.00644	0.05073	0.00136	31.44	19.16	0.03848	7-39
D-14 (14 transl.)	10^{-1}	10^{-2}	10^{-6}	10^{-17}	0.02025	0.03204	0.00188	0.02124	0.06888	0.001883	15.84	9.2	0.01347	7-36
D-9a (9 transl.)	10^{-1}	10^{-2}	10^{-6}	10^{-17}	0.0257	0.03317	0.00345							7-29
E-5 (5 rot.)	10^1	10^{-1}	10^{-5}	10^{-17}	0.05587	0.04776	0.00496	0.06019	0.16216	0.00496				7-33
G-23 (23 transl.)	10^0	10^{-1}	10^{-5}	10^{-15}	0.02868	0.08904	0.00360							7-61
G-17 (17 transl.)	10^0	10^0	10^{-5}	10^{-15}	0.03469	0.00381	0.00378							7-33

singular value cross below 0 db. Such frequency domain behavior is certainly not in the spirit of the design goal represented by Eq. (6-10), and indeed Table 6-1 indicates that the system does become unstable when mode 34 (10.4 Hz) is added to form an evaluation model of modes 7-34.

The σ -plot of Fig. 6-3a is for the transfer matrix of our LQG design where estimates of the state are being fed back to the linear-quadratic regulator gain G . Consider now the situation where the actual states are being fed back, namely that of the LQ regulator which is depicted in closed-loop form in Fig. 6-2.

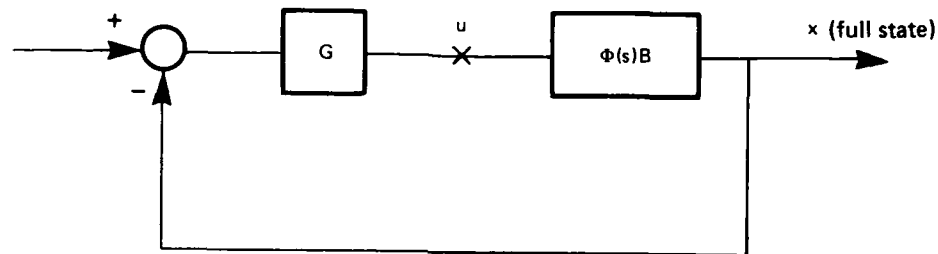


Figure 6-2. LQ regulator.

By breaking the loop at the plant input we get the open-loop transfer matrix for an LQ regulator which is $G\Phi(s)B$, where $\Phi(s)$ denotes the resolvent matrix $(sI - A)^{-1}$ associated with the state-variable representation of the structural dynamics:

$$\dot{\mathbf{x}} = \mathbf{A}\mathbf{x} + \mathbf{B}\mathbf{u}$$

The σ -plot associated with the LQ loop for the state-feedback design employing 5 rotational actuators is shown in Fig. 6-3b. Clearly this

state feedback open-loop transfer matrix, with $\bar{\sigma}$ crossover at 30 Hz, has frequency domain properties more in line with our design goal than does the LQG loop matrix HP_d . Our estimator, as reflected in HP_d , has ruined what was a more desirable loop shape when the actual states were being fed back. This degradation in loop shape caused by using a Kalman filter to estimate the states is apparently quite common [Ref. 6-9] and is observed in all of our examples.

Recent studies [Refs. 6-9, 6-5] have shown that the loop shape of the LQG loop matrix HP_d can be made to approach the loop shape of its corresponding LQ regulator $G\Phi(s)B$ by the use of a full-state loop transfer recovery procedure. Such a procedure is desirable of course because our LQ loop shapes have lower gains at high frequency than those of HP_d .

The derivation of the recovery procedure can be found in References 6-9 and 6-5. Here we only sketch the details.

We first require the design model of the plant, which in our case is augmented with a disturbance model, to have outputs greater than or equal in number to the inputs. The design model should also be minimum phase, though the recovery procedure is possible with a nonminimum phase plant (except that recovery will generally be poor at frequencies corresponding to the nonminimum phase zeros).

To achieve full-state loop transfer recovery, the Kalman filter is redesigned using a modified algebraic Riccati equation for the determination of the filter gain:

$$A_a L + L A_a^T + B_{aw} B_{aw}^T + q B_a B_a^T - L C_a^T (\rho_0 I)^{-1} C_a L = 0 \quad (6-11)$$

where the subscript "a" on the state, control, and observation matrices A, B, and C, respectively, makes reference to the fact that the design model of the plant is augmented by a model of the disturbance [Refs.

Figures 6-3. σ -plots for designs with 5 rotational transducers;
elastic modes 7 through 24.

(on following pages)

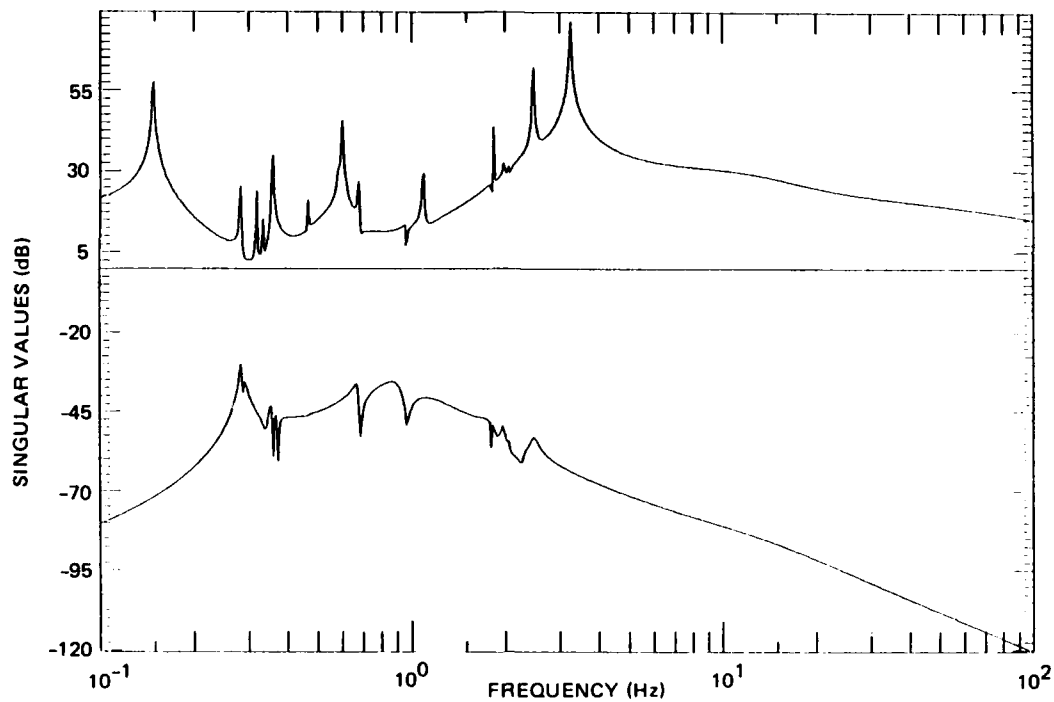


Figure 6-3a. LQG loop transfer matrix HP_d .

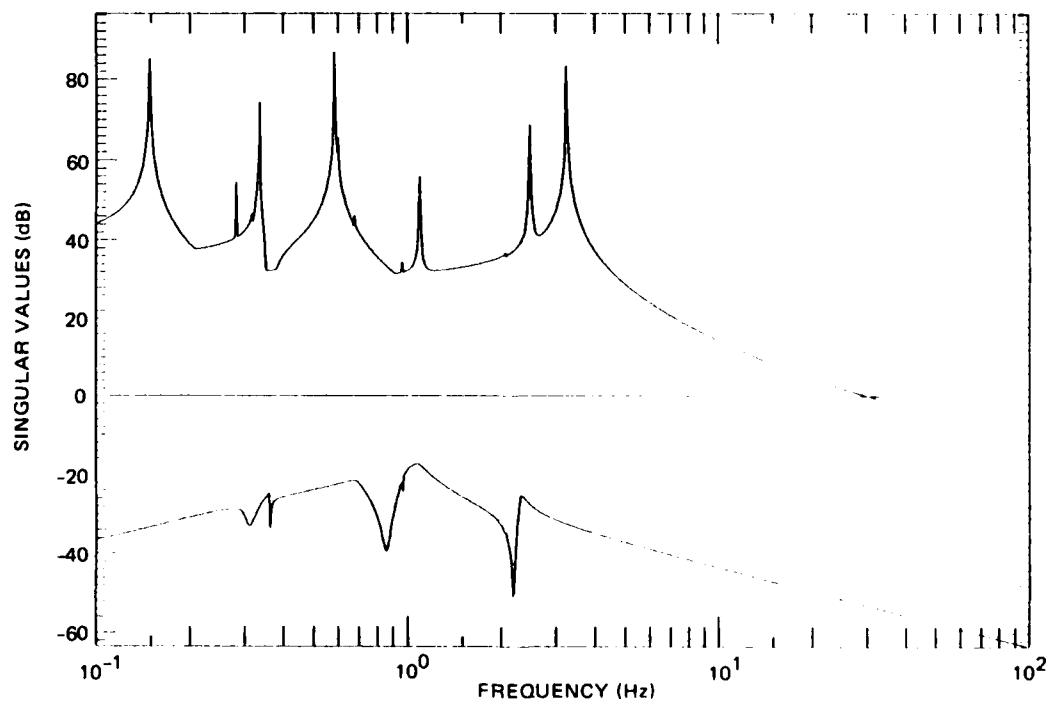


Figure 6-3b. Loop transfer matrix $G\Phi B$ of LQ regulator.

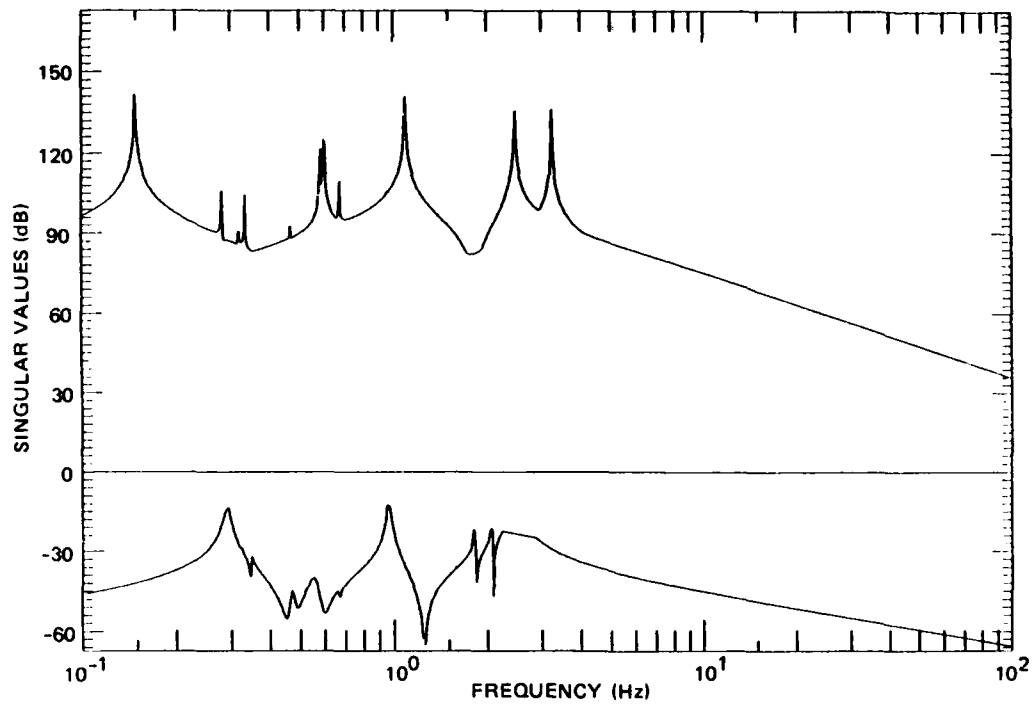


Figure 6-3c. Loop transfer matrix $C\Phi K$ of Kalman filter.

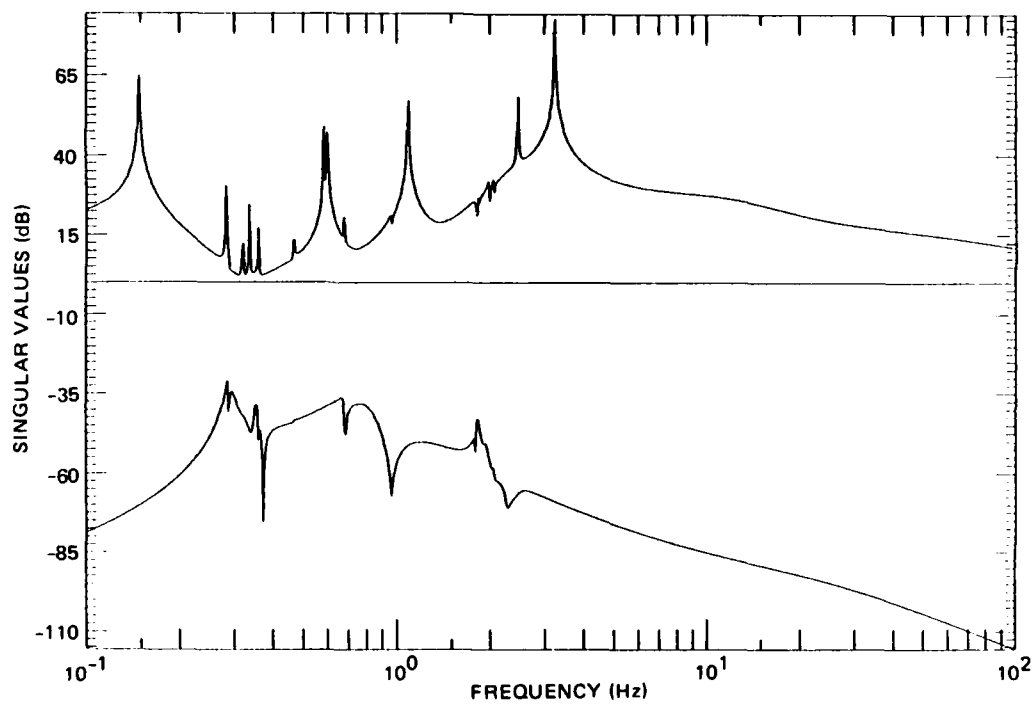


Figure 6-3d. LQG loop transfer matrix $P_d H$.

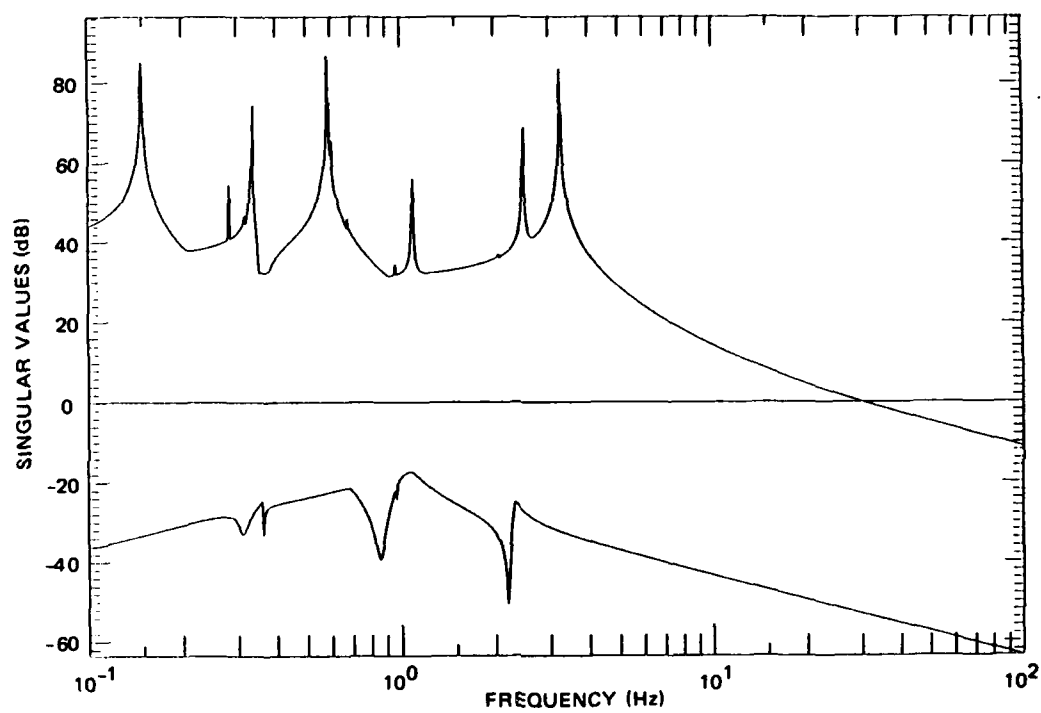


Figure 6-3e. Recovered LQG loop transfer matrix HP_d ; $q = 10^{10}$.

Table 6-2. Designs with five rotational transducers.

Actuator/ Sensor Selection	Weights				LQ (modes 7-24)			Recovery Parameter	LQG (modes 7-24)			Modes in Stable Eval- uation
	q_1	q_2	q_3	ρ_R and ρ_0	LOSX (μ rad)	LOS (μ rad)	DEFOCUS (10^{-3} m)		LOSX (μ rad)	LOS (μ rad)	DEFOCUS (10^{-3} m)	
Design Objective	-	-	-	-	0.05	0.05	0.025	-	0.05	0.05	0.025	7-156
E-5 (5 rot.)	10^1	10^{-1}	10^{-5}	10^{-17}	0.05587	0.04776	0.00496	0	0.06012	0.1622	0.00495	7-33
E-5 (5 rot.)	10^1	10^{-1}	10^{-5}	10^{-17}	0.05587	0.04776	0.00496	10^{10}	7.521	1.917	0.00491	7-156

6-10, 6-11], and the matrix B_{aw} is the influence matrix of the white noise source upon the augmented state. The new term in Eq. (6-11), $qB_a B_a^T$, can be interpreted as representing an additive fictitious process noise. By allowing $q \rightarrow \infty$, it can be shown [Ref. 6-9] that asymptotically, the Kalman gain, K , satisfies:

$$\frac{K}{\sqrt{q}} \rightarrow B_a W(\rho_0 I)^{-1/2} \quad (6-12)$$

where W is an orthogonal matrix. It is shown in Reference 6-5 that with the proper substitution of Eq. (6-12) into the expression for the open loop transfer matrix (where the subscript "a" is suppressed for simplification)

$$H(s)P_d(s) = (G[sI - A - BG - KC]^{-1}K)C\Phi(s)B$$

along with appropriate matrix algebra, that indeed:

$$HP_d \rightarrow G\Phi B$$

pointwise in s , though not uniformly, as q increases to infinity.

Our discussion up to this point has concerned loop shapes corresponding to breaking the loop at the input to the plant (cf. Fig. 6-2). The same robustness results can be stated for loops broken at the output of the plant, where in this case the relevant loop transfer matrix is $P_d H$. Likewise the full-state loop transfer recovery procedure has a dual for loops broken at the plant output. For such a recovery procedure, the LQ regulator is modified so that the open loop transfer matrix, $P_d H$, approaches the Kalman filter loop transfer matrix, $C\Phi K$. This is a desirable course to follow presuming that the Kalman filter loop has frequency domain properties superior to those of $P_d H$. To

explore this alternative a little further, examine Figs. 6-3c and 6-3d which show the Kalman filter loop shape and the loop shape of $P_d H$, respectively, for the controller designs employing five rotational actuators and sensors. In this case $P_d H$ has smaller loop gains in the high frequency region than does the Kalman filter loop, so recovery of the filter loop would be counterproductive.

Because our LQ design has been specially tailored to ensure adequate LOS performance, and because the LQ loop already provides desirable high frequency behavior, we have chosen, for all the examples to be discussed, to modify only the Kalman filter via the full-state loop recovery procedure so that the LQG loop matrix HP_d approaches the LQ loop matrix $G\Phi B$ asymptotically. In the traditional jargon associated with the active control of flexible space structures, our focus on achieving low gains at high frequency for loops broken at the plant input is similar to minimizing the "control spillover".

6.4 Demonstration of Stability Enhancement

This subsection illustrates how the full-state loop recovery procedure may be used in achieving our goal of low loop gains at high frequency for compensators connected with three distinct actuator/sensor placements on ACOSS Model No. 2. Some of the practical problems associated with the entire design procedure are noted.

The desirability of using full-state loop transfer recovery for the compensator associated with the five rotational actuators and sensors has been discussed in the previous subsection. A value of $q = 1 \times 10^{16}$ for the recovery procedure was found to give numerical problems. With $q = 1 \times 10^{10}$ in the adjustment procedure, excellent stability robustness results were achieved. First examine Fig. 6-3e which is the σ -plot of HP_d after the recovery procedure. This is virtually an exact copy of the target LQ loop shape of Fig. 6-3b, indicating good full-state recovery. Indeed an evaluation of this new compensator on all 150

elastic modes of the structural model produced a stable closed-loop system. So the compensator, which had previously maintained closed-loop stability in the presence of modes 7-33, has been adjusted to maintain stability with modes 7-156.

For this new LQG compensator design, closed-loop performance when the compensator is connected to the 18 design modes was tested (see Table 6-2). Compared to the LQG/18-mode performance results of the original compensator, the errors in LOSX and LOSY increase substantially. Reference 6-9 clearly indicates that values of q sufficiently high result in filters that do a poor job of noise rejection, and this is manifesting itself in the poorer performance results we have noted here. Because the original LQG/18-mode controller ($q = 0$) also violates the performance specification, a later design example was deemed more appropriate for investigating potential performance improvements by lowering the q value.

Our design procedure is next demonstrated on the control system originally designed to employ nine translational actuators and sensors, denoted D-9a in Table 6-1, and originally discussed in Ref. 6-2. The frequency domain behavior of the LQG loop matrix HP_d and the LQ loop matrix $G\Phi B$ for this design is shown in Figs. 6-4a and 6-4b respectively. The maximum singular value $\bar{\sigma}$ of the LQ loop crosses the 0 db line at 35 Hz while the maximum singular value $\bar{\sigma}$ of the LQG loop HP_d crosses the 0 db line well beyond 100 Hz. Apparently the LQ loop presents desirable target dynamics for recovery and hence for stability robustness enhancement. A value for the recovery parameter, q , of 1×10^9 gave numerical problems, but values of 1×10^7 and lower gave acceptable results. Figure 6-4c shows the recovered LQG loop matrix, HP_d , indicating good recovery and a 0 db crossover at 35 Hz.

However, when this new compensator is evaluated on modes 7-62 of the structural model, five pairs of poles occur in the right-half plane. These unstable poles include a pole corresponding to mode 30 and poles at frequencies between those of modes 34 and 38. These results indicate

Figures 6-4. σ -plots for designs with 9 translational transducers;
elastic modes 7 through 24.

(on following pages)

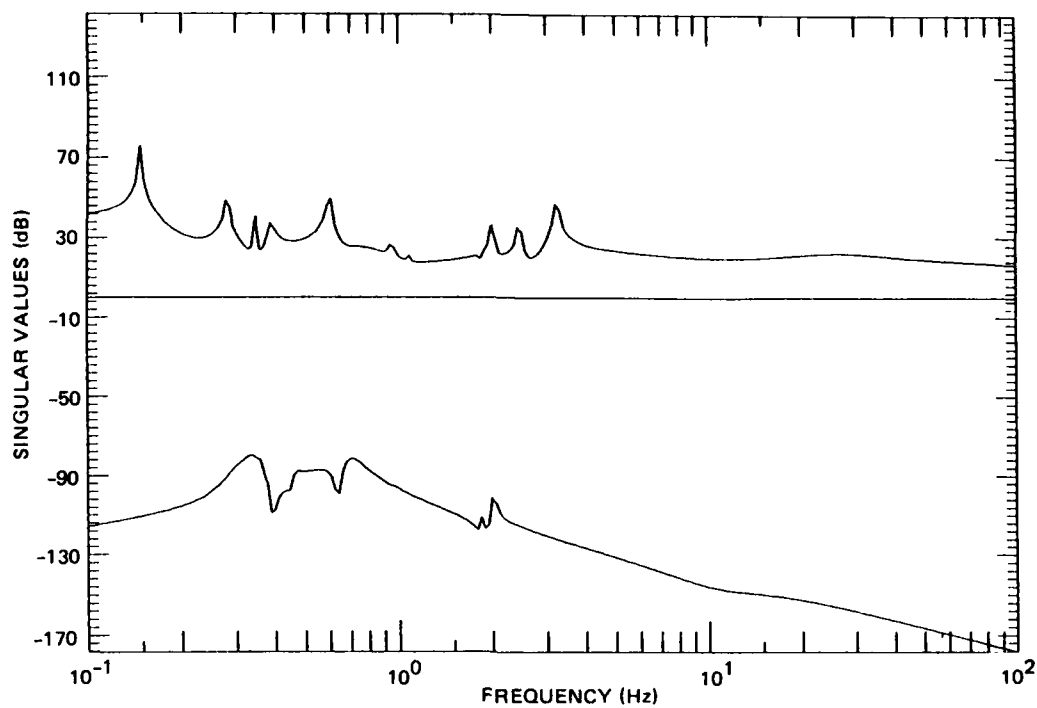


Figure 6-4a. LQG loop transfer matrix HP_d .

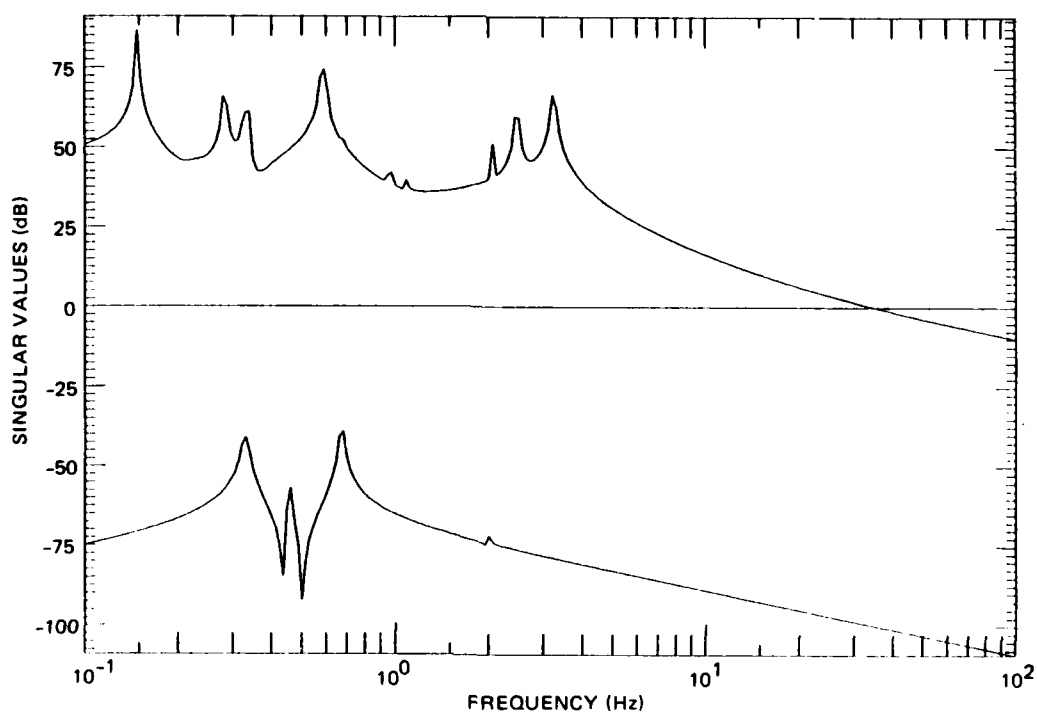


Figure 6-4b. Loop transfer matrix $G\Phi B$ of LQ regulator.

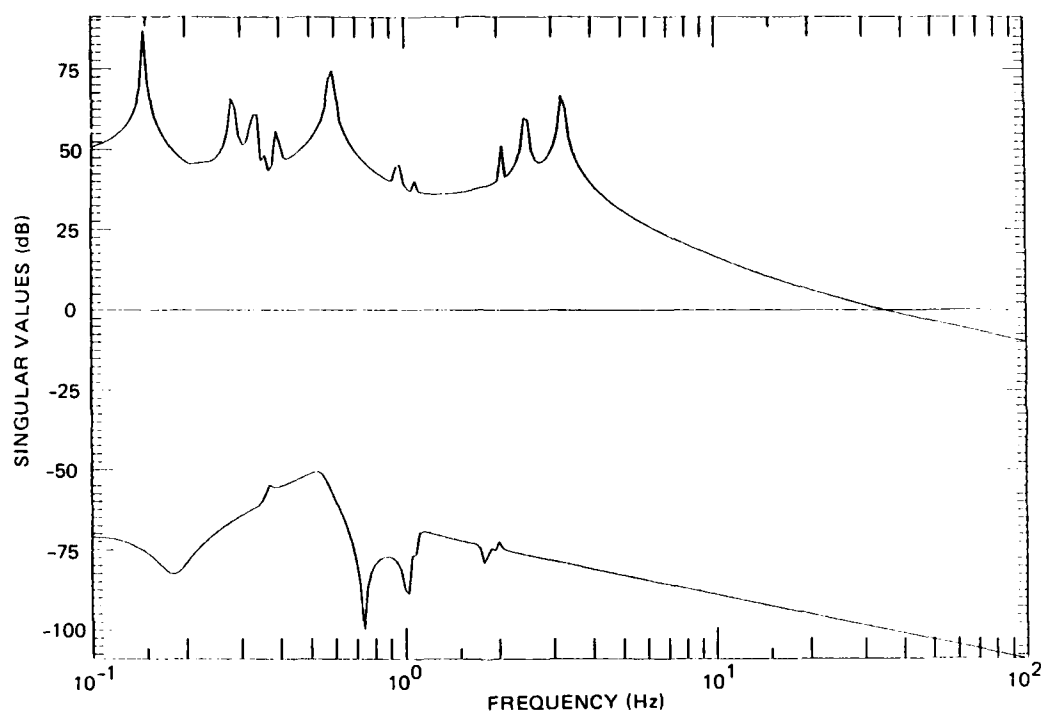


Figure 6-4c. Recovered LQG loop transfer matrix HP_d ; $q = 10^7$.

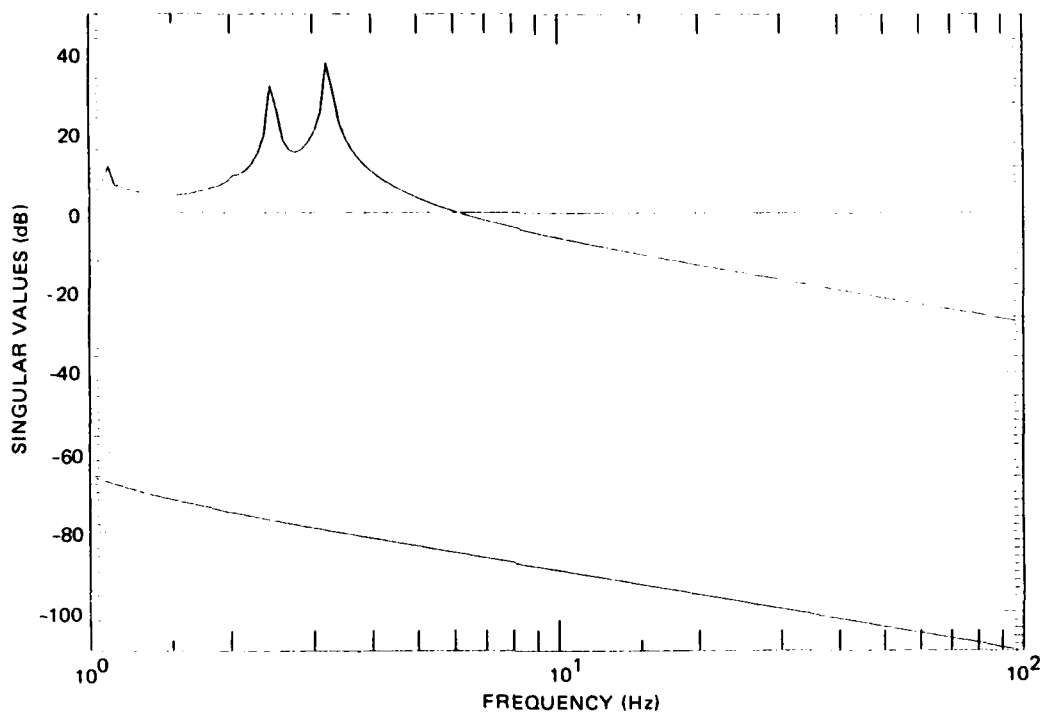


Figure 6-4d. LQ loop transfer matrix $G\Phi B$; redesigned for stability robustness, $\rho_R = 10^{-13}$.

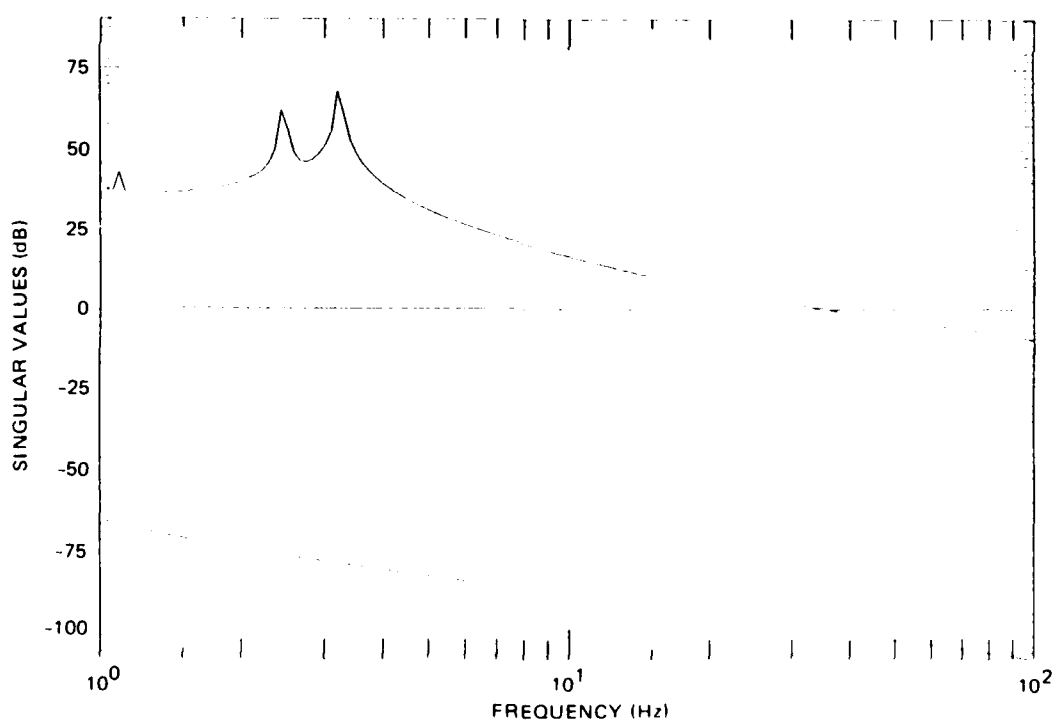


Figure 6-4e. LQ loop transfer matrix $G^\dagger B$; redesigned for LOS performance, modified Q.

Table 6-3. Designs with nine translational transducers.

Actuator/ Sensor Selection	Weights				LQ (modes 7-24)			Recovery Parameter	Modes in Stable Eval- uation
	q_1	q_2	q_3	ρ_R and ρ_0	LOSX (μ rad)	LOS (μ rad)	DEFOCUS (10^{-3} m)		
Design Objective	-	-	-	-	0.05	0.05	0.025	-	7-156
D-9a (9 transl.)	10^{-1}	10^{-2}	10^{-6}	10^{-17}	0.0257	0.03317	0.00345	0 & 10^7	7-29
D-9a (9 transl.)	10^0	10^{-1}	10^{-5}	10^{-13}	1.40	8.609	0.00432	10^7	7-62*
D-9a (9 transl.)	10^3	10^2	10^{-5}	10^{-13}	0.0257	0.03317	0.00429	10^7	7-29

* largest evaluation model tested

that this design is particularly sensitive to the addition of high frequency dynamics, and even the crossover at 35 Hz provided by the LQ loop is not sufficient to bring any improvement to the original compensator.

To explore how this stability problem might be alleviated, the LQ regulator was redesigned employing a much larger control weighting, $\rho_R = 1 \times 10^{-13}$. Reference 6-5 indicates that by raising the control weighting, the entire LQ loop shape tends to be lowered in magnitude, which implies that the 0 db crossover would occur at a much lower frequency. This indeed is the effect as indicated by Fig. 6-4d, which shows 0 db crossover occurring at 6.1 Hz for the new regulator design. Note that this σ -plot is shown between only 1 Hz and 100 Hz. The compensator, $H(s)$, is completed by designing a Kalman filter using $\rho_0 = 1 \times 10^{-13}$ and full-state loop recovery with $q = 1 \times 10^7$. An evaluation on modes 7-62 produces closed-loop stability.

The price that is paid for this improved stability result is a decrease in performance, which was checked for the state-feedback portion of the design. This poorer performance is indicated by the higher root-mean-square (RMS) LOS error shown in Table 6-3 for the LQ regulator using $\rho_R = 1 \times 10^{-13}$ compared to the errors produced by the regulator using $\rho_R = 1 \times 10^{-17}$ also shown in Table 6-3 for actuator/sensor selection D-9a.

Because acceptable LQ LOS-performance is considered a minimum requirement, we need to modify this regulator design. To achieve LOS performance within the specification, the Q matrix weighting the LOS outputs in the performance index is modified to:

$$Q = \begin{bmatrix} 1000 & 0 & 0 \\ 0 & 100 & 0 \\ 0 & 0 & 1 \times 10^{-5} \end{bmatrix}$$

while retaining the control weighting $\rho_R = 1 \times 10^{-13}$. The performance of the regulator is thereby brought within the specification and is shown in Table 6-3. The σ -plot of the LQ loop for this modified design is shown in Fig. 6-4e and indicates a 0 db crossover at 35 Hz, exactly the same crossover frequency of the original design.

To complete the compensator design, the Kalman filter with $\rho_0 = 1 \times 10^{-13}$ is modified via the full-state recovery procedure using $q = 1 \times 10^7$. An evaluation with modes 7-62 produces the same five pairs of unstable poles noted earlier. These results indicate an apparent conflict between the objectives of meeting the LOS performance specifications with the LQ design and meeting stability robustness requirements of the LQG design for this selection of nine translational actuators and sensors.

Such stability/performance conflicts are common in control system design. One could continue iterating on the compensator design, but the approach more likely to bring success is to examine a new actuator/sensor selection. This is in the spirit of our "experimental" approach.

The final controller design examined is that employing twelve translational actuators and sensors (selection C-12a in Table 6-1). The LQ and LQG designs (prior to the use of loop transfer recovery) for this transducer selection achieve performance and stability results quite favorable in comparison to most of the other designs (see Table 6-1).

The striking characteristic of the σ -plot for the LQG loop matrix HP_d shown in Fig. 6-5a is that the maximum singular value remains at a virtually constant value, well above the 0 db line, for most of the high frequencies of the plot. The σ -plot for the LQ loop matrix shown in Fig. 6-5b indicates crossover at 51 Hz.

An appropriate value of q for the full-state loop recovery is 1000; values higher than this result in numerical problems. The frequency domain response of HP_d is shown in Fig. 6-5c after applica-

tion of the adjustment procedure. When the new LQG compensator is evaluated on all 150 elastic modes in the model, closed-loop stability is maintained.

For this new LQG compensator design, performance is tested when the compensator is connected to the 18 design modes (see Table 6-4). Compared to the LQG/18-mode performance results of the original compensator, the RMS LOS error has increased substantially and even violates the performance specification. As noted earlier, sufficiently high values of q in the recovery procedure result in increased LOS error. We expect, therefore, that lowering the value of q should result in better performance, but may decrease our stability robustness. Indeed, a value of $q = 0.1$ in the adjustment procedure leads to excellent performance results for the "recovered" LQG compensator evaluated with the 18-mode design model (see Table 6-4). Closed-loop stability with the full 150-mode model is also maintained.

While we have demonstrated acceptable performance at the design model level and stability robustness, we must also examine performance robustness, i.e., whether adequate performance is maintained in the face of high frequency dynamics. An evaluation of the compensator ($q = 0.1$) with modes 7-36 produces unacceptable degradation in the LOS errors as indicated in Table 6-4. Not reflected in the table is the fact that the major contribution to LOS error comes from the disturbance located at node 37 on the upper portion of the optical support structure.

We believe that a remedy for the poor performance robustness must begin with a reexamination of the modes in the design model, somehow taking into account those modes not presently in the model that nevertheless make a substantial contribution to open-loop LOS error. Careful selection of actuators and sensors, and then careful design of a compensator for stability and performance robustness must follow.

Figures 6-5. σ -plots for designs with 12 translational transducers;
elastic modes 7 through 24.

(on following pages)

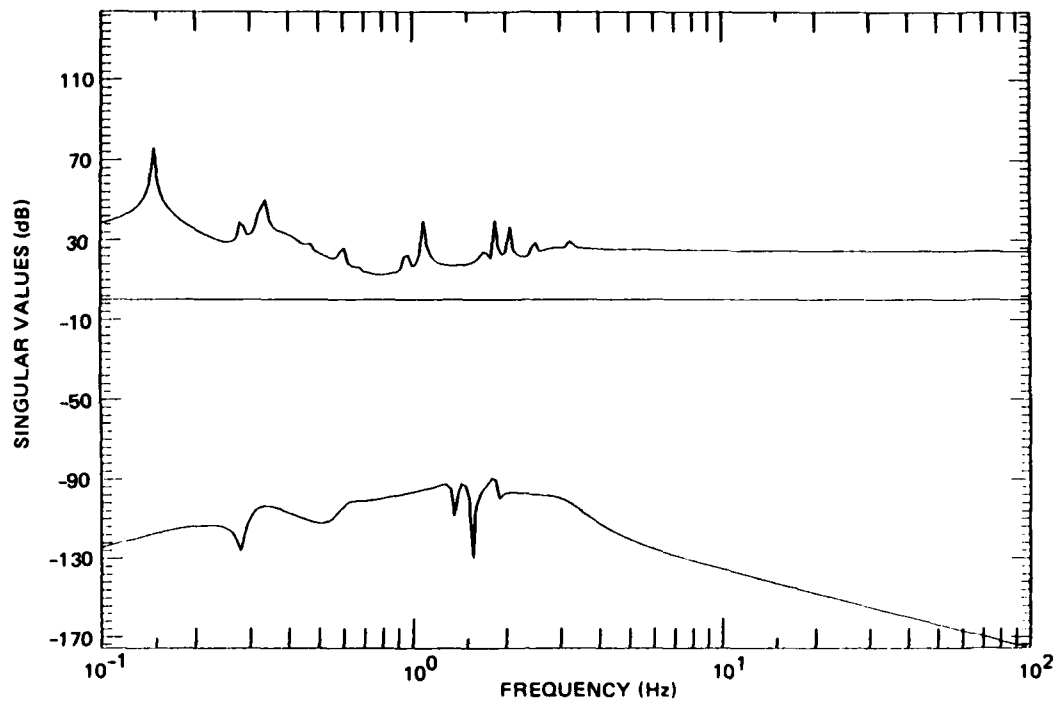


Figure 6-5a. LQG loop transfer matrix HP_d .

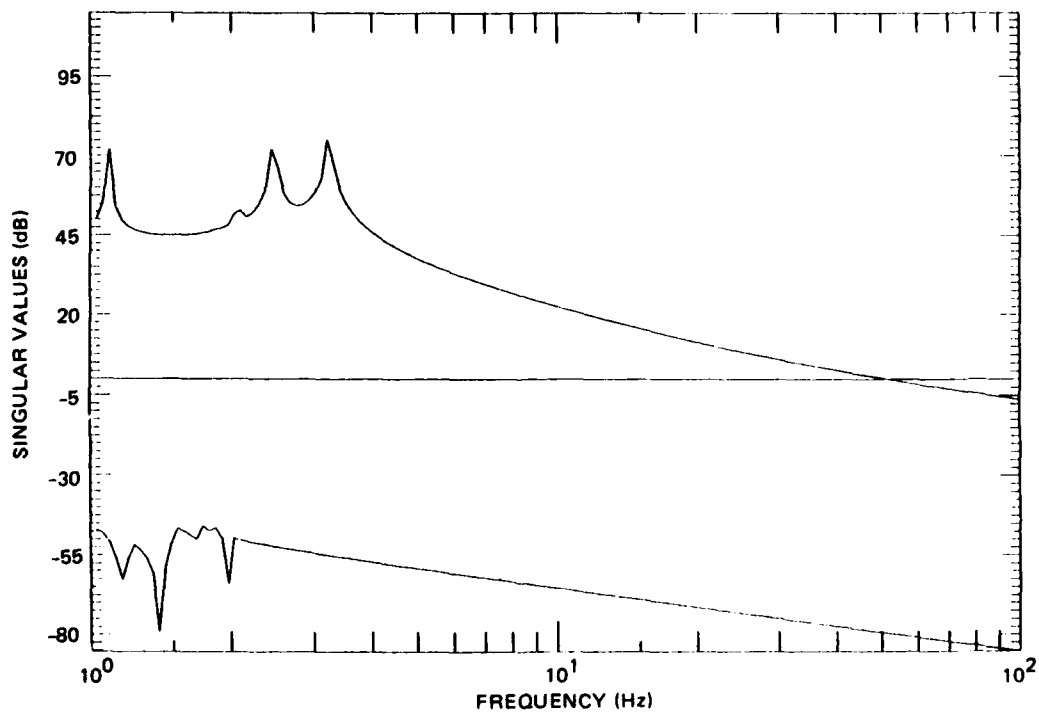


Figure 6-5b. Loop transfer matrix $G\Phi B$ of LQ regulator.

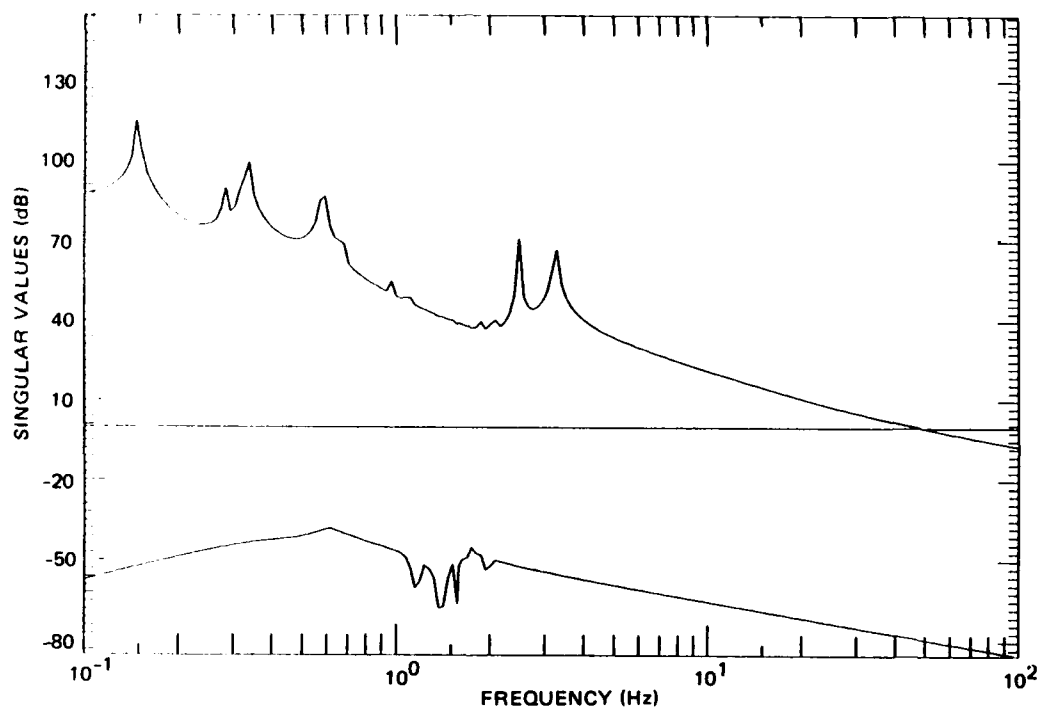


Figure 6-5c. Recovered LQG loop transfer matrix HP_d , $q \approx 10^3$.

Table 6-4. Designs with twelve translational transducers.

Actuator/ Sensor Selection	Weights				LQ (modes 7-24)			Recovery Parameter	LOG (modes 7-24)			LOG (modes 7-36)			Modes in Stable Eval- uation
	q_1	q_2	q_3	ρ_R and ρ_0	LOSX (μ rad)	LOSX (μ rad)	LOSX (μ rad)		LOSX (μ rad)	LOSX (μ rad)	LOSX (μ rad)	LOSX (μ rad)	LOSX (μ rad)	LOSX (μ rad)	
Design Objective	-	-	-	-	0.05	0.05	0.05	-	0.05	0.05	0.05	0.05	0.05	0.05	7-156
C-12a (12 transl.)	10^0	10^{-1}	10^{-5}	10^{-17}	0.00532	0.00851	0.00136	0	0.00644	0.05073	0.00136	31.44	19.16	0.03848	7-39
C-12a (12 transl.)	10^0	10^{-1}	10^{-5}	10^{-17}	0.00532	0.00851	0.00136	10^3	0.1973	15.57	0.00132	-	-	-	7-156
C-12a (12 transl.)	10^0	10^{-1}	10^{-5}	10^{-17}	0.00532	0.00851	0.00136	10^{-1}	0.00729	0.03596	0.00136	17.35	20.54	0.01640	7-156

6.6 Discussion, Conclusions and Recommendations

In the foregoing we first described how our control system designs for the numerous actuator/sensor placements on the space structure model are geared almost entirely toward achieving acceptable performance with the state feedback (or LQ) portion of our compensators. The observed lack of stability robustness of the LQG designs is the result of high frequency dynamics not included in the design model of the plant. Second, we derived from the multivariable Nyquist criterion a design goal of low loop gains at high frequency as a means of enhancing stability robustness. Third, we discussed a design technique, full-state loop transfer recovery, that is a systematic aid to achieving the stated design goal, given that the LQ regulator has desirable high frequency properties. Finally, we demonstrated our revised design procedure on three compensators and noted the problems that can arise in practice. In particular, we saw for the design with nine translational transducers that the frequency domain requirements for LQG stability robustness conflict with the achievement of adequate performance even at the design model level of the LQ regulator. For the other two compensators, the recovery procedure allows us to achieve lower loop gains at high frequency and even stability with all 150 elastic modes. In every design, excessive values of the recovery parameter q produce numerical problems. The upper bound for q that can be tolerated must be determined for each design. We also noted in the final design that a value of q could be adequate for enhancing stability robustness, but may be sufficiently high that performance is severely degraded even at the LQG/design-model level. Again q will have to be adjusted for each design to achieve the desired results.

We have not achieved performance robustness with our designs and have suggested that a remedy must begin with a reexamination of the design model of the plant.

In the broader context of our experiment we can see that reduced-order model selection, active transducer selection, and compensator design must not be considered in isolation. On the one hand, no matter how carefully a design model and active transducers have been selected, a poor controller design may preclude even the achievement of stability. On the other hand, a robust control system design cannot make up for an inadequate design model, or ill-considered actuator and sensor selections.

One of the major robustness questions we have yet to address explicitly is robustness to variation of parameters in the model of the structure. In the frequency domain context we require high loop gains in the frequency band containing the design model -- usually residing in the low end of the frequency spectrum -- to achieve robustness to parameter variations. Other significant questions for control design include the addition of actuator and sensor dynamics in our models and the examination of digital controllers.

Clearly the stringent performance requirements in the face of significant disturbances acting on a flexible space structure continue to pose a formidable challenge in active control synthesis.

References

- 6-1. Hegg, D. R., "A Controlled Experiment for ACOSS Design," ACOSS-Eleven Third Interim Technical Report, Vol. 2, Report CSDL-R-1598, Charles Stark Draper Laboratory, Cambridge, MA, December 1982; Section 5.
- 6-2. Hegg, D. R. and Kissel, G. J., "Progress on Synthesis of Active Control for Broadband Disturbance Accommodation," ACOSS-Eleven Fourth Interim Technical Report, Vol. 2, Report CSDL-R-1648, Charles Stark Draper Laboratory, Cambridge, MA, August 1983; Sections 2 and 3.

- 6-3. Hegg, D. R. and Kissel, G. J., "Progress on Synthesis of Active Control for Wideband Disturbance Accommodation with ACOSS Model No. 2," ACOSS-Eleven Fifth Semiannual Technical Report, Report CSDL-R-1687, Charles Stark Draper Laboratory, Cambridge, MA, March 1984; Section 5.
- 6-4. Safonov, M. G., Laub, A. J. and Hartmann, G. L., "Feedback Properties of Multivariable Systems: The Role and Use of the Return Difference Matrix," IEEE Trans. Automatic Control, Vol. AC-26, No. 1, February 1981, pp. 47-65.
- 6-5. Doyle, J. C. and Stein, G., "Multivariable Feedback Design: Concepts for a Classical/Modern Synthesis," IEEE Trans. Automatic Control, Vol. AC-26, No. 1, February 1981, pp. 4-16.
- 6-6. Lehtomaki, N. A., Sandell, N. R., Jr., and Athans, M., "Robustness Results in Linear-Quadratic Gaussian Based Multivariable Control Designs," IEEE Trans. Automatic Control, Vol. AC-26, No. 1, February 1981, pp. 75-93.
- 6-7. Rosenbrock, H. H., Computer-Aided Control System Design, Academic Press, London, 1974.
- 6-8. Lehtomaki, N. A., "Practical Robustness Measures in Multivariable Control System Analysis," Ph.D. Dissertation, Department of Electrical Engineering and Computer Science, Massachusetts Institute of Technology, Cambridge, MA, May 1981.
- 6-9. Doyle, J. C. and Stein, G., "Robustness with Observers," IEEE Trans. Automatic Control, Vol. AC-24, No. 4, August 1979, pp. 607-611.
- 6-10. Kwakernaak, H. and Sivan, R., Linear Optimal Control Systems, Wiley, New York, NY, 1972.
- 6-11. Fogel, E., "Disturbance Rejection Control Design," ACOSS-Eleven Second Semiannual Technical Report, Vol. 2, Report CSDL-R-1583, Charles Stark Draper Laboratory, Cambridge, MA, August 1982; Section 4.

SECTION 7

MODELING FOR FLEXIBLE STRUCTURE CONTROL WITH ELECTROMECHANICAL ACTUATOR DYNAMICS

7.1 Introduction

There are a variety of possible actuation devices that could be selected for use in achieving vibration control of large flexible space structures. Our recent research [Refs. 7-1, 7-2] has focused on electromechanical devices as actuators for achieving such vibration control. In the present section, we clarify our approach to the incorporation of electromechanical actuator dynamics by placing it in a unified context, and distinguish its principal features from other relevant work.

An electromechanical actuator (also called a voice coil actuator) consists of two mass elements and an associated electrical circuit. As current is caused to flow through the circuit due to an applied actuator input voltage, an electromagnetic force is generated between the two actuator mass elements. A schematic is shown in Fig. 7-1.

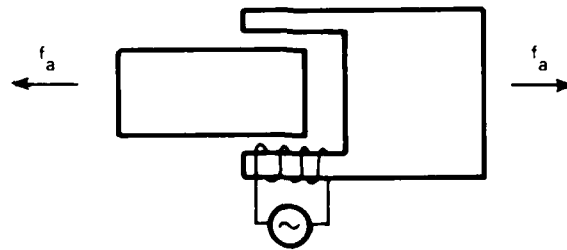


Figure 7-1. Basic electromechanical actuator.

Our motivation for use of electromechanical actuators is as follows. Electromechanical actuators are simple, reliable, and adaptable to use as actuators for a wide variety of distributed structures in many different configurations. They can be used as linear (i.e., translational) actuators to generate control forces; and they can be used as rotary actuators to generate control torques.

7.2 A Generic Case: Models for Possible Actuator Configurations

Consider the control of the axial motion of a bar with distributed mass and distributed stiffness. There are three conceptually different structure/actuator configurations. These three configurations are presented and the general form of mathematical models used to describe the dynamics in each case is given. The derivation of the models follows a Lagrangian approach similar to that presented in References 7-1 and 7-2 and is therefore omitted. To clarify the main issues we wish to emphasize, it is assumed that inherent structural damping is negligible and that mechanical motion of the actuator does not of itself (i.e., kinematically) give rise to significant forces on the actuator. The form of the models is considerably more general in that they arise in cases where the structure is more complicated than a simple bar. Our consideration of this simple physical case should give an indication of the fundamental differences in the three configurations. In each configuration, certain simplifications of the mathematical models are indicated; in each case, conclusions are stated in terms of the overall way in which the actuator dynamics affect the structural dynamics.

7.2.1 Structure and Inertial-Based Actuator

Assumptions for this case are as follows. One actuator element is fixed in an inertial frame; the other actuator element is connected directly to (or is part of) the structure. A schematic of the generic case is shown in Fig. 7-2.

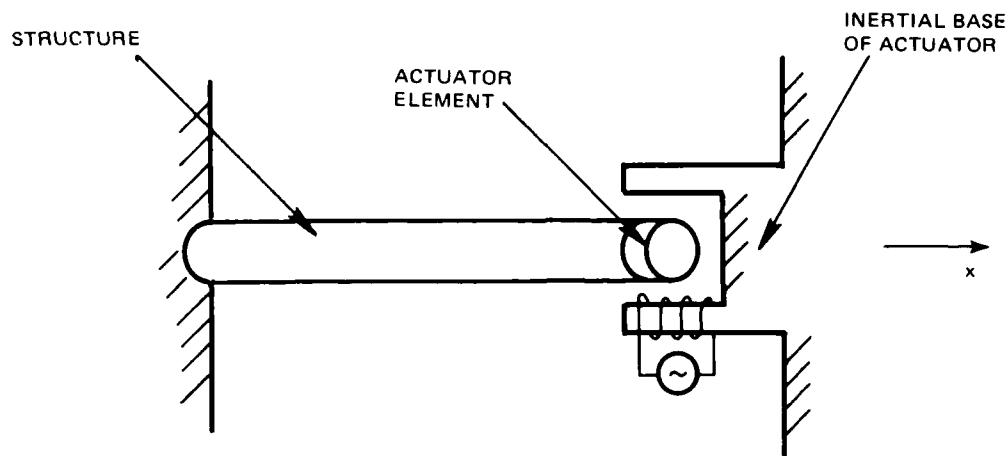


Figure 7-2. Representation of an inertial-based actuator.

The dynamic model of the structure, for this configuration, can be shown to be given by

$$M\ddot{q} + Kq = Bf_a$$

where q is the vector of generalized structural displacements, M and K are generalized mass and stiffness matrices, respectively, for the structure, and B is the influence matrix of the actuator forces upon the structure. The electromagnetic actuator force f_a on the structure is linearly related to the circuit current I :

$$f_a = \xi I \quad (7-1)$$

which in turn satisfies the electromechanical coupling equation:

$$L\dot{I} + RI + \xi B^T \dot{q} = u \quad (7-2)$$

where L and R are the inductance and resistance parameters, respectively, of the circuit, and u is the actuator input voltage.

There are a number of reasonable simplifications of this model. For example, the inductance parameter L is typically small; if L is assumed to be zero, then the model can be described by

$$M\ddot{q} + \xi^2 BR^{-1} B^T \dot{q} + Kq = \xi BR^{-1} u$$

Thus, under appropriate assumptions, the dynamic characteristics of the structure are modified by the coupling with the actuator dynamics. In the special case that $L = 0$ is assumed, a structural damping effect is introduced into the structure dynamics through the actuator "back emf".

Since there is no inertial base in a space environment, this configuration would not be a possible implementation to achieve vibration control of a flexible structure in space. The configuration is mentioned here primarily for comparison with the other two configurations to be discussed next.

7.2.2 Structure and Structure-based Transmission-type Actuator

Assumptions for this case are as follows. Each actuator element is connected to the structure through an elastic "transmission device". A schematic of the generic case is shown in Fig. 7-3.

The dynamic model of the structure, for this configuration, can be shown to be given by

$$M\ddot{q} + Kq = BK_a(z - B^T \dot{q})$$

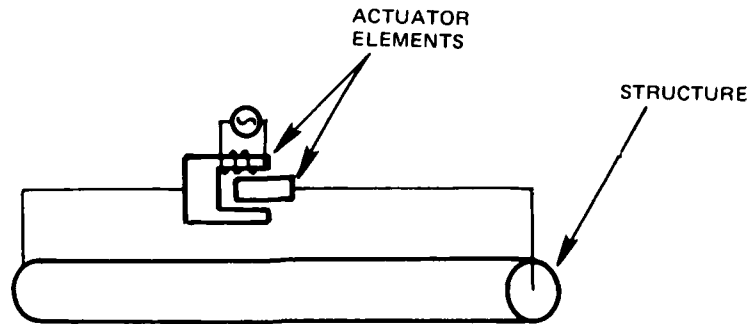


Figure 7-3. Representation of a structure-based transmission-type actuator.

and the model of the actuator elements is given by

$$M_a \ddot{z} + K_a(z - B_a^T q) = B_a f_a$$

where z is the vector of generalized displacements of the actuator, M_a and K_a are generalized mass and stiffness matrices, respectively, for the actuator, and B_a is the influence matrix of the actuator forces upon the actuator elements. The electromagnetic actuator force f_a satisfies an equation of the form Eq. (7-1), where in this case the circuit current I satisfies

$$L \dot{I} + RI + \xi B_a^T \dot{z} = u \quad (7-3)$$

instead of Eq. (7-2).

These equations are inherently coupled through the actuator flexibility term. The effective actuator force on the structure is given by

$$f = K_a(z - B_a^T q)$$

which can be viewed as a force transmitted from the actuator mass to the structure. It is this view that motivates the designation of the actuator as being of transmission type. Note that the above equations for the structure and the actuator are intrinsically coupled; it is not possible to view the actuator dynamics as a pure series connection with the structural dynamics.

As with the preceding configuration, we look for reasonable simplifications of the model. The inductance parameter L is typically small; if L is assumed to be zero, then the model can be described by

$$M\ddot{q} + Kq = BK_a(z - B^T q)$$

$$M_a \ddot{z} + \xi^2 B_a R^{-1} B_a^T \dot{z} + K_a(z - B^T q) = \xi B_a R^{-1} u$$

If, in addition, the stiffness of the "transmission device" is sufficiently large so that it is reasonable to assume that $K_a \rightarrow \infty$, then the model can be described by

$$(M + BM_a B^T) \ddot{q} + \xi^2 BB_a R^{-1} B_a^T B^T \dot{q} + Kq = \xi BB_a R^{-1} u$$

Thus, under appropriate assumptions, the dynamic characteristics of the structure are modified by the coupling with the actuator dynamics. Even in the limiting case where $L = 0$ and $K_a \rightarrow \infty$ are assumed, there is a modification of the structural mass characteristics and a structural damping effect is introduced into the structure dynamics through the actuator "back emf".

7.2.3 Structure and Structure-based Reaction-type Actuator

Assumptions for this case are as follows. One actuator element is connected directly to (or is part of) the structure; the other actuator

element is free to act as a "proof mass". The two actuator elements are connected through a "reaction spring". A schematic of the generic case is shown in Fig. 7-4.

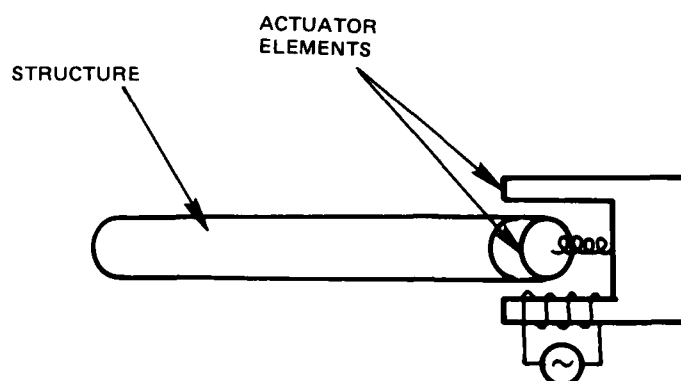


Figure 7-4. Representation of a structure-based reaction-type actuator.

The dynamic model of the structure, for this configuration, can be shown to be given by

$$M\ddot{q} + Kq = -BM_a(z + B^T q)$$

and the model of the proof-mass actuator element is given by

$$M_a(\ddot{z} + B^T \ddot{q}) + K_a z = B_a f_a$$

where (in contrast to the preceding configuration) z is the vector of generalized relative displacements between the two actuator elements, and M_a , K_a , and B_a are associated with the proof-mass element of the actuator. The electromagnetic actuator force f_a satisfies Eqs. (7-1) and (7-3) (with the appropriate revision in the interpretation of the z -variable).

These equations are inherently coupled through the actuator inertial term. The effective actuator force on the structure is given by

$$f = -M_a(\ddot{z} + B^T \ddot{q})$$

which can be viewed as a force in reaction to the acceleration of the proof-mass element of the actuator. It is this view that motivates the designation of the actuator as being of reaction type. Note that the above equations for the structure and the actuator are intrinsically coupled; it is not possible to view the actuator dynamics as a pure series connection with the structural dynamics.

Again we look for reasonable simplifications of the model. The inductance parameter L is typically small; if L is assumed to be zero, then the model can be described by

$$M \ddot{q} + Kq = -BM_a(\ddot{z} + B^T \ddot{q})$$

$$M_a(\ddot{z} + B^T \ddot{q}) + \xi^2 B_a R^{-1} B_a^T \dot{z} + K_a z = \xi B_a R^{-1} u$$

If, in addition, the mass of the "proof mass" is sufficiently large so that it is reasonable to assume that $M_a \rightarrow \infty$, then the model can be described by

$$M \ddot{q} + \xi^2 B B_a R^{-1} B_a^T B^T \ddot{q} + (K + B K_a B^T)q = -\xi B B_a R^{-1} u$$

Thus, under appropriate assumptions, the dynamic characteristics of the structure are modified by the coupling with the actuator dynamics. Even in the limiting case where $L = 0$ and $M_a \rightarrow \infty$ are assumed, there is a modification of the structural stiffness characteristics and a structural

damping effect is introduced into the structure dynamics through the actuator "back emf".

7.3 Feedback Control Issues

By explicitly considering the structure and actuators together as the system to be controlled, our viewpoint is that the control input is the voltages applied to the actuator input circuits.

There are many possible feedback control laws that could be examined as a means of achieving some (vibration) control objective. Only a few cases are mentioned here.

- a. The simplest control law is to assume that $u = 0$. In such a case the actuators are essentially used as passive dampers.
- b. Suppose that u depends only upon feedback of z and \dot{z} ; then only internal feedback of the motion of the actuator elements is required. In such a case the actuators are essentially used as "active" passive dampers.
- c. The general case is to assume that u depends on feedback of both the motion of the actuator elements and the motion of the structure.

Certain aspects of the general case have been considered in References 7-1 through 7-4. The emphasis in References 7-1 and 7-2 (and in the present section) is on the development of general models for transmission-type and reaction-type devices as control actuators for a flexible structure. In the case where the structure is controlled by multiple actuators, a special form of decentralized control law is suggested and analyzed. A special form of centralized control law is also briefly examined.

In contrast, the emphasis in References 7-3 and 7-4 is on the practical development of a linear reaction-type actuator. No attention is given to the development of a general model which characterizes the

coupling between the structure and the actuator. Control issues are considered solely in the context of the developed device.

Although there is a considerable literature on the design of control laws for achieving vibration control of flexible structures, the developed control laws must be suitably modified if the dynamics of electromechanical actuators are to be taken into account.

7.4 Summary

If electromechanical devices are used as control actuators for a distributed flexible structure, it is claimed that the dynamics of the actuator should be carefully examined as an integral part of the structural system to be controlled. Apparently, there are several different structure/actuator configurations which differ in their physical characteristics and in the form of suitable mathematical models for these configurations.

The important feature, from a control design standpoint, is that it is relatively easy to incorporate any actuator dynamics into the structural dynamics in such a way that existing control design techniques, such as those considered in Sections 5 and 6 of this report, remain valid.

References

- 7-1. McClamroch, N. H., "Control of Large Space Structures Using Electromechanical Actuators," ACROSS-Eleven Third Semiannual Technical Report, Vol. 2, Report CSDL-R-1598, Charles Stark Draper Laboratory, Cambridge, MA, December 1982; Section 3.
- 7-2. McClamroch, N. H., "Modelling and Control of Large Flexible Structures Using Electromechanical Actuators," Proc. Fourth VPI&SU/AIAA Symposium on Dynamics and Control of Large Structures, Blacksburg, VA, June 1983, pp. 421-438.

- 7-3. Aubrun, J. N. and Margulies, G., "Low-Authority Control Synthesis for Large Space Structures," National Aeronautics and Space Administration Contractor Report NASA-CR-3495, Lockheed Missiles and Space Company, Palo Alto, CA, September 1982.
- 7-4. Aubrun, J. N., et. al., "Vibration Control of Space Structures--VCOSS A: High- and Low-Authority Hardware Implementations," Air Force Wright Aeronautical Laboratories Contractor Report AFWAL-TR-83-3074, Lockheed Missiles and Space Company and Integrated Systems, Inc., Palo Alto, CA, July 1983.

SECTION 8

POLE LOCATION MANIPULATION FOR IMPROVED SPECTRAL RESOLUTION

8.1 Introduction

The problem of obtaining high-resolution power spectrum estimates has been of concern to researchers in the area of signal processing for a very long time. This is due to the wide range of technical problems with solutions that are made feasible by the availability of such estimates. A classic application of high resolution techniques is in the area of radar Doppler processing. Another application which happens to be of current relevance is the system identification problem for large flexible space structures. Because such structures characteristically exhibit vibrational modes which are very close in frequency, any identification procedure based on power spectrum analysis must employ a spectrum estimation technique with the ability to resolve closely spaced spectral peaks.

In Reference 8-1, the problem of improving the resolution of power spectrum estimates was discussed. In particular, an estimation procedure was considered which is based on parametric analysis of the autocorrelation sequence $\{r(k)\}$ corresponding to the wide-sense stationary discrete-time process $\{x(k)\}$ of interest. The procedure uses the estimates $\{\hat{r}(d), \hat{r}(d+1), \dots, \hat{r}(d+N-1)\}$ of the actual autocorrelation sequence (hereafter we shall assume $d = 0$) to obtain estimates of the parameters $\{A_1, \dots, A_n\}$ and $\{z_1, \dots, z_n\}$ of the following assumed structure for $\{r(k)\}$:

$$r(k) = \sum_{i=1}^n A_i z_i^k \quad (8-1)$$

It was demonstrated in Reference 8-1 that the locations of the poles $\{z_1, \dots, z_n\}$ in the complex plane have a significant effect on the sensitivity of the parameter estimates to errors in the autocorrelation estimates $\{\hat{r}(0), \hat{r}(1), \dots, \hat{r}(N-1)\}$ (see Guideline 1, p. 211, and Guideline 2, p. 223 in Reference 8-1). Since the accuracy of the parameter estimates determines the accuracy and therefore the resolution of the resulting spectrum estimate, the implication is that if pole locations could be manipulated, then resolution could be improved.

In Reference 8-1, the use of desampling as a means for manipulating pole locations was considered, and a modified power spectrum estimation procedure based on desampling was constructed. In this section the improved resolution obtainable by the desampling procedure is demonstrated. But first, we consider the use of the autocorrelation sampling period as another means of manipulating pole locations when discrete-time techniques are to be applied to the spectrum estimation problem for continuous-time processes.

8.2 Sampling Considerations for Continuous-Time Spectrum Estimation

Consider a real, wide-sense stationary, continuous-time process x_c , and let its autocorrelation function r_c , which is defined by

$$r_c(\tau) \triangleq E[x_c(t) x_c(t + \tau)]$$

be representable by the analog of Eq. (8-1) for continuous-time processes:

$$r_c(\tau) = \sum_{i=1}^n C_i e^{p_i \tau} \quad (8-2)$$

Here $\{C_1, \dots, C_n\}$ and $\{p_1, \dots, p_n\}$ occur in complex conjugate pairs, and due to physical constraints we have $\text{Re}(p_i) \leq 0$, $i = 1, \dots, n$. Since the power spectral density function R_c of the process x_c is

$$R_c(\Omega) = 2 \cdot \sum_{i=1}^n \frac{C_i p_i}{(j\Omega - p_i)(j\Omega + p_i)} \quad , \quad -\infty < \Omega < +\infty \quad (8-3)$$

a spectrum estimate may be obtained by estimating the parameters $\{C_1, \dots, C_n\}$ and $\{p_1, \dots, p_n\}$ (assuming n is known). This may be done by applying the spectrum estimation procedure from Section 7.2 of Reference 8-1 to the sequence $\{r(k)\}$ obtained by periodically sampling r_c :

$$r(k) = r_c(kT) \quad , \quad -\infty < k(\text{integer}) < +\infty \quad (8-4)$$

where T is the autocorrelation function sampling period. Combining Eq. (8-4) with Eq. (8-2) we get

$$r(k) = \sum_{i=1}^n C_i e^{p_i T |k|} \quad , \quad -\infty < k < +\infty \quad (8-5)$$

Comparing Eq. (8-5) with Eq. (8-1), note that

$$A_i = C_i \quad , \quad z_i = e^{p_i T} \quad , \quad i = 1, \dots, n \quad (8-6)$$

Letting

$$\sigma_i = \text{Re}(p_i) \quad , \quad \Omega_i = \text{Im}(p_i) \quad , \quad i = 1, \dots, n$$

and assuming T is chosen such that

$$-\pi < \Omega_i T < \pi, \quad i = 1, \dots, n \quad (8-7)$$

we may calculate $\{\hat{A}_1, \dots, \hat{A}_n\}$ and $\{\hat{z}_1, \dots, \hat{z}_n\}$ (where " $\hat{\cdot}$ " denotes an estimate of the indicated variable) via the procedure of Reference 8-1, and then obtain estimates $\{\hat{C}_1, \dots, \hat{C}_n\}$ and $\{\hat{p}_1, \dots, \hat{p}_n\}$ as follows:

$$\begin{aligned} \hat{C}_i &= \hat{A}_i \\ \hat{\sigma}_i &= \frac{\ln |\hat{z}_i|}{T}, \quad \hat{\Omega}_i = \frac{\text{Arg } \hat{z}_i}{T}, \quad i = 1, \dots, n \end{aligned}$$

where $\text{Arg } \hat{z}_i$ denotes the principal argument (i.e., the unique real number which satisfies $z = |z| \exp(j \cdot \text{Arg } z)$ and $-\pi < \text{Arg } z \leq \pi$ for any nonzero complex number z) of \hat{z}_i . Note that if $\text{Arg } \hat{z}_i = \pi$, then in light of Eq. (8-7), \hat{z}_i should be considered a numerical artifact and ignored by forcing $\hat{C}_i = \hat{A}_i = 0$. This may be done by eliminating the columns of $\hat{\underline{V}}_r$ and $\hat{\underline{V}}_i$, and the elements of $\hat{\underline{A}}_r$ and $\hat{\underline{A}}_i$ corresponding to \hat{A}_i and \hat{z}_i before solving Eq. (7-18) of Reference 8-1.

Referring to Eq. (8-6), we see that there is an explicit relationship between z_i and T . Clearly, T may be used to manipulate the position of z_i in the complex plane. Furthermore, if $\sigma_i \approx 0$, $i = 1, \dots, n$, then $z_i \approx e^{j\Omega_i T}$, $i = 1, \dots, n$, and Guidelines 1 and 2 may be used to judge the effect of T on the sensitivity of the spectrum analysis procedure to errors in the estimates $\{\hat{r}(0), \dots, \hat{r}(N-1)\}$. If n is even and the set $\{\Omega_1, \dots, \Omega_n\}$ is ordered such that $0 < \Omega_1 T < \Omega_{i+1} T < \pi$, $i = 1, \dots, n/2$, we may set

$$\omega_i = \Omega_i T, \quad i = 1, \dots, n/2$$

(see Eq. (7-30) in Reference 8-1) and then use Guidelines 1 and 2 to determine values of T which will decrease the sensitivity of the spectrum estimation algorithm, implying an improvement in the resolution of the resulting spectrum estimates.

In this subsection, emphasis is placed on the use of Guideline 2 to improve resolution. Guideline 2 states that it is desirable to have $\omega_c = \pi/2$, where

$$\omega_c = \frac{(\omega_1 + \omega_{n/2})}{2} = \left(\frac{\Omega_1 + \Omega_{n/2}}{2} \right) \cdot T$$

Since estimates for $(\Omega_1 + \Omega_{n/2})/2$ are readily available in a number of applications (for example, radar Doppler processing), frequently T may be chosen on the basis of prior knowledge such that $\omega_c \approx \pi/2$. Thus Guideline 2 is a practical tool for improving resolution.

The use of Guideline 2 is demonstrated here via three examples. In all three cases, the power spectrum of a continuous-time process x_c is estimated via the algorithm of Section 7.2 of Reference 8-1. The required estimates for the samples $r(k) = r_c(kT)$, $k = 0, \dots, N-1$, are obtained from the data sequence

$$\{y(k) = x(k) + w(k), k = 0, \dots, N_d - 1\}$$

where $x(k)$ denotes the sample

$$x(k) = x_c(kT)$$

of the continuous-time process x_c , and $w(k)$ is a Gaussian, zero mean, white noise sequence with variance σ_w^2 . The autocorrelation estimator used is

$$\hat{r}(k) = \frac{1}{N_d - k} \sum_{\ell=0}^{N_d-1-k} y(\ell) y(\ell+k) \quad (8-8)$$

which presumes the ergodicity of the process x_c . Note that since

$$E[y(l) y(l + k)] = \begin{cases} r(k) + \sigma_w^2 & , \quad k=0 \\ r(k) & , \quad k \neq 0 \end{cases} \quad (8-9)$$

and because in this section it has been assumed that $d = 0$, the first equation in Eq. (7-16) of Reference 8-1, and the first and $(N + 1)$ st equations in Eq. (7-18) of Reference 8-1 were deleted prior to obtaining $\{\hat{a}_1, \dots, \hat{a}_n\}$ (the autoregressive coefficient estimates) and $\{\hat{A}_1, \dots, \hat{A}_n\}$ for the examples which follow.

For the first example we have $N_d = 128$, $N = 30$, $\sigma_w^2 = 0.1$, and

$$x_c(t) = \cos(0.9\pi t) + \cos(\pi t)$$

Nine cases are considered by choosing T so that $\omega_c = (0.95\pi)T$ varies from 0.1π to 0.9π in increments of 0.1π . For each case, ten power spectrum estimates are calculated, with each corresponding to a different realization of the noise sequence $\{w(k)\}$. Figures 8-1a through 8-1i contain plots of these estimates, where \hat{R} (see Eq. (7-4) of Reference 8-1) instead of \hat{R}_c (see Eq. (8-3)) is plotted to emphasize the relationship between resolution and ω_c . Clearly, the choice of T according to Guideline 2 provides beneficial results.

Because Guideline 2 was developed based essentially on analysis of the two-sinusoid case, the second example considers its application to a case involving other than two sinusoids. Letting $N_d = 128$, $N = 30$, $\sigma_w^2 = 0.1$, and

$$x_c(t) = \cos(0.7\pi t) + 2 \cos(0.9\pi t) + 1.5 \cos(\pi t)$$

T is chosen so that $\omega_c = (0.85\pi)T$ varies from 0.1π to 0.8π . The results of spectrum analysis are presented in Figures 8-2a through 8-2h, demonstrating the usefulness of Guideline 2 when n is an even integer other than four.

A common practice used to improve spectrum estimation is the assumption that n is larger than its actual value. The reason behind this is that the additional parameters estimated tend to model the errors in the autocorrelation estimates. Although n was assumed equal to its actual value in the analysis leading to Guideline 2, that Guideline may be applied with success when n is assumed greater than its actual value. The third example demonstrates this. With $N_d = 256$, $N = 100$, $\sigma_w^2 = 0.1$, and

$$\begin{aligned} x_c(t) = & 2 \cos(0.7\pi t) + \cos(0.8\pi t) + 1.5 \cos(0.9\pi t) \\ & + 2 \cos(0.95\pi t) + 1.5 \cos(\pi t) \end{aligned}$$

spectrum estimates are calculated for values of T such that $\omega_c = (0.85\pi)T$ varies from 0.1π to 0.825π . It is assumed that $n = 20$ when spectrum analysis is performed (although actually $n = 10$). The estimates obtained are presented in Figures 8-3a through 8-3i. Although the results obtained when $\omega_c = \pi/2$ might not be considered the best, each spectral magnitude peak is clearly resolved, which is not the situation for all the values of ω_c considered.

Thus, it appears that spectral resolution may be improved considerably if the autocorrelation sampling period is selected to place the autocorrelation sequence poles in desirable positions from a parameter sensitivity viewpoint. In addition, the results presented here concerning sampling period selection have added importance because of a result presented by Kay [Ref. 8-2]. He suggests that when calculating

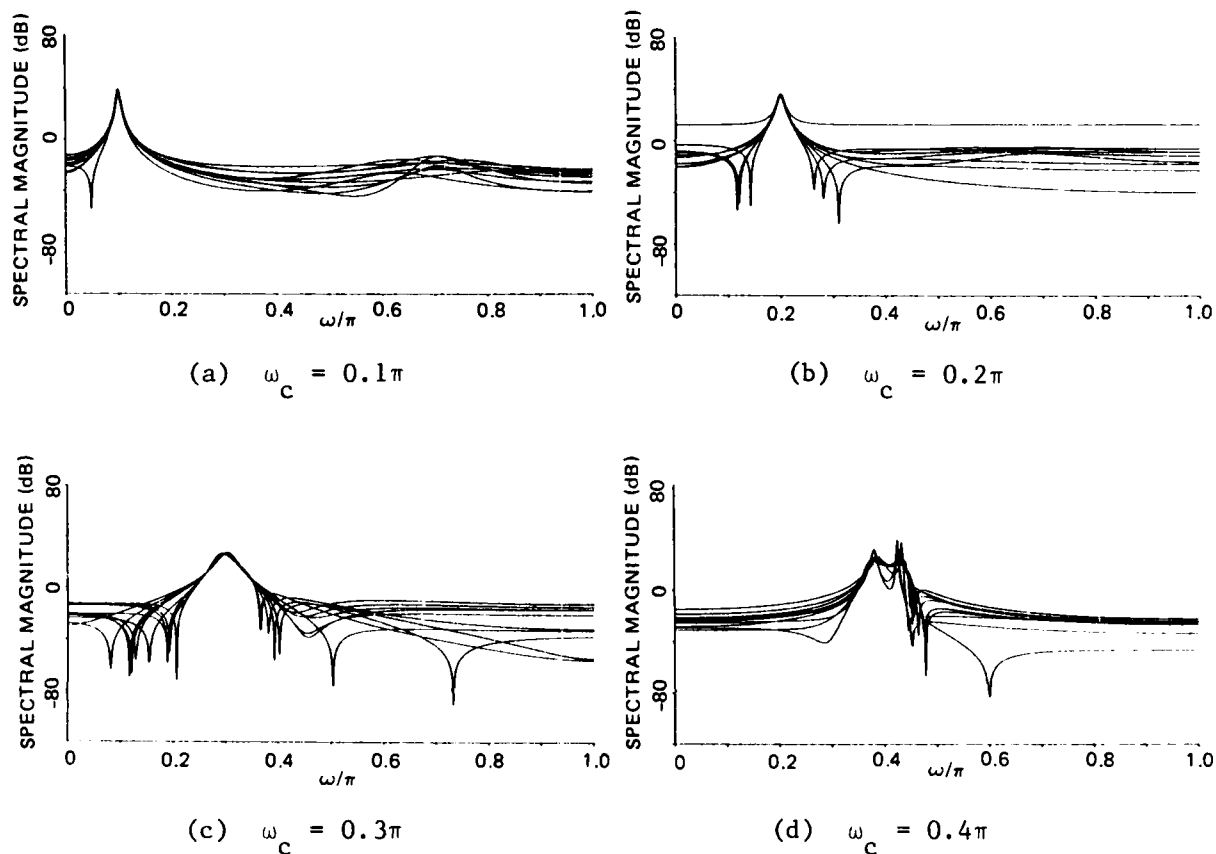
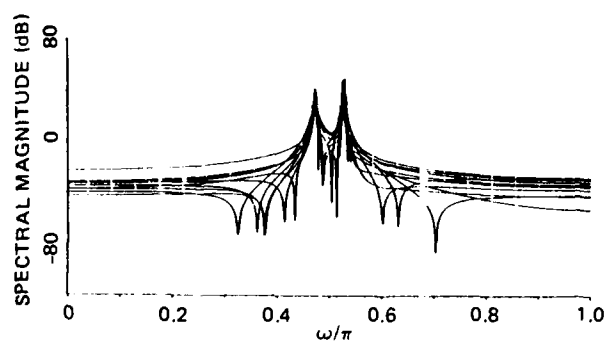
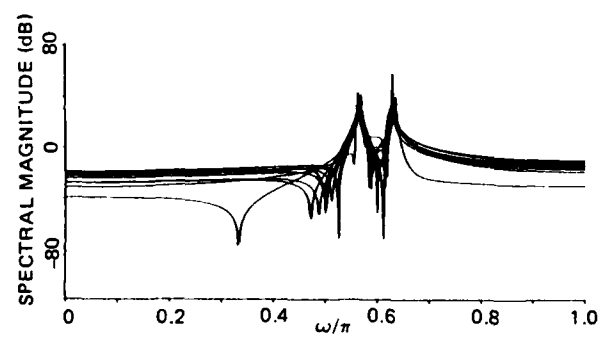


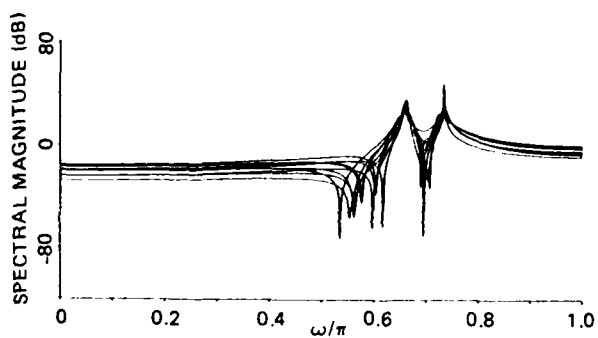
Figure 8-1. Power spectrum estimates for $x_c(t) = \cos(0.9\pi t) + \cos(\pi t)$, with $N_d = 128$, $N = 30$, $\sigma_w^2 = 0.1$, and T chosen so that ω_c varies from 0.1π to 0.9π .



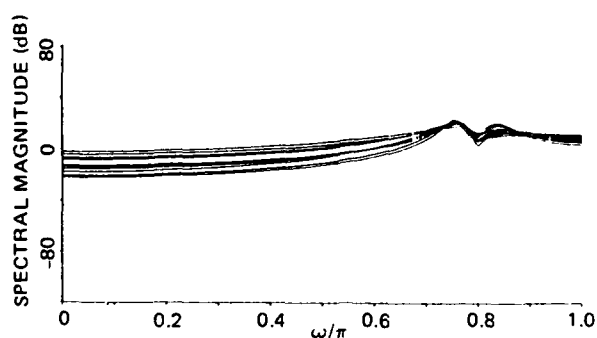
(e) $\omega_c = 0.5\pi$



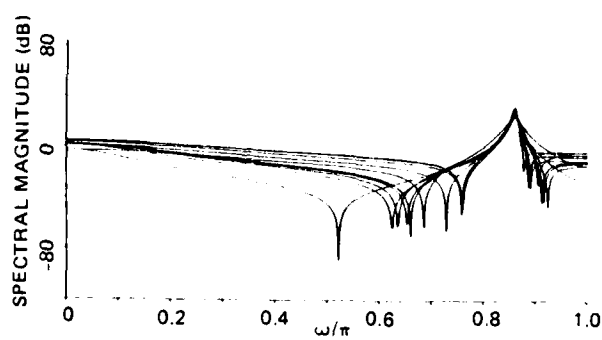
(f) $\omega_c = 0.6\pi$



(g) $\omega_c = 0.7\pi$



(h) $\omega_c = 0.8\pi$



(i) $\omega_c = 0.9\pi$

Figure 8-1 (Continued).

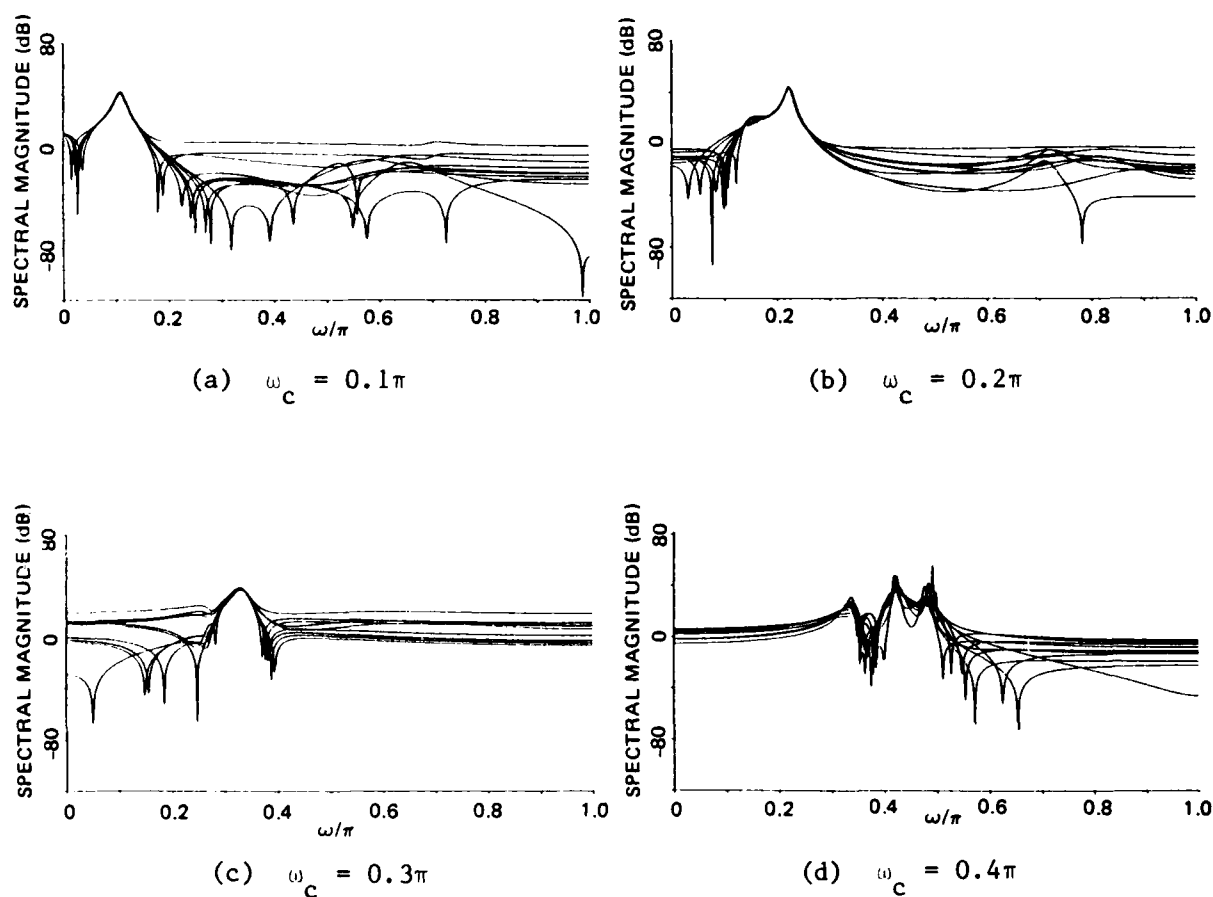
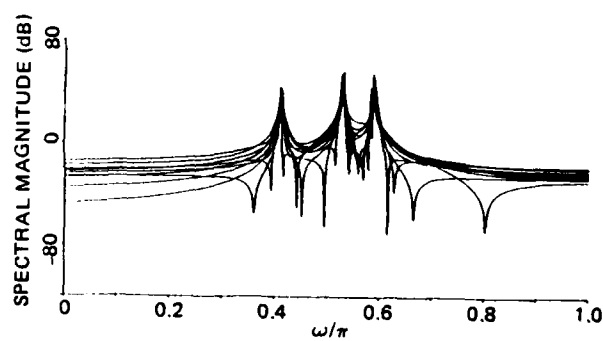
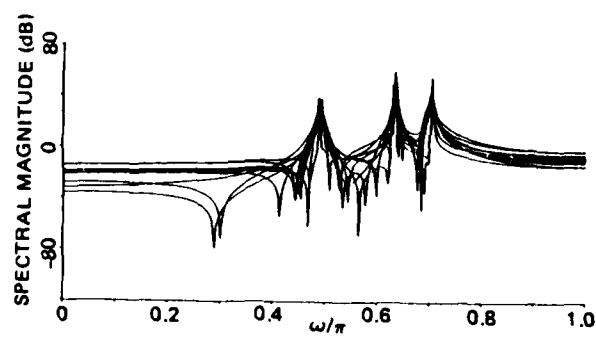


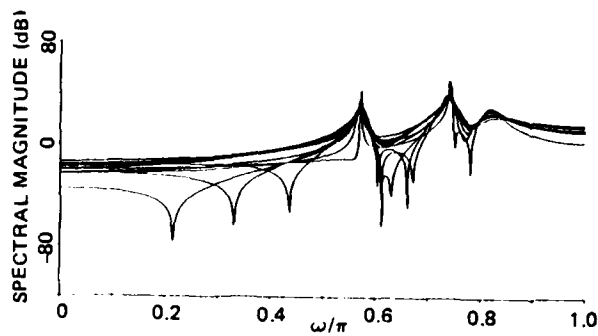
Figure 8-2. Power spectrum estimates for $x_c(t) = \cos(0.7\pi t) + 2\cos(0.9\pi t) + 1.5\cos(\pi t)$, with $N_d = 128$, $N = 30$, $\sigma_w^2 = 0.1$, and T chosen so that ω_c varies from 0.1π to 0.8π .



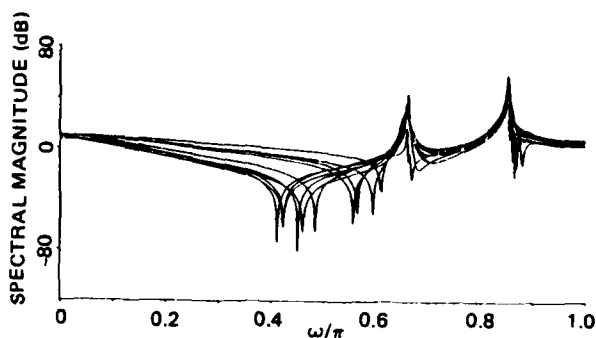
(e) $\omega_c = 0.5\pi$



(f) $\omega_c = 0.6\pi$



(g) $\omega_c = 0.7\pi$



(h) $\omega_c = 0.8\pi$

Figure 8-2 (Continued).

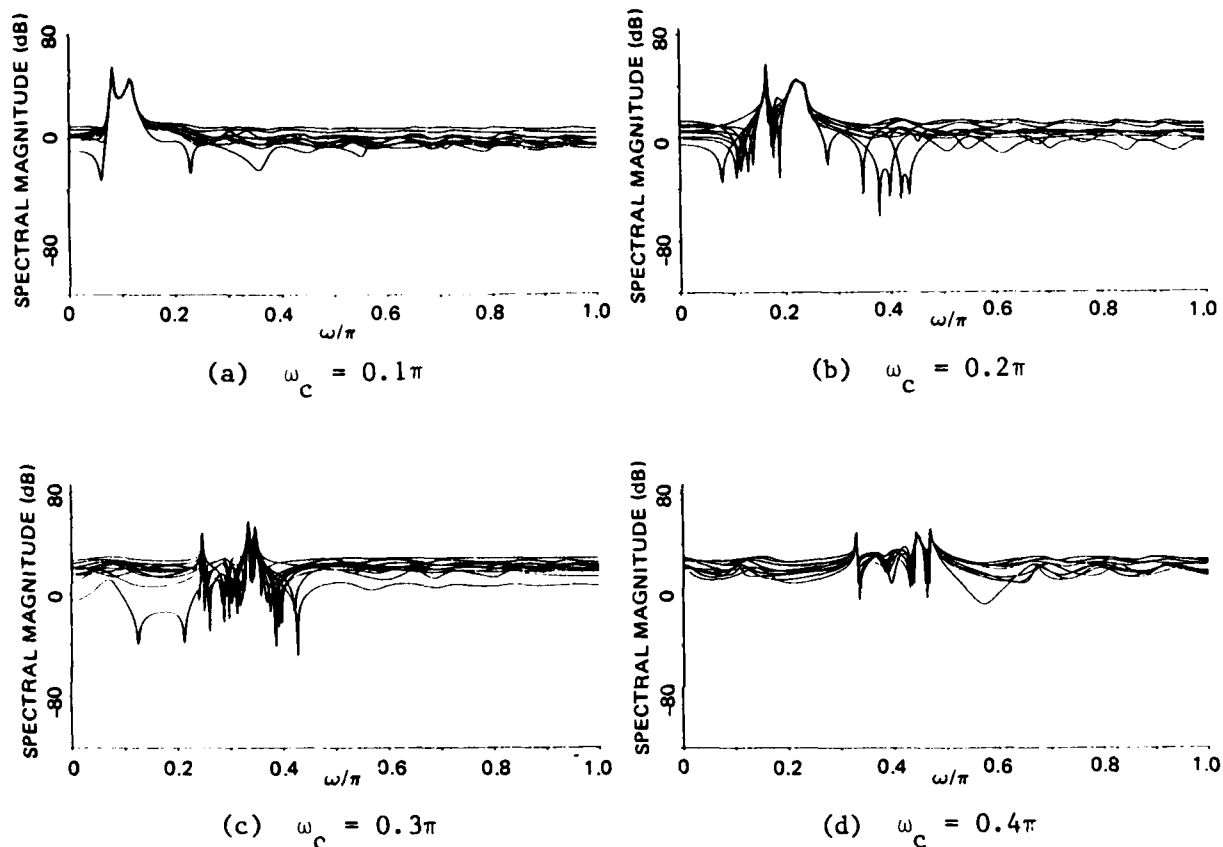
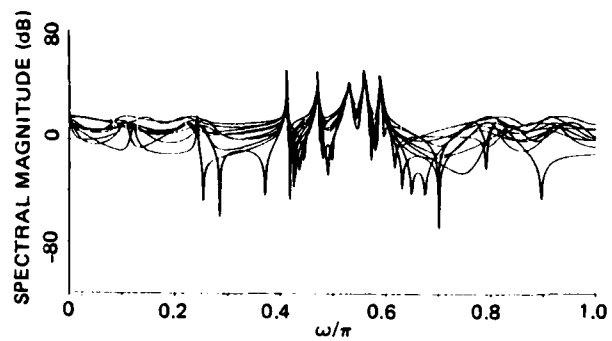
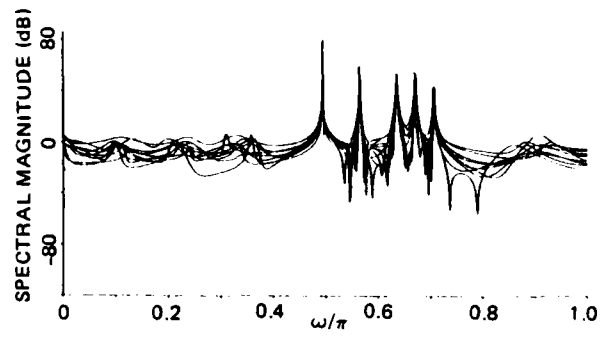


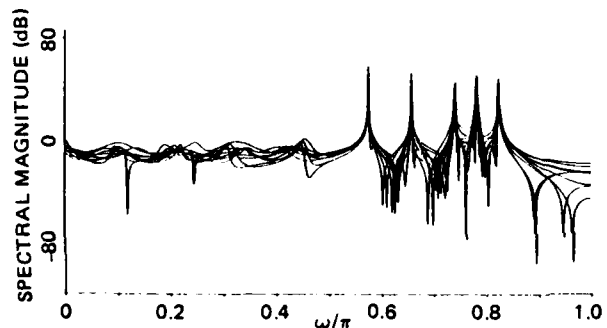
Figure 8-3. Power spectrum estimates for $x_c(t) = 2 \cos(0.7\pi t) + \cos(0.8\pi t) + 1.5 \cos(0.9\pi t) + 2 \cos(0.95\pi t) + 1.5 \cos(\pi t)$, with $N_d = 256$, $N = 100$, $\sigma_w^2 = 0.1$, and T chosen so that ω_c varies from 0.1π to 0.825π ; assume $n = 20$.



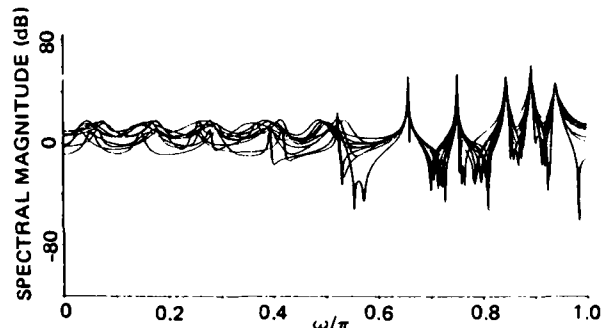
(e) $\omega_c = 0.5\pi$



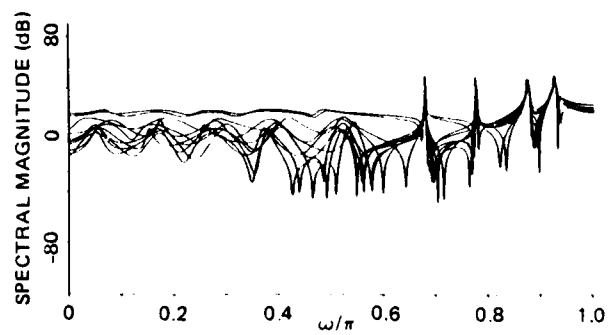
(f) $\omega_c = 0.6\pi$



(g) $\omega_c = 0.7\pi$



(h) $\omega_c = 0.8\pi$



(i) $\omega_c = 0.825\pi$

Figure 8-3 (Continued).

autocorrelation estimates for a Gaussian process, the data should be sampled at least as often as twice the Nyquist rate of the underlying process. Denoting the corresponding sampling period by T_{2N} , autocorrelation estimates would then be available at integer multiples of T_{2N} . Recalling that according to Guideline 2 the autocorrelation sampling period T should be chosen so that $\omega_c = \pi/2$ (assuming $\sigma_1 \approx 0$, $i = 1, \dots, n$), or

$$T = \frac{\pi}{\Omega_1 + \Omega_{n/2}}$$

we see that $T \approx T_{2N}$ when Ω_1 is very close to $\Omega_{n/2}$. Since the set $\{\Omega_1, \dots, \Omega_n\}$ has been ordered such that $0 < \Omega_1 < \Omega_{i+1}$, $i = 1, \dots, n/2$, we note that when the elements of $\{\Omega_1, \dots, \Omega_{n/2}\}$ are tightly clustered (that is, when high resolution is required), setting T according to Guideline 2 will force the data to be sampled at a rate which produces good autocorrelation estimates. Thus, choosing T according to Guideline 2 will yield good autocorrelation estimates, in addition to reducing the sensitivity of spectrum analysis to errors in those estimates.

8.3 The Use of Desampling to Improve Spectral Resolution

The results presented so far concerning proper choices for T are obviously of no help when T is fixed or when a purely discrete-time process is of interest. Even if T is adjustable, it may be necessary to separate the poles further than afforded by constraint Eq. (8-7) to reduce spectrum estimation sensitivity to a reasonable level (see Guideline 1, p. 211 in Reference 8-1). In these circumstances it is necessary to desample the autocorrelation sequence to move the poles to desirable locations.

In Reference 8-1, the subject of desampling was considered in detail, and a modified spectrum estimation procedure based on desampling was constructed. The essence of this procedure is the decomposition of

the autocorrelation sequence $\{r(k)\}$ into the M desampled sequences $\{r_{M,J}(k)\}$: $J = 0, \dots, M-1$ defined by

$$r_{M,J}(k) = r(M|k| + J)$$

The integer M is known as the "desampling interval". Assuming the poles of $\{r(k)\}$ are $\{z_1, \dots, z_n\}$ as in Eq. (8-1), the poles of each desampled sequence $\{r_{M,J}(k)\}$ will be $\{z_1^M, \dots, z_n^M\}$. Thus desampling $\{r(k)\}$ has the effect of relocating each autocorrelation pole in the complex plane:

$$z_i \rightarrow z_i^M, \quad i = 1, \dots, n$$

If $|z_i| \approx 1$, $i = 1, \dots, n$ and the desampling interval M is chosen to place the poles of the desampled autocorrelation sequences in desirable locations according to Guidelines 1 and 2 of Reference 8-1, then we might suspect that spectrum analysis of the desampled sequences $\{r_{M,J}(k)\}$: $J = 0, \dots, M-1$ would provide higher quality results than spectrum analysis of the sequence $\{r(k)\}$ as a whole. The modified spectrum estimation procedure in Section 7.4 of Reference 8-1 exploits this idea by estimating the parameters $\{A_1, \dots, A_n\}$ and $\{z_1, \dots, z_n\}$ of $\{r(k)\}$ by first estimating the corresponding parameters of the desampled sequences.

The improved resolution obtainable by the modified procedure when the desampling interval M is chosen based on consideration of Guidelines 1 and 2 is demonstrated here via three examples. In all three examples the power spectrum of a discrete-time process $\{x(k)\}$ is estimated, with the required autocorrelation estimates being obtained from the data sequence $\{y(k) = x(k) + w(k), k = 0, \dots, N_d - 1\}$ where $\{w(k)\}$ is a Gaussian, zero mean, white noise sequence with variance σ_w^2 . The autocorrelation estimator used is defined by Eq. (8-8). Note that in light

of Eq. (8-9), the first equation in Eq. (7-33) of Reference 8-1 as well as the first and $(N + 1)$ st equations of Eq. (7-18) of Reference 8-1 are deleted prior to obtaining $\{\hat{a}_{M,1}, \dots, \hat{a}_{M,n}\}$ (the autoregressive coefficient estimates for the desampled sequences) and $\{\hat{A}_1, \dots, \hat{A}_n\}$ for the examples which follow.

The first example demonstrates the benefit of choosing M according to Guideline 2. We have $N_d = 256$, $N = 100$, $\sigma_w^2 = 0.1$, and

$$x(k) = 2 \cos(0.09474\pi k) + 2 \cos(0.10530\pi k)$$

Figures 8-4a through 8-4i contain the results of spectrum estimation for different values of M . Each figure contains ten spectrum estimates with each corresponding to a different realization of the noise process $\{w(k)\}$. A diagram is included with each figure to indicate the locations of the poles of $\{r_{M,j}(k)\}$. Noting that Guideline 2 implies that M should be chosen so that the poles of $\{r_{M,j}(k)\}$ are "centered" around the imaginary axis, we see that choosing M in this manner yields good results.

The second example considers the case where the poles of $\{r(k)\}$ are already centered around the imaginary axis, but nevertheless are too close to be resolved (see Guideline 1). For situations such as this, desampling may be used to increase the angular separation of the poles while keeping them centered around the imaginary axis. For this example we have $N_d = 512$, $N = 400$, $\sigma_w^2 = 1$, and

$$x(k) = 2 \cos(0.49\pi k) + 2 \cos(0.5\pi k) + \cos(0.51\pi k)$$

Figures 8-5a through 8-5d contain the results of spectrum estimation when $M = 1, 13, 23$, and 33 , respectively. It can easily be seen that increasing the angular separation of the closely spaced poles via desampling improves resolution considerably.

Up to this point, all analysis and examples have dealt with cases where the poles of $\{r(k)\}$ are on the unit circle. The final example demonstrates the applicability of the results of this report and of Reference 8-1 to those cases where the poles are slightly inside the unit circle. In particular, the process $\{x(k)\}$ is generated by driving a filter of impulse response

$$h(k) = 0.99^k \cos(0.23\pi k) u(k) \\ + 2(0.99^k) \cos(0.27\pi k) u(k) \quad , \quad -\infty < k < +\infty$$

with a Gaussian, zero mean, white noise process $\{v(k)\}$ of variance $\sigma_v^2 = 1$ ($\{u(k)\}$ is the unit step sequence). The power spectrum of $\{x(k)\}$ is plotted in Figure 8-6. Spectrum estimates are calculated for various values of M , and for $N_d = 512$, $N = 200$, and $\sigma_w^2 = 1$. Figures 8-7a through 8-7d contain the results of spectrum estimation, with the ten estimates in each figure corresponding to different realizations of the noise processes $\{w(k)\}$ and $\{v(k)\}$. As implied by Guideline 2, resolution improves when M is chosen so that the poles of $\{r_{M,J}(k)\}$ are centered around the imaginary axis (see Figures 8-7a and 8-7b). When M is increased further to increase the separation of the closely spaced poles, small improvements in the spectrum estimates are evident (see Figures 8-7c and 8-7d) as implied by Guideline 1.

8.4 Conclusion

The results of this section together with Reference 8-1 represent a new approach to the problem of improving spectral resolution. Specifically, a procedure for obtaining spectrum estimates from autocorrelation sequence estimates is analyzed to determine its sensitivity to errors in the autocorrelation estimates. The results of this analysis clearly demonstrate that the locations of the autocorrelation poles in the complex plane have a significant effect on the error sensitivity of the

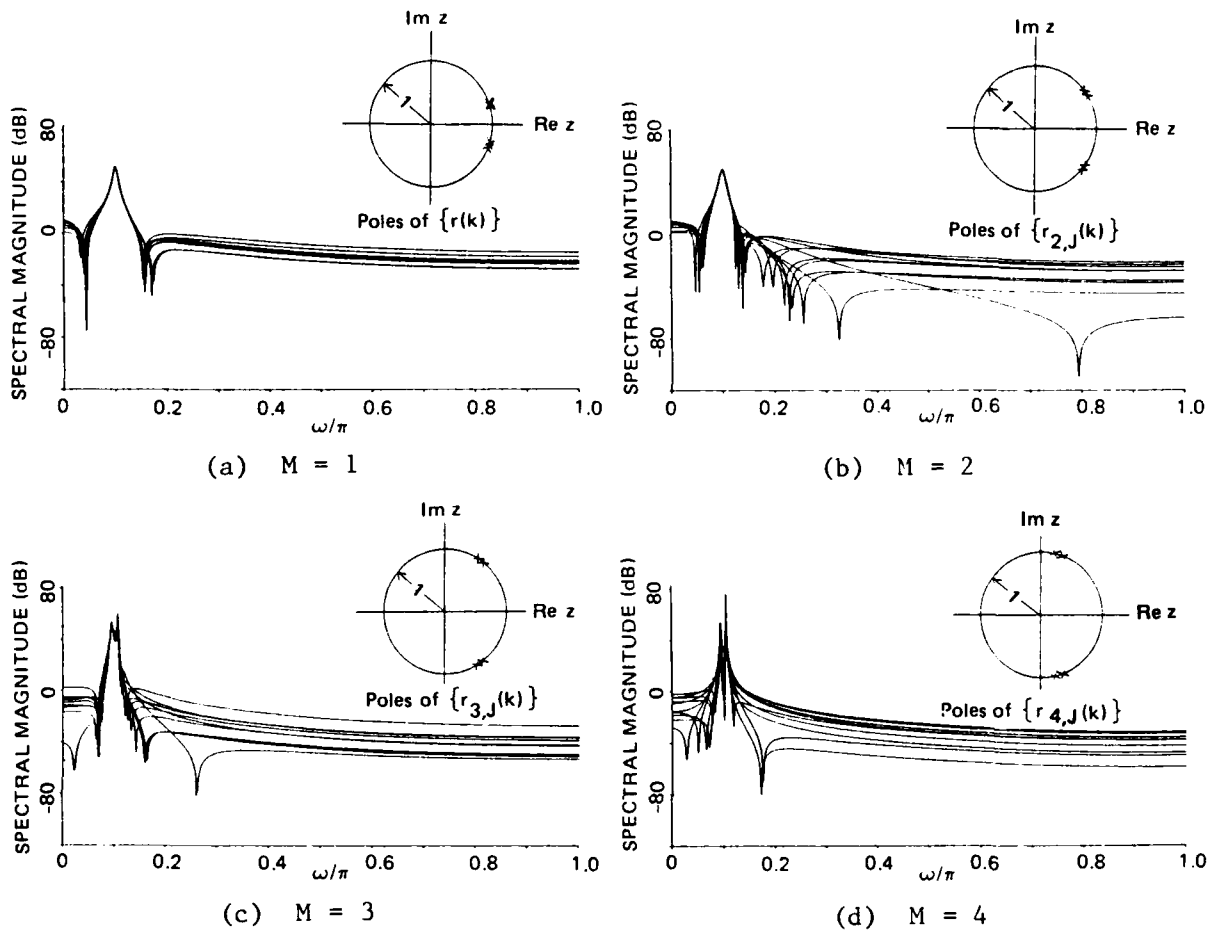
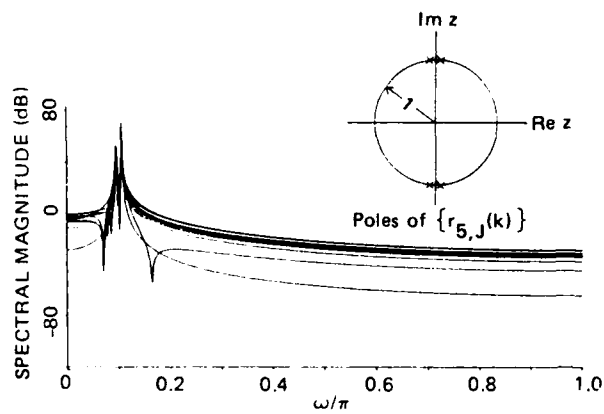
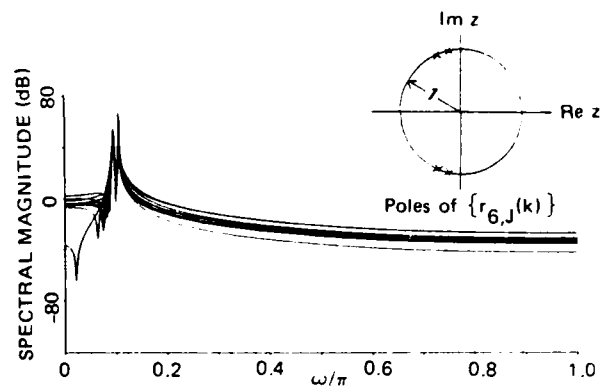


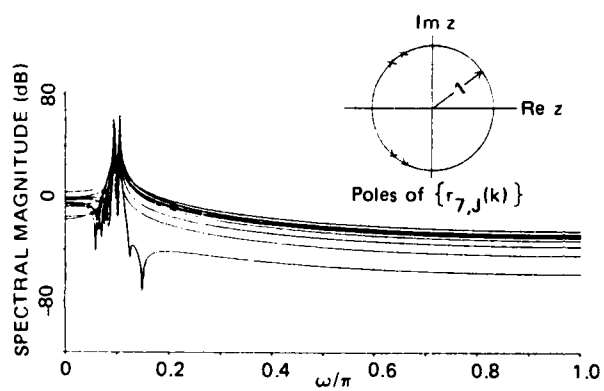
Figure 8-4. Power spectrum estimates for $x(k) = 2 \cos(0.09474 \pi k) + 2 \cos(0.10530 \pi k)$, with $N_d = 256$, $N = 100$, $\sigma_w^2 = 0.1$, and M varied from 1 to 9.



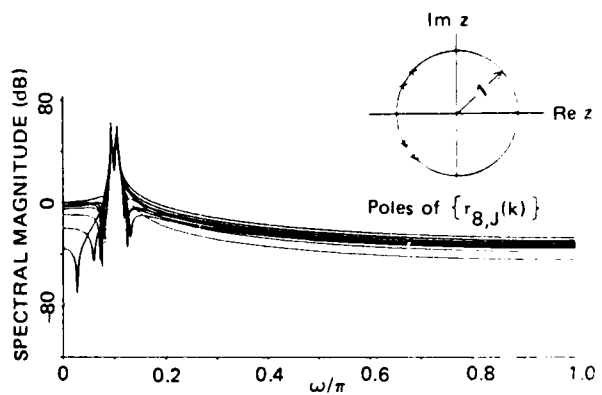
(e) $M = 5$



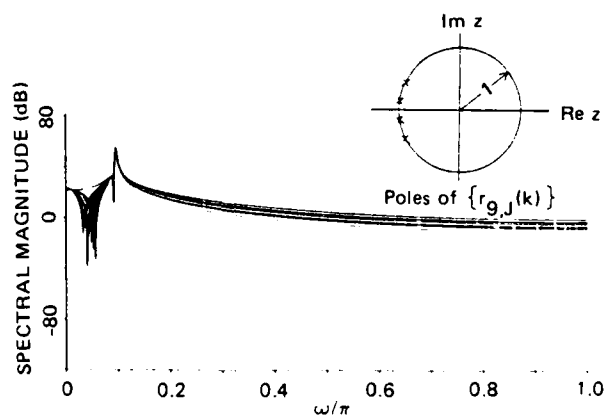
(f) $M = 6$



(g) $M = 7$



(h) $M = 8$



(i) $M = 9$

Figure 8-4 (Continued).

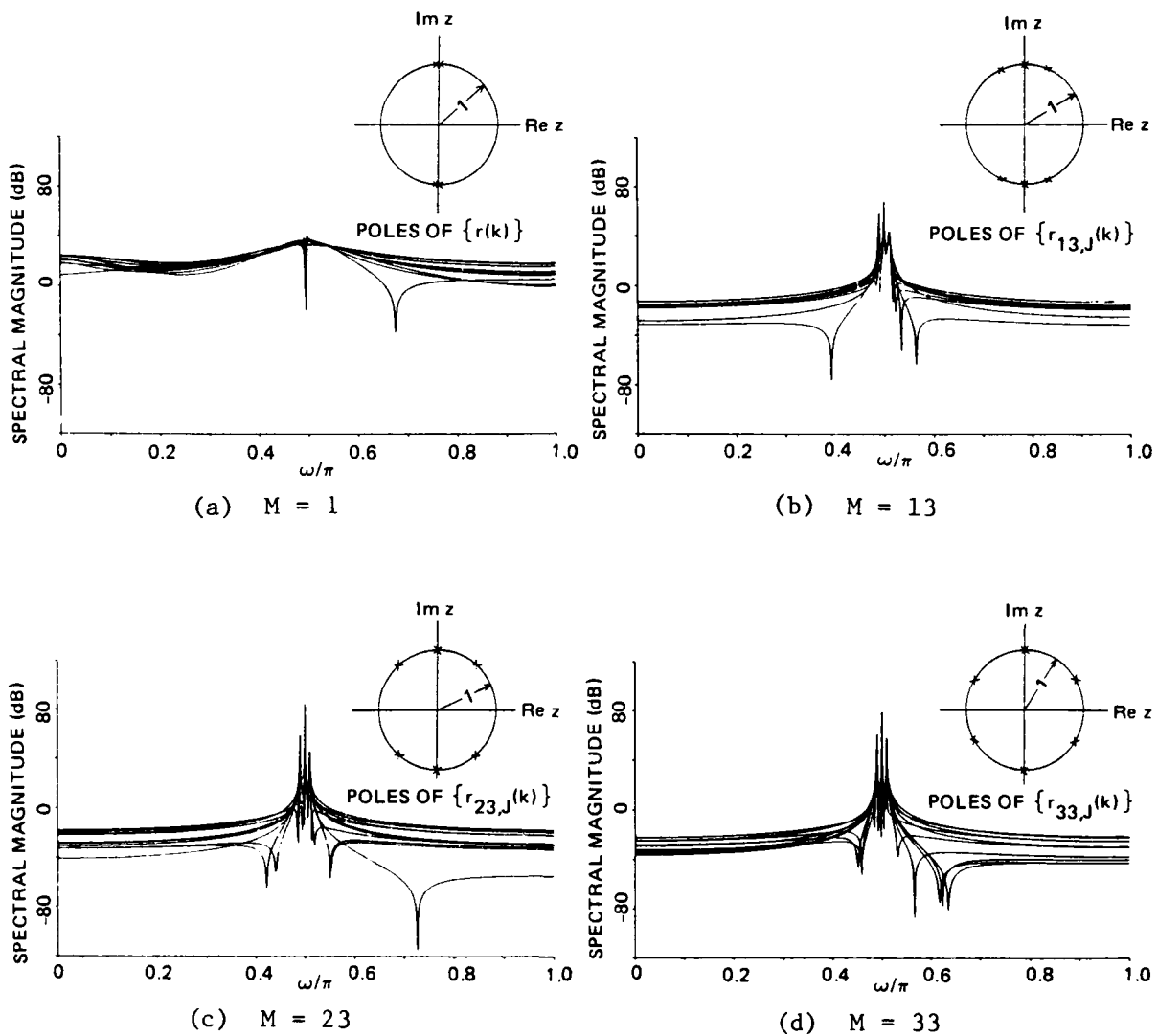


Figure 8-5. Power spectrum estimates for $x(k) = 2 \cos(0.49 \pi k) + 2 \cos(0.5 \pi k) + \cos(0.51 \pi k)$, with $N_d = 512$, $N = 400$, $\sigma_w^2 = 1$, and M varied from 1 to 33.

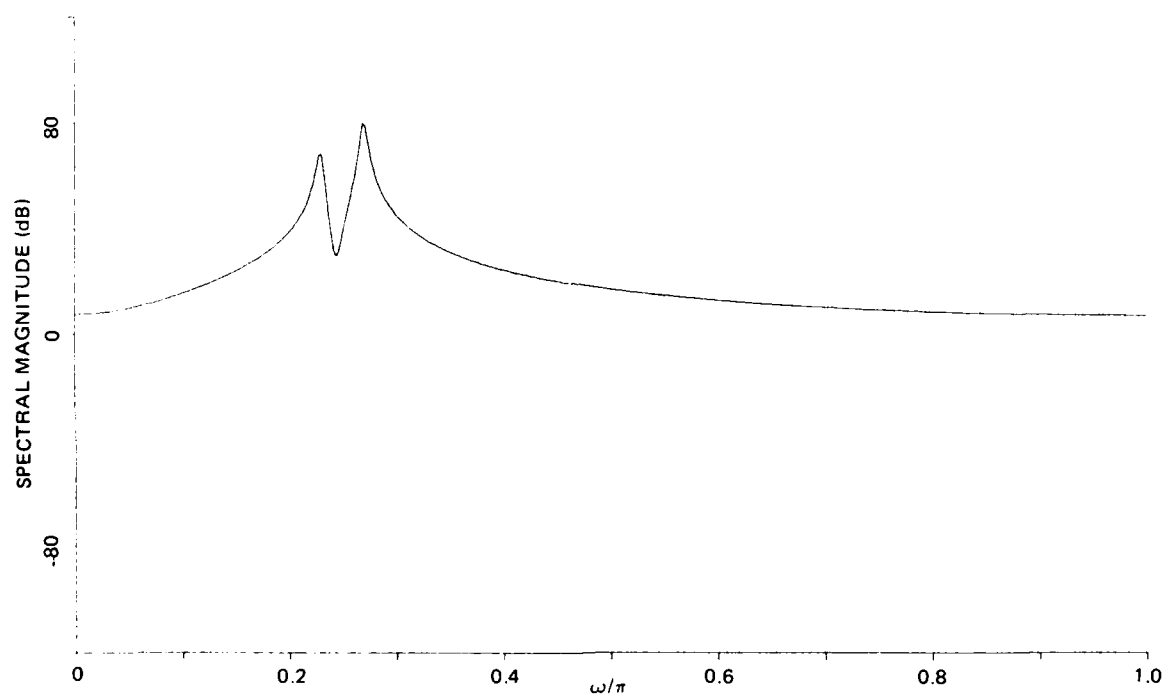


Figure 8-6. Power spectrum of process obtained driving a filter of impulse response $h(k) = 0.99^k \cos(0.23 \pi k) u(k) + (2)(0.99^k) \cos(0.27 \pi k) u(k)$ with white noise.

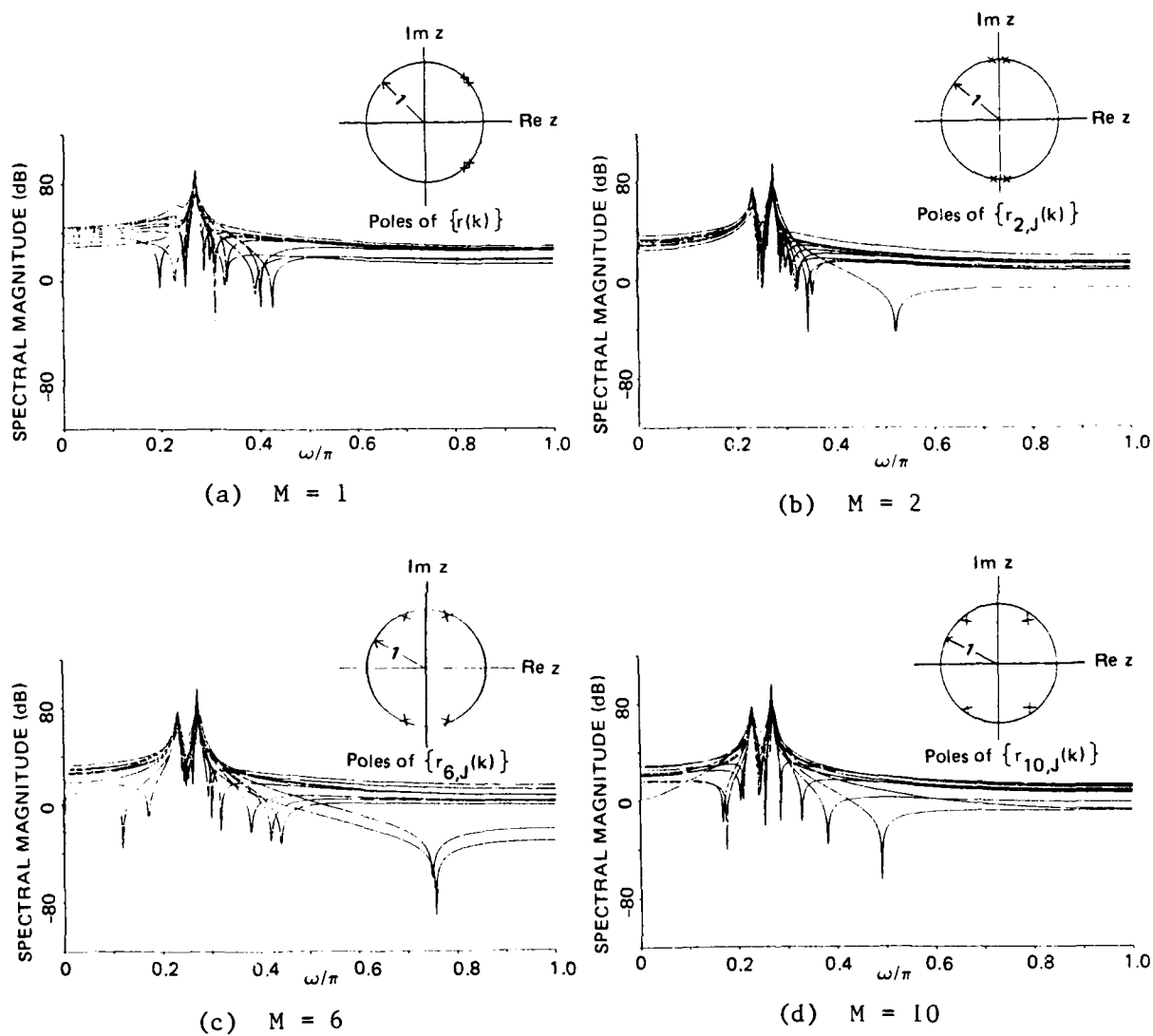


Figure 8-7. Power spectrum estimates of a process obtained by driving a filter of impulse response $h(k) = 0.99^k \cos(0.23 \pi k) u(k) + (2)(0.99^k \cos(0.27 \pi k) u(k))$ with unity variance, zero-mean, Gaussian white noise. Also, $N_d = 512$, $N = 200$, and $\sigma_w^2 = 1$.

spectrum analysis procedure. Specifically, it appears that error sensitivity becomes a particularly acute problem when poles are closely spaced, thus indicating the difficulty encountered when high resolution spectrum estimates are sought.

As a remedy for this problem, a modified spectrum estimation procedure is proposed which employs autocorrelation desampling as a means of artificially separating closely spaced poles, thus relieving the error sensitivity problem. The unique features of this procedure are that it employs all available autocorrelation estimates, and that the size of the desampling interval used is not bounded by spectral aliasing considerations (see Eq. (7-36) of Reference 8-1). The improved resolution obtained by this modified procedure is demonstrated via numerical examples.

Also addressed in this report is the selection of autocorrelation sampling periods when discrete-time techniques are used to estimate the spectra of continuous-time processes. It is demonstrated that if the sampling period is chosen to "center" the poles of the sequence obtained by sampling the continuous-time autocorrelation function around the imaginary axis, then spectral resolution can be improved substantially.

Thus, by posing the spectral resolution problem as one of decreasing error sensitivity, we have observed that resolution can be considerably improved by placing the poles of the autocorrelation sequence in desirable locations either by desampling or by making an appropriate choice for the autocorrelation sampling period. Since appropriate choices for desampling intervals and sampling periods may be obtained easily with knowledge only of approximate pole locations, these results should prove to be quite valuable in situations requiring high resolution power spectrum estimates.

References

- 8-1. Villalba, M. J., "On the Use of Autocorrelation Desampling in High Resolution Spectrum Estimation," ACROSS-Eleven Fifth Semiannual Technical Report, CSDL-R-1687, Charles Stark Draper Laboratory, Cambridge, MA, March 1984; Section 7.
- 8-2. Kay, S. M., "The Effect of Sampling Rate on Autocorrelation Estimation," IEEE Trans. Acoustics, Speech, and Signal Processing, Vol. ASSP-29, No. 4, Aug. 1981, pp. 859-867.

SECTION 9

APPROXIMATION TECHNIQUES FOR PARAMETER ESTIMATION AND FEEDBACK CONTROL WITH DISTRIBUTED MODELS OF LARGE FLEXIBLE STRUCTURES

9.1 Introduction

In this section we discuss some approximation techniques that may be used in algorithms for parameter estimation and/or feedback control in distributed models such as those arising in models typical of large flexible space structures. The focus of our recent efforts has been the development and analysis of computational algorithms, e.g., convergence analysis, numerical implementation (software development) and testing. While the ideas involved are also applicable to the computation of feedback controls, we restrict our discussions here to some of our efforts on techniques in the context of parameter estimation or "inverse" problems: given observations of a system, determine parameters in models which best describe structural/material properties manifested by the system in response to perturbations (e.g., loading).

The importance of such problems is twofold: (i) parameter estimation can be viewed as a primary tool in on-orbit model development and analysis where one seeks to understand elastic/viscoelastic material properties (e.g., damping or stiffness) and to detect changes in these properties (e.g., due to aging or prolonged stress); (ii) parameter estimation is a precursor to and an integral part of development of sophisticated feedback control laws (via feedback operators satisfying infinite-dimensional Riccati equations involving functional parameters of the system).

Many of the structures of interest to aerospace engineers entail systems composed of composite materials in rather complex geometric/structural configurations. The need for methods to investigate such variable-structure distributed models has, in our opinion, been clearly established in a number of recent efforts including References 9-1 through 9-4. A number of investigations of parameter estimation in models for elastic beams has involved approximation results (the Trotter-Kato theorem) from linear semigroup theory. In particular, problems for simple beams have been treated in this manner in References 9-5 through 9-9. In Reference 9-10 the Trotter-Kato ideas are employed to establish results for hybrid models similar to those introduced later in this section and which are important in the study of shuttle-deployed payloads. However, in some instances it is advantageous to use an alternate approach involving a variational (weak) formulation of the system equations along with estimates in the spirit of those found in numerous papers on finite-element techniques in structural problems. In Reference 9-11 such a treatment was given for damped cantilevered Euler-Bernoulli beams. In this section we outline this approach in the context of models for the transverse vibration of flexible beams with attached tip bodies and base acceleration.

Fundamental to our discussions is a conceptual framework in which one has a dynamical model of the physical system with "states" $u(t,x)$, $0 \leq t \leq T$, $x \in \Omega$, and "parameters" $q(t,x)$, $q \in Q$, where Q is an admissible class of parameter functions. The equations of motion for the type of problem considered generally take the form of a hybrid system of coupled partial (governing the vibration of the beam) and ordinary (describing the motion of the tip bodies) differential equations with appropriate geometric boundary conditions and initial data. The identification problem is formulated as follows. One is given observations (data) \bar{u}_{ij} for $u(t_i, x_j)$ and seeks to solve the optimization problem of finding--in the feasible parameter set Q --parameters \bar{q} which give a best (in the least-squares sense) fit of the model to the data. By

feasible we mean of course that throughout the optimization, the "states" and "parameters" must jointly satisfy the dynamic constraints (i.e., the hybrid system of equations describing the motion of the beam and tip bodies). The resulting identification problems therefore, tend to have infinite-dimensional constraints. Moreover, if the parameters to be identified are functional (e.g., spatially varying stiffness and/or linear mass density; temporally and/or spatially varying loads), the admissible parameter space is a function space and as such is infinite-dimensional as well. The solution of the resulting constrained optimization problem, therefore, necessitates the use of some form of finite-dimensional approximation. We formulate this problem in an abstract setting with Hilbert state space V and parameter space Q . For computational purposes we then approximate V and Q by finite-dimensional spaces V^N and Q^M respectively. We illustrate these ideas with a specific model and particular classes of approximations in our subsequent discussions.

The scheme we develop here is based upon the reformulation of the equations of motion in weak form. A cubic spline based Rayleigh-Ritz-Galerkin method is used to define a finite-dimensional approximation to the state equations. Using finite-dimensional subspaces to discretize the admissible parameter space, we obtain a doubly-indexed sequence of approximating finite-dimensional identification problems. Using standard variational arguments, we derive a convergence result for the state approximations. We show next that each of the approximating identification problems admits a solution and that from the resulting sequence of optimal parameter values a convergent subsequence can be extracted, the limit of which is a solution to the original infinite-dimensional identification problem. The approximating identification problems can be solved using standard techniques and readily available software. Numerical results which demonstrate the feasibility of our method are provided for a variety of examples.

The approach described in this section represents a significant improvement over the method developed in Reference 9-10. Indeed, we have developed a scheme which is computationally simpler and, by relaxing the necessary hypotheses on the admissible parameter space (i.e., with regard to the smoothness requirements on the spatially-varying stiffness and linear mass density of the beam), is applicable to a wider class of problems. Our results are similar in spirit to those presented in Reference 9-12 in the context of parabolic systems, in Reference 9-13 for hyperbolic systems, and in Reference 9-11 for beam equations with standard boundary conditions (e.g., clamped, simply supported, cantilevered).

We simplify our presentation by considering a cantilevered beam with an attached tip (point) mass. As is discussed in Section 9.4, however, our general approach is applicable to a broad class of beam/tip-body vibration problems. In Section 9.2 we derive the weak form of the equations of motion, define weak and strong solutions and formulate the identification problem. In Section 9.3 we define the approximation scheme and discuss convergence. Numerical results are presented in Section 9.4.

We employ standard notation throughout. The Sobolev spaces of real-valued functions on the closed interval $[a,b]$ whose k -th derivatives are L_2 (i.e., Lebesgue-measurable and square-integrable) are denoted by $H^k(a,b)$, $k = 0,1,2,\dots$. The corresponding Sobolev inner products and their induced norms on the spaces $H^k(a,b)$ are denoted by $\langle \cdot, \cdot \rangle_k$ and $\|\cdot\|_k$, respectively. For Z a normed linear space with norm $\|\cdot\|_Z$ and given a map $f: [0,T] \rightarrow Z$, we say that $f \in L^2([0,T], Z)$ if $\int_0^T \|f(t)\|_Z^2 dt < +\infty$. Similarly, f is said to be an element in $C^l([0,T], Z)$ if the map $t \rightarrow f(t)$ from $[0,T]$ into Z is l times continuously differentiable on the open interval $(0,T)$. Finally, for a function of one or more real variables, the symbol $D_\theta f$ ($D_\theta^k f$) will be used to denote the 1st (k -th) derivative of f with respect to the independent variable θ . If f is a function of a single variable only, the subscript

may be deleted. On occasion the short-hand notation $D_{\theta}f(\theta_0)$ or $Df(\theta_0)$ will be used in place of $D_{\theta}f \big|_{\theta_0}$ or $Df \big|_{\theta_0}$ to denote the derivative of f evaluated at θ_0 .

9.2 The Identification Problem

9.2.1 A Distributed Parameter Model

We consider a long slender beam of length ℓ with spatially varying stiffness EI and linear mass density ρ which is clamped at one end and free at the other end with an attached tip mass of magnitude m (see Figure 9-1).

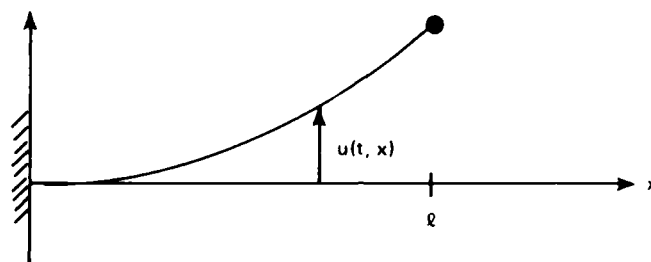


Figure 9-1. Clamped beam with tip mass; deformed.

Using the Euler-Bernoulli theory to describe the transverse vibrations of the beam, we obtain the partial differential equation [Refs. 9-14, 9-15]

$$\rho(x)D_t^2 u(t, x) + D_x^2 (EI(x) D_x^2 u(t, x)) = D_x (\sigma(t, x) D_x u(t, x)) + f(t, x), \quad (9-1)$$

$$x \in (0, \ell), \quad t \in (0, T)$$

for the transverse displacement u , where σ denotes the internal tension (as a result of axial loading), and f is the net externally-applied transverse or lateral load. Use of the principles of elementary

Newtonian mechanics (i.e., force and moment balance equations) yields the boundary conditions at the free end. From translational equilibrium in the in-plane direction transverse to the beam, we have

$$mD_t^2 u(t, \ell) - D_x(EI(\ell) D_x^2 u(t, \ell)) = -\sigma(t, \ell) D_x u(t, \ell) + g(t) \quad , \quad t \in (0, T) \quad (9-2)$$

where g is the net external force (directed transversely) on the tip mass. In a similar manner, requiring rotational equilibrium about an axis normal to the plane of Fig. 9-1, we have

$$D_x^2 u(t, \ell) = 0 \quad , \quad t \in (0, T) \quad (9-3)$$

The geometric boundary conditions (zero displacement and zero slope) at the clamped end are given by

$$u(t, 0) = 0 \quad , \quad t \in (0, T) \quad (9-4a)$$

and

$$D_x u(t, 0) = 0 \quad , \quad t \in (0, T) \quad (9-4b)$$

respectively. The initial conditions are in the form of initial displacement

$$u(0, x) = \phi(x), \quad x \in [0, \ell] \quad (9-5a)$$

and initial velocity

$$D_t u(0, x) = \psi(x), \quad x \in [0, \ell] \quad (9-5b)$$

In order to characterize solutions to the hybrid system Eqs. (9-1) through (9-5) of ordinary and partial differential equations together

with boundary and initial conditions, we formally represent it as an abstract second-order system. We make the standing assumptions that $m > 0$, $EI, \rho \in L_\infty(0, \ell)$ with $EI, \rho > 0$, $\sigma \in L_2([0, T], H^1(0, \ell))$, $g \in L_2(0, T)$, $f \in L_2([0, T], H^0(0, T))$, $\phi \in H^2(0, \ell)$, and $\psi \in H^0(0, \ell)$ with $\psi(\ell)$ specified in R (the set of all real numbers). Define the Hilbert space $H \triangleq R \times H^0(0, \ell)$ with inner product

$$\langle (\eta, \phi), (\zeta, \psi) \rangle_H \triangleq \eta \zeta + \langle \phi, \psi \rangle_0$$

We then rewrite Eqs. (9-1) through (9-5) as

$$M_0 D_t^2 \hat{u}(t) + A_0 \hat{u}(t) = B_0(t) \hat{u}(t) + F_0(t), \quad t \in (0, T) \quad (9-6)$$

$$\gamma_0 \hat{u}(t) \Big|_{x=0} = 0, \quad \gamma_1 \hat{u}(t) \Big|_{x=0} = 0, \quad \gamma_2 \hat{u}(t) \Big|_{x=\ell} = 0, \quad t \in [0, T] \quad (9-7)$$

$$\hat{u}(0) = \hat{\phi}, \quad D_t \hat{u}(0) = \hat{\psi} \quad (9-8)$$

where $\hat{u}(t) \equiv (u(t, \ell), u(t, \cdot)) \in H$, $F_0(t) \equiv (g(t), f(t, \cdot))$, $\hat{\phi} \equiv (\phi(\ell), \phi)$, $\hat{\psi} \equiv (\psi(\ell), \psi)$ and the operators M_0 , A_0 , $B_0(t)$ and γ_i , $i = 0, 1, 2$ on H are defined formally by

$$M_0(\eta, \phi) \triangleq (m\eta, \rho\phi)$$

$$A_0(\eta, \phi) \triangleq (-D(EI(\ell) D^2 \phi(\ell)), D^2(EI D^2 \phi))$$

$$B_0(t)(\eta, \phi) \triangleq (-\sigma(t, \ell) D\phi(\ell), D(\sigma D\phi))$$

$$\gamma_i(\eta, \phi) \triangleq D^i \phi, \quad i = 0, 1, 2$$

respectively.

There exist several ways in which the notion of a solution to the system Eqs. (9-6) through (9-8) can be made precise. Of particular interest to us here are the ideas of a weak or variational solution and a strong solution.

9.2.2 Weak Solutions

Define the Hilbert space $\{V, \langle \cdot, \cdot \rangle_V\}$ by

$$V \triangleq \{(\eta, \phi) \in H: \phi \in H^2(0, \ell), \phi(0) = D\phi(0) = 0, \eta = \phi(\ell)\}$$

$$\langle (\phi(\ell), \phi), (\psi(\ell), \psi) \rangle_V \triangleq \langle D^2\phi, D^2\psi \rangle_0$$

It is not difficult to show that V can be densely embedded in H . Choosing H as our pivot space, we have therefore the continuous embeddings $V \subset H \subset V'$, where V' denotes the space of continuous linear functionals on V . We now rewrite Eqs. (9-6) through (9-8) in variational form as the second-order initial value problem

$$\langle M_0 D_t^2 \hat{u}(t), \hat{\theta} \rangle_H + a(\hat{u}(t), \hat{\theta}) = b(t)(\hat{u}(t), \hat{\theta}) + \langle F_0(t), \hat{\theta} \rangle_H, \quad (9-9)$$

$$\hat{\theta} \in V, t \in (0, T)$$

$$\hat{u}(0) = \hat{\phi}, \quad D_t \hat{u}(0) = \hat{\psi} \quad (9-10)$$

where $\hat{\theta} \equiv (\theta(\ell), \theta)$ and the bilinear forms $a: V \times V \rightarrow \mathbb{R}$ and $b(t): V \times V \rightarrow \mathbb{R}$ are given by

$$a(\hat{\phi}, \hat{\psi}) \triangleq \langle EI D^2\phi, D^2\psi \rangle_0$$

and

$$b(t)(\hat{\phi}, \hat{\psi}) \stackrel{\Delta}{=} \langle -\sigma D\phi, D\psi \rangle_0$$

respectively. A solution \hat{u} to Eqs. (9-9) and (9-10) with $\hat{u}(t) \in V$ is known as a weak or variational solution to Eqs. (9-6) through (9-8). Indeed, if the derivatives in Eqs. (9-6) and (9-7) are taken in the distributional sense [Ref. 9-16], A_0 and $B_0(t)$ become bounded linear operators from V into V' with

$$\langle A_0 \hat{\phi}, \hat{\psi} \rangle_H = a(\hat{\phi}, \hat{\psi})$$

and

$$\langle B_0(t) \hat{\phi}, \hat{\psi} \rangle_H = b(t)(\hat{\phi}, \hat{\psi})$$

where the H -inner-product is interpreted as its natural extension to the duality pairing between V and V' [Refs. 9-17, 9-18, 9-19]. Since $F_0(T) \in H \subset V'$ we have therefore that the systems Eqs. (9-6), (9-7), (9-8) and Eqs. (9-9), (9-10) are two representations for the same initial value problem in V' .

Under the standing assumptions which we have made above, standard arguments [Refs. 9-20, 9-21] can be used to demonstrate the existence of a unique solution \hat{u} to Eqs. (9-9), (9-10) with $\hat{u} \in C([0, T], H)$, $D_t \hat{u} \in C([0, T], H)$ and $D_t^2 \hat{u} \in L_2([0, T], V')$.

9.2.3 Strong Solutions

In order to characterize strong solutions we rewrite Eqs. (9-6) through (9-8) as an equivalent abstract first order system and then rely upon the theory of semigroups and evolution operators. Define $Z \stackrel{\Delta}{=} V \times H$ with inner product defined by

$$\langle (\hat{v}_1, \hat{h}_1), (\hat{v}_2, \hat{h}_2) \rangle_Z \stackrel{\Delta}{=} a(\hat{v}_1, \hat{v}_2) + \langle M_0 \hat{h}_1, \hat{h}_2 \rangle_H$$

We assume that $EI \in H^2(0, \ell)$ and $\sigma \in C^1([0, T], H^1(0, \ell))$ and define the operator $A: \text{Dom}(A) \subset Z \rightarrow Z$ by

$$\text{Dom}(A) \stackrel{\Delta}{=} \text{Dom}(A_0) \times V$$

$$A \stackrel{\Delta}{=} \begin{bmatrix} 0 & I \\ -M_0^{-1}A_0 & 0 \end{bmatrix}$$

where I is the identity on V , M_0 and A_0 are as they were defined above, and

$$\text{Dom}(A_0) = \{\hat{\phi} \equiv (\phi(\ell), \phi) \in V: \phi \in H^4(0, \ell), D^2\phi(\ell) = 0\}$$

Similarly, define the operators $B(t): Z \rightarrow Z$ by

$$B(t) \stackrel{\Delta}{=} \begin{bmatrix} 0 & 0 \\ M_0^{-1}B_0(t) & 0 \end{bmatrix}$$

and define $A(t): \text{Dom}(A) \subset Z \rightarrow Z$ by $A(t) \stackrel{\Delta}{=} A + B(t)$. Let $F(t) \in Z$ be defined by $F(t) \stackrel{\Delta}{=} (0, M_0^{-1}F_0(t))$, $z_0 \in Z$ by $z_0 \stackrel{\Delta}{=} (\hat{\phi}, \hat{\psi})$ and consider the initial value problem

$$D_t z(t) = A(t)z(t) + F(t), \quad t \in (0, T) \quad (9-11)$$

$$z(0) = z_0 \quad (9-12)$$

It is not difficult to argue that the operator A is densely defined and conservative; that is:

$$\langle Az, z \rangle_Z = 0, \quad z \in \text{Dom}(A) \quad (9-13)$$

Moreover, we have the following result.

Theorem 9-1. The operator $A: \text{Dom}(A) \subset Z \rightarrow Z$ is skew self adjoint.

Proof. We first argue that $-A \subset A^*$; that is: $\text{Dom}(A) \subset \text{Dom}(A^*)$ and for each $z \in \text{Dom}(A)$, $A^*z = -Az$. Let $z_1, z_2 \in \text{Dom}(A)$ with $z_1 = (\hat{\phi}_1, \hat{\psi}_1)$. Then

$$\begin{aligned} \langle Az_1, z_2 \rangle_Z &= a(\hat{\psi}_1, \hat{\phi}_2) + \langle -A_0 \hat{\phi}_1, \hat{\psi}_2 \rangle_H \\ &= \langle EI D^2 \psi_1, D^2 \phi_2 \rangle_0 - \langle EI D^2 \phi_1, D^2 \psi_2 \rangle_0 \\ &= -\langle \hat{\psi}_1, -A_0 \hat{\phi}_2 \rangle_H - a(\hat{\phi}_1, \hat{\psi}_2) \\ &= -\langle z_1, Az_2 \rangle_Z \end{aligned}$$

where we have used integration by parts, the definition of $\text{Dom}(A_0)$ and the definition of V in performing the above computation. This, of course, implies that $z_2 \in \text{Dom}(A^*)$ and $A^*z_2 = -Az_2$.

We next argue that $\text{Dom}(A^*) \subset \text{Dom}(A)$. Let $w \in \text{Dom}(A^*)$ and set $y = A^*w$. Then for $z \in \text{Dom}(A)$:

$$\langle z, y \rangle_Z = \langle z, A^*w \rangle_Z = \langle Az, w \rangle_Z$$

Recalling that $z, w, y \in Z$, we can write $z \equiv (\hat{z}_1, \hat{z}_2)$, $w \equiv (\hat{w}_1, \hat{w}_2)$ and $y \equiv (\hat{y}_1, \hat{y}_2)$, where $\hat{y}_2 \equiv (\hat{y}_2^1, \hat{y}_2^2) \in H$ and $\hat{w}_2 \equiv (\hat{w}_2^1, \hat{w}_2^2) \in H$. Then

$$\begin{aligned}
0 &= \langle z, y \rangle_Z - \langle Az, w \rangle_Z \\
&= a(\hat{z}_1, \hat{y}_1) + \langle M_0 \hat{z}_2, \hat{y}_2 \rangle_H - a(\hat{z}_2, \hat{w}_1) + \langle A_0 \hat{z}_1, \hat{w}_2 \rangle_H \\
&= \langle EI D^2 z_1, D^2 y_1 \rangle_0 + m z_2(\ell) \hat{y}_2^1 + \langle \rho z_2, \hat{y}_2^2 \rangle_0 - \\
&\quad \langle EI D^2 z_2, D^2 w_1 \rangle_0 - D(EI(\ell) D^2 z_1(\ell)) \hat{w}_2^1 + \langle D^2(EI D^2 z_1), \hat{w}_2^2 \rangle_0
\end{aligned} \tag{9-14}$$

Let $\theta \in H^2(0, \ell)$ be defined by

$$D^2 \theta \stackrel{\Delta}{=} \rho \hat{y}_2^2 \quad ; \quad \theta(\ell) \stackrel{\Delta}{=} 0 \quad , \quad D\theta(\ell) \stackrel{\Delta}{=} -m \hat{y}_2^1$$

Then substituting into Eq. (9-14) and integrating by parts, we obtain

$$\begin{aligned}
0 &= -D(EI(\ell) D^2 z_1(\ell))(y_1(\ell) + \hat{w}_2^1) \\
&\quad + \langle D^2(EI D^2 z_1), (y_1 + \hat{w}_2^2) \rangle_0 + \langle D^2 z_2, (\theta - EI D^2 w_1) \rangle_0
\end{aligned}$$

which implies that:

$$(i) \quad -D(EI(\ell) D^2 z_1(\ell))(y_1(\ell) + \hat{w}_2^1) + \langle D^2(EI D^2 z_1), (y_1 + \hat{w}_2^2) \rangle_0 = 0$$

and

$$(ii) \quad \langle D^2 z_2, (\theta - EI D^2 w_1) \rangle_0 = 0$$

Let (η, ϕ) be an arbitrary element in H . Choose $z_1 \in H^4(0, \ell)$ which satisfies

$$D^2(EI D^2 z_1) = \phi$$

with boundary conditions

$$D(EI(\ell) D^2 z_1(\ell)) = -\eta, \quad D^2 z_1(\ell) = 0$$

$$Dz_1(0) = 0, \quad z_1(0) = 0$$

Then $\hat{z}_1 \triangleq (z_1(\ell), z_1) \in \text{Dom}(A_0)$ and condition (i) therefore implies that

$$\langle (y_1(\ell) + \hat{w}_2^1), (y_1 + \hat{w}_2^2), (\eta, \phi) \rangle_H = 0, \quad (\eta, \phi) \in H$$

from which it follows that $y_1(\ell) = -\hat{w}_2^1$ and $y_1 = -\hat{w}_2^2 \in H^0(0, \ell)$. We have therefore, that $\hat{w}_2 = -\hat{y}_1 \in V$.

Next, let ϕ be an arbitrary element in $H^0(0, \ell)$. Choosing $z_2 \triangleq \int_0^\ell \int_0^\ell \phi$, condition (ii) implies that

$$\langle (\theta - EI D^2 w_1), \phi \rangle_0 = 0, \quad \phi \in H^C(0, \ell)$$

and hence that $\theta = EI D^2 w_1$. This in turn implies that $w_1 \in H^4(0, \ell)$ and $D^2 w_1(\ell) = \frac{1}{EI(\ell)} \theta(\ell) = 0$. Since $w \in Z$, we have $\hat{w}_1 \in V$ and therefore $\hat{w}_1 \in \text{Dom}(A_0)$; we conclude that $w \equiv (\hat{w}_1, \hat{w}_2) \in \text{Dom}(A_0) \times V = \text{Dom}(A)$ and the theorem is proved. \square

Since A is densely defined, it follows [Ref. 9-22, Theorem 3, p. 142] that A^* is closed and, by Theorem 9-1 above, that A is closed as well. This fact together with Eq. (9-13) and Theorem 9-1 yield that A is maximal dissipative and hence [Ref. 9-23, Theorem 4.2, page 84] that it is the infinitesimal generator of a C_0 -semigroup of contractions $\{S(t): t \geq 0\}$ on Z . It is in fact the case [see Refs. 9-23, 9-24] that $S(t)$ is defined for $t < 0$ and that $\{S(t): -\infty < t < +\infty\}$ forms a

C_0 -group of unitary operators on Z . Since the operators $B(t)$, $0 \leq t \leq T$ are bounded, it follows [Ref. 9-25, Theorem 2.3, page 132] that $\{A(t)\}_{t \in [0, T]}$ is a stable family of infinitesimal generators. Since $\text{Dom}(A)$ is independent of t , it follows [Ref. 9-25, Theorem 4.8, page 145] that the family $\{A(t)\}_{t \in [0, T]}$ generates an evolution system $\{U(t, s): 0 \leq s \leq t \leq T\}$ on Z .

Define

$$z(t) \equiv (\hat{u}(t), \hat{v}(t)) \quad (9-15)$$

in Z by

$$z(t) \stackrel{\Delta}{=} U(t, 0)z_0 + \int_0^t U(t, s)F(s)ds \quad (9-16)$$

The continuous function z given by Eq. (9-16) above is the unique mild solution to the initial value problem Eqs. (9-11), (9-12). If in addition $z_0 \in \text{Dom}(A)$ (that is $\hat{\phi} \in \text{Dom}(A_0)$ and $\hat{\psi} \in V$), then z is a strong solution to Eqs. (9-11), (9-12). Indeed z is differentiable almost everywhere (a.e.) on $[0, T]$ with $D_t z \in L_2([0, T], Z)$, satisfies Eq. (9-12), satisfies Eq. (9-11) for almost every $t \in [0, T]$, and is such that $z(t) \in \text{Dom}(A)$ a.e. on $[0, T]$.

We shall call \hat{u} given by Eqs. (9-15), (9-16) a strong solution to the initial value problem Eqs. (9-6) through (9-8). The following result is easily obtained.

Theorem 9-2. Suppose $EI \in H^2(0, \ell)$, $\sigma \in C^1([0, T], H^1(0, \ell))$, $\hat{\phi} \in \text{Dom}(A_0)$ and $\hat{\psi} \in V$. Then \hat{u} given by Eqs. (9-15), (9-16) is the unique strong solution to the initial value problem Eqs. (9-6) through (9-8). We have that \hat{u} satisfies Eq. (9-8) and Eqs. (9-6), (9-7) a.e. on $[0, T]$. Moreover, \hat{u} is twice differentiable in H and differentiable in V a.e. on $[0, T]$ with $D_t^2 \hat{u} \in L_2([0, T], H)$ and $D_t \hat{u} \in L_2([0, T], V)$.

It is also not difficult to show that if a strong solution \hat{u} to Eqs. (9-6) through (9-8) exists, then it coincides with the weak solution, and in such a case, it is given either by Eqs. (9-15), (9-16) or as the solution to the initial value problem Eqs. (9-9), (9-10).

9.2.4 Formulation of the Identification Problem

For ease of exposition in formulating the identification problem, we consider a (reasonably broad) class of inverse problems which are of particular interest in the structural modeling of large flexible spacecraft and shuttle-attached payloads [see Refs. 9-15, 9-26]. We assume that we are only interested in estimating the parameters $m \in \mathbb{R}$, $EI, \rho \in L_\infty(0, \ell)$ and $\sigma \in L_2([0, T], H^1(0, \ell))$ where $\sigma = \sigma(a_0, m, \rho)$ with $a_0 \in L_2(0, T)$. It is not difficult to further generalize the results which follow to allow for the identification of initial data, the external loads f and g , and more general forms of the internal tension σ [see Ref. 9-12]. The motivation for choosing σ to be dependent upon a time-varying function a_0 , the magnitude m of the tip mass, and the linear mass density ρ of the beam is made clear below.

Form the Cartesian product $\mathcal{Q} \triangleq \mathbb{R} \times L_\infty(0, \ell) \times L_\infty(0, \ell) \times L_2(0, T)$ with the usual product topology. Let Q be a subset of \mathcal{Q} which satisfies:

(H1) Q is compact;

(H2) There exist constants $m_1, M_1, i = 1, 2, 3$ such that

$$0 < m_1 \leq m \leq M_1$$

$$0 < m_2 < EI < M_2$$

$$0 < m_3 < \rho < M_3$$

for all $q = (m, EI, \rho, a_0) \in Q$; and

(H3) For all $q \in Q$, $\sigma(q) \in L_2([0, T], H^1(0, \ell))$ with the mapping $q \rightarrow \sigma(q)$ continuous from Q into $L_2([0, T], H^1(0, \ell))$.

We assume that we have been provided with displacement measurements $\{\bar{u}(t_i, x_j): i=1, \dots, \mu, j=1, \dots, \nu\}$ for the beam at positions $x_j \in [0, \ell]$,

$j = 1, 2, \dots, v$, and at times $t_i \in [0, T]$, $i = 1, 2, \dots, \mu$, which result from a known input disturbance applied to the system in a known initial state. The identification problem is formulated as a least-squares fit to data:

(ID)

Find $q = (m, EI, \rho, a_0) \in Q$ which minimizes

$$J(q; \hat{u}(q)) \triangleq \sum_{i=1}^{\mu} \sum_{j=1}^v \|\bar{u}(t_i, x_j) - u(t_i, x_j; q)\|^2 \quad (9-17)$$

subject to $\hat{u}(t; q) \equiv (u(t, l; q), u(t, \cdot; q))$ being the solution to Eqs. (9-9), (9-10) corresponding to $q \in Q$.

The infinite dimensionality of both the state, which is governed by the system Eqs. (9-9), (9-10), and of the admissible parameter space Q (being a function space) necessitates the use of some form of approximation in solving Problem (ID). We develop and analyze one particular scheme in the next section. We note that the approximation theory to be developed below will also permit the formulation of the identification problem based upon criteria other than displacement; for example, based upon velocity [see Ref. 9-10].

9.3 An Approximation Scheme

9.3.1 Approximating Identification Problems

Our approximation scheme is based upon the construction of a sequence of approximating identification problems, in each of which both the state constraint and the admissible parameter space are finite-dimensional. We argue that each of the approximating problems admits a solution. The resulting sequence is shown to have a sub-sequential limit

which is a solution to the original identification problem. The state approximation is constructed using a spline-based Galerkin method. The admissible parameter space is discretized using splines as well. We begin by discussing the state approximation.

Working abstractly at first, for each $N = 1, 2, \dots$, let $V^N \subset V$ be a finite-dimensional subspace of H and let P^N denote the orthogonal projection of H onto V^N with respect to the inner product on H . The Galerkin equations corresponding to Eqs. (9-9), (9-10) are given by

$$\langle M_0 D_t^2 \hat{u}^N(t), \hat{\theta}^N \rangle_H + a(\hat{u}^N(t), \hat{\theta}^N) = b(t)(\hat{u}^N(t), \hat{\theta}^N) + \langle F_0(t), \hat{\theta}^N \rangle_H, \quad (9-18)$$

$$\hat{\theta}^N \in V^N, \quad t \in (0, T)$$

$$\hat{u}^N(0) = P^N \hat{\phi} \quad D_t \hat{u}^N(0) = P^N \hat{\psi} \quad (9-19)$$

where $\hat{u}^N(t) = (u^N(t, \ell), u^N(t, \cdot)) \in V^N$. We define the following sequence of approximating identification problems.

(IDN)

Find $q^N = (m^N, EI^N, \rho^N, a_0^N) \in Q$ which minimizes $J(q; \hat{u}^N(q))$, where J is defined by Eq. (9-17) and $\hat{u}^N(t; q) \equiv (u^N(t, \ell; q), u^N(t, \cdot; q))$ is the solution to Eqs. (9-18), (9-19) corresponding to $q \in Q$.

Of particular interest to us here is a scheme involving the use of cubic spline functions. Let $\{\bar{B}_j^N\}_{j=-1}^{N+1}$ denote the standard cubic B-splines on the interval $[0, \ell]$ corresponding to the uniform partition $\Delta^N \equiv \{0, \frac{\ell}{N}, \frac{2\ell}{N}, \dots, \ell\}$ [Ref. 9-27]. Let $\{B_j^N\}_{j=1}^{N+1}$ denote the modified cubic B-splines which satisfy $B_j^N(0) = DB_j^N(0) = 0$, $j = 1, 2, \dots, N+1$; that is:

$$B_1^N = \bar{B}_0^N - 2\bar{B}_1^N + \bar{B}_2^N$$

$$B_j^N = \overline{B}_j^N, \quad j = 2, 3, \dots, N+1$$

Denote $\hat{B}_j^N \triangleq (B_j^N(\ell), B_j^N)$ and define $V^N \subset V$ by

$$V^N \triangleq \text{span} \{ \hat{B}_j^N \}_{j=1}^{N+1}$$

The Galerkin equations Eqs. (9-18), (9-19) take the form

$$M_0^{N \times N}(\tau) + A_0^{N \times N}(\tau) = B_0^N(\tau) w^N(\tau) + F_0^N(\tau), \quad \tau \in (0, T) \quad (9-20)$$

$$w^N(0) = (W^N)^{-1} \hat{\phi}^N, \quad \dot{w}^N(0) = (W^N)^{-1} \hat{\psi}^N \quad (9-21)$$

where for $i, j = 1, 2, \dots, N+1$, the elements of the coefficient matrices are

$$[M_0^N]_{ij} = m B_i^N(\ell) B_j^N(\ell) + \int_0^\ell \rho B_i^N B_j^N dx$$

$$[A_0^N]_{ij} = \int_0^\ell (EI D^2 B_i^N)(D^2 B_j^N) dx$$

$$[B_0^N(\tau)]_{ij} = - \int_0^\ell (\sigma(\tau, \cdot) D B_i^N)(D B_j^N) dx$$

$$[F_0^N(\tau)]_i = g(\tau) B_i^N(\ell) + \int_0^\ell f(\tau, \cdot) B_i^N dx$$

$$[\hat{\phi}^N]_i = \phi(\ell) B_i^N(\ell) + \int_0^\ell \phi B_i^N dx$$

$$[\hat{\psi}^N]_i = \psi(\ell) B_i^N(\ell) + \int_0^\ell \psi B_i^N dx$$

$$[W^N]_{ij} = B_i^N(\ell) B_j^N(\ell) + \int_0^\ell B_i^N B_j^N dx$$

and $\hat{u}^N(t)$ has the representation

$$\hat{u}^N(t) = \sum_{j=1}^{N+1} w_j^N(t) \hat{B}_j^N$$

9.3.2 Convergence Results

Our convergence arguments are based upon the approximation properties of spline functions. Denote $\bar{S}_3(\Delta^N) \triangleq \text{span}\{\bar{B}_j^N\}_{j=-1}^{N+1}$ and $S^3(\Delta^N) \triangleq \text{span}\{B_j^N\}_{j=1}^{N+1}$. For each function ϕ defined on the interval $[0, \ell]$, let $\bar{I}^N \phi$ denote that element in $\bar{S}_3(\Delta^N)$ which satisfies the interpolatory constraints $(\bar{I}^N \phi)(\frac{j\ell}{N}) = \phi(\frac{j\ell}{N})$, $j = 0, 1, \dots, N$, $D(\bar{I}^N \phi)(\frac{j\ell}{N}) = D\phi(\frac{j\ell}{N})$, $j = 0, N$, and let $I^N \phi$ denote that element in $S^3(\Delta^N)$ which satisfies the interpolatory constraints $(I^N \phi)(\frac{j\ell}{N}) = \phi(\frac{j\ell}{N})$, $j = 1, 2, \dots, N$, $D(I^N \phi)(\ell) = D\phi(\ell)$. The interpolatory spline $\bar{I}^N \phi$ will be well defined whenever ϕ is well defined at the node points and $D\phi$ at the end points. A similar statement can be made for $I^N \phi$.

We require the following two standard results concerning the approximation properties of interpolatory splines [Ref. 9-28].

Proposition 9-3: For each $\phi \in H^2(0, \ell)$:

$$\|D^k(\bar{I}^N \phi - \phi)\|_0 \leq C_k^1 N^{-2+k} \|D^2 \phi\|_0, \quad k = 0, 1$$

where C_k^1 is independent of ϕ and N .

Proposition 9-4: For each $\phi \in H^4(0, \ell)$:

$$\|D^k(\bar{I}^N \phi - \phi)\|_0 \leq C_k^2 N^{-4+k} \|D^4 \phi\|_0, \quad k = 0, 1, 2$$

where C_k^2 is independent of ϕ and N .

The following lemma is key to establishing the desired convergence results.

Lemma 9-5.

(1) Let $\hat{\phi} \equiv (\phi(\ell), \phi) \in V$ and let $\hat{\phi}^N = P^N \hat{\phi} = (\phi^N(\ell), \phi^N)$.

Then $\phi^N \rightarrow \phi$ in $H^2(0, \ell)$ and consequently $\hat{\phi}^N \rightarrow \hat{\phi}$ in V ;

(2) $P^N \rightarrow I$ strongly in H .

Proof. We prove assertion (1) in detail. Using the Schmidt inequality [Ref. 9-28] together with Proposition 9-3, we obtain the following estimates:

$$\begin{aligned} \|\phi^N - \phi\|_0 &\leq \|\hat{\phi}^N - \hat{\phi}\|_H \leq \|\widehat{(\bar{I}^N \phi)} - \hat{\phi}\|_H \\ &= \|\bar{I}^N \phi - \phi\|_0 = \|\bar{I}^N \phi - \phi\|_0 \\ &\leq C_0^1 N^{-2} \|D^2 \phi\|_0 \rightarrow 0 \quad \text{as } N \rightarrow \infty \end{aligned}$$

where $\widehat{(\bar{I}^N \phi)} \triangleq ((\bar{I}^N \phi)(\ell), \bar{I}^N \phi)$; and

$$\|D(\phi^N - \phi)\|_0 \leq \|D(\phi^N - \bar{I}^N \phi)\|_0 + \|D(\bar{I}^N \phi - \phi)\|_0$$

$$\begin{aligned}
&\leq k_1 N \|\phi^N - \bar{\Gamma}^N \phi\|_0 + C_1^1 N^{-1} \|D^2 \phi\|_0 \\
&\leq k_1 N \|\phi^N - \phi\|_0 + k_1 N \|\bar{\Gamma}^N \phi - \phi\|_0 + C_1^1 N^{-1} \|D^2 \phi\|_0 \\
&\leq k_1 C_0^1 N^{-1} \|D^2 \phi\|_0 + k_1 C_0^1 N^{-1} \|D^2 \phi\|_0 + C_1^1 N^{-1} \|D^2 \phi\|_0 \\
&= (2k_1 C_0^1 + C_1^1) N^{-1} \|D^2 \phi\|_0 \rightarrow 0 \text{ as } N \rightarrow \infty
\end{aligned}$$

Using the Schmidt inequality together with the first integral relation [Ref. 9-28], we obtain:

$$\begin{aligned}
\|D^2 \phi^N\|_0^2 &\leq 2 \|D^2(\phi^N - \bar{\Gamma}^N \phi)\|_0^2 + 2 \|D^2 \bar{\Gamma}^N \phi\|_0^2 \\
&\leq 2k_2 N^4 \|\phi^N - \bar{\Gamma}^N \phi\|_0^2 + 2 \|D^2 \phi\|_0^2 - 2 \|D^2(\phi - \bar{\Gamma}^N \phi)\|_0^2 \\
&\leq 2k_2 N^4 \|\phi^N - \phi\|_0^2 + 2k_2 N^4 \|\bar{\Gamma}^N \phi - \phi\|_0^2 + 2 \|D^2 \phi\|_0^2 \\
&\leq \alpha^2 \|D^2 \phi\|_0^2
\end{aligned}$$

where α is independent of ϕ and N . Choose a function $\psi \in \{\theta: \theta \in H^4(0, \ell), \theta(0) = D\theta(0) = 0\}$. Using arguments similar to those used above together with Proposition 9-4, it can be shown that

$$\|D^2(\psi^N - \psi)\|_0 \leq \tilde{k} N^{-2} \|D^4 \psi\|_0$$

where \tilde{k} is independent of ψ and N . It follows that

$$\|D^2(\phi^N - \phi)\|_0 \leq \|D^2(\phi^N - \psi^N)\|_0 + \|D^2(\psi^N - \psi)\|_0 + \|D^2(\psi - \phi)\|_0$$

$$\leq (\alpha + 1) \|D^2(\psi - \phi)\|_0 + \tilde{k}N^{-2} \|D^4\psi\|_0$$

Since $H^4(0, \ell)$ is a dense subset of $H^2(0, \ell)$, ψ can be chosen so as to make the first term on the right arbitrarily small and therefore that

$$\|D^2(\phi^N - \phi)\|_0 \rightarrow 0 \quad \text{as } N \rightarrow \infty$$

This proves assertion (1) of the lemma.

Assertion (2) follows from assertion (1) and the facts that V is dense in H and that the P^N , being orthogonal projections, are uniformly bounded. \square

Theorem 9-6. Suppose that $\{q^N\} \subset Q$ with $q^N \rightarrow q$ as $N \rightarrow \infty$. Let \hat{u} denote the solution to Eqs. (9-9), (9-10) corresponding to q and let \hat{u}^N denote the solution to Eqs. (9-18), (9-19) corresponding to q^N . Suppose further that \hat{u} is a strong solution (see Theorem 9-2). Then $\hat{u}^N(q^N) \rightarrow \hat{u}(q)$ in V and $D_t \hat{u}^N(q^N) \rightarrow D_t \hat{u}(q)$ in H as $N \rightarrow \infty$ for each $t \in [0, T]$.

Proof. Our argument is similar in spirit to the one used by Dupont [Ref. 9-29] to demonstrate the convergence of a Galerkin method for the integration of a class of hyperbolic systems. We adopt the convention that the superscript N on a form or operator indicates that it be computed with respect to $q^N = (m^N, EI^N, \rho^N, a_0^N)$, while no superscript indicates that it be computed with respect to $q = (m, EI, \rho, a_0)$.

Applying the triangle inequality, we have

$$\|\hat{u}^N - \hat{u}\|_V \leq \|\hat{u}^N - P^N \hat{u}\|_V + \|P^N \hat{u} - \hat{u}\|_V \quad (9-22)$$

and

$$\|D_t \hat{u}^N - D_t \hat{u}\|_H \leq \|D_t \hat{u}^N - D_t P^N \hat{u}\|_H + \|P^N D_t \hat{u} - D_t \hat{u}\|_H \quad (9-23)$$

Lemma 9-5 and the fact that \hat{u} has been assumed to be a strong solution imply that $\|P^N \hat{u} - \hat{u}\|_V \rightarrow 0$ and $\|P^N D_t \hat{u} - D_t \hat{u}\|_H \rightarrow 0$ as $N \rightarrow \infty$ for each $t \in [0, T]$.

Since \hat{u}^N satisfies Eqs. (9-18), (9-19) and \hat{u} satisfies Eqs. (9-9), (9-10), for each $\hat{\theta}^N \in V^N$ we have

$$\begin{aligned} & \langle M_0^N D_t^2 (\hat{u}^N - P^N \hat{u}), \hat{\theta}^N \rangle_H + a^N(\hat{u}^N - P^N \hat{u}, \hat{\theta}^N) \\ &= \langle M_0^N D_t^2 (\hat{u} - P^N \hat{u}), \hat{\theta}^N \rangle_H + \langle (M_0 - M_0^N) D_t^2 \hat{u}, \hat{\theta}^N \rangle_H \\ &+ a^N(\hat{u} - P^N \hat{u}, \hat{\theta}^N) + a(\hat{u}, \hat{\theta}^N) - a^N(\hat{u}, \hat{\theta}^N) \\ &+ b^N(t)(\hat{u}^N - P^N \hat{u}, \hat{\theta}^N) + b^N(t)(P^N \hat{u} - \hat{u}, \hat{\theta}^N) \\ &+ b^N(t)(\hat{u}, \hat{\theta}^N) - b(t)(\hat{u}, \hat{\theta}^N) \end{aligned}$$

Denote $\hat{u}_N \equiv (u_N(\ell), u_N) \triangleq P^N \hat{u}$, denote $\hat{v}^N \equiv (v^N(\ell), v^N) \triangleq \hat{u}^N - \hat{u}_N$, and choose $\hat{\theta}^N = D_t \hat{v}^N \in V^N$. Then

$$\begin{aligned} & \langle M_0^N D_t^2 \hat{v}^N, D_t \hat{v}^N \rangle_H + a^N(\hat{v}^N, D_t \hat{v}^N) \\ &= \langle M_0^N D_t^2 (\hat{u} - P^N \hat{u}), D_t \hat{v}^N \rangle_H + \langle (M_0 - M_0^N) D_t^2 \hat{u}, D_t \hat{v}^N \rangle_H \\ &+ a^N(\hat{u} - P^N \hat{u}, D_t \hat{v}^N) + a(\hat{u}, D_t \hat{v}^N) - a^N(\hat{u}, D_t \hat{v}^N) \\ &+ b^N(t)(\hat{v}^N, D_t \hat{v}^N) + b^N(t)(P^N \hat{u} - \hat{u}, D_t \hat{v}^N) \\ &+ b^N(t)(\hat{u}, D_t \hat{v}^N) - b(t)(\hat{u}, D_t \hat{v}^N) \end{aligned}$$

or

$$\frac{1}{2} D_t (\langle M_0^N D_t \hat{v}^N, D_t \hat{v}^N \rangle_H + a^N(\hat{v}^N, \hat{v}^N))$$

$$\begin{aligned}
&= \langle M_0^N(I - P^N)D_t^2 \hat{u}, D_t \hat{v}^N \rangle_H + \langle (M_0 - M_0^N)D_t^2 \hat{u}, D_t \hat{v}^N \rangle_H \\
&\quad + D_t a^N((I - P^N)\hat{u}, \hat{v}^N) - a^N((I - P^N)D_t \hat{u}, \hat{v}^N) \\
&\quad + D_t (a(\hat{u}, \hat{v}^N) - a^N(\hat{u}, \hat{v}^N)) - (a(D_t \hat{u}, \hat{v}^N) - a^N(D_t \hat{u}, \hat{v}^N)) \\
&\quad + b^N(t)(\hat{v}^N, D_t \hat{v}^N) + b^N(t)(P^N \hat{u} - \hat{u}, D_t \hat{v}^N) \\
&\quad + b^N(t)(\hat{u}, D_t \hat{v}^N) - b(t)(\hat{u}, D_t \hat{v}^N)
\end{aligned}$$

Integrating both sides of the above expression from 0 to t , invoking hypotheses (H1) through (H3) on Q , and using standard estimates we obtain

$$\begin{aligned}
&\min(m_1, m_2, m_3)(\|D_t \hat{v}^N\|_H^2 + \|\hat{v}^N\|_V^2) \\
&\leq \int_0^t \{ \max(M_1^2, M_3^2) \|(I - P^N)D_s^2 \hat{u}\|_H^2 + \|D_s \hat{v}^N\|_H^2 \\
&\quad + \max(\|m - m^N\|^2, \|\rho - \rho^N\|_\infty^2) \cdot \|D_s^2 \hat{u}\|_H^2 + \|D_s \hat{v}^N\|_H^2 \\
&\quad + M_2^2 \|(I - P^N)D_s \hat{u}\|_V^2 + \|\hat{v}^N\|_V^2 + \|EI - EI^N\|_\infty^2 \cdot \|D_s \hat{u}\|_V^2 \\
&\quad + \|\hat{v}^N\|_V^2 + C_0 \|\sigma(q^N)\|_1 \cdot \|\hat{v}^N\|_V^2 + C_0 \|\sigma(q^N)\|_1 \cdot \|D_s \hat{v}^N\|_H^2 \\
&\quad + C_0^2 \|\sigma(q^N)\|_1^2 \cdot \|(I - P^N)\hat{u}\|_V^2 + \|D_s \hat{v}^N\|_H^2 \\
&\quad + C_1 \|\sigma(q) - \sigma(q^N)\|_1^2 \cdot \|\hat{u}\|_V^2 + \|D_s \hat{v}^N\|_H^2 \} ds \\
&\quad + \frac{1}{C_2} \|(I - P^N)\hat{u}\|_V^2 + C_2 \|\hat{v}^N\|_V^2 + \|(I - P^N)\hat{\phi}\|_V^2 \\
&\quad + \frac{1}{C_3} \|EI - EI^N\|_\infty^2 \cdot \|\hat{u}\|_V^2 + C_3 \|\hat{v}^N\|_V^2 + \|EI - EI^N\|_\infty^2 \cdot \|\hat{\phi}\|_V^2
\end{aligned}$$

where C_0 and C_1 are constants which are independent of N and C_2 and C_3 may be chosen arbitrarily. Choosing C_2 and C_3 sufficiently small (i.e., $C_2 + C_3 < \min(m_1, m_2, m_3)$), we obtain

$$\|D_t \hat{v}^N\|_H^2 + \|\hat{v}^N\|_V^2 \leq \Delta^N(t) + \int_0^t K_0^N(s) \{ \|D_s \hat{v}^N\|_H^2 + \|\hat{v}^N\|_V^2 \} ds$$

where

$$\begin{aligned} \Delta^N(t) &\triangleq K_1 \{ \|(I - P^N) \hat{u}(t)\|_V^2 + \|(I - P^N) \hat{\phi}\|_V^2 \\ &+ \|EI - EI^N\|_\infty^2 \cdot \|\hat{u}(t)\|_V^2 + \|EI - EI^N\|_\infty^2 \cdot \|\hat{\phi}\|_V^2 \\ &+ \int_0^t \{ \|(I - P^N) D_s^2 \hat{u}(s)\|_H^2 + \max(\|m - m^N\|^2, \|\rho - \rho^N\|_\infty^2) \cdot \|D_s^2 \hat{u}(s)\|_H^2 \\ &+ \|(I - P^N) D_s \hat{u}(s)\|_V^2 + \|EI - EI^N\|_\infty^2 \cdot \|D_s \hat{u}(s)\|_V^2 \\ &+ \|\sigma(s, \cdot; q^N)\|_1^2 \cdot \|(I - P^N) \hat{u}(s)\|_V^2 \\ &+ \|\sigma(s, \cdot; q) - \sigma(s, \cdot; q^N)\|_1^2 \cdot \|\hat{u}(s)\|_V^2 \} ds \} \end{aligned}$$

and

$$K_0^N(s) \triangleq K_2 \{ K_3 + \|\sigma(s, \cdot; q^N)\|_1 \}$$

where K_i , $i = 1, 2, 3$ are constants independent of N . Using the facts that $q^N \rightarrow q$ in Q as $N \rightarrow \infty$, that $\hat{u}(q)$ is a strong solution, that Lemma 9-5 holds, and that Q satisfies hypotheses (H1) and (H3), we have that $\Delta^N \rightarrow 0$ and that K_0^N is uniformly bounded in $L_2(0, T)$ as $N \rightarrow \infty$. An application of the Gronwall inequality, therefore, yields

$$\|D_t \hat{v}^N\|_H^2 + \|\hat{v}^N\|_V^2 \rightarrow 0 \quad \text{as } N \rightarrow \infty$$

for each $t \in [0, T]$. Consequently, $\|D_t \hat{u}^N - D_t P^N \hat{u}\|_H \rightarrow 0$ and $\|\hat{u}^N - P^N \hat{u}\|_V \rightarrow 0$ as $N \rightarrow \infty$. Together with Eqs. (9-22), (9-23), this completes the proof of the theorem. \square

The continuous dependence results given in Theorems 9-7 and 9-8 below can be verified using arguments similar to those used in the proof of Theorem 9-6.

Theorem 9-7. Let $\{q_k\} \subset \mathcal{Q}$ with $q_k \rightarrow q^*$ as $k \rightarrow \infty$. If for each N fixed, $\hat{u}^N(q)$ denotes the solution to Eqs. (9-18), (9-19) corresponding to q , then $\hat{u}^N(q_k) \rightarrow \hat{u}^N(q^*)$ in V and $D_t \hat{u}^N(q_k) \rightarrow D_t \hat{u}^N(q^*)$ in H for each $t \in [0, T]$ as $k \rightarrow \infty$. That is, the mapping $q \rightarrow (\hat{u}^N(q), D_t \hat{u}^N(q))$ from Q into $V \times H$ is continuous for each $N = 1, 2, \dots$

Theorem 9-8. Let $\{q_k\} \subset \mathcal{Q}$ with $q_k \rightarrow q^*$ as $k \rightarrow \infty$ and let $\hat{u}(q)$ denote the solution to Eqs. (9-9), (9-10) corresponding to q . If $\hat{u}(q^*)$ is a strong solution, then $\hat{u}(q_k) \rightarrow \hat{u}(q^*)$ in V and $D_t \hat{u}(q_k) \rightarrow D_t \hat{u}(q^*)$ in H for each $t \in [0, T]$ as $k \rightarrow \infty$. The mapping $q \rightarrow (\hat{u}(q), D_t \hat{u}(q))$ is continuous as a mapping from Q into $V \times H$ in neighborhoods of those $q \in Q$ for which $\hat{u}(q)$ is a strong solution.

We are now prepared to prove our first major convergence result.

Theorem 9-9. For each $N = 1, 2, \dots$ fixed, problem (IDN) has a solution \bar{q}^N . The sequence $\{\bar{q}^N\}$ admits a convergent subsequence $\{\bar{q}^{N_k}\}$ with $\bar{q}^{N_k} \rightarrow \bar{q} \in Q$ as $k \rightarrow \infty$. If $\hat{u}(\bar{q})$ is a strong solution to Eqs. (9-9), (9-10), then \bar{q} is a solution to Problem (ID).

Proof. Theorem 9-7 implies that the mapping $q \rightarrow J(q; \hat{u}^N(q))$ from Q into R is continuous. This together with the fact that Q is compact yields the existence of a solution \bar{q}^N to problem (IDN). The existence of a convergent subsequence $\{\bar{q}^{N_k}\} \subset \{\bar{q}^N\}$ also follows from the compactness of Q . If $\bar{q}^{N_k} \rightarrow \bar{q}$ as $k \rightarrow \infty$ and $\hat{u}(\bar{q})$ is a strong solution to Eqs. (9-9), (9-10), then Theorem 9-6 implies that

$$J(\bar{q}, \hat{u}(\bar{q})) = \lim_{k \rightarrow \infty} J(\bar{q}^{N_k}; \hat{u}^{N_k}(\bar{q}^{N_k}))$$

$$\leq \lim_{k \rightarrow \infty} J(q; \hat{u}^{N_k}(q)) = J(q; \hat{u}(q))$$

for all $q \in Q$. The theorem is proved. \square

Although the state equation Eq. (9-18) in problem (IDN) is finite-dimensional, the admissible parameter space Q is a function space and hence the minimization of J is over an infinite-dimensional space. We briefly indicate a means of overcoming this difficulty which involves the introduction of a second level of approximation into our scheme.

For each $M = 1, 2, \dots$, define the sets $Q^M \subset Q$ by $\mathcal{J}^M(Q)$, where the mappings \mathcal{J}^M satisfy:

(P1) $\mathcal{J}^M: Q \rightarrow \mathcal{Q}$ is continuous; and

(P2) $\mathcal{J}^M(q) \rightarrow q$ as $M \rightarrow \infty$, uniformly in q , for all $q \in Q$.

We assume further that the sets Q^M have the property:

(P3) For each $q \in Q^M$, $\hat{u}(q)$ is a strong solution.

We define the following doubly-indexed sequence of approximating identification problems.

(IDNM)

Find $q_M^N = (m_M^N, EI_M^N, \rho_M^N, a_{OM}^N) \in Q^M$ which minimizes $J(q; \hat{u}^N)$ subject to \hat{u}^N being the solution to Eqs. (9-18), (9-19) corresponding to q .

Note that if the sets Q^M are of dimension $k_M < \infty$, then the optimization specified in Problem (IDNM) is simply over a compact subset of the space R^{k_M} and is subject to finite-dimensional constraints--a computationally tractable problem.

The convergence arguments now go as follows. Property (P1) of the mappings \mathcal{J}^M and the compactness of Q imply that the sets Q^M are compact as well. For each $N = 1, 2, \dots$ and each $M = 1, 2, \dots$, Problem (IDNM) therefore has a solution \bar{q}_M^N . For each $M = 1, 2, \dots$ fixed, the sequence $\{\bar{q}_M^N\}_{N=1}^{\infty}$ admits a convergent subsequence $\{\bar{q}_M^{N_k}\}$ with $\bar{q}_M^{N_k} \rightarrow \bar{q}_M$

as $k \rightarrow \infty$. Recalling property (P3) and arguing as we have in the proof of Theorem 9-9, we conclude that \bar{q}_M is a solution to the problem of minimizing $J(q; \hat{u})$ over Q^M . Since $Q^M = \mathcal{J}^M(Q)$, there exists $\tilde{q}_M \in Q$ such that $\bar{q}_M = \mathcal{J}^M(\tilde{q}_M)$. Since $\{\tilde{q}_M\} \subset Q$ and Q is compact, there exists a convergent subsequence $\{\tilde{q}_{M_j}\}$ of $\{\tilde{q}_M\}$ with $\tilde{q}_{M_j} \rightarrow \bar{q}$ as $j \rightarrow \infty$. Property (P2) then implies that $\mathcal{J}^{M_j}(\tilde{q}_{M_j}) \rightarrow \bar{q}$ as $j \rightarrow \infty$ and hence that $\bar{q}_{M_j} \rightarrow \bar{q}$ as $j \rightarrow \infty$ as well. Since for each $q \in Q$:

$$J(\bar{q}_{M_j}; \hat{u}) \leq J(q; \hat{u})$$

and since $Q^{M_j} \equiv \mathcal{J}^{M_j}(Q)$, it follows that for each $q \in Q$:

$$J(\bar{q}_{M_j}; \hat{u}(\bar{q}_{M_j})) \leq J(\mathcal{J}^{M_j}(q); \hat{u}(\mathcal{J}^{M_j}(q))) \quad (9-24)$$

Taking the limit as $j \rightarrow \infty$ on both sides of Eq. (9-24) and recalling Theorem 9-8 and Property (P3), we infer that for each $q \in Q$:

$$J(\bar{q}; \hat{u}(\bar{q})) \leq J(q; \hat{u}(q))$$

from which we conclude that \bar{q} is a solution to Problem (ID). In summary, we have proved the following result:

Theorem 9-10: Each of the approximating identification problems

(IDNM) has a solution \bar{q}_M^N . From the tableau $\{\bar{q}_M^N\}$, a sequence $\{\bar{q}(k)\}$ can be extracted with $\bar{q}(k) \rightarrow \bar{q}$, a solution to Problem (ID), as $k \rightarrow \infty$.

Typically, an appropriate choice for the sets Q^M are finite-dimensional spaces of interpolating linear or cubic spline functions with the mappings \mathcal{J}^M being constructed from the usual interpolation operators. If the elements in Q are sufficiently regular, it is not difficult to verify that the mappings \mathcal{J}^M satisfy Properties (P1) through (P3) for this approximation. A detailed discussion and several examples of this particular choice for the sets Q^M in the context of inverse problems for parabolic systems can be found in Reference 9-30. Similar results for identification problems involving the estimation of functional parameters in beam equations with simple boundary conditions (e.g., clamped, simply supported, cantilevered) are presented in References 9-8 and 9-11.

9.4 Numerical Results

In this subsection, we discuss numerical results for a variety of examples. Although the analysis presented in the preceding subsections is based primarily on a simple example involving a cantilevered beam with tip mass, only minor modifications are required so as to make our general approach applicable to a broad class of inverse problems for beam vibration. Some of these will be considered and outlined below.

Although one of the major features of our scheme is its ability to identify or estimate functional (spatially and/or temporally varying) parameters, our numerical findings for this important class of problems are, at present, incomplete. For this reason, this section includes examples involving the identification of constant parameters only. Our results for functional parameters will appear in a forthcoming paper.

In all of the examples below, the fits were based upon artificially-generated "observations". By this we mean that so-called "true" values for the parameters were selected and a modal-based Galerkin method was used to generate the solution to the resulting system of equations from

which the sampled displacement measurements $\{\bar{u}(t_i, x_j): i=1, \dots, \mu, j=1, \dots, \nu\}$ were obtained. Results for examples involving fits based upon actual experimental data will be discussed elsewhere.

The finite-dimensional optimization problems were solved using an iterative steepest-descent routine, ZXSSQ, from the IMSL Library. The algorithm used is the one suggested in the papers by Levenberg [Ref. 9-31] and Marquardt [Ref. 9-32]. The finite-dimensional second order initial value problem given by Eqs. (9-20), (9-21) which has to be solved at each iteration to compute the value of the least-squares payoff functional J , approximations to its gradient, and the corresponding Jacobian matrix, is integrated using a variable-order Adams predictor-corrector method (IMSL routine DGEAR). The system of Eqs. (9-20), (9-21) does not in general demonstrate stiff behavior.

The integral inner products in the generalized mass and stiffness matrices and the generalized Fourier coefficient vectors for the external loads and initial data were computed using a composite two-point Gauss-Legendre quadrature rule. The four-subinterval support of the cubic B-splines and their derivatives leads to 7-banded matrices and consequently contributes to the overall computational efficiency of the method.

All examples were run on the IBM 3081 processor at Draper Laboratory.

Example 1. In this example, we consider a cantilevered beam of length $\ell \triangleq 1.0$ with an attached tip mass. We seek to identify the spatially-invariant stiffness EI and linear mass density ρ of the beam and the magnitude m of the tip mass. We assume that the system is initially at rest ($\phi \triangleq 0, \psi \triangleq 0$), and is subsequently excited by the distributed lateral load along the beam given by

$$f(t, x) \triangleq e^x \sin 2\pi t$$

and the point force applied to the tip mass

$$g(t) \triangleq 2 e^{-2t}$$

We assume that there is no axial loading ($\sigma \triangleq 0$).

Displacement observations were generated by taking $EI \triangleq 1.0$, $\rho \triangleq 3.0$ and $m \triangleq 1.5$ to be the true values of the indicated parameters. Measurements were taken at positions $x_j = 0.25j$, $j = 2, 3, 4$, and at times $t_i = 0.5i$, $i = 1, 2, \dots, 10$, from a solution to the system Eqs. (9-1) through (9-5) generated using a Galerkin method and the first two natural modes of the unforced unaccelerated system [see Ref. 9-26]. The "start up" values for the steepest descent routine were $EI_0 = 0.7$, $\rho_0 = 2.7$ and $m_0 = 0.7$. The final converged values for \overline{EI}^N , $\overline{\rho}^N$, and \overline{m}^N together with the residual sum of squares \overline{J}^N and required CPU times for various values of N are given in Table 9-1 below.

Table 9-1. Convergence results, Example 1.

N	\overline{EI}^N	$\overline{\rho}^N$	\overline{m}^N	\overline{J}^N	CPU (min:sec)
2	1.00057	3.04455	1.48957	0.12×10^{-3}	0:09.19
3	1.00067	3.01256	1.49707	0.11×10^{-3}	0:22.10
4	1.00027	3.00922	1.49721	0.11×10^{-3}	0:57.60
5	1.00016	2.98936	1.50262	0.11×10^{-3}	1:22.52
6	0.99912	2.99720	1.49952	0.11×10^{-3}	2:52.76

Example 2. We consider the system described in the previous example. As in that case, we assume that it is initially at rest and then excited by the distributed load

$$f(t,x) = e^x \sin 2\pi t$$

along the beam. The point force acting on the tip mass is (modified):

$$g(t) = 2 e^{-t}$$

In this case, we assume that the entire system is subjected to a time-varying base acceleration which is given by

$$a_0(t) \triangleq \begin{cases} 1 & , \quad 0 \leq t \leq 1.5 \\ 0 & , \quad t > 1.5 \end{cases} \quad (9-25)$$

The internal tension resulting from the axial load [see Refs. 9-15, 9-26] is given by

$$\sigma(t,x) = -a_0(t)(\rho(\ell - x) + m)$$

We are interested once again in estimating the stiffness EI , the linear mass density ρ , and the magnitude m of the tip mass. The true values of the parameters were taken to be $EI \triangleq 1.0$, $\rho \triangleq 3.0$, and $m \triangleq 1.5$, with the reference solution being generated using the first two natural modes of vibration for the unforced, unaccelerated system. Displacement measurements were taken at positions $x_j = 0.625 + 0.125j$, $j = 1, 2, 3$ and at times $t_i = 0.5i$, $i = 1, 2, \dots, 10$. The start up values for the iterative search routine were taken as $EI_0 = 0.7$, $\rho_0 = 2.7$, and $m_0 = 1.7$. Our results are summarized in Table 9-2.

Table 9-2. Convergence results, Example 2.

N	\overline{EI}^N	$\overline{\rho}^N$	\overline{m}^N	\overline{J}^N	CPU (min:sec)
2	1.00057	3.09966	1.47928	0.17×10^{-4}	0:18.01
3	1.00121	3.06360	1.48727	0.18×10^{-4}	0:35.93
4	1.00092	3.04144	1.49207	0.19×10^{-4}	1:26.19
5	1.00057	3.03063	1.49413	0.19×10^{-4}	4:15.87
6	1.00117	3.03186	1.49436	0.35×10^{-4}	5:21.34

We note that although strictly speaking the convergence theory developed in Section 9-3 requires that $a_0 \in C^1$, the scheme performed satisfactorily with the discontinuous a_0 given by Eq. (9-25) above.

Example 3. In this example we consider a free-free beam of length $\ell = 1.0$ with an attached tip body at each end (see Fig. 9-2).

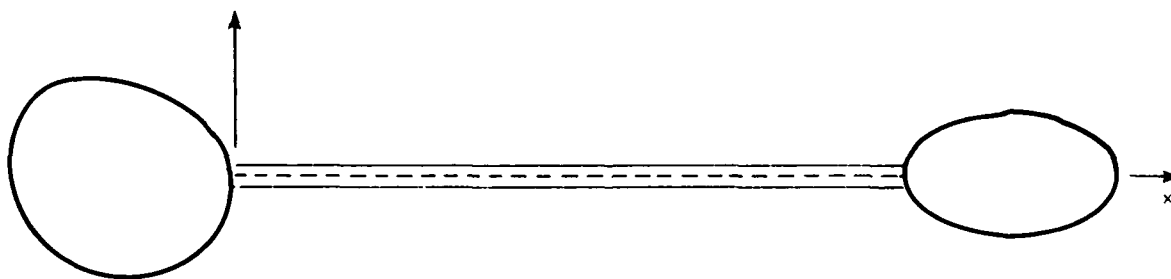


Figure 9-2. Free-free beam with tip body affixed to each end.

The tip bodies are assumed to have known mass properties which are given by:

Tip Body 0 (at $x = 0$):

$$m_0 = 0.75, \quad c_0 = 0.1, \quad \delta_0 = \pi/6, \quad J_0 = 0.6$$

Tip Body 1 (at $x = 1$):

$$m_1 = 1.50, \quad c_1 = 0.2, \quad \delta_1 = \pi/3, \quad J_1 = 0.4$$

where for tip body i , $i = 0, 1$, the indicated parameters represent, respectively, its mass m_i , the distance c_i from its center of mass to the tip of the beam, its mass center offset δ_i as measured from the extension of the longitudinal axis of the beam, and its moment of inertia J_i about its center of mass.

The equations describing the transverse displacement of the beam and the translational and rotational equilibrium of the tip bodies are given by [see Refs. 9-15, 9-26]:

$$\rho D_t^2 u + D_x^2 (EI D_x^2 u) = f, \quad x \in (0, 1), \quad t \in (0, T) \quad (9-26)$$

$$m_0 D_t^2 u - m_0 c_0 \cos \delta_0 D_t^2 D_x u + D_x (EI D_x^2 u) = 0, \quad x = 0, \quad t \in (0, T)$$

$$-m_0 c_0 \cos \delta_0 D_t^2 u + (J_0 + m_0 c_0^2) D_t^2 D_x u - EI D_x^2 u = 0, \quad x = 0, \quad t \in (0, T)$$

$$m_1 D_t^2 u + m_1 c_1 \cos \delta_1 D_t^2 D_x u + D_x (EI D_x^2 u) = 0, \quad x = 1, \quad t \in (0, T)$$

$$m_1 c_1 \cos \delta_1 D_t^2 u + (J_1 + m_1 c_1^2) D_t^2 D_x u + EI D_x^2 u = 0, \quad x = 1, \quad t \in (0, T)$$

The initial conditions are of the form

$$u = \phi, \quad D_t u = \psi, \quad x \in [0,1], \quad t = 0 \quad (9-27)$$

Setting $H \triangleq R^4 \times H^0(0,1)$ with inner product

$$\langle (\eta, \phi), (\zeta, \psi) \rangle_H \triangleq \eta^T \zeta + \langle \phi, \psi \rangle_0$$

and

$$V \triangleq \{ \hat{\phi} \in H: \hat{\phi} = (\eta, \phi), \phi \in H^2(0,1), \eta = (\phi(0), D\phi(0), \phi(1), D\phi(1))^T \}$$

with inner product

$$\langle \hat{\phi}, \hat{\psi} \rangle_V \triangleq \langle \phi, \psi \rangle_2$$

the weak form of the system given by Eqs. (9-26), (9-27) above becomes

$$\langle M_0 D_t^2 \hat{u}(t), \hat{\theta} \rangle_H + a(\hat{u}(t), \hat{\theta}) = \langle F_0(t), \hat{\theta} \rangle_H, \quad t \in (0,T), \quad \hat{\theta} \in V \quad (9-28)$$

$$\hat{u}(0) = \hat{\phi}, \quad D_t \hat{u}(0) = \hat{\psi} \quad (9-29)$$

where the indicated operations are defined as follows:

$$\hat{u}(t) \triangleq ((u(t,0), D_x u(t,0), u(t,1), D_x u(t,1))^T, u(t, \cdot)) \in V$$

$$M_0(\eta, \phi) \triangleq (\bar{M}_0 \eta, \rho \phi)$$

with

$$\bar{M}_0 \triangleq \begin{bmatrix} m_0 & -m_0 c_0 \cos \delta_0 & \vdots & & 0 \\ -m_0 c_0 \cos \delta_0 & J_0 + m_0 c_0^2 & \vdots & & \\ \vdots & \vdots & \ddots & & \\ 0 & & & m_1 & m_1 c_1 \cos \delta_1 \\ \vdots & & & m_1 c_1 \cos \delta_1 & J_1 + m_1 c_1^2 \end{bmatrix}$$

a: $V \times V \rightarrow R$ is given by

$$a(\hat{\phi}, \hat{\psi}) \triangleq \langle EI D^2 \phi, D^2 \psi \rangle_0$$

$$F_0(t) \triangleq (0, f(t, \cdot))$$

$$\hat{\phi} \triangleq ((\phi(0), D\phi(0), \phi(1), D\phi(1))^T, \phi)$$

and

$$\hat{\psi} \triangleq ((\psi(0), D\psi(0), \psi(1), D\psi(1))^T, \psi)$$

The approximation scheme for the system Eqs. (9-28), (9-29) is constructed in essentially the same manner as it was in Section 9-3.

In this example we seek to identify EI and ρ . The system is assumed to be initially at rest and subsequently excited via the input disturbance

$$f(t, x) = 10 e^x \sin 2\pi t$$

Observations at positions $x_j = 0.25j$, $j = 0, 1, \dots, 4$ and at times $t_i = 0.2i$, $i = 1, 2, \dots, 10$, were generated using the first six natural modes of the system: rigid-body translation (transverse to the beam--in plane) and rotation (about an axis normal to the plane) and four flexible modes. The true values of the parameters were assumed to be $EI = 1.0$ and $\rho = 3.0$ with start up values taken as $EI_0 = 0.7$ and $\rho_0 = 2.7$. Our results are given in Table 9-3.

Table 9-3. Convergence results, Example 3.

N	\overline{EI}^N	$\overline{\rho}^N$	\overline{J}^N
2	0.99567	3.00092	0.20×10^{-4}
3	0.99374	2.99900	0.16×10^{-4}
4	0.99849	2.99798	0.78×10^{-5}
5	0.99888	2.99910	0.28×10^{-5}

Example 4. In this example we estimate the flexural stiffness EI and linear mass density ρ for a cantilevered beam of length $\ell = 1.0$ with an attached tip body (see Fig. 9-3).

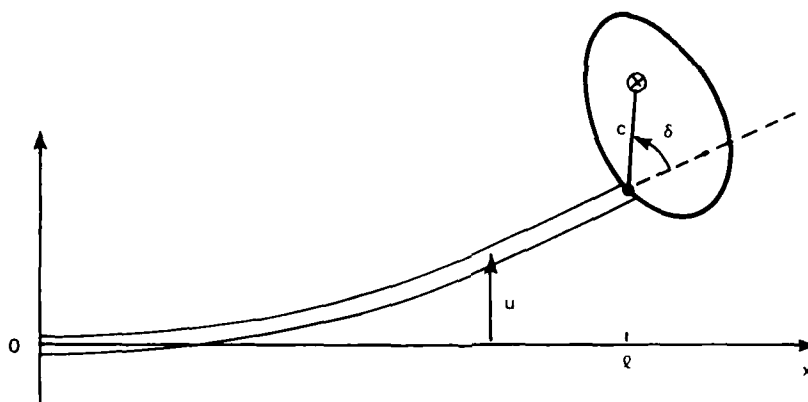


Figure 9-3. Clamped beam with tip body; deformed.

We assume that the system is initially at rest and subsequently acted upon by the distributed load

$$f(t, x) \triangleq 20 e^{-2t} e^{-20(1-x)}$$

and base acceleration

$$a_0(t) \triangleq \begin{cases} 1.0 & , \quad 0 \leq t \leq 1.5 \\ 0 & , \quad 1.5 < t < 3.0 \\ 1.0 & , \quad 3.0 \leq t < 4.0 \\ 0 & , \quad 4.0 \leq t \end{cases}$$

The equations of motion are given by [see Ref. 9-15]

$$\rho D_t^2 u + EI D_x^4 u = -a_0 D_x (\rho(1-x) + m) D_x u + f, \quad x \in (0,1), \quad t \in (0,T)$$

$$m D_t^2 u + mc(\cos \delta) D_t^2 D_x u - EI D_x^3 u = m a_0 D_x u, \quad x = 1, \quad t \in (0,T)$$

$$mc(\cos \delta) D_t^2 u + (J + mc^2) D_t^2 D_x u + EI D_x^2 u = mc(\cos \delta) c_0 D_x u + mc(\sin \delta) a_0, \\ x = 1, \quad t \in (0,T) \quad (9-30)$$

with boundary and initial conditions

$$u = 0, \quad D_x u = 0; \quad x = 0, \quad t \in [0,T] \quad (9-31)$$

and

$$u = \phi, \quad D_t u = \psi; \quad x \in [0,1], \quad t = 0 \quad (9-32)$$

respectively, where the quantities m , c , δ , and J are as they were defined in Example 3. Once again only minor modifications (similar to those outlined in the previous example) are necessary so as to make the theory presented in Sections 9-2 and 9-3 applicable to the system given by Eqs. (9-30) through (9-32) above. Taking the true values of EI and ρ to be 1.0 and 2.0, respectively, and setting $m = 4.0$, $c = 0.2$, $\delta = \pi/3$, and $J = 0.4$, displacement observations at positions $x_j = 0.625 + 0.125j$, $j = 1,2,3$ and at times $t_i = 3.5 + 0.5i$, $i = 1,2,3$ were generated using the first three natural modes of the unforced, unaccelerated system.

The start-up values were taken as $EI_0 = 0.7$ and $\rho_0 = 2.5$. The final converged values for \overline{EI}^N and $\overline{\rho}^N$ together with the residual sum of squares \overline{J}^N for several values of N are given in Table 9-4 below.

Table 9-4. Convergence results, Example 4.

N	\overline{EI}^N	$\overline{\rho}^N$	\overline{J}^N
2	1.00046	2.07731	0.40×10^{-3}
3	1.00135	2.06652	0.22×10^{-3}
4	1.00117	2.05180	0.23×10^{-3}
5	1.00086	2.04776	0.26×10^{-3}

References

- 9-1. Sun, C. T., Kim, B. J., and Bogdanoff, J. L., "On the Derivation of Equivalent Simple Models for Beam and Plate-like Structures in Dynamic Analysis," Proc. AIAA Dynamics Specialists Conference, Atlanta, GA, April 1981, pp. 523-532.
- 9-2. Chen, C. C. and Sun, C. T., "Transient Analysis of Large Frame Structures by Simple Models," J. Astronaut. Sci., Vol. 31, No. 3, Jul.-Sep. 1983, pp. 359-379.
- 9-3. Noor, A. K. and Anderson, C. M., "Analysis of Beam-like Lattice Trusses," Comput. Methods Appl. Mech. Engrg., Vol. 20, 1979, pp. 53-70.

- 9-4. Juang, J. N. and Sun, C. T., "System Identification of Large Flexible Structures by Using Simple Continuum Models," J. Astronaut. Sci., Vol. 31, No. 1, Jan.-Mar. 1983, pp. 77-98.
- 9-5. Banks, H. T. and Crowley, J. M., "Parameter Estimation for Distributed Systems Arising in Elasticity," Proc. NKCU/AAS Symposium on Engineering Sciences and Mechanics, National Cheng Kung University, Taiwan, December 1981, pp. 158-177; also Advances in the Astronautical Sciences, Vol. 50 (to appear).
- 9-6. Banks, H. T. and Crowley, J. M., "Parameter Estimation in Timoshenko Beam Models," J. Astronaut. Sci., Vol. 31, No. 3, Jul.-Sep. 1983, pp. 381-397.
- 9-7. Banks, H. T. and Crowley, J. M., "Parameter Identification in Continuum Models," Proc. 1983 American Control Conference, San Francisco, CA, June 1983.
- 9-8. Kunisch, K. and Graif, E., "Parameter Estimation for the Euler-Bernoulli Beam," Inst. für Math. Bericht 83-26, Techn. Universität Graz, December 1983.
- 9-9. Crowley, J. M., Numerical Methods of Parameter Identification for Problems Arising in Elasticity, Ph.D. Thesis, Division of Applied Mathematics, Brown University, Providence, RI, May 1982.
- 9-10. Rosen, I. G., "A Cubic Spline Based Approximation Scheme for the Estimation of Parameters in Hybrid Systems Involving Beams with Attached Tip Bodies," ACROSS-Eleven Fifth Semiannual Technical Report, CSDL-R-1687, Charles Stark Draper Laboratory, Cambridge, MA, March 1984; Section 8 (also submitted to J. Math. Anal. Appl.).
- 9-11. Banks, H. T. and Crowley, J. M., "Estimation of Material Parameters in Elastic Systems," Report LCDS-84-20, Lefschetz Center for Dynamical Systems, Brown University, Providence, RI, June 1984.

- 9-12. Banks, H. T., Crowley, J. M., and Kunisch, K., "Cubic Spline Approximation Techniques for Parameter Estimation in Distributed Systems," IEEE Trans. Automatic Control, Vol. AC-28, No. 7, July 1983, pp. 773-786.
- 9-13. Banks, H. T. and Murphy, K. A., "Estimation of Coefficients and Boundary Parameters in Hyperbolic Systems," Report LCDS-84-5, Lefschetz Center for Dynamical Systems, Brown University, Providence, RI, February 1984.
- 9-14. Clough, R. W. and Penzien, J., Dynamics of Structures, McGraw-Hill, New York, NY, 1975.
- 9-15. Storch, J. and Gates, S., "Transverse Vibration and Buckling of a Cantilevered Beam with Tip Body Under Axial Acceleration," J. Sound and Vibration (to appear, 1985); also Report CSDL-R-1675, Charles Stark Draper Laboratory, Cambridge, MA, October 1983.
- 9-16. Schwartz, L., Théorie des Distributions, Vol. I, II, Hermann & Cie, Paris, 1951.
- 9-17. Aubin, J. P., Approximation of Elliptic Boundary Value Problems, Wiley-Interscience, New York, NY, 1972.
- 9-18. Oden, J. T. and Reddy, J. N., Mathematical Theory of Finite Elements, Wiley-Interscience, New York, NY, 1976.
- 9-19. Showalter, R. E., Hilbert Space Methods for Partial Differential Equations, Pitman, London, England, 1977.
- 9-20. Lions, J. L., Optimal Control of Systems Governed by Partial Differential Equations, Springer-Verlag, New York, NY, 1971.
- 9-21. Lions, J. L. and Magenes, E., Non-Homogeneous Boundary Value Problems and Applications, Vol. I, Springer-Verlag, New York, NY, 1972.
- 9-22. Helmborg, G., Introduction to Spectral Theory in Hilbert Space, North Holland, Amsterdam, Netherlands, 1969.

- 9-23. Krein, S. G., Linear Differential Equations in Banach Space, American Mathematical Society, Providence, RI, 1971.
- 9-24. Yosida, K., Functional Analysis, Springer-Verlag, New York, NY, 1966.
- 9-25. Pazy, A., Semigroups of Linear Operators and Applications to Partial Differential Equations, Springer-Verlag, New York, NY, 1983.
- 9-26. Storch, J. and Gates, S., "Planar Dynamics of a Uniform Beam with Rigid Bodies Affixed to the Ends," Report CSDL-R-1629, Charles Stark Draper Laboratory, Cambridge, MA, May 1983.
- 9-27. Prenter, P. M., Splines and Variational Methods, Wiley, New York, NY, 1975.
- 9-28. Schultz, M. H., Spline Analysis, Prentice-Hall, Englewood Cliffs, NJ, 1973.
- 9-29. Dupont, T., " L^2 -Estimates for Galerkin Methods for Second-Order Hyperbolic Equations," SIAM J. Numer. Anal., Vol. 10, 1973, pp. 880-889.
- 9-30. Banks, H. T. and Daniel, P. L., "Estimation of Variable Coefficients in Parabolic Distributed Systems," Report LCDS-82-22, Lefschetz Center for Dynamical Systems, Brown University, Providence, RI, September 1982; also IEEE Trans. Automatic Control (to appear).
- 9-31. Levenberg, K., "A Method for the Solution of Certain Non-linear Problems in Least Squares," Quart. Appl. Math., Vol. 2, 1944, pp. 164-168.
- 9-32. Marquardt, D. W., "An Algorithm for Least-Squares Estimation of Nonlinear Parameters," J. SIAM, Vol. 11, No. 2, 1963.

SECTION 10

LARGE ANGLE SPACECRAFT MANEUVERS USING AN ANALYTIC SOLUTION FOR TRACKING AND DISTURBANCE ACCOMMODATION

10.1 Overview

In this section we consider the problem of maneuvering a flexible spacecraft through a large angle, where the disturbance-accommodating feedback control tracks a desired output state. The desired output state is provided from an open-loop solution for the linear system model. The components of the disturbance vector are assumed to be represented in terms of Fourier series. Closed-form solutions are provided for the Riccati, prefilter, state trajectory, and residual-state trajectory equations which define the optimal control. Example maneuvers are presented where control-rate penalties have been included in the performance index for frequency-shaping, in order to smooth both the open-loop and closed-loop control commands.

A common method for investigating the effectiveness of various control designs consists of studying frequency domain characteristics of the control, by numerically evaluating the required Fourier transform. For finite-time open-loop and closed-loop control problems this can be accomplished by either numerically integrating the integral definition of the Fourier transform for each frequency of interest, or by using a fast-Fourier-transform algorithm. Alternatively, we present in this section a computationally efficient closed-form solution for the Fourier transform of finite-time open-loop and closed-loop control problems, where the dynamics of the control is governed by matrix exponentials.

10.2 Introduction

The determination of a control time history for maneuvering a flexible spacecraft has been the subject of many recent investigations in the area of spacecraft attitude control [Refs. 10-1 through 10-24]. Many early papers developed open-loop methods [Refs. 10-1 through 10-11, 10-13, 10-19, 10-24] by assuming that the control can be obtained from either Pontryagin's principle or by assuming that the control can be expressed in terms of a Fourier series. More recent papers have developed closed-loop methods [Refs. 10-6, 10-10, 10-12, 10-15 through 10-18, 10-20 through 10-23] which consider classical regulator, tracking, and terminal-tracking control formulations. Moreover, in an effort to minimize the deleterious effects of control spillover, a number of authors have proposed frequency-shaping techniques [Refs. 10-2, 10-14 through 10-17, 10-19, 10-21 through 10-25, 10-27], which attempt to roll-off the high frequency content of the applied control.

The dual tracking and disturbance-accommodation control problem described in this section extends the closed-loop tracking results of Turner, Chun, and Juang [Refs. 10-15, 10-16] by permitting simultaneous frequency-shaped tracking and deterministic disturbance rejection. The resulting control algorithm is applied to the problem of maneuvering a flexible spacecraft through large angles about a single axis.

In Section 10.3 the dual tracking and disturbance-accommodation control problem is formulated by defining an inhomogeneous linear-quadratic optimization problem, where the plant dynamics equation is forced by the control and a disturbance vector. The state variable description for the disturbance is specified in terms of a Fourier series. The performance index for the control problem consists of integral quadratic terms in the state, control, and control-rates [Refs. 10-16 through 10-18, 10-21 through 10-23, 10-25, 10-27]. The necessary conditions defining the solution for the control problem are given by two

coupled time-varying Riccati-like differential equations [Ref. 10-28]. The first equation is the standard Riccati equation, which possesses a well-known solution in terms of a steady-state plus transient term [Refs. 10-12, 10-14 through 10-18, 10-28 through 10-34]. The second equation is a vector prefilter equation which has foreknowledge of the desired output state and of the deterministic disturbance which is to be suppressed. A closed-form solution is presented in Section 10.4 for the pre-filter equation. In Section 10.4.2 the solutions for the Riccati and prefilter equations are cast in recursive form for efficient computer implementation. Closed-form solutions are presented for the state trajectory equation in Section 10.5 and for the residual-state trajectory equation in Section 10.6. Maneuver simulations are presented in Section 10.7 for frequency-shaped control-rate penalty designs [Refs. 10-14 through 10-18, 10-25, 10-27]. An analytic Fourier transform for the control is presented in Section 10.8 for a class of finite-time control problems.

10.3 The Optimal Tracking and Disturbance-Accommodation Control Problem

The optimal reference tracking problem is formulated by finding the control inputs $u(t)$ to minimize

$$J = \frac{1}{2} \|y^*(t_f) - y(t_f)\|_S^2 + \frac{1}{2} \int_0^{t_f} \{ \|y^*(t) - y(t)\|_Q^2 + \|u(t)\|_R^2 \} dt \quad (10-1)$$

for the system

$$\dot{x} = Ax + Bu + d, \quad x_0 = x(t_0) \quad (10-2)$$

$$y = Cx$$

where $\|p\|_W = p^T W p$, y^* is the desired output state, A is the system dynamics matrix, B is the control influence matrix, d is the disturbance state which is modeled in terms of Fourier series, C is the output matrix, S is the terminal state weight matrix, Q is the state weight matrix, R is the control weight matrix, x is the N -dimensional state vector, and u is the N_c -dimensional control vector. Moreover, we assume that the system is controllable and observable.

In order for the control system to track in the presence of known disturbances, we need a state variable model which generates the deterministic disturbance that excites the spacecraft response. To this end, we model the disturbance state vector as [Ref. 10-19]

$$d(t) = \Lambda e^{Mt} \beta \quad (10-3)$$

where Λ is a constant matrix whose rows consist of the Fourier series coefficients for individual disturbances, M is a constant block-diagonal matrix containing the frequencies of the disturbances, and β is a constant vector. Note, however, that Eq. (10-3) is a general expression for either a Fourier series or a trigonometric series which models sub-harmonic terms for nonlinear effects [Ref. 10-23].

For maneuvers where the state is augmented by the control and control-rates for frequency-shaping, the A and B matrices are modified as shown in References 10-14 through 10-18 and 10-27.

The desired output vector is modelled by

$$y^*(t) = Cx^*(t) = CH e^{\Omega t} s_0 \quad (10-4)$$

$$s_0 = (x^*(0), \lambda^*(0))^T$$

where $H = [I : 0]$ is a $N \times 2N$ selection operator, Ω is a $2N \times 2N$ constant matrix, and $\lambda(t)$ is the open-loop costate vector [Refs. 10-8 through 10-11, 10-13].

As shown in what follows, the explicit presence of a matrix exponential in Eq. (10-4) permits a closed-form solution to be obtained for the prefilter equation of the tracking/disturbance-accommodation control problem.

10.4 Necessary Conditions and Solutions for the Optimal Control

The necessary conditions defining the tracking/disturbance-accommodation problem for Eqs. (10-1), (10-2), and (10-3) are given by the following Riccati-like differential equations [Ref. 10-28]:

$$\dot{P} = -PA - A^T P + PBR^{-1}B^T P - C^T Q C \quad (10-5)$$

$$P(t_f) = C^T S C$$

$$\dot{\xi} = -[A - BR^{-1}B^T P]^T \xi - C^T Q C x^*(t) + P d(t) \quad (10-6)$$

$$\xi(t_f) = C^T S C x^*(t_f)$$

and the optimal control is given by

$$u = -R^{-1}B^T [Px - \xi] \quad (10-7)$$

10.4.1 Closed Form Solution for the Riccati Equation

As shown in References 10-10, 10-14 through 10-18, and 10-27 through 10-34, the solution for Eq. (10-5) can be written in terms of a steady-state plus transient term, as follows:

$$P(t) = P_{ss} + Z^{-1}(t)$$

where P_{ss} is the solution for the algebraic Riccati equation
[Refs. 10-28, 10-29, 10-31, 10-33, 10-35]

$$-P_{ss}A - A^T P_{ss} + P_{ss}BR^{-1}B^T P_{ss} - C^TQC = 0$$

and the closed form solution for $Z(t)$ can be shown to be [Refs. 10-33, 10-36, 10-37]:

$$Z(t) = Z_{ss} + e^{\bar{A}(t-t_f)} [Z(t_f) - Z_{ss}] e^{\bar{A}^T(t-t_f)} \quad (10-8)$$

where $\bar{A} \triangleq A - BR^{-1}B^T P_{ss}$ is the system stability matrix,

$Z(t_f) = (C^TSC - P_{ss})^{-1}$, $\dot{Z} = \bar{A}Z + Z\bar{A}^T - BR^{-1}B^T$, and Z_{ss} satisfies the algebraic Lyapunov equation [Refs. 10-26, 10-33, 10-38, 10-39]

$$\bar{A}Z_{ss} + Z_{ss}\bar{A}^T = -BR^{-1}B^T$$

10.4.2 Closed Form Solution for the Prefilter Equation

The solution for ξ in Eq. (10-6) follows on assuming the product form solution [Refs. 10-16, 10-17]

$$\xi(t) = Z^{-1}(t)r(t) \quad (10-9)$$

where Z is defined by Eq. (10-8) and the linear constant-coefficient vector differential equation for r can be shown to be

$$\dot{r} - \bar{A}r = Z(t)P_{ss}d(t) + d(t) - Z(t)C^TQCx^*(t)$$

$$r(t_f) = Z(t_f)C^TSCx^*(t_f)$$

The solution for r follows as

$$r(t) = e^{\bar{A}t} [r_0 - \gamma(t)] \quad (10-10)$$

where

$$\gamma(t) \triangleq \int_0^t e^{-\bar{A}\tau} \{Z(\tau)C^TQCx^*(\tau) - d(\tau) - Z(\tau)P_{ss}d(\tau)\} d\tau$$

and the initial condition for r is given by

$$r_0 = e^{-\bar{A}t_f} Z(t_f) C^TSCx^*(t_f) + \gamma(t_f)$$

The solution for the integral expression in Eq. (10-10) follows on introducing $Z(t)$ from Eq. (10-8), $x^*(t)$ from Eq. (10-4), and $d(t)$ from Eq. (10-3) into Eq. (10-10), leading to

$$\begin{aligned} \gamma(t) = & \Psi(-\bar{A}, D_1, \Omega, t)s_0 + D_2\Psi(\bar{A}^T, D_3, \Omega, t)s_0 \\ & - \Psi(-\bar{A}, D_4, M, t)\beta - D_2\Psi(\bar{A}^T, D_5, M, t)\beta \end{aligned} \quad (10-11)$$

where

$$\Psi(A, B, C, t) \triangleq \int_0^t e^{A\tau} B e^{C\tau} d\tau \quad (10-12)$$

$$D_1 \triangleq Z_{ss}C^TQCH, \quad D_2 \triangleq e^{-\bar{A}t_f} [Z(t_f) - Z_{ss}]e^{-\bar{A}^T t_f}$$

$$D_3 \triangleq C^TQCH, \quad D_4 \triangleq Z_{ss}P_{ss}\Lambda + \Lambda, \quad D_5 \triangleq P_{ss}\Lambda$$

and A is $n_1 \times n_1$, B is $n_1 \times n_2$, C is $n_2 \times n_2$, and $\Psi(\cdot)$ is $n_1 \times n_2$. The matrix exponential solution for $\Psi(\cdot)$ in Eq. (10-12) is presented in Section 10.9.1. Also presented there are the recursive equations for generating the solution for $\Psi(\cdot)$ at discrete times.

Subject to the recursion relationships of Section 10.9.1, the time histories for P and ξ in Eq. (10-7) easily follow, where $Z[(n+1)\Delta t]$ in Eq. (10-8) is given by

$$Z[(n+1)\Delta t] = Z_{ss} + e^{\bar{A}\Delta t} [Z(n\Delta t) - Z_{ss}] e^{\bar{A}^T \Delta t}$$

and

$$Z(0) = Z_{ss} + e^{-\bar{A}t_f} [Z(t_f) - Z_{ss}] e^{-\bar{A}^T t_f}$$

10.5 Closed-Form Solution for the State Trajectory Equation

The closed-loop state trajectory equation is obtained by introducing Eq. (10-7) into Eq. (10-2), yielding

$$\dot{x} = (\bar{A} - BR^{-1}B^T Z^{-1}(t))x + BR^{-1}B^T \xi(t) + d(t) \quad (10-13)$$

The solution for $x(t)$ in Eq. (10-13) is obtained by carrying out two steps. First, the homogeneous part of Eq. (10-13) is solved in terms of a state transition matrix solution. Second, using a variation of parameters technique, the complete solution for $x(t)$ is obtained.

As shown in References 10-10, 10-12, and 10-18, the homogeneous solution for Eq. (10-13) is given by

$$x_h(t) = \phi(t)x_0$$

where

$$\phi(t) = Z(t)e^{-A^T t} Z^{-1}(0) \quad (10-14a)$$

$$\dot{\phi}(t) = [\bar{A} - BR^{-1}B^T Z^{-1}(t)]\phi(t); \quad \phi(0) = I \quad (10-14b)$$

Denoting

$$\phi_1(t) \triangleq \phi^{-1}(t) \equiv Z(0)e^{\bar{A}^T t} Z^{-1}(t) \quad (10-15a)$$

it follows that

$$\dot{\phi}_1(t) = -\phi_1(t)[\bar{A} - BR^{-1}B^T Z^{-1}(t)]; \quad \phi_1(0) = I \quad (10-15b)$$

Equation (10-15) is recorded above since it is required for the solution of Eq. (10-13).

Let us assume that the general solution for Eq. (10-13) is given by

$$x(t) = \phi(t)[x_0 + x_p(t)] \quad (10-16)$$

where $x_p(t)$ is to be determined. Introducing Eq. (10-16) into Eq. (10-13), while recalling Eqs. (10-14) and (10-15) leads to

$$\dot{x}_p(t) = \phi_1(t)BR^{-1}B^T\xi(t) + \phi_1(t)d(t)$$

where the solution for $\xi(t)$ is defined by Eq. (10-9) and $d(t)$ is defined by Eq. (10-3). The solution for $x_p(t)$ can be shown to be

$$x_p(t) = \phi_1(t)r(t) + r_1(t) + r_2(t) + x_{p0} \quad (10-17)$$

where $r(t)$ is defined by Eq. (10-10), and

$$r_1(t) \triangleq \int_0^t \phi_1(\tau) Z(\tau) C^T Q y^*(\tau) d\tau \quad (10-18)$$

$$r_2(t) \triangleq -\int_0^t \phi_1(\tau) Z(\tau) P_{ss} d(\tau) d\tau \quad (10-19)$$

$$x_{p0} \triangleq -r_0 \quad (\text{See Eq. (10-10)})$$

Substituting Eq. (10-17) into Eq. (10-16) yields the following solution for the state trajectory equation

$$x(t) = \phi(t) \{x_0 + r_1(t) + r_2(t) + x_{p0}\} + r(t) \quad (10-20)$$

The solutions for $r_1(t)$ and $r_2(t)$ are obtained by introducing Eq. (10-15) into Eqs. (10-18) and (10-19), leading to

$$r_1(t) = Z(0) \Psi(\bar{A}^T, D_3, \Omega, t) s_0 \quad (10-21)$$

$$r_2(t) = Z(0) \Psi(\bar{A}^T, D_5, M, t) \beta \quad (10-22)$$

where $\Psi(\cdot)$ is defined by Eq. (10-12). Moreover, we observe that the integrals appearing in Eq. (10-21) and (10-22) have been previously defined in Eq. (10-11); thus no additional computational effort is required in order to produce $r_1(t)$ and $r_2(t)$.

10.6 Closed-Form Solution for the Residual State Trajectory Equation

Assume that the residual state trajectory equation is given by

$$\dot{x}_r = A_r x_r + B_r u + d_r, \quad x_r(0) \text{ given} \quad (10-23)$$

where u is defined by Eq. (10-7) and $d_r \triangleq \Lambda_r e^{Mt} \beta$ is analogous to Eq. (10-3). By introducing Eq. (10-7) into Eq. (10-23) we obtain

$$\dot{x}_r = A_r x_r - B_r R^{-1} B^T [P_{ss} x + Z^{-1}(x - r)] + d_r$$

where x is defined by Eq. (10-20). The solution for x_r can be shown to be

$$\begin{aligned} x_r(t) = & e^{A_r t} x_{r0} - e^{A_r t} \int_0^t e^{-A_r \tau} B_r R^{-1} B^T [P_{ss} x(\tau) + Z^{-1}(\tau) \{x(\tau) - r(\tau)\}] d\tau \\ & + \{e^{A_r t} \int_0^t e^{-A_r \tau} \Lambda_r e^{M\tau} d\tau\} \beta \end{aligned}$$

where r is defined by Eq. (10-10). After considerable labor, the integrals above can be expressed as

$$x_r(t) = e^{A_r t} x_{r0} + \sum_{i=1}^{11} I_i(t) \quad (10-24)$$

where

$$I_1(t) \triangleq -[r_1(t)]_{12}^\alpha, \quad I_2(t) \triangleq -[r_1(t)]_{13}^{s_0}, \quad I_3(t) \triangleq [r_2(t)]_{13}^\beta$$

$$I_4(t) \triangleq -[\Gamma_3(t)]_{12} D_2 \alpha, \quad I_5(t) \triangleq -[\Gamma_3(t)]_{12} r_0, \quad I_6(t) \triangleq [\Gamma_3(t)]_{13} s_0$$

$$I_7(t) \triangleq -[\Gamma_4(t)]_{13} \beta, \quad I_8(t) \triangleq -[\Gamma_5(t)]_{12} \alpha, \quad I_9(t) \triangleq -[\Gamma_5(t)]_{13} s_0$$

$$I_{10}(t) \triangleq [\Gamma_6(t)]_{13} \beta, \quad I_{11}(t) \triangleq e^{A_r t} \psi(-A_r, \Lambda_r, M, t) \beta,$$

$$\alpha \triangleq Z^{-1}(0)(x_0 - r_0)$$

$$\Gamma_1(t) \triangleq \Gamma(A_r, D_6, -\bar{A}^T, D_3, \Omega, t), \quad \Gamma_2(t) \triangleq \Gamma(A_r, D_6, -\bar{A}^T, D_5, M, t)$$

$$\Gamma_3(t) \triangleq \Gamma(A_r, D_7, \bar{A}, D_1, \Omega, t), \quad \Gamma_4(t) \triangleq \Gamma(A_r, D_7, \bar{A}, D_4, M, t)$$

$$\Gamma_5(t) \triangleq \Gamma(A_r, D_8, -\bar{A}^T, D_3, \Omega, t), \quad \Gamma_6(t) \triangleq \Gamma(A_r, D_8, -\bar{A}^T, D_5, M, t)$$

and Γ is defined by Eq. (10-48), $[\Gamma]_{12} \triangleq G_1(t)$ is defined by Eq. (10-46), $[\Gamma]_{13} \triangleq H_1(t)$ is defined by Eq. (10-47), and

$$D_6 \triangleq B_r R^{-1} B^T P_{ss} Z_{ss} \quad D_7 \triangleq B_r R^{-1} B^T P_{ss} \quad D_8 \triangleq B_r R^{-1} B^T$$

10.7 Illustrative Examples

The specific model considered in this subsection consists of a rigid hub with four identical elastic appendages attached symmetrically about the central hub, and is derived from the experimental structure of Reference 10-41 using NASTRAN data (see Fig. 10-1). In particular, the following idealizations are considered: (i) single-axis maneuvers; (ii) in-plane motion; (iii) anti-symmetric deformations; (iv) small

linear flexural deformations; (v) only the linear time-invariant form of the equations of motion are considered; and (vi) the control actuators are modelled as concentrated torque-generating devices. Figure 10-2 shows the first three antisymmetric modes which, together with the rigid body mode, defines the full-order model. The control system for the vehicle consists of a single controller in the rigid part of the structure. The structural parameters of the model are given in Reference 10-41. Because of the above assumptions, only the anti-symmetric modes are used for the example cases of this subsection. In addition, full-state feedback is assumed.

The output vector is assumed to be given by

$$y = (y_1, y_2, y_3, y_4, y_5^T)^T$$

where

- $y_1 \triangleq$ central hub angular velocity
- $y_2 \triangleq$ angular velocity at the mid-span location
relative to the central hub
- $y_3 \triangleq$ central hub angular position
- $y_4 \triangleq$ tip deflection of each appendage
- $y_5 \triangleq$ controls and control-rates

The output sub-vector y_5 is present in the formulation when control-rates are penalized. The elements of y_5 correspond to the additional augmented states. In the following cases, the augmented states consist of the control torque and control-torque rate, since the performance index includes a penalty on the second time derivative of the control torque.

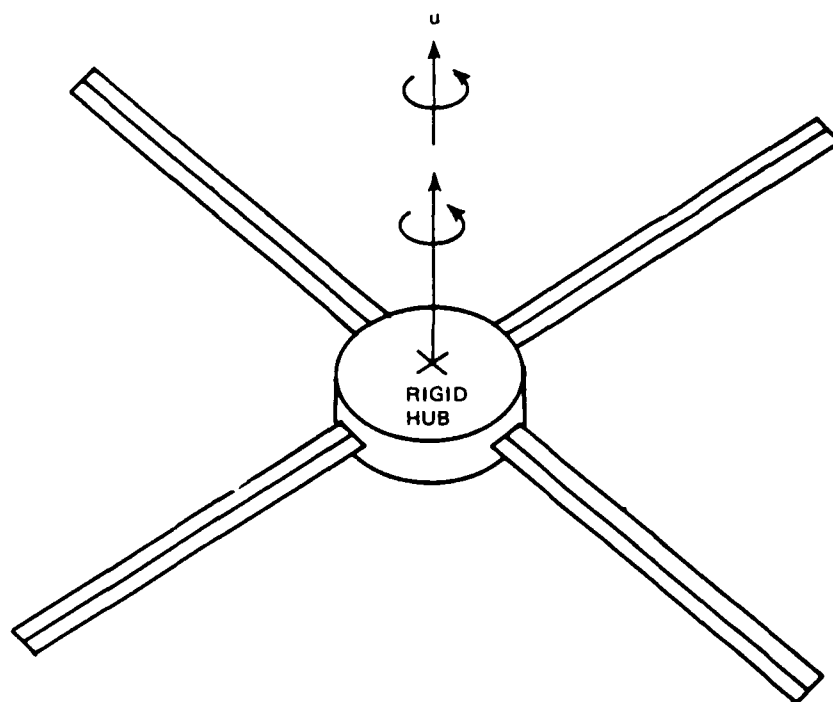
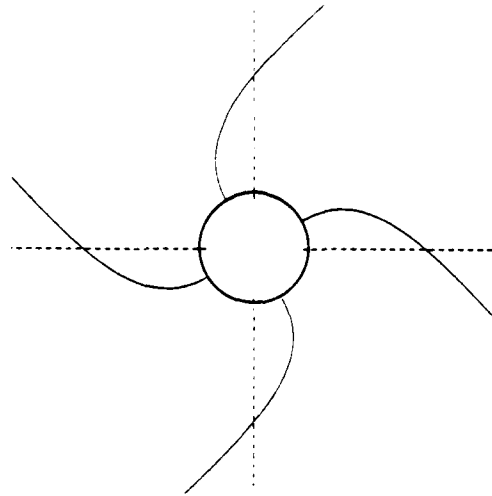
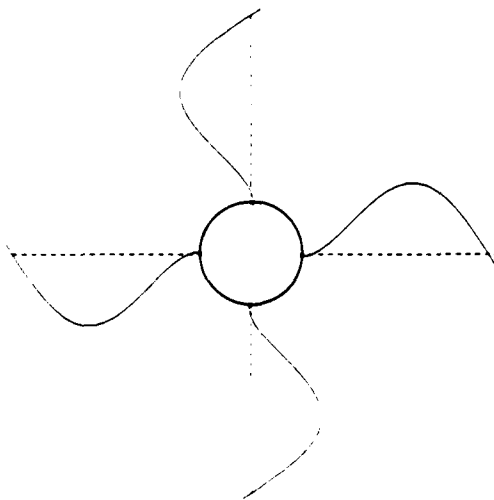


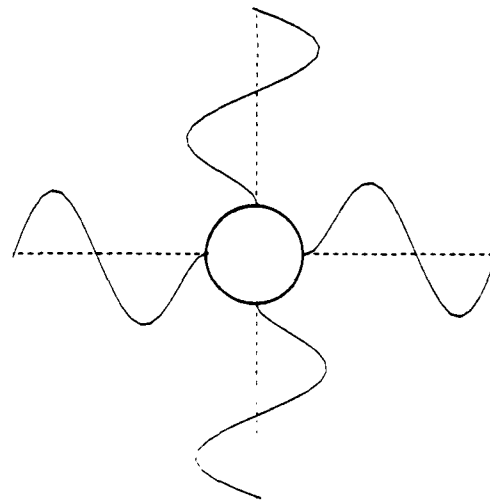
Figure 10-1. Undeformed experimental structure.



MODE 1 (1.261 Hz)



MODE 2 (8.396 Hz)



MODE 3 (24.905 Hz)

Figure 10-2. Antisymmetric deformation modes of experimental structure.

The state vectors x and x^* consist of the following elements:

$$x = (x_1, x_2, x_3, x_4, x_5, x_6)^T$$

where

- $x_1 \triangleq$ central hub angle
- $x_2 \triangleq$ first mode amplitude
- $x_3 \triangleq$ central hub angular velocity
- $x_4 \triangleq$ first mode amplitude rate
- $x_5 \triangleq$ control torque
- $x_6 \triangleq$ control torque rate

The second and third flexible modes are treated as unmodelled residual modes, which are excited by the control torque and which affect the output variables y_1, y_2, y_3 , and y_4 .

Table 10-1 shows the weight matrices which are used for all of the test cases. Each test case involves a 5 second, 10° maneuver, starting at rest and ending at rest. The graphical results of the test case maneuvers are shown in Figs. 10-3 through 10-7 and are described qualitatively in what follows.

Case 1 (Fig. 10-3) shows the results for a tracking controller which does not take into account the presence of disturbances. The disturbance in this case is provided at the central hub by a disturbance torque described by

$$T_d = 0.1 \sin 2\pi t + 0.1 \sin 4\pi t$$

Table 10-1. Weight matrices for test case maneuvers.

$$Q^* = \text{diag} [0.1, 0.5, 1.0, 0.1, 1(-9), 1(-9)]^{(1)}$$

$$R^* = 1.0$$

$$Q = \text{diag} [0.001, 1.0, 0.001, 1.0, 1(-9), 1(-9)]$$

$$R = 1.0$$

$$S = \begin{bmatrix} 5.38(9) & & & & & \\ 1.83(9) & 1.86(9) & & & & \\ 1.58(9) & 5.44(8) & 3.63(9) & & & \\ 2.22(9) & -1.58(8) & 7.52(8) & 6.21(10) & & \\ 3.75(7) & 7.71(6) & 1.04(7) & 1.20(8) & 6.84(5) & \\ 2.03(5) & 4.85(4) & 5.60(4) & 6.75(5) & 3.80(3) & 5.12(2) \end{bmatrix} \quad \text{SYMMETRIC}$$

Note 1. $b(a)$ denotes $b \times 10^a$

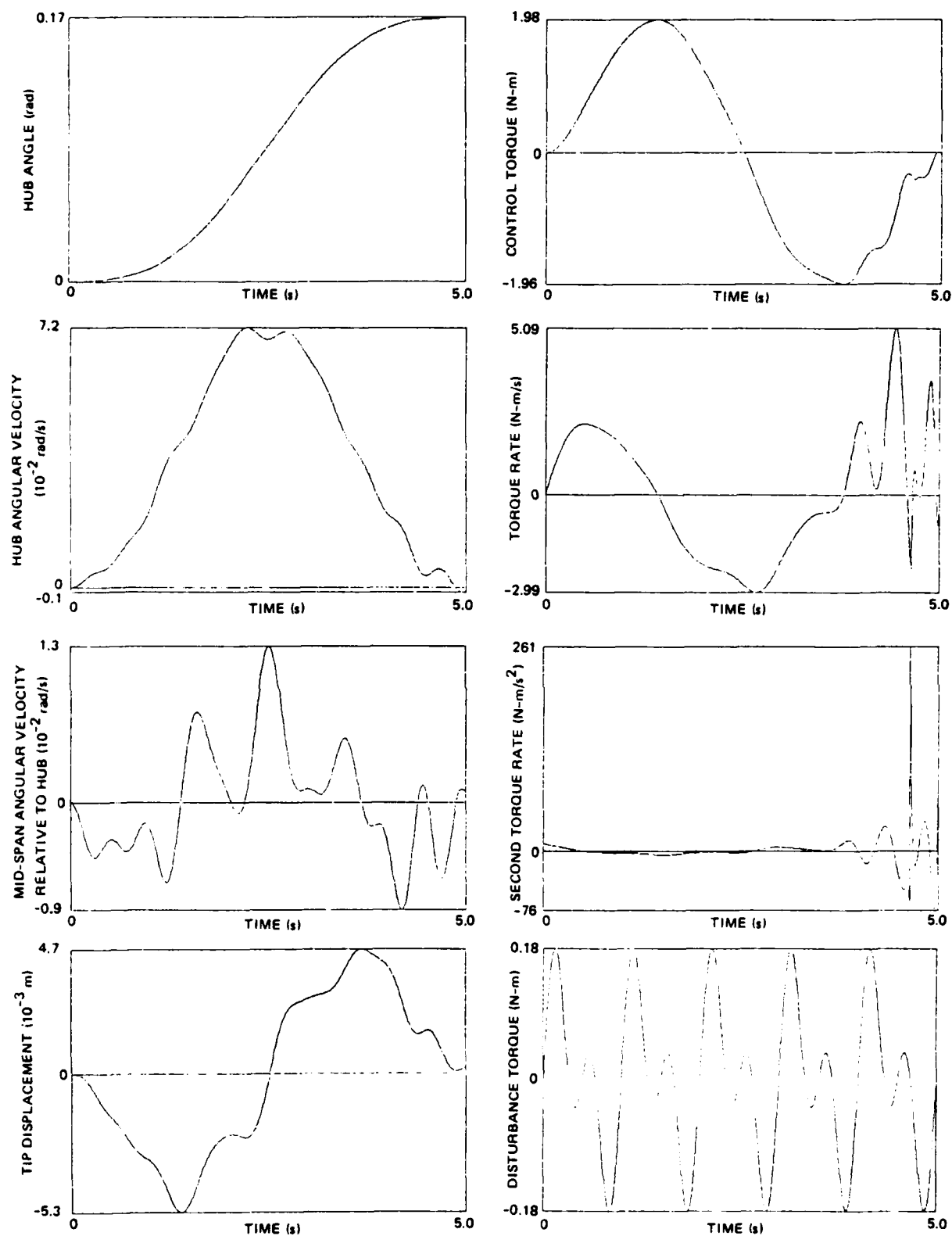


Figure 10-3. Case 1: Linear tracking controller.

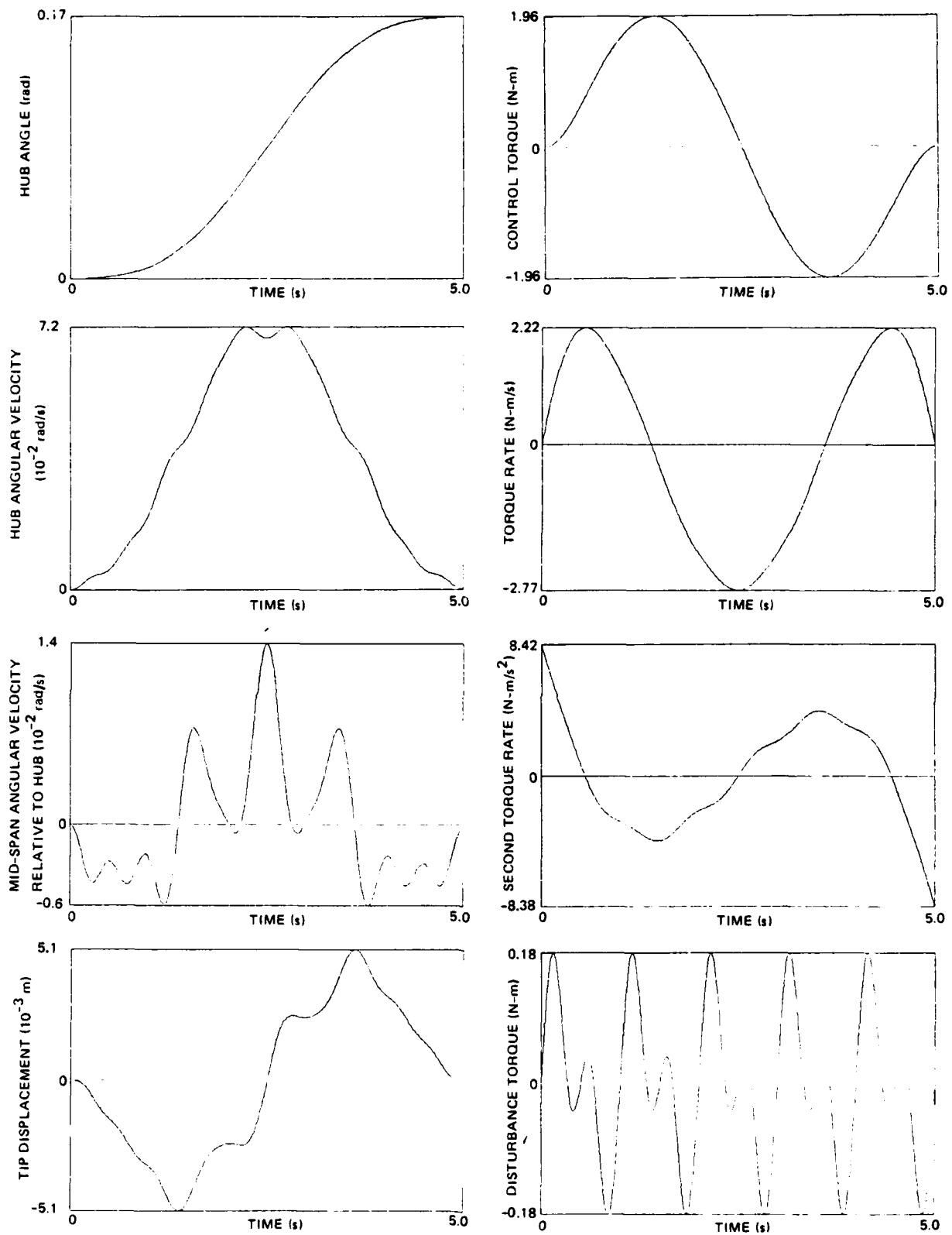


Figure 10-4. Case 2: Dual tracking/disturbance-accommodation controller.

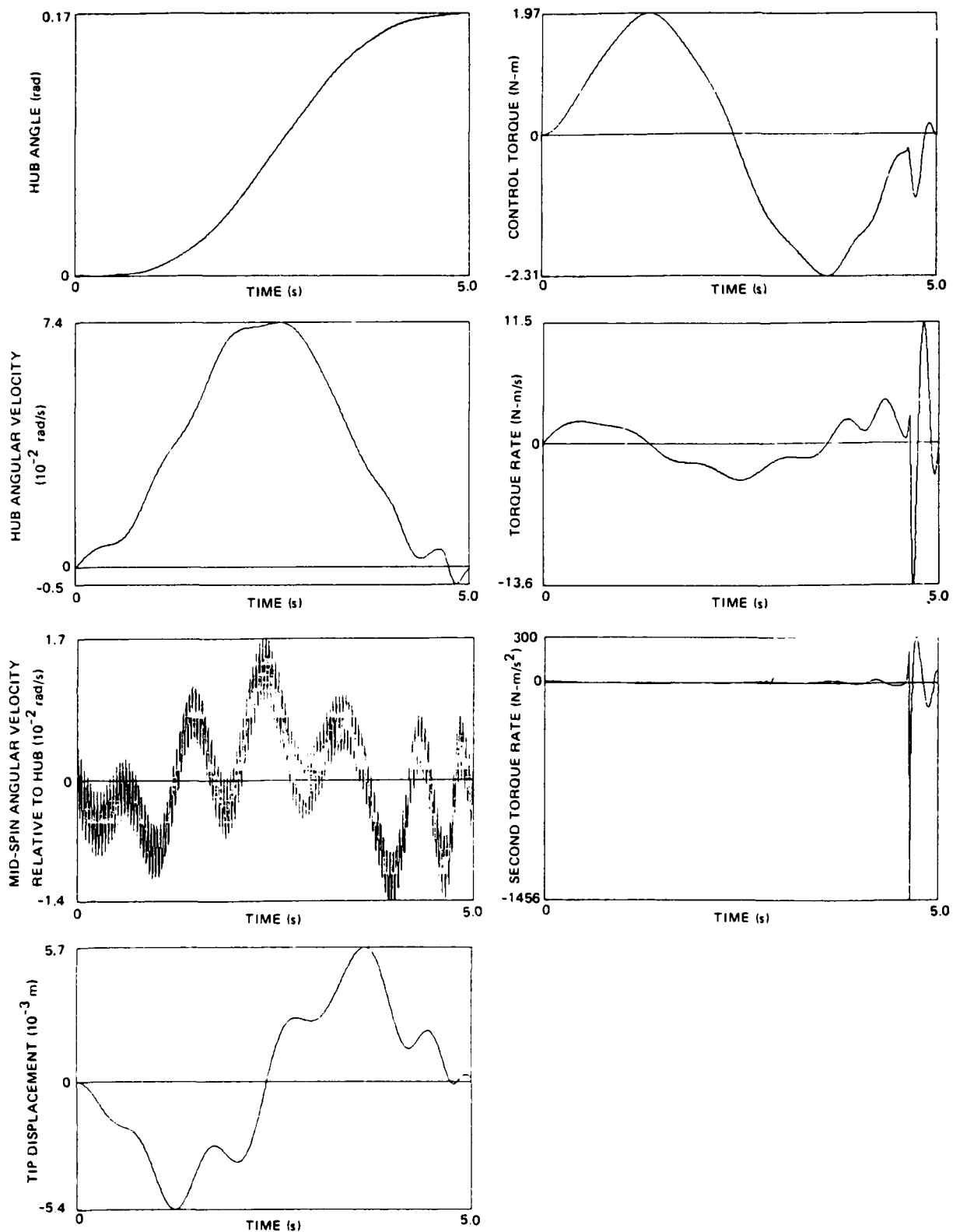
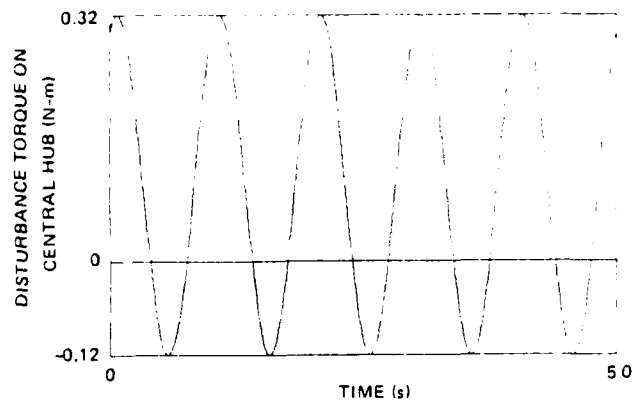
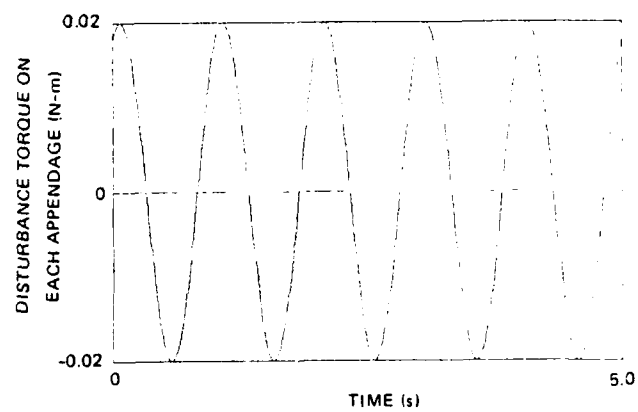


Figure 10-5. Case 3: Linear tracking controller with multiple disturbance torques.



$$T_d = 0.1 + 0.1 \sin(2\pi t) + 0.2 \cos(2\pi t)$$



$$T_d = 0.01 \sin(2\pi t) + 0.02 \cos(2\pi t)$$

Figure 10-6. Disturbance torques for Cases 3 and 4.

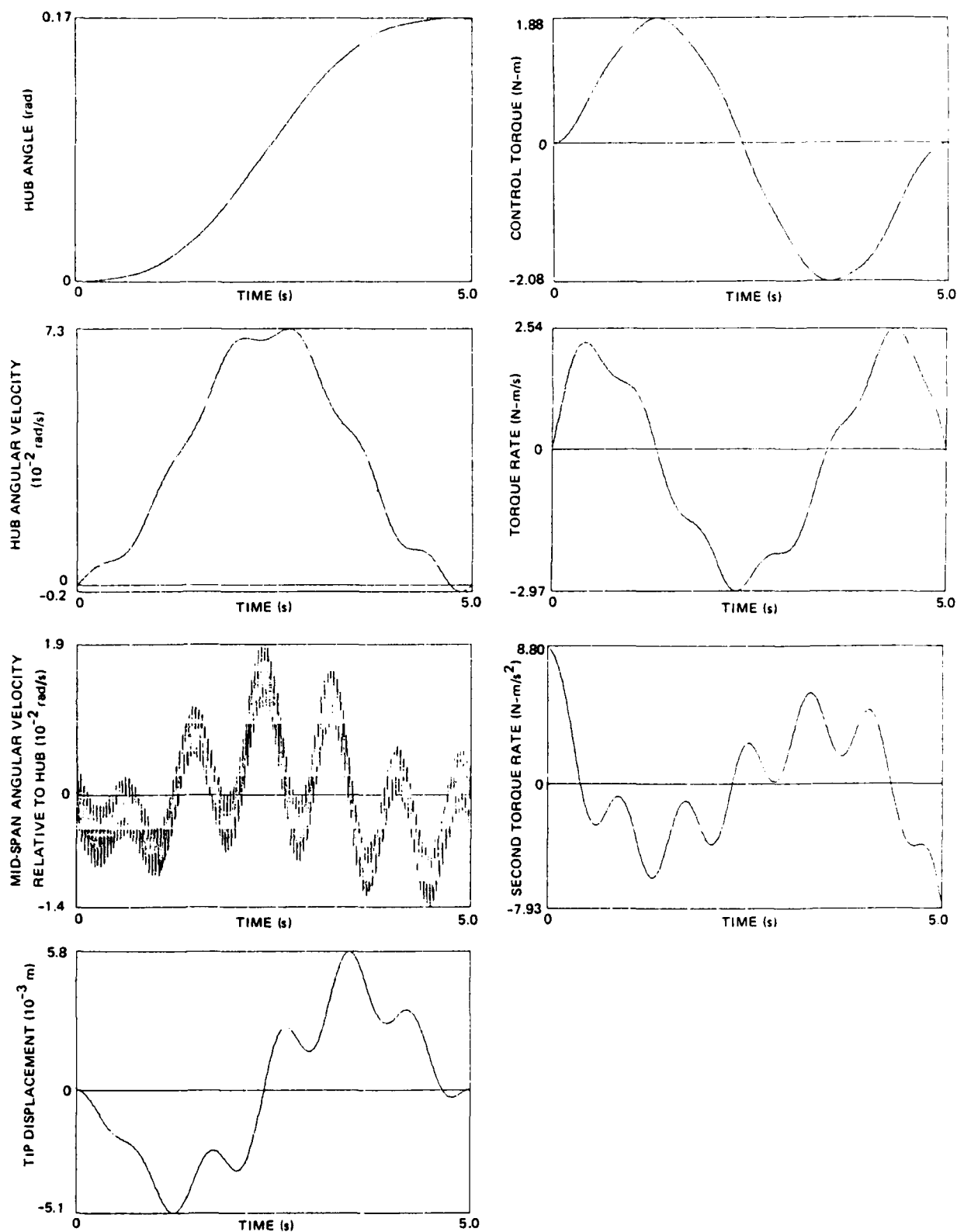


Figure 10-7. Case 4: Dual tracking/disturbance-accommodation controller with multiple disturbance torques.

Notice that the hub angular velocity, mid-span relative angular velocity, and tip displacement do not reach their desired zero values. Also note that the first and second torque rates have spikes near the final time in their time histories. Undoubtedly, the spikes may be reduced by lowering the terminal weight matrix. However, this increases the error in the final states. The fact that no spikes occur in the output states and control-torque time histories must be attributed to the use of control-rate smoothing, since the large spike in the second torque rate is integrated twice to obtain the control torque.

Case 2 (Fig. 10-4) presents the tracking/disturbance-accommodation controller which is exposed to the same disturbance as shown in Case 1. Since this controller utilizes disturbance information in its controller design, it is able to meet the desired final conditions. Note that the state and control time-histories are nearly symmetric about the mid-maneuver time, as the open-loop reference solution should be. Notice that the control and control-rates are much smoother than for Case 1, and that the peak torque requirement is slightly lower than for Case 1.

Case 3 (Fig. 10-5) shows the simple tracking controller subjected to multiple disturbances, one at the central hub and one at the mid-span of each of the four appendages (Fig. 10-6). The appendage disturbances are all identical in order to satisfy the anti-symmetric deformation assumption. The central hub disturbance torque is given by

$$T_d = 0.1 + 0.1 \sin 2\pi t + 0.2 \cos 2\pi t$$

and the appendage disturbance torques are given by

$$T_d = 0.01 \sin 2\pi t + 0.02 \cos 2\pi t$$

Notice that the output states deviate slightly from their desired final values. Also note the large spikes in the first and second torque rates. The high frequency content seen in the mid-span relative angular velocity time history is due to the unmodelled residual modes which are excited by the jump discontinuities in the disturbance torques at the initial time.

Case 4 (Fig. 10-7) shows the tracking/disturbance-accommodation controller subjected to the disturbances of Fig. 10-6. In this case the states and control achieve their desired final values, and the control and control-rate time histories are smooth. Note that since the central hub disturbance torque has a non-zero bias and is non-symmetric, the resulting state and control time-histories are no longer symmetric about the mid-maneuver time. The residual mode response is also evident in the mid-span relative angular velocity time-history. Also note that the peak torque requirement is 10% lower than for the simple tracking controller of Case 3.

We further observe that the formulation of Section 10.4.2 reduces to the special case of a tracking solution by setting $\beta = 0$ in Eq. (10-11), or to the special case of a disturbance-accommodation solution by setting $s_0 = 0$ in Eq. (10-11).

10.8 Analytic Fourier Transform for the Control

The following subsection provides an analytic Fourier transform for the control with a class of finite-time control problems. The fundamental definition of the complex Fourier transform is given by

$$\bar{u}(\omega) \triangleq \int_0^{\tau} dt \, u(t) e^{-i\omega t} \quad (10-25)$$

where $u(t)$ is assumed to be given by [Refs. 10-9 through 10-12]

$$u(t) = Ae^{Bt}c \quad (10-26)$$

In the above, A is $n \times m$, B is $m \times m$, c is $m \times 1$, and $e^{(\cdot)}$ is the matrix exponential function.

Introducing Eq. (10-26) into Eq. (10-25) yields

$$\bar{u}(\omega) = A\xi(\omega) \quad (10-27)$$

where

$$\xi(\omega) \triangleq \int_0^{\tau} dt e^{Bt} c e^{-i\omega t} \quad (10-28)$$

The integral appearing in Eq. (10-28) can be evaluated by the approach given in Section 10.9.1. In particular:

$$\Pi(\omega) = \underbrace{\begin{bmatrix} -B & c \\ 0 & -i\omega \end{bmatrix}}_{\substack{n \\ 1}} \underbrace{\begin{matrix} \} n \\ \} 1 \end{matrix}}_{1} \quad (10-29)$$

and

$$e^{\Pi(\omega)\tau} = \begin{bmatrix} F_1(\tau) & G_1(\tau; \omega) \\ 0 & F_2(\tau; \omega) \end{bmatrix} = \begin{bmatrix} e^{-B\tau} & e^{-B\tau}\xi(\omega) \\ 0 & e^{-i\omega\tau} \end{bmatrix} \quad (10-30)$$

from which it follows that

$$\xi(\omega) = e^{B\tau} G_1(\tau; \omega) \quad (10-31)$$

Since the numerical effort required to compute $G_1(\cdot; \omega)$ for each desired value of ω is prohibitive, we present in the next section a coordinate transformation which greatly reduces the computational burden required to produce $\xi(\omega)$ in Eq. (10-31).

10.8.1 Reducing Subspace Coordinate Transformation

In this subsection we present an algorithm for reducing the complex matrix $\Pi = \Pi(\omega)$ in Eq. (10-29) to block diagonal form by a similarity transformation [Ref. 10-42]. In particular, we seek a complex nonsingular matrix ϕ such that $\phi^{-1}\Pi\phi$ has the form

$$\phi^{-1}\Pi\phi = \tilde{\Pi}(\omega) = \text{diag}(-B, -i\omega) \quad (10-32)$$

The transformation matrix ϕ is assumed to have the special form

$$\phi = \begin{bmatrix} I & -p \\ 0 & 1 \end{bmatrix}$$

Since the inverse of ϕ is:

$$\phi^{-1} = \begin{bmatrix} I & p \\ 0 & 1 \end{bmatrix}$$

it follows that

$$\phi^{-1}\Pi\phi = \begin{bmatrix} -B & Bp - i\omega p + c \\ 0 & -i\omega \end{bmatrix}$$

Thus, the problem of determining ϕ becomes that of solving the following linear equation for p :

$$[B - i\omega I]p = -c \quad (10-33)$$

which leads to a well defined solution for p provided that $i\omega$ is not an eigenvalue of B .

From Eq. (10-32) it follows that the matrix exponential of Eq. (10-30) can be written as

$$e^{\Pi(\omega)\tau} = \phi e^{\tilde{\Pi}(\omega)\tau} \phi^{-1} = \begin{bmatrix} e^{-B\tau} & e^{-B\tau}p - pe^{-i\omega\tau} \\ 0 & e^{-i\omega\tau} \end{bmatrix} \quad (10-34)$$

Comparing Eqs. (10-30) and (10-34) it follows that the desired integral for $\xi(\omega)$ in Eq. (10-31) is given by

$$\xi(\omega) = p(\omega) - e^{B\tau}p(\omega)e^{-i\omega\tau} \quad (10-35)$$

where the entire solution follows after determining $p(\omega)$ from Eq. (10-33), for each frequency of interest. The significant feature of Eq. (10-35) is that the computationally intensive solution for $e^{B\tau}$ must be carried out only once, thus greatly reducing the labor required to produce $\xi(\omega)$.

10.8.2 Solution for the Uncoupling Transformation Vector

Since the B matrix in Eq. (10-33) is constant and generally fully populated, we seek a solution technique which minimizes the computational effort. However, we recognize that there are two classes of solutions possible. First, systems where B is diagonalizable; and second, systems where the eigensystem for B is ill-conditioned.

The solution for both classes of problems are obtained via a "transformation method". In particular, such methods are based upon the equivalence of the problems [Refs. 10-26, 10-39]

$$[B - i\omega I]p(\omega) = -c$$

and (10-36)

$$[\Lambda - i\omega I]\rho(\omega) = -\gamma$$

where Λ is the appropriate canonical form of B under the appropriate transformation, with $\rho(\omega)$ and γ arising from the same transformation.

The solution algorithms for both classes of problems are listed in Table 10-2. However, if ω is an eigenvalue of B , then Eq. (10-30) must be used to obtain a solution.

The desired solution for $\bar{u}(\omega)$ follows upon introducing Eq. (10-35) into Eq. (10-27), yielding

$$\bar{u}(\omega) = A\{p(\omega) - e^{B\tau}p(\omega)e^{-i\omega\tau}\} \quad (10-37)$$

In order to evaluate Eq. (10-37) efficiently, it is necessary to recast the equation in the form

$$\bar{u}(\omega) = Ap(\omega) - \bar{A}p(\omega)e^{-i\omega\tau} \quad (10-38)$$

where $\bar{A} \triangleq Ae^{B\tau}$ is $n \times m$ with $n < m$.

10.8.3 Example Application

Given the first-order system

$$\dot{x} = -x + u ; \quad x(0) = 0 , \quad x(\tau) = 1$$

Table 10-2. Solution techniques for $p(\omega)$.

B Diagonalizable		B Ill-Conditioned Eigensystem	
Λ	= $\text{diag} (\lambda_1, \dots, \lambda_n)$	Λ	= Upper Quasi-triangular*
γ	= $L^T c$	γ	= $U^T c$
ρ_j	= $\gamma_j / (\lambda_j - i\omega)$, $j = 1, \dots, n$	$[\Lambda - i\omega I] \rho$	= $-\gamma$
$p(\omega)$	= $R\rho(\omega)$	$p(\omega)$	= $U\rho(\omega)$
R	= Right Eigenvector of B	$U^T B U$	= Λ (real Schur decomposition)
L	= Left Eigenvector of B	$U^T U$	= I (orthogonal)
$L^T R$	= I (Biorthogonality)		

* A quasi-triangular matrix is triangular with possible nonzero 2×2 blocks on the diagonal.

we seek the control u to minimize

$$J = \frac{1}{2} \int_0^{\tau} u^2 dt$$

The open-loop optimal control can be shown to be

$$u(t) = -\lambda(t) \quad (10-39)$$

where $\lambda(\cdot)$ is the costate trajectory, satisfying:

$$\begin{pmatrix} x(t) \\ \lambda(t) \end{pmatrix} = e^{Bt} \begin{pmatrix} x(0) \\ \lambda(0) \end{pmatrix}, \quad B \triangleq \begin{bmatrix} -1 & -1 \\ 0 & 1 \end{bmatrix}$$

Moreover,

$$e^{Bt} = \begin{bmatrix} e^{-t} & -\sinh t \\ 0 & e^t \end{bmatrix} \quad (10-40)$$

and $\lambda(0) = -1/\sinh \tau$. Thus the control of Eq. (10-39) can be written as

$$u(t) = Ae^{Bt}c = e^t/\sinh \tau$$

where $A = [0 \ -1]$, e^{Bt} is defined by Eq. (10-40), and $c = (0 \ -1/\sinh \tau)^T$. The analytic Fourier transform of $u(t)$ follows as

$$\bar{u}(\omega) = \left(\int_0^{\tau} e^{(1-i\omega)t} dt \right) / \sinh \tau = [e^{(1-i\omega)\tau} - 1] / [(1 - i\omega) \sinh \tau] \quad (10-41)$$

Since B is diagonalizable, we use the right and left eigenvector transformation method to solve Eq. (10-36), leading to

$$R = \begin{bmatrix} 1/\sqrt{2} & -1/\sqrt{2} \\ 0 & 2/\sqrt{2} \end{bmatrix}, \quad L = \begin{bmatrix} 2/\sqrt{2} & 0 \\ 1/\sqrt{2} & 1/\sqrt{2} \end{bmatrix}, \quad \Lambda = \begin{bmatrix} -1 & 0 \\ 0 & 1 \end{bmatrix}$$

from which it follows that

$$\gamma = -L^T c = (1/(\sqrt{2} \sinh \tau), 1/(\sqrt{2} \sinh \tau))^T$$

$$\rho(\omega) = (-1/[(1 + i\omega)\sqrt{2} \sinh \tau], 1/[(1 - i\omega)\sqrt{2} \sinh \tau])^T$$

$$p(\omega) = R\rho(\omega) =$$

$$= (-1/[2(1 + i\omega) \sinh \tau] - 1/[2(1 - i\omega) \sinh \tau], 1/[(1 - i\omega) \sinh \tau])^T$$

$$\bar{A} = Ae^{B\tau} = \begin{bmatrix} 0 & -e^\tau \end{bmatrix}$$

Thus, from Eq. (10-38) we have

$$\bar{u}(\omega) = [e^{(1-i\omega)\tau} - 1]/[(1 - i\omega) \sinh \tau] \quad (10-42)$$

We note that Eq. (10-42) agrees with Eq. (10-41).

10.9 Appendix

10.9.1 Closed-Form Solution for the Prefilter Equation Matrix Integrals

In order to evaluate the prefilter equation presented in Section 10.4.2, we must compute four matrix integrals of the form

$$\Psi(t) \equiv \Psi(A, B, C, t) \triangleq \int_0^t e^{A\tau} B e^{C\tau} d\tau \quad (10-43)$$

where the (constant) matrices A, B, and C are specified. The integral involving the matrix exponentials in Eq. (10-43) can be easily evaluated by forming the constant matrix

$$\Pi \triangleq \begin{bmatrix} -A & B \\ 0 & C \end{bmatrix} \begin{matrix} \} n_1 \\ \} n_2 \end{matrix}$$

$\underbrace{\quad}_{n_1} \quad \underbrace{\quad}_{n_2}$

and computing the corresponding matrix exponential $e^{\Pi t}$. As shown in Reference 10-40, the latter has the representation:

$$e^{\Pi t} = \begin{bmatrix} F_1(t) & G_1(t) \\ 0 & F_2(t) \end{bmatrix} \begin{matrix} \} n_1 \\ \} n_2 \end{matrix}$$

$\underbrace{\quad}_{n_1} \quad \underbrace{\quad}_{n_2}$

where

$$F_1(t) \triangleq e^{-At}, \quad F_2(t) \triangleq e^{Ct}$$

$$G_1(t) \triangleq \int_0^t e^{-A(t-\tau)} B e^{C\tau} d\tau$$

Thus the solution for the integral in Eq. (10-43) follows as

$$\Psi(A, B, C, t) = e^{At} G_1(t) \quad (10-44)$$

In order to evaluate Eq. (10-44) at discrete time steps, the semi-group properties of exponential matrices are exploited, yielding the following recursion relationships for the matrix partitions of e^{At} :

$$F_i(t + \Delta t) = F_i(\Delta t) F_i(t) \quad , \quad F_i(0) = I \quad , \quad i = 1, 2$$

$$G_1(t + \Delta t) = F_1(\Delta t) G_1(t) + G_1(\Delta t) F_2(t) \quad , \quad G_1(0) = 0$$

where $\Delta t = (t_f - t_0)/m$ and m is the total number of discrete time steps. The matrix $F_3(t) \triangleq e^{At}$ is obtained in a separate calculation. As a result, the integral in Eq. (10-43) can be written (at $t = (n + 1)\Delta t$) as

$$\Psi(A, B, C, (n + 1)\Delta t) = F_3[(n + 1)\Delta t] G_1[(n + 1)\Delta t]$$

Since each Ψ -function in Eq. (10-11) is post multiplied by a vector, we can write

$$\Psi(A, B, C, (t + \Delta t))\sigma = F_3(t + \Delta t)v_1(t + \Delta t) \quad (10-45)$$

where σ is a vector and the recursion relationship for v_1 is given by

$$v_1(t + \Delta t) = F_1(\Delta t)v_1(t) + G_1(\Delta t)v_2(t) \quad ; \quad v_1(0) = 0$$

$$v_2(t + \Delta t) = F_2(\Delta t)v_2(t) \quad ; \quad v_2(0) = \sigma$$

A separate recursion relationship of the form of Eq. (10-45) is set up for each term in Eq. (10-11) consisting of the product of a Psi-function times a vector.

10.9.2 Closed-Form Solutions for the Residual-State Trajectory Matrix Integrals

In order to evaluate the residual-state trajectory equation presented in Section 10.6, we must compute eleven matrix integrals which can be expressed as one of the following two forms:

$$G_1(t) \triangleq \int_0^t e^{A(t-s)} B e^{Cs} ds \quad (10-46)$$

or

$$H_1(t) = \int_0^t \int_0^s e^{A(t-s)} B e^{C(s-r)} D e^{Er} dr ds \quad (10-47)$$

where the (constant) matrices A, B, C, D, and E are specified. This problem, and its solution, are analogous to that discussed in the preceding subsection. In order to compute G_1 and H_1 , we define the following matrix exponential:

$$\Gamma(t) \triangleq \Gamma(A, B, C, D, E, t) \triangleq e^{vt} \quad (10-48)$$

where v is the constant matrix [Ref. (10-40)]

$$v \triangleq \begin{bmatrix} \overbrace{A}^{n_1} & \overbrace{B}^{n_2} & \overbrace{0}^{n_3} \\ 0 & C & D \\ 0 & 0 & E \end{bmatrix} \begin{matrix} \} n_1 \\ \} n_2 \\ \} n_3 \end{matrix}$$

As shown in Reference 10-40, Γ has the representation:

$$\Gamma(t) = \begin{bmatrix} F_1(t) & G_1(t) & H_1(t) \\ 0 & F_2(t) & G_2(t) \\ 0 & 0 & F_3(t) \end{bmatrix} \begin{matrix} \} n_1 \\ \} n_2 \\ \} n_3 \end{matrix}$$

$$\begin{matrix} \widetilde{n_1} & \widetilde{n_2} & \widetilde{n_3} \end{matrix}$$

which includes the desired integrals G_1 and H_1 . In addition,

$$F_1(t) \triangleq e^{At}, \quad F_2(t) \triangleq e^{Ct}, \quad F_3(t) \triangleq e^{Et}$$

$$G_2(t) \triangleq \int_0^t e^{C(t-s)} D e^{Es} ds$$

Using the semi-group properties of matrix exponentials, the partitions of Γ can be recursively generated from the following formulas:

$$F_i(t + \Delta t) = F_i(\Delta t)F_i(t), \quad F_i(0) = I, \quad i = 1, 2, 3$$

$$G_i(t + \Delta t) = F_i(\Delta t)G_i(t) + G_i(\Delta t)F_{i+1}(t), \quad G_i(0) = 0, \quad i = 1, 2$$

$$H_1(t + \Delta t) = F_1(\Delta t)H_1(t) + G_1(\Delta t)G_2(t) + H_1(\Delta t)F_3(t), \quad H_1(0) = 0$$

When the recursion relationships above are post-multiplied by vectors, the following modified propagation equations result:

$$x_i(t + \Delta t) = F_i(t + \Delta t)x_0 = F_i(\Delta t)x_i(t) \quad , \quad i = 1, 2, 3 \quad (10-49)$$

$$x_i(t + \Delta t) = G_{i-3}(t + \Delta t)x_0 = F_{i-3}(\Delta t)x_i(t) + G_{i-3}(\Delta t)x_{i-2}(t) \quad , \quad i = 4, 5 \quad (10-50)$$

$$x_6(t + \Delta t) = H_1(t + \Delta t)x_0 = F_1(\Delta t)x_6(t) + G_1(\Delta t)x_5(t) + H_1(\Delta t)x_3(t)$$

where

$$x_i(0) \triangleq \begin{matrix} x_0 & , & i = 1, 2, 3 \\ 0 & , & i = 4, 5, 6 \end{matrix}$$

The vector recursion relationships above are particularly useful for generating the integral solution for $x_r(t)$ in Eq. (10-24) at discrete times, since matrix-vector multiplications are much less costly than matrix-matrix multiplications. Furthermore, in generating matrix-vector products involving matrices of the form in Eq. (10-46), only x_2 and x_4 in Eqs. (10-49), (10-50) must be propagated. Similarly, in generating matrix-vector products involving matrices of the form in Eq. (10-47), only x_3 , x_5 and x_6 must be propagated.

10.10 Conclusions

Closed-form solutions for the feedback gains, state trajectory, and residual mode response have been developed for the tracking/disturbance-accommodation controller. This has been made possible by the fact that the Fourier series representation of the disturbances may be expressed in an exponential matrix form. In addition, recursion relationships have been developed for propagating the gains, state trajectory and residual mode response in a computationally efficient way. Numerical results of several test case maneuvers demonstrate the utility of the

formulations and show that the tracking/disturbance-accommodation controller outperforms the simple linear tracking controller which does not use information about the disturbances. The test case examples also show the effect that control-rate smoothing has on smoothing out the control time history for the linear tracker.

A computationally efficient algorithm has also been presented for obtaining the complex Fourier transform of a class of vector functions which frequently occur in modern control theory. The basic algorithm requires: (1) evaluation of a single matrix exponential for the dynamics of the time-varying control; (2) solution for either the right and left eigenvectors or a real Schur decomposition of the constant control dynamics matrix; (3) sequential solution for the reducing subspace transformation vector; and (4) evaluation of a single scalar complex exponential. A low order example application is shown to demonstrate the utility of the above formulation.

References

- 10-1. Farrenkopf, R. L., "Optimal Open-Loop Maneuver Profiles for Flexible Spacecraft," J. Guidance and Control, Vol. 2, No. 6, Nov.-Dec. 1979, pp. 491-498.
- 10-2. Swigert, C. J., "Shaped Torque Techniques," J. Guidance and Control, Vol. 3, No. 5, Sept.-Oct. 1980, pp. 460-467.
- 10-3. Alfriend, K. T., Longman, R. W., and Bercaw, W. S., "On Frequency Response Interpretations of Optimal Slewing Maneuvers," Proc. Second VPI&SU/AIAA Symposium on Dynamics and Control of Large Flexible Spacecraft, Blacksburg, VA, June 1979, pp. 65-79.
- 10-4. Markley, F. L., "Large-Angle Maneuver Strategy for Flexible Spacecraft," Paper No. 79-156, AAS/AIAA Astrodynamics Conference, Provincetown, MA, June 1979.

- 10-5. Longman, R. W. and Alfriend, K. T., "Optimal Control of Large Angle Attitude Maneuvers for Flexible Spacecraft," Proc. 8th IFAC Symposium on Automatic Control in Space, Oxford, England, July 1979, pp. 57-62.
- 10-6. Breakwell, J. A., "Optimal Control of Distributed Systems," J. Astronaut. Sci., Vol. 29, No. 4, Oct.-Dec. 1981, pp. 343-372.
- 10-7. Hefner, R., Kawauchi, B., Melzer, S., and Williamson, R., "A Terminal Controller for the Pointing of Flexible Spacecraft," Paper No. 80-1670, AIAA Astrodynamics Conference, Danvers, MA, August 1980.
- 10-8. Turner, J. D., Chun, H. M., and Junkins, J. L., "Optimal Large-Angle Maneuvers with Vibration Suppression," Workshop on Modelling, Analysis and Optimization Issues for Large Space Structures, Williamsburg, VA, May 13-14, 1982.
- 10-9. Turner, J. D. and Junkins, J. L., "Optimal Large Angle Single-Axis Rotational Maneuvers of Flexible Spacecraft," J. Guidance and Control, Vol. 3, No. 6, Nov.-Dec. 1980, pp. 578-585.
- 10-10. Breakwell, J. A., "Optimal Feedback Slewing of Flexible Spacecraft," J. Guidance and Control, Vol. 4, No. 5, Sept.-Oct. 1981, pp. 472-479.
- 10-11. Turner, J. D. and Chun, H. M., "Optimal Distributed Control of a Flexible Spacecraft Using Control-Rate Penalties in the Controller Design," Paper No. 82-1438, AIAA Astrodynamics Conference, San Diego, CA, August 1982.
- 10-12. Turner, J. D., Chun, H. M., and Juang, J.-N., "An Analytic Solution for the State Trajectories of Feedback Control Systems," J. Guidance, Control and Dynamics (to appear).
- 10-13. Turner, J.D. and Chun, H.M., "Optimal Distributed Control of a Flexible Spacecraft During a Large-Angle Rotational Maneuver," J. Guidance, Control and Dynamics (to appear)

- 10-14. Juang, J.-N., Turner, J. D., and Chun, H. M., "Closed-Form Solutions of Control Gains for a Terminal Controller," Proc. Fourth VPI&SU/AIAA Symposium on Dynamics and Control of Large Structures, Blacksburg, VA, June 1983, pp. 17-32.
- 10-15. Turner, J. D., Chun, H. M., and Juang, J.-N., "Optimal Tracking and Terminal Tracking Maneuvers for Flexible Spacecraft, ACOSS-Eleven Fourth Semiannual Technical Report, Vol. 2, Report CSDL-R-1648, Charles Stark Draper Laboratory, Cambridge, MA, August 1983; Section 5.
- 10-16. Turner, J. D., Chun, H. M., and Juang, J. N., "Closed-Form Solutions for a Class of Optimal Quadratic Tracking Problems," J. Optimization Theory Appl. (to appear).
- 10-17. Juang, J.-N., Turner, J. D., and Chun, H.M., "Closed-Form Recursive Formula for an Optimal Tracker with Terminal Constraints," Proc. 1984 American Control Conference, San Diego, CA, June, 1984, pp. 1665-1673.
- 10-18. Skaar, S. B. and Tucker, D., "The Optimal Control of Flexible Systems Using a Convolution Integral Description of Motion," Proc. 22nd IEEE Conference on Decision and Control, San Antonio, TX, December 1983, pp. 825-829.
- 10-19. Turner, J. D., Mozzicato, R. and Chun, H. M., "An Analytic Solution for the State when the Control is Specified as a Fourier Series," submitted to the Journal of Dynamic Systems, Measurement, and Control, January 1984.
- 10-20. Floyd, M. A., Brown, M. E., Turner, J. D., and Vander Velde, W. E., "Implementation of a Minimum Time and Fuel On/Off Thruster Control System for Flexible Spacecraft," submitted to the Journal of the Astronautical Sciences, January 1984.
- 10-21. Gupta, N. K., "Frequency Shaping of Cost Functionals: An Extension of Linear-Quadratic-Gaussian Design Methods," J. Guidance and Control, Vol. 3, No. 6, Nov.-Dec. 1980, pp. 529-535.

- 10-22. Gupta, N. K., "Robust Control/Estimator Design by Frequency-Shaped Cost Functionals," Proc. 20th IEEE Conference on Decision and Control, San Diego, CA, December 1981, pp. 1167-1172.
- 10-23. Aubrun, J. N., Breakwell, J. A., Gupta, N. K., Lyons, M. G., and Margulies, G., "ACOSS FIVE (Active Control of Space Structures) Phase 1A," Rome Air Development Center Contractor Report RADC-TR-82-21, Lockheed Missiles & Space Company, Palo Alto, CA, March 1982.
- 10-24. Aspinwall, D. M., "Acceleration Profiles for Minimizing Residual Responses," J. Dynamic Systems, Measurement and Control, Vol. 102, No. 1, Mar. 1980, pp. 3-6.
- 10-25. Junkins, J. L., "Comment on Optimal Feedback Slewing of Flexible Spacecraft," J. Guidance, Control, and Dynamics, Vol. 5, No. 3, May-June 1982, p. 318.
- 10-26. Golub, G. H., Nash, S., and Van Loan, C., "A Hessenburg-Schur Method for the Problem $AX + XB = C$," IEEE Trans. Automatic Control, Vol. AC-24, No. 6, pp. 909-913, December 1979.
- 10-27. Moore, J. B., and Anderson, B. D. O., "Optimal Linear Control Systems with Input Derivative Constraints," Proc. IEE, Vol. 114, No. 12, Dec. 1967, pp. 1987-1990.
- 10-28. Bryson, A. and Ho, Y. C., Applied Optimal Control, Wiley, New York, NY, 1975.
- 10-29. Brockett, R. W., Finite Dimensional Linear Systems, Wiley, New York, NY, 1970.
- 10-30. Potter, J. E., "A Matrix Equation Arising in Statistical Filter Theory," NASA CR-270, 1965.
- 10-31. Mårtensson, K., "On the Matrix Riccati Equation," Information Sci. Vol. 3, 1971, pp. 17-49.
- 10-32. Prussing, J. E., "A Simplified Method for Solving the Matrix Riccati Equation," Internat. J. Control, Vol. 15, No. 5, May 1972, pp. 995-1000.

- 10-33. Jamshidi, M., "An Overview on the Solutions of the Algebraic Matrix Riccati Equation and Related Problems," Large Scale Systems: Theory and Applications, Vol. 1, No. 3, Aug. 1980, pp. 167-192.
- 10-34. Potter, J. E. and Vander Velde, W. E., "Optimal Mixing of Gyroscope and Star Tracker Data," J. Spacecraft Rockets, Vol. 5, No. 5, May 1968, pp. 536-540.
- 10-35. Potter, J. E., "Matrix Quadratic Solutions," SIAM J. Appl. Math., Vol. 14, No. 3, May 1966, pp. 496-501.
- 10-36. Davison, E. J., "The Numerical Solution of $\dot{X} = A_1 X + X A_2 + D$, $X(0) = C$," IEEE Trans. Automatic Control, Vol. AC-20, No. 4, Aug. 1975, pp. 566-567.
- 10-37. Serbin, S. M. and Serbin, C. A. "A Time-Stepping Procedure for $\dot{X} = A_1 X + X A_2 + D$, $X(0) = C$," IEEE Trans. Automatic Control, Vol. AC-25, No. 6, Dec. 1980, pp. 1138-1141.
- 10-38. Pace, I. S. and Barnett, S., "Comparison of Numerical Methods for Solving Lyapunov Matrix Equations," Internat. J. Control, Vol. 15, No. 5, May 1972, pp. 907-915.
- 10-39. Bartels, R. H. and Stewart, G. W., "Solution of the Matrix Equation $AX + XB = C$," Comm. ACM, Vol. 15, No. 9, Sept. 1972, pp. 820-826.
- 10-40. Van Loan, C. F., "Computing Integrals Involving Matrix Exponentials," IEEE Trans. Automatic Control, Vol. AC-23, No. 3, June 1978, pp. 395-404.
- 10-41. Brown, M. E., "Rapid Slewing Maneuvers of a Flexible Spacecraft Using On/Off Thrusters," S.M. Thesis, Department of Aeronautics and Astronautics, Massachusetts Institute of Technology, Cambridge, MA, September 1983.
- 10-42. Bavely, C. C. and Stewart, G. W., "An Algorithm for Computing Reducing Subspaces by Block Diagonalization," SIAM J. Numer. Anal., Vol. 16, No. 2, Apr. 1979, pp. 359-367.

DISTRIBUTION LIST

addresses	number of copies
Richard W. Carman RADC/OCSP	5
RADC/TSTD GRIFFISS AFB NY 13441	2
RADC/DAP GRIFFISS AFB NY 13441	2
ADMINISTRATOR DEF TECH INF CTR ATTN: DTIC-DDA CAMERON STA BG 5 ALEXANDRIA VA 22304-6145	12
Charles Stark Draper Lab 555 Technology Square M.S. -95 Cambridge, MA 02139	5
NASA Headquarters ATTN: Mr. J. B. Dahlgren Code RTH-6 Washington, DC 20546	1
Charles Stark Draper Lab Attn: Mr. R. Strunce 555 Technology Square M.S. -60 Cambridge, MA 02139	1
Charles Stark Draper Lab Attn: Dr. Daniel R. Hegg 555 Technology Square M.S. -60 Cambridge, MA 02139	1

ARPA/STO 1
Attn: Lt Col A. Herzberg
1400 Wilson Blvd
Arlington, VA 22209

ARPA/STO 1
Attn: Maj E. Dietz
1400 Wilson Blvd
Arlington, VA 22209

Riverside Research Institute 2
Attn: Mr. A. DeVilliers
1701 N. Ft. Myer Drive, Suite 711
Arlington, VA 22209

Riverside Research 1
Attn: HALO Library, Mr. Bob Passut
1701 N. Ft. Myer Drive
Arlington, VA 22209

Itek Corp 1
Optical Systems Division
10 Maguire Rd.
Lexington, MA 02173

Ferkin Elmer Corp 1
Attn: Mr. H. Levenstein
Electro Optical Division
Main Avenue
Norwalk, CT 06856

Air Force Flight Dynamics Lab 1
Attn: Dr. Lynn Rogers
Wright Patterson AFB, OH 45433

AFWL/FIBG 1
Attn: Mr. Jerome Pearson
Wright Patterson AFB, OH 45433

Air Force Wright Aero Lab. FIGC 1
Attn: Siva S. Banda
Wright Patterson AFB, OH 45433

Air Force Institute of Technology 1
Attn: Prof. R. Calico/ENY
Wright Patterson AFB, OH 45433

Aerospace Corp. 2
Attn: Dr. G.T. Tseng
2350 E. El Segundo Blvd
El Segundo, CA 90245

Aerospace Corp. 1
Attn: Mr. J. Mosich
2350 E. El Segundo Blvd
El Segundo, CA 90245

SD/SD/YLVS 1
Attn: Mr. Lawrence Weeks
P. O. Box 92960
Worldway Postal Center
Los Angeles CA 90009

SD/YCD 1
Attn: YCPT/Capt Gajewski
P. O. Box 92960
Worldway Postal Center
Los Angeles, CA 90009

Grumman Aerospace Corp 1
Attn: Dr. A. Mendelson
South Oyster Bay Road
Bethpage, NY 11714

CDR&E DS 1
Attn: Mr. A. Santapelli
Room 2D136
Pentagon, Washington, DC 20301

Jet Propulsion Laboratory 2
Dr. S. Szermay
4800 Oak Grove Drive
Pasadena, CA 91103

MIT/Lincoln Laboratory 1
Attn: S. Wright
P.O. Box 73
Lexington, MA 02173

MIT/Lincoln Laboratory 1
Attn: Dr. D. Hyland
P.O. Box 73
Lexington, MA 02173

MIT/Lincoln Laboratory 1
Attn: Dr. N. Smith
P.O. Box 73
Lexington, MA 02173

Control Dynamics Co. 1
Attn: Dr. Sherman Seltzer
Suite 1414 Executive Plaza
555 Sparkman Drive
Huntsville, AL 35805

Lockheed Space Missile Corp. 5
Attn: A. A. Woods, Jr., O/62-E6
P.O. Box 504
Sunnyvale, California 94088-3504

Lockheed Missiles Space Co. 1
Attn: Mr. Paul Williamson
3251 Hanover St.
Palo Alto, CA 94304

General Dynamics 1
Attn: Ray Halstenberg
Convair Division
3701 Keary Villa Rd
San Diego, CA 92123

STI 1
Attn: Mr. R. C. Stroud
20065 Stevens Creek Blvd.
Cupertino, CA 95014

NASA Langley Research Ctr 2
Attn: Dr. Earle K. Huckins III
Dr. M. F. Card
Langley Station, Bldg 1293B, MS 230
Hampton, VA 23665

NASA Johnson Space Center 1
Attn: Robert Piland
Ms. EA
Houston, TX 77058

McDonald Douglas Corp 1
Attn: Mr. Read Johnson
Douglas Missile Space Systems Div
5301 Bulsa Ave
Huntington Beach, CA 92607

Integrated Systems Inc. 2
Attn: Dr. N. K. Gupta and M. G. Lyons
151 University Avenue, Suite 400
Palo Alto, California 94301

TRW Defense Space Sys Group Inc. 1
Attn: Ralph Iwens
Bldg 82/2054
One Space Park
Redondo Beach, CA 90278

TRW 1
Attn: Mr. Len Pincus
Bldg R-5, Room 2031
Redondo Beach, CA 90278

Department of the NAVY 1
Attn: Dr. K. T. Alfrend
Naval Research Laboratory
Code 7920
Washington, DC 20375

Airesearch Manuf. Co. of Calif. 1
Attn: Mr. Oscar Buchmann
2525 West 190th St.
Torrance, CA 90509

Analytic Decisions, Inc. 1
Attn: Mr. Gary Glaser
1401 Wilson Blv.
Arlington, VA 22209

Ford Aerospace & Communications Corp. 1
Ers. I. P. Leliakov and P. Barba, MS/G80
3939 Fabian way
Palo Alto, California 94304

Center for Analysis 1
Mr. James Justice
13 Corporate Plaza
Newport Beach, CA 92660

W. J. Schafer Associates 1
Dr. R. Kappesser
Suite 800
1901 Fort Meyer Drive
Arlington, VA 22209

General Research Corp 1
Attn: Mr. Thomas Zakrzewski
7655 Old Springhouse Road
McLean, VA 22101

Harman Sciences Corp. 1
Attn: Dr. Walter E. Ware
1500 Garden of the Gods Road
P.O. Box 7463
Colorado Springs, CO 80933

Photon Research Associates 1
Attn: Mr. Jim Myer
P.O. Box 1318
La Jolla, CA 92038

Rockwell International 1
Attn: Russell Loftman (Space Systems Group)
(Mail Code - SL56)
12214 Lakewood Blvd.
Downey, CA 90241

Science Applications, Inc. 1
Attn: Mr. Richard Ryan
3 Preston Court
Bedford, MA 01730

U.S. Army Missile Command 1
Attn: DRSMI-RAS/Mr. Fred Haak
Redstone Arsenal, AL

Naval Electronic Systems Command 1
Attn: Mr. Charles Good
FME_106-4
National Center I
Washington, DC 20360

Lockheed Palo Alto Research Laboratory 2
Attn: Dr. J. N. Aubrun, O/52-36
3251 Hanover Street
Palo Alto, California 94304-1167

U.S. Army/DAPCOM 1
Attn: Mr. Bernie Chasnov
MC Bldg
1101 Eisenhower Ave
Alexandria, VA 22332

Rockwell Inc 2
Attn: Dr. Thomas B. Cunningham
Attn: Dr. Michael F. Barnett
2000 Ridgway Parkway MN 17-2275
Minneapolis, MN 55413

NASA Marshall Space Flight Center 2
Attn: Dr. J. C. Blair, EEO1
Larry E. Waites
Marshall Space Flight Center, AL 35812

TRW
Attn: Robert Benhabib
Bldg 82/2024
One Space Park
Redondo Beach, CA 90278

1

NASA Langley Research Center
Attn: Dr. L. Pinson
MS - 230
Hampton, VA 23665

1

H. R. Textron
Attn. Mr. Richard Quartararo
2485 McCabe Way
Irvine, CA 92714

1

Naval Research Lab
Attn: W. Bennett
Mail Code: 7926
Washington, DC 20375

1

Charles Stark Draper Lab
Attn: Dr. Keto Soosaar
555 Technology Square
M.S. -95
Cambridge, MA 02139

1

NASA Headquarters
ATTN: Mr. J. B. Dahlgren
Code RTH-6
Washington, DC 20546

1

Charles Stark Draper Lab
Attn: Mr. R. Strunce
555 Technology Square
M.S. -60
Cambridge, MA 02139

1

Charles Stark Draper Lab
Attn: Dr. Daniel R. Hegg
555 Technology Square
M.S. -60
Cambridge, MA 02139

1

ARPA/STO
Attn: Lt Col A. Herzberg
1400 Wilson Blvd
Arlington, VA 22209

1

ARPA/STO
Attn: Maj E. Dietz
1400 Wilson Blvd
Arlington, VA 22209

1

Riverside Research Institute
Attn. Mr. A. DeVilliers
1701 N. Ft. Myer Drive, Suite 711
Arlington, VA 22209

2

Riverside Research
Attn: HALO Library, Mr. Bob Passut
1701 N. Ft. Myer Drive
Arlington, VA 22209

1

Itek Corp
Optical Systems Division
10 Maguire Rd.
Lexington, MA 02173

1

Perkin Elmer Corp
Attn. Mr. H. Levenstein
Electro Optical Division
Main Avenue
Norwalk, CT 06856

1

Hughes Aircraft Company
Attn. Mr. George Speak
Rm. S. B_156
Silver City, CA 90230

1

Hughes Aircraft Company
Attn: Mr. Ken Beale
Sentinela Teale Sts
Silver City, CA 90230

1

Air Force Flight Dynamics Lab 1
Attn: Dr. Lynn Rogers
Wright Patterson AFB, OH 45433

AFWL/FIBG 1
Attn: Mr. Jerome Pearson
Wright Patterson AFB, OH 45433

Air Force Wright Aero Lab. FIGC 1
Attn: Siva S. Banda
Wright Patterson AFB, OH 45433

Air Force Institute of Technology 1
Attn: Prof. R. Calico/ENY
Wright Patterson AFB, OH 45433

Aerospace Corp. 2
Attn: Dr. G.T. Tseng
2350 E. El Segundo Blvd
El Segundo, CA 90245

Aerospace Corp. 1
Attn: Mr. J. Mosich
2350 E. El Segundo Blvd
El Segundo, CA 90245

Aerospace Corp/Bldg 125/1054 1
Attn: Mr. Steve Burrin
Advanced Systems Tech Div.
2400 E El Segundo Blvd
El Segundo, CA 90245

SD/SD/YLVS 1
Attn: Mr. Lawrence Weeks
P.O. Box 92960
Worldway Postal Center
Los Angeles CA 90009

SD/YCD Attn: YCPT/Capt Gajewski P.O. Box 92960 Worldway Postal Center Los Angeles, CA 90009	1
Grumman Aerospace Corp Attn: Dr. A. Mendelson South Oyster Bay Road Bethpage, NY 11714	1
OUSD&E/DS Attn: Mr. A. Bertapelli Room 3D136 Pentagon, Washington, DC 20301	1
Jet Propulsion Laboratory Dr. S. Szermay 4800 Oak Grove Drive Pasadena, CA 91103	2
MIT/Lincoln Laboratory Attn: S. Wright P.O. Box 73 Lexington, MA 02173	1
MIT/Lincoln Laboratory Attn: Dr. D. Hyland P.O. Box 73 Lexington, MA 02173	1
MIT/Lincoln Laboratory Attn: Dr. N. Smith P.O. Box 73 Lexington, MA 02173	1
Control Dynamics Co. Attn: Dr. Sherman Seltzer Suite 1414 Executive Plaza 355 Sparkman Drive Montsville, AL 35805	1

Lockheed Space Missile Corp.
Attn: A. A. Woods, Jr., D/62-E6
P.O. Box 504
Sunnyvale, California 94088-3504

5

Lockheed Missiles Space Co.
Attn: Mr. Paul Williamson
3251 Hanover St.
Palo Alto, CA 94304

1

General Dynamics
Attn: Ray Halstenberg
Convair Division
5001 Kearny Villa Rd
San Diego, CA 92123

1

STI
Attn: Mr. R. C. Stroud
20065 Stevens Creek Blvd.
Cupertino, CA 95014

1

NASA Langley Research Ctr
Attn: Dr. Earle K. Huckins III
Dr. M. F. Card
Langley Station, Bldg 1293B, MS 230
Hampton, VA 23665

2

NASA Johnson Space Center
Attn: Robert Piland
Ms. EA
Houston, TX 77058

1

McDonald Douglas Corp
Attn: Mr. Read Johnson
Douglas Missile Space Systems Div
5201 Bolsa Ave
Huntington Beach, CA 92607

1

Integrated Systems Inc.
Attn: Dr. N. K. Gupta and M. G. Lyons
151 University Avenue, Suite 400
Palo Alto, California 94301

2

Boeing Aerospace Company 1
Attn: Mr. Leo Cline
P.O. Box 3999
Seattle, WA 98124
MS 8 W-23

TRW Defense Space Sys Group Inc. 1
Attn: Ralph Iwens
Bldg 82/2054
One Space Park
Redondo Beach, CA 90278

TRW 1
Attn: Mr. Len Pincus
Bldg R-5, Room 2031
Redondo Beach, CA 90278

Department of the NAVY 1
Attn: Dr. K.T. Alfrend
Naval Research Laboratory
Code 7920
Washington, DC 20375

Airresearch Manuf. Co. of Calif. 1
Attn: Mr. Oscar Buchmann
2525 West 190th St.
Torrance, CA 90509

Analytic Decisions Inc. 1
Attn: Mr. Gary Glaser
1401 Wilson Blv.
Arlington, VA 22209

Ford Aerospace & Communications Corp 1
Drs. I. P. Leliakov and P. Barba, MS/G80
3939 Fabian way
Palo Alto, California 94304

Center for Analysis 1
Mr. James Justice
13 Corporate Plaza
Newport Beach, CA 92660

W. J. Schafer Associates 1
Dr. R. Kappesser
Suite 800
1901 Fort Meyer Drive
Arlington, VA 22209

General Research Corp 1
Attn: Mr. Thomas Zakrzewski
7655 Old Springhouse Road
McLean, VA 22101

Air Force Weapons Laboratory 2
Attn: Lt Col D. Washburn
ARAA
Kirtland AFB, NM 87117

Harman Sciences Corp. 1
Attn: Dr. Walter E. Ware
1500 Garden of the Gods Road
P.O. Box 7463
Colorado Springs, CO 80933

MSJ, Inc. 1
10400 Eaton Place
Suite 300
Fairfax, VA 22030

Photon Research Associates 1
Attn: Mr. Jim Myer
P.O. Box 1318
La Jolla, CA 92038

Rockwell International 1
Attn: Russell Loftman (Space Systems Group)
Mail Code - SL36)
13214 Lakewood Blvd.
Downey, CA 90241

Science Applications, Inc. 1
Attn: Mr. Richard Ryan
1 Preston Court
Bedford, MA 01730

U.S. Army Missile Command 1
Attn: DRSMI-RAS/Mr. Fred Haak
Redstone Arsenal, AL

Naval Electronic Systems Command 1
Attn: Mr. Charles Good
PME_106-4
National Center I
Washington, DC 20360

Lockheed Palo Alto Research Laboratory 2
Attn: Dr. J. N. Aubrun, 0/52-56
3251 Hanover Street
Palo Alto, California 94304-1187

U.S. Army/DARCOM 1
Attn: Mr. Bernie Chasnov
AMC Bldg
3001 Eisenhower Ave
Alexandria, VA 22332

Honeywell Inc. 2
Attn: Dr. Thomas B. Cunningham
Attn: Dr. Michael F. Barrett
2600 Ridgway Parkway MN 17-2375
Minneapolis, MN 55413

NASA Marshall Space Flight Center 2
Attn: Dr. J. C. Blair, ED01
Henry B. Waites
Marshall Space Flight Center, AL 35812

TRW 1
Attn: Robert Benhabib
Bldg 82/2024
One Space Park
Redondo Beach, CA 90278

NASA Langley Research Center 1
Attn: Dr. L. Pinson
MS - 230
Hampton, VA 23665

H. R. Textron
Attn: Mr. Richard Quartararo
2485 McCabe Way
Irvine, CA 92714

1

Naval Research Lab
Attn: W. Bennett
Mail Code: 7926
Washington, DC 20375

1

A decorative rectangular border with a repeating scroll-like pattern surrounds the central text.

MISSION of Rome Air Development Center

RADC plans and executes research, development, test and selected acquisition programs in support of Command, Control Communications and Intelligence (C³I) activities. Technical and engineering support within areas of technical competence is provided to ESD Program Offices (POs) and other ESD elements. The principal technical mission areas are communications, electromagnetic guidance and control, surveillance of ground and aerospace objects, intelligence data collection and handling, information system technology, ionospheric propagation, solid state sciences, microwave physics and electronic reliability, maintainability and compatibility.